ACTIVE SCREEN PLASMA SURFACE ENGINEERING OF AUSTENITIC STAINLESS STEEL FOR ENCHANCED TRIBOLOGICAL AND CORROSION PROPERTIES

by SANTIAGO CORUJEIRA GALLO

A thesis submitted to

The University of Birmingham

for the degree of

DOCTOR OF PHILOSOPHY

School of Metallurgy and Materials

College of Engineering and Physical Sciences

The University of Birmingham

January 2009

Abstract

Low temperature plasma surface engineering has proved to be a useful method for increasing the hardness and wear resistance of austenitic stainless steel without reducing the corrosion resistance of this alloy. Plasma carburising is of particular interest as it produces a thicker hardened layer than plasma nitriding, and an equivalent improvement in the tribological and corrosion performance of the base material.

In this project, the novel active screen (AS) plasma technique was used to carburise austenitic stainless steel AISI 316. The layers of carbon expanded austenite obtained after active screen treatments were compared with the one produced by conventional direct current (DC) plasma treatments. The hardening and wear resistance produced by AS and DC plasma carburising were equivalent. With regard to corrosion, the AS treated material performed better than its DC counterpart as a consequence of the improved surface quality achieved with the former.

The mechanism of AS carburising was comparatively studied with its AS nitriding counterpart. Different experimental arrangements and two plasma diagnostic techniques were used for this purpose: optical emission spectroscopy and electrostatic probes. The evidence shows that AS nitriding relies on the deposition of iron nitrides and the active species in the plasma to produce hardening, whilst AS carburising relies on plasma activation and moderate ion bombardment.

Finally, the working principles of AS plasma furnaces are discussed with regard to the generation of additional charged particles and their electrostatic confinement.

Acknowledgements

In first place, I would like to express my gratitude to Prof. T. Bell and Dr. H. Dong for giving me the chance to develop this project in the Surface Engineering Group. I also want to thank Dr. E. Forlerer, from Comisión Nacional de Energía Atómica (CNEA-CAC), for her continuous assistance and encouragement.

I would like to extend my appreciation to the following institutions, which made vital financial contributions to this research project: Roberto Rocca Education Programme, Alßan Programme (scholarship E05M060379AR), The University of Birmingham, and Universidad Tecnológica Nacional (UTN-FRBA).

I must acknowledge the help I received from members of the Centre for Electron Microscopy, specially Ms. M.Q. Chu and Dr. Y.Y. Tse, and also Dr. J. Bowen and Dr. X. Y. Li, for their help with different microscopy techniques. I am also grateful to Dr. V. R. Machavaram, Dr. L. Wang and Prof. G. F. Fernando, whose assistance was very important for the development of the optical fibre probe; and I am enormously thankful to Prof. N. Braithwaite, from the Open University, for his valuable discussions and advice on electrostatic plasma diagnostic techniques.

It would be unfair not to mention here the constant help and support I received from all the academic community in Metallurgy and Materials, especially from research fellows, technicians and colleagues. This project would simply not have been possible without them; and I want to thank Mr. M. T. Cunningham in particular for keeping an eye on, virtually, every daily issue.

Finally, I would like to express my deepest gratitude to my family and friends, for their joy in the moments of success and their support in the difficult times.

TABLE OF CONTENTS

List of tables

List of figures and illustrations

List of abbreviations and acronyms

AFM	Atomic Force Microscopy
AS	Active Screen
ASP	Active Screen Plasma
ASPC	Active Screen Plasma Carburising
ASPCN	Active Screen Plasma Nitrogen enhanced Carburising
ASPN	Active Screen Plasma Nitriding
ASS	Austenitic Stainless Steel
BS	British Standards
BSE	Back Scattered Electron (imaging)
CCD	Charge - Coupled Device
CF	Corrosion Factor
COF	Coefficient of Friction
COM	Crystal Orientation Map
CSL	Coincident Site Lattice
CVD	Chemical Vapour Deposition
DC	Direct Current
DCPC	Direct Current Plasma Carburising
DCPCN	Direct Current Plasma Nitrogen enhanced Carburising
DCPN	Direct Current Plasma Nitriding
EA	Expanded Austenite
EBSD	Electron Back Scattered Diffraction
EDP	Electron Diffraction Pattern
EDX	Energy Dispersive X-Ray spectroscopy
EEDF	Electron Energy Distribution Function
fcc	face centred cubic
FEG	Field Emission Gun
FP	Floating Potential
GDOES	Glow Discharge Optical Emission Spectroscopy
IFP	Ion Flux Probe
LBC	Load Bearing Capacity

LTE	Local Thermal Equilibrium
M_S	Martensitic transformation Start temperature
M_F	Martensitic transformation Finish temperature
OES	Optical Emission Spectroscopy
OM	Optical Microscopy
PC	Plasma Carburising
PE	Para - Equilibrium
PIPS	Precision Ion Polishing System
PMT	Photo Multiplier Tube
PN	Plasma Nitriding
PSE	Plasma Surface Engineering
PVD	Physical Vapour Deposition
RS	Residual Stresses
SE	Surface Engineering
SEI	Secondary Electron Image
SEM	Secondary Electron Microscopy
TEM	Transmission Electron Microscopy
UT	Un-Treated substrate material (in reference to AISI 316)
XRD	X-Ray Diffraction

CHAPTER 1: INTRODUCTION

Austenitic stainless steels are commonly selected because of their high corrosion resistance, which is the main advantage of these alloys. On the other hand, low hardness and wear resistance are usually mentioned among their downsides. Surface engineering processes have been traditionally used to improve these aspects. Furthermore, thermochemical treatments conducted at low temperature are a valuable method to improve the tribological performance of austenitic stainless steel, without affecting the corrosion behaviour of this alloy. This is achieved by the formation of a supersaturated solution of carbon or nitrogen in austenite, usually called *expanded austenite*, which confers significant hardening, increased tribological performance, and corrosion resistance comparable or even superior to the untreated substrate.

Several processes can be used to produce the so called expanded austenite layers. The evidence indicates that plasma treatments outperform the conventional gas processes in terms of operative costs and environmental friendliness. DC plasma thermochemical treatment is a well-established technology, although some intrinsic defects of this technique, such as edge effects, hollow cathode effects and arcing, have blighted their industrial potential. To this end, a novel active screen plasma technique has shown its potential to solve the problems of DC plasma treatments. The benefits are principally related with a considerable improvement in the surface quality and the uniformity of the diffusion layer.

Whilst most of the work on active screen has been focused on nitriding, very little work has been conducted on active screen plasma carburising. The latter treatments are of interest because they produce thicker layers of expanded austenite, with a smoother gradient of chemical composition and mechanical properties. Thus, carbon expanded austenite shows hardening effect, wear resistance and

corrosion resistance comparable to nitrogen expanded austenite, but with increased layer thickness and additional load bearing capacity. Moreover, the better surface quality obtained with active screen plasma carburising, compared with the DC plasma technique, yields greater improvement in the performance of the substrate.

Even though the effectiveness of the active screen plasma technology is a fact, the mechanisms involved in this treatment remain unclear. This makes it difficult to optimise the processing conditions, and it also generates some scepticism among the potential users. Therefore, the present work has been directed at developing active screen plasma carburising (ASPC) technology to enhance the corrosion and wear properties of austenitic stainless steel. The scientific and technological objectives of the present project are the following:

- To explore the feasibility of active screen plasma carburising of AISI 316 austenitic stainless steel, to form carbon expanded austenite.
- To study the effect of different treatment parameters (i.e. pressure, gas composition and bias) on the ASPC process and optimise it.
- To conduct systematic characterisation on ASPC treated materials.
- To assess the wear and corrosion properties of the ASPC treated AISI 316 austenitic stainless steel.
- To develop and use plasma diagnostic techniques to evaluate the active species in ASP and advance the scientific understanding of carbon mass transfer and carburising mechanism involved in ASPC.

CHAPTER 2: LITERATURE REVIEW

1. Stainless steel

1.1. Introduction, history and development

There is no doubt that the field of materials engineering is now developing faster than at any other time in the history of mankind, and that the rate of innovation continues to accelerate. The diagram in figure 2.1.1-1 summarises the historical evolution of the different classes of materials [1]. The increasing number of choices of materials provides a better coverage of the applications' demands, but this also represents a great challenge for design engineers to select the optimum one.

The difficulties associated with the selection of engineering materials have been addressed by Ashby in his book *Materials selection in mechanical design*. The use of indices based on the materials properties, relevant for a given application, helps in the identification of the most convenient class of materials. Furthermore, by plotting these indexes in so called *materials selection charts*, the range of applicability for each material class becomes evident. Some of these charts will be used here as a reference frame for the material of interest to this thesis, i.e. austenitic stainless steel.

With regard to physical and mechanical properties, it is possible to say, from the charts displayed in figures 2.1.1-2 to 2.1.1-4, that steel covers a wide range of strength values, with a high level of stiffness and toughness, only penalised by its high density. In addition to this, figure 2.1.1-5 shows that the relative cost of steel is low compared to other engineering alloys, although this chart is not updated and the information is not as reliable as the other three charts.

In any case, it is this combination of good mechanical properties and low cost which makes steel an extremely valuable material for engineering applications, and stainless steel inherits these general properties, to some extent. However, it is its high corrosion resistance that makes stainless steel unique. As it can be seen from the materials selection chart in figure 2.1.1-6, stainless steel shows excellent corrosion resistance in a wide range of harsh environments, putting it ahead of other engineering alloys.

For over a hundred years, several scientists (including Berthier, Baur, Hadfield, Osmond, Faraday and Stodart) had collected evidence regarding the corrosion properties of iron-chromium alloys, but it was not until early in the 20th century that the commercial potential of such material became evident [2, 3]. Harry Brearley is usually referred to as the inventor of a ferritic Fe - 13% Cr alloy firstly called “rustless steel”, which subsequently became “stainless steel”. Although the discovery of the alloy is disputed by Strauss, Maurer and Monnartz, Brearley was undoubtedly the first one to identify an application and to commercialise stainless steel products, in the form of cutlery. In Germany, Maurer and Strauss developed, in parallel, an austenitic alloy of Fe-Cr-Ni, which was soon applied in the food and chemical industries, in Europe and in the United States.

From then onwards, the development of stainless steel was very fast, impelled by the great number of industrial and domestic applications. Significant work was conducted to research and develop ferritic, martensitic and the well known austenitic alloys with a number of different alloying elements. In all cases, high chromium contents in excess of 10% are required to form a stable passive oxide film on the surface and exert the characteristic resistance to corroding agents [4].

There is no doubt that the distinct property of stainless steels is their corrosion resistance. As it is usual in engineering applications, this property is attained at the expense of other factors, such as hardness,

strength, toughness, weldability, formability, creep resistance, etc. Consequently much of the work done on stainless steel has been focused on improvements of these other mechanical, engineering and manufacturing characteristics [5].

An impressive level of refinement has been achieved in the metallurgical practices to produce stainless steel with a wide range of properties. In the next section, stainless steels of different compositions and phases will be introduced, and a summary of their advantages, disadvantages and applications will be presented.

1.2. Classification

Stainless steels are usually classified according to their phase constitution, i.e. martensitic, ferritic, austenitic or duplex. The stability of these phases is dictated by the alloying elements, which can be separated in two main groups: α forming elements and γ forming elements [6]. Two main constituents of stainless steels, chromium and nickel, head each group, and it is customary to express the contribution made by all the elements in the alloy as *chromium equivalent* and *nickel equivalent* according to the following equations:

$$\%Cr \cdot equivalent = (Cr) + 2 \cdot (Si) + 1.5 \cdot (Mo) + 5 \cdot (V) + 5.5 \cdot (Al) + 1.75(Nb) + 1.5(Ti) + 0.75(W) \qquad (2.1\text{-}1)$$

$$\%Ni \cdot equivalent = (Ni) + (Co) + 0.5 \cdot (Mn) + 0.3 \cdot (Cu) + 25 \cdot (N) + 30 \cdot (C) \qquad (2.1\text{-}2)$$

where the element symbols between brackets represent the alloy composition expressed as mass fraction (wt%).

By plotting these two parameters, the Schaeffler diagram shown in figure 2.1.2-1 is obtained, which gives a rough but generally good map of the phases that can be expected for a given alloy composition and, consequently, its mechanical properties. In this way, it is possible to see that high chromium equivalents render martensitic and ferritic structures, while high nickel equivalents stabilise the austenitic phase. Notwithstanding, the design of the alloy composition is a rather more complicated matter which involves both technical and economical factors. It is usually intended to produce the best possible material for a given application at the lowest possible cost and, as it is the case for most engineering alloys, heat treatments play an important role in this regard.

It is important to mention that other phases, intermetallic compounds, carbides and nitrides are commonly found in the Fe-Cr-Ni system with addition of other alloying elements, e.g. Ti, V, Mo, Co, Mn, Al, Nb, C, N. Although present in only small fractions, these secondary phases can significantly affect the metallurgical characteristics, corrosion properties and mechanical properties of stainless steels. Some of them will be briefly introduced in the following sections.

In what follows, each one of the generic categories of stainless steel will be examined in some further detail.

1.2.1. Martensitic stainless steels [5-8]

These alloys typically contain 12% to 17% Cr and 0.1% to 1.0% C with additions of other alloying elements such as Mo, V, Nb, Al and Cu. The austenitic structure, which is stable over 1050ºC, undergoes full martensitic transformation on cooling, producing components with high strength and hardness, but also low toughness. Therefore, it is necessary to temper these alloys at the highest

possible temperature in order to obtain a good combination of mechanical properties, namely strength, toughness and ductility.

Alloying elements such as Mo, W, V and Nb are of interest to increase the tempering resistance by secondary hardening reactions, which increase the strength but also reduce the toughness and the resistance to stress corrosion. In addition, their tendency to retain δ ferrite has to be balanced by austenite forming elements. The allowable amount of C and N is limited because these elements significantly reduce the toughness, so that Ni, Co, Mn and Cu have to be used, thus increasing the cost of the alloy. In addition, this introduces another detrimental effect since the M_S - M_F temperature range is depressed, thus a small fraction of austenite can be retained at grain boundaries and subsequently transformed to martensite during tempering, causing distortion and embrittlement. The austenite forming elements also lower the A_{C1} temperature, and consequently limit the range of tempering conditions.

This rather delicate balance between alloying elements acquires one more degree of complexity when considering the precipitation hardening effects associated with additions of Ti, Al, Cu and Mo. The precipitation of intermetallic compounds provides an alternative hardening and strengthening mechanism, independent of the carbon content. The strength and ductility can usually be tailored by changing the tempering temperature, although some large intermetallic particles (Fe_2Mo) and secondary phases (Cr rich α'-phase, Fe-Cr-Mo χ-phase) can form on over-ageing, leading to severe embrittlement.

In summary, the advantage of martensitic stainless steels is their high strength and high hardness, but this is achieved at expense of the corrosion resistance. The applications include tools, gears, shafts, valves, bearings, engine and wear resistant parts in chemical and petrochemical industries, hydroelectric power generation and aeronautic applications.

1.2.2. Controlled transformation and precipitation hardening stainless steels [5, 6, 8]

Martensitic stainless steel components were found to be difficult to produce in the fully hardened condition, and complex shapes could not be heat treated without severe distortions. Therefore, there was a requirement for a stainless steel with a preliminary austenitic structure to permit good formability, which could subsequently undergo martensitic transformation and produce precipitation hardening, keeping a high tempering and corrosion resistance. It is not difficult to recognise the metallurgical challenges associated with such requirements.

In order to fulfil the specifications, the alloy requires low C content and 16% to 19% Cr, balanced with austenite forming elements (typically 4% to 7% Ni and/or Mn) to reduce the tendency to form δ ferrite, but keeping M_S high enough to allow martensitic transformation when necessary. The alloy composition to produce the right balance between δ ferrite and M_S is critical. Furthermore, Mo and V are added for tempering resistance and Ti, Al, Cu and Co to induce precipitation hardening.

The martensitic transformation can be induced by refrigeration (sub-zero heat treatment) or by a primary ageing treatment to precipitate $M_{23}C_6$ and control the amount of C in solution, available for the martensitic transformation (increase in M_S). Cold working is an alternative way, though not usually relied upon because the transformation is not uniform. Although achievable, the accurate adjustment of the M_S - M_F temperature range is difficult and requires stringent control of the alloy composition, with an obvious impact in the economical viability. Therefore, most of these alloys are manufactured in the fully transformable and precipitation hardened condition.

The applications are very limited and include the skin of high speed rockets and aircraft, high strength stainless fasteners, wire and cables.

1.2.3. Ferritic stainless steels [5-8]

As their name indicates, these are ferritic alloys up to the melting point, containing 17% to 26% Cr, and only a small fraction of austenite forms at high temperature depending on the amount of other alloying elements, mainly C and N. The ferritic structure is stronger than the austenitic one, and the absence of Ni in their composition represents a significant advantage over the austenitic counterparts in terms of cost, although they are penalised in corrosion resistance, formability and toughness.

The occurrence of Fe-Cr σ-phase, Fe-Cr-Mo χ-phase and Cr rich α'-phase is of importance in ferritic stainless steel and can lead to some embrittlement phenomena. Care should also be taken to avoid embrittlement by martensitic transformation of the retained austenite present at grain boundaries in alloys with high content of austenite forming elements. Moreover, alloys containing Ni, Co, Mo, Ti, Al additions precipitate β-phase intermetallic compounds, which together with carbides ($M_{23}C_6$ and M_7C_3) and nitrides (M_2N) reduce the toughness. This list of embrittlement effects explains why ferritic stainless steels exhibit ductile to brittle transition temperature, and puts into evidence one of the main weak points of these alloys: their low toughness.

On the other hand, the same mechanisms that reduce ductility also produce strengthening, so ferritic stainless steels are superior to the austenitic ones in terms of yield and ultimate stresses. The stacking fault energy is higher, thus ferritic stainless steels have low work hardening rate, which reduces the flow stresses upon forming but affects the uniform strain and stretch formability. On hot rolling, a problematic crystallographic texture called *roping* develops and, while being very ductile, ferritic stainless steels are also soft and can get easily marked.

The corrosion resistance of ferritic stainless steels is appropriate in mild corrosive environments, although in the most severe conditions they do not perform as well as their austenitic counterparts. Addition of molybdenum increases their corrosion resistance, and stabilisation with Ti and Nb helps to avoid grain boundary attack due to precipitation of chromium carbides. Perhaps one of the greatest advantages offered by ferritic stainless steels is their high resistance to stress corrosion cracking, making them interesting for applications in chemical plants.

Ferritic stainless steels are increasingly displacing austenitic stainless steels in the less demanding applications, mainly because of economic reasons. Efforts have been made to improve their weldability and toughness, and thus increase the range of applications, which is for the moment focused on indoor stainless applications.

1.2.4. Duplex stainless steels [5-9]

Duplex stainless steels were developed in an attempt to fuse in one material the positive aspects of austenitic and ferritic alloys. Therefore, they are constituted by a ferritic-austenitic or ferritic-martensitic duplex structure with a typical composition of 18% to 30% Cr, relatively low Ni content and some additions of Mo, Nb and Ti. The reduction in the amount of Ni provides some cost reduction over the austenitic stainless steels, while having superior yield and ultimate stresses, and resistance to corrosion and pitting that compares favourably with the austenitic benchmark alloy.

The presence of ferrite and the induced reduction in the grain size of austenite increases the strength. Moreover, the austenite undergoes martensitic transformation upon deformation, increasing the strength to even higher levels than the pure ferritic structures. This is achieved without a significant reduction in toughness, which is somewhere between the austenitic and ferritic alloys. The physical and mechanical

properties can be widely tailored by changing the volume fraction of each phase, which at the same time depends on the alloy composition and processing conditions.

The relatively high occurrence of secondary phases is perhaps the weakness of duplex stainless steels, and several embrittlement effects have been reported in the temperature range 300ºC - 1000ºC, related to Fe-Cr-Mo σ and χ-phases, Fe-Mo-N π-phase, and some degree of partitioning of alloying elements between the austenitic and ferritic phases. Nevertheless, appropriate heat treatments and cooling rates seem to be successful in avoiding or minimising these effects.

The applications of these alloys are expanding and, due to their high corrosion resistance and good mechanical properties, include: chemical, petrochemical, oil, wood pulp, pharmaceutical, textile and nuclear industries.

1.2.5. Austenitic stainless steels [4-8, 10, 11]

Austenitic stainless steel (ASS) is undoubtedly the most widely used, and currently accounts for 70% to 80% of the stainless steel world production volume, with its emblematic 18/8 composition, i.e. 18% Cr and 8% Ni. ASS typically contains 18% to 25% Cr and 8% to 20% Ni, making them fully austenitic and consequently non-magnetic, although martensitic phase transformation may occur during deformation. Additions of Mo and other alloying elements further increase its outstanding resistance to general and pitting corrosion, and it is this property that makes it unique, not so its mechanical properties, which are meagre.

In general, austenitic stainless steel is the first choice in the most severe corrosive conditions. The C content of these alloys is usually kept at very low levels to avoid precipitation of $Cr_{23}C_6$ carbides at grain

boundaries, which significantly reduce their corrosion resistance. Ti and Nb can also be added to produce the so called *stabilised* grades. The high Ni and Mo contents make ASS an expensive material, although its relative cost compares favourably with other non-ferrous alloys, e.g. Ni or Ti based alloys. Some attempts have been made to use Mn, Cu and N to replace Ni in the alloy composition with some degree of success, although the corrosion resistance is inferior to the traditional Ni alloyed ASS.

To complete the selection grid, ASS is tough and shows no ductile-brittle transition temperature, it is easily weldable and, having a low yield stress, it exhibits high ductility and is especially suitable for stretch forming. Nevertheless, its low resistance to stress corrosion cracking, low ultimate stress and low hardness pose some limitations in its applications.

Being the subject of this research project, the metallurgical aspects, corrosion properties and wear resistance of ASS, and of AISI 316 in particular, will be discussed in further detail in the following sections.

1.3. Metallurgical aspects and properties of ASS – AISI 316

The Fe-Ni-Cr ternary phase diagram is the basis for the study of ASS. Additions of Ni and other austenite stabilising elements expand the γ loop and, with sufficiently large amounts, make the austenitic structure stable (or metastable) up to room temperature [12]. In general, the effect of alloying elements depends on the composition of the material to which they are added, and that is the case of chromium in ASS. Being an α stabilising element, chromium tends to shrink the γ loop, although in the presence of Ni it retards the $\gamma \rightarrow \alpha$ transformation. From the ternary phase diagram in figure 2.1.3-1, it is possible to conclude that the 18% Cr - 8% Ni composition minimises the amount of Ni for a fully

austenitic structure [4, 13]. This basic 18/8 composition is subsequently modified to obtain the properties of interest.

The typical chemical compositions of commercial ASS alloys are shown in table 2.3-1. Differences in composition and processing conditions have a profound effect in the type and volume fraction of the secondary phases present in the alloy and, consequently, in their physical and mechanical properties [14]. A detailed and comprehensive description of the secondary phases observed in ASS is out of the scope of this review and only the ones most significant to the material under study (i.e. AISI 316) will be discussed, namely: martensite, carbides and intermetallic phases (σ, χ and Laves phases) [15].

1.3.1. Martensite

By calculating the Cr and Ni equivalents with equations (2.1-1) and (2.1-2), and making use of the Schaeffler diagram in figure 2.1.2-1, it is evident that the basic 18/8 composition of ASS is on the border line of the pure austenitic structure domain [5]. The Ni content of these ASS is only enough to reduce M_S to just below room temperature, and substantial martensitic transformation takes place if the material is cooled to sufficiently low temperatures [4]. The M_S temperature is determined by the chemical composition of the alloy and the following equation can be used as a reference [6]:

$$M_S[^oC] = 502 - 810(C) - 1230(N) - 13(Mn) - 30(Ni) - 12(Cr) - 54(Cu) - 6(Mo) \qquad (2.1\text{-}3)$$

where the element symbols between brackets represent the alloy composition expressed as mass fraction (wt%).

It is interesting to note that all the alloying elements have the same effect: reduce M_S and thus stabilise the austenite against martensitic transformation [16]; the effect of Ni being twofold: it stabilises the austenitic structure and lowers the M_S temperature [5]. In this way, AISI 316 exhibits higher stability to martensitic transformation, compared to the basic 18/8 AISI 304 [17]. However, the γ (fcc) structure is said to be metastable at room temperature and martensitic phase transformation can occur on plastic deformation at temperatures even higher than M_S [16].

To explain this phenomenon it is useful to recall the thermodynamic basics of the phase transformation: in order to happen, the transformation has to reduce the free energy of the system and, at the same time, sufficient energy must be given for the system to initiate the transformation (activation threshold). The schematics in figure 2.1.3-2 illustrates these principles, so that if T_O is the equilibrium temperature for the γ and α phases, the transformation will occur spontaneously below M_S since the thermal energy at that point is enough to mount the activation threshold ΔG_{th}. Between T_O and M_S, the γ phase is not thermodynamically stable, but the thermal energy is insufficient to initiate the transformation. It is in this region that the transformation can be activated by plastic deformation, taking the name of *strain induced martensitic transformation* [16, 18]. Hence, a reference temperature M_{d30} can be estimated, from the alloy composition, using the following equation [6]:

$$M_{d30}[^{o}C] = 497 - 462(C+N) - 9.2(Si) - 8.1(Mn) - 13.7(Cr) - 20(Ni) - 18.5(Mo) \qquad (2.1\text{-}4)$$

where M_{d30} is the temperature at which 50% martensite is obtained under a true strain of 0.3, and the element symbols between brackets represent the alloy composition expressed as mass fraction (wt%).

Figure 2.1.3-3 shows the strain induced martensitic transformation, for a given ASS alloy composition, as a function of the temperature and the strain [18]. This behaviour was found to be the result of the competition of two deformation modes. At low temperatures, no slip takes place and all the deformation is due to martensitic transformation, whilst at higher temperatures, slip becomes dominant and the martensitic transformation decreases [16].

The inset of martensite has a marked effect in the corrosion and mechanical properties of AISI 316, and some of these effects will be mentioned in following sections.

1.3.2. Carbides

Carbides and, to lesser extent, nitrides have attracted particular attention in high alloy steels, and ASS is no exception. The mechanical properties and corrosion performance of ASS are significantly affected by precipitation of carbides and nitrides, being beneficial at times, but catastrophic in some other cases [6]. The effect of these phases is very much dependent on their composition, stoichiometry, morphology and precipitation sites [19]; whilst the kinetics of precipitation is mainly governed by the availability of carbon, nitrogen and carbide/nitride forming elements in the alloy, together with some energetic considerations related to diffusion [20, 21].

As it is evident from figure 2.1.3-4, the solubility of carbon in austenite is reduced by the chromium content, to about 0.05% in the case of the 18/8 ASS [4]. Therefore, carbon contents in the order of 0.05% or higher will remain in solution in the austenitic structure only if the material is solution treated and quenched. However, during heat treatments or slow cooling in the temperature range 550ºC - 800ºC, precipitation of carbides takes place. Below 500ºC, precipitation is hindered by the low mobility of substitutional elements [22].

The most common carbides in ASS are of the type $M_{23}C_6$, although other carbides also precipitate according to the reference sequence presented in figure 2.1.3-5. The letter M accounts for transition elements (e.g. Fe, Cr, Ni, W, Mo) and carbides of mixed composition are usually found, depending on the temperature of the ageing treatment and the composition of the alloy [5]. However, the chromium carbide has received special attention because of its implications for the corrosion properties of ASS, and will be discussed in one of the following sections.

The $M_{23}C_6$ carbide is fcc in structure, with a lattice parameter about three times that of austenite, and grows with a cube on cube orientation relationship [23]:

$$\{100\}_{\gamma} \parallel \{100\}_{M_{23}C_6}$$

$$\langle 010\rangle_{\gamma} \parallel \langle 010\rangle_{M_{23}C_6}$$

Regarding location, carbides are prone to follow the precipitation sequence: random grain boundaries, non-coherent twin boundaries, coherent twin boundaries and, finally, intragranular dislocations [19, 20, 23]. This phenomenon puts into evidence the existence of a carbon content threshold and an energy threshold inversely proportional to the interfacial energy of the grain boundary [24].

Upon long ageing treatments, cellular precipitates can form at grain boundaries, together with MC_{1-X} and M_6C carbides [5, 23, 25]. Although they are important for the mechanical properties of ASS, and particularly to its creep resistance, these precipitates are of no significant relevance to this particular project and thus will not be treated in detail.

1.3.3. Intermetallics

A number of intermetallic compounds may precipitate in ASS, depending on the alloy composition, during relatively long ageing heat treatments [15]. These usually involve some degree of partition of alloying elements, and thus affect the mechanical and corrosion properties. Table 2.3-2 lists some of the most common phases, and figure 2.1.3-6 shows some experimental observations on the time-to-precipitation in ASS at 550ºC - 600ºC. The formation and evolution of these secondary phases have been extensively discussed and remain disputed, although evidence indicates that the presence of δ ferrite has a strong effect in their occurrence and that they nucleate and grow faster through a collaborative-eutectoid reaction [26].

The Fe-Cr σ-phase is, perhaps, the most studied intermetallic phase in ASS, and has negative effects in toughness and corrosion resistance [15]. Increasing contents of Cr, Mo and Si are known to ease precipitation of σ-phase and the presence of δ ferrite, being richer than austenite in these alloying elements, provides nucleation sites. Furthermore, the diffusion rate of Cr and Mo is significantly higher in ferrite than in austenite, thus requiring shorter times and lower temperatures for precipitation of σ-phase to occur. At the same time, the solubility of carbon in σ-phase is very low, so that this phase usually precipitates in carbon impoverished regions, i.e. after precipitation of $M_{23}C_6$ carbides [27]. According to calculations done by Sourmail and Bhadeshia [28], the precipitation of σ-phase is more difficult than $M_{23}C_6$ carbides, and is consequently restricted to high energy sites in the microstructure.

The (η) Fe_2M Laves phase (where M usually represents Mo, Nb or Ti) is a hexagonal intermetallic compound found in minor volume fractions in ASS, and exhibits similar precipitation kinetics to σ-phase, although there is no general agreement on the temperatures and times required for this precipitation to take place [25]. Laves phase has been reported as a transient phase, preceding the formation of M_6C

carbides [23]. Retained δ ferrite hinders the formation of Laves phase, and the latter shows some competitive interaction with σ-phase and also χ-phase [26].

χ-phase is a Fe-Cr-Mo intermetallic compound that may precipitate in ASS in minor quantities and after longer soaking times at relatively high temperatures, typically over 750ºC [23]. Its formation is related to the presence of $M_{23}C_6$ carbides and δ ferrite in the primary microstructure [29], and it is mainly found in AISI 316 at high ageing temperatures.

Other precipitates, although of importance to the properties and applications of ASS, have not been mentioned in this section because of their low incidence in this particular study, and they will be introduced at a later stage only when necessary. Some examples are: G-phase silicide, Z-phase carbide, nitrides, phosphides, sulphides, copper and nickel containing intermetallics.

The following section deals with the corrosion properties of ASS, and relates some of the metallurgical features here presented with their iconic corrosion resistance.

1.4. Corrosion properties of AISI 316

The corrosion resistance is the most important property for ASS, and these alloys were designed and are usually selected for service under mild to severe operating conditions. A suitable grade of stainless steel will generally serve well for many years, but the selection of the wrong grade or heat treatment can lead to catastrophic failures [30]. This is because ASS owe their corrosion resistance to the formation of a passive film at the surface, which isolates and protects the bulk material from the corrosive environment. The nature of the passive film is dynamic, and dissolution and repair take place

continuously, although under especial conditions this protective layer may be destroyed, leading to severe corrosion [2, 31].

The existence and protective role of this oxide film was first proposed by Faraday, but confirmation had to wait for many years until a suitable method was developed to isolate it and to study it [32-34]. From then onwards, much research work has been conducted on the nature of this passive layer, and the properties that different alloying elements impart to it, given that the electronic properties of the film are believed to play an important role on its stability through ion and electron transport reactions [35, 36]. To this end, the fundamental explanation is still a matter of dispute, but it is widely accepted that the availability of oxygen is crucial for the formation of the passive film; chromium is the main and most important constituent, although minor additions of other alloying elements also have an important effect.

The content of chromium is critical to provide the steel with corrosion resistance, and the minimum amount required is a function of the operating conditions, namely the type of acid, its concentration and temperature. As a general rule, the onset of a passive film is found at chromium contents in the order of 12% [37], although 17% to 20% is usually required to impart passivity to ASS in many corrosive environments [2, 31]. In any case, higher chromium contents do not always improve corrosion resistance, and the opposite trend may be observed in some acids, for example sulphuric and hydrochloric.

The effect of nickel in the corrosion properties of ASS depends on the presence and quantity of other alloying elements, as some kind of synergistic effect with chromium has been suggested [2]. For the particular amounts and proportions found in ASS, nickel is reported to promote repassivation and

increase the corrosion resistance in reducing and mineral acids, while having a weak but beneficial effect on pitting corrosion [2, 31, 38].

Additions of molybdenum produce a marked improvement in the resistance of ASS against reducing acids, pitting and crevice corrosion [2, 31]. Even though molybdenum is not an integral part of the passive Cr-rich film, it was found to stabilise it, particularly in the presence of chlorides [36]. On the other hand, ASS with large amounts of this alloying element are prone to segregation and precipitation of secondary phases and, consequently its use is limited to moderate contents [39].

Nitrogen is beneficial in reducing the segregation of Mo-containing phases and providing further resistance to pitting corrosion [31]. Silicon, vanadium, tungsten and copper are respectively found to provide some beneficial effects to ASS under different service conditions [38]. Figures 2.1.4-1 and 2.1.4-2 show the schematics of the polarisation curve of ASS in sulphuric acid and the effects of different alloying elements on it.

The corrosion resistance of ASS is defined not only by the content and proportion of alloying elements, but also by the way in which these elements are dispersed in the microstructure. In this way, segregation and precipitation of secondary phases play a very important role in determining the form of corrosion, i.e. general corrosion or some localised attack of the kind of pitting, crevice, intergranular corrosion, or even galvanic corrosion [31].

Perhaps the most important phenomenon for the corrosion resistance of ASS, and one that has taken much attention from researchers, is the precipitation of chromium carbides of the form $M_{23}C_6$. The negative effect is not a product of the carbide itself, but of the depletion of chromium in the area

surrounding the precipitate, where corrosion takes place in a very rapid way [40, 41]. This phenomenon is usually referred to as *sensitisation* and may lead to intergranular corrosion and, ultimately, to the complete failure of the component in service.

In order to avoid sensitisation, the carbon content of ASS is kept at the lowest possible level, at expense of the mechanical properties, and other alloying elements (Ti, Nb) might also be added as stabilisers, i.e. to combine with the remaining carbon and form MC carbides instead of the harmful $Cr_{23}C_6$ [2, 38]. At the same time, heat treatments or slow cooling in the temperature range 550°C - 800°C should also be avoided.

Precipitation of carbides has also been found to depend on the crystallography of grain boundaries, with random grain boundaries being more prone to precipitate carbides and also some other secondary phases, as opposed to the coherent twin boundaries [19, 20, 42]. This is a result of the high number of atoms common to both grains of the coherent twin boundary, which reduces the energy of the boundary [43]. More recent studies have reported some correlation between the crystallographic texture [44] and also the type, distribution and connectivity of grain boundaries [45, 46], with the corrosion behaviour of the alloy.

These models make use of the theory of Coincident Site Lattice (CSL), which classifies the grain boundaries according to the misorientation of the neighbouring grains and, consequently, according to the fraction of coincident atoms between neighbouring lattices [47]. This is usually expressed as the reciprocal density of coincident sites Σ, and boundaries with high fraction of coincident sites, i.e. low Σ number, are believed to exhibit special properties [48]. In the case of alloys of low stacking fault energy,

Σ3 twin boundaries are the simplest and most prominent ones because of their high number fraction and length fraction [47, 49].

A grain boundary can be defined by five parameters or, in other words it can be said to have five degrees of freedom: 3 account for the crystallographic relationship between neighbouring lattices and 2 define the plane orientation of the grain boundary [49]. Therefore, the CSL model is not restrictive enough inasmuch as it fails to account for the plane orientation of the grain boundary [48, 50]. Consequently, a coincident site relationship between neighbouring lattices does not always imply a coincident site boundary or special boundary [43]. Nevertheless, the CSL theory is useful to categorise grain boundaries in view of the relative difficulty to define all five degrees of freedom [50].

Finally, the presence of deformation slip bands and also MnS inclusions in the microstructure can reduce the corrosion performance of ASS [38]. The latter inclusions are reported to be favourable sites for pitting. Generally speaking, every discontinuity or weak point in the passive film will be susceptible to corrosion (figure 2.1.4-3).

H. Brearly, known as the father of stainless steel, used to be called *the inventor of the knife that would not cut*. This rather anecdotal comment on the difficulties found in keeping stainless steel knives sharp is timely when introducing one not so positive aspect of these alloys: their low hardness and wear resistance.

1.5. Tribological properties of AISI 316

As opposed to corrosion, the wear properties of ASS are moderate, and it is fair to say that ASS are not usually selected because of their tribological performance (figure 2.1.5-1). However, it is sometimes

difficult to completely avoid sliding or tribological interactions of some kind during service [51, 52]. Furthermore, ASS could be selected because of their corrosion resistance or their non-magnetic nature, at the expense of the wear performance. In any case, the wear properties of ASS are of interest in order to select the material correctly and predict its failure.

The phenomenon of wear involves several material properties (e.g. strength, hardness, toughness, thermal conductivity) and also the operating conditions (e.g. contact geometry, load, sliding speed, temperature). Therefore, it can be said that wear poses a problem with a relatively high level of complexity. The models and theories proposed in the literature are usually limited to a relatively small range of materials and conditions, and the diversity of theories and terminology can be misleading.

For the sake of clarity, and at the expense of accuracy, the different wear mechanisms will be introduced by using the wear map shown in figure 2.1.5-2 [53-55]. The normalised pressure and normalised velocity are respectively defined as:

$$\tilde{F} = \frac{F}{A_n \cdot H} \qquad (2.1\text{-}5)$$

$$\tilde{v} = \frac{v \cdot r_o}{a} \qquad (2.1\text{-}6)$$

where F is the applied load, A_n is the contact area, H is the material hardness, v is the sliding velocity, r_o is the radius of the contact area and a is the thermal diffusivity. The range of conditions relevant to this project is that of medium-low velocity and medium-high load (i.e. top left quarter of the map in figure 2.1.5.2).

The wear of ASS has been studied by a number of authors, under different testing conditions [52, 56-61]. There is a good degree of coincidence in the experimental results and observations, although not so with regard to the fundamental explanation of the wear mechanisms. In general, the poor tribological properties of ASS are associated with damage by galling or seizing [56], especially at high loads and low sliding speeds, so that it can be said that wear of severe nature takes place by adhesion [62, 63].

In this wear mode, junctions are formed between the sliding elements, at the interacting asperities, and subsequently deformed until rupture occurs, producing very rough wear tracks [64]. In this way, material is transferred from one of the contacting surfaces to its counterpart throughout sliding (figure 2.1.5-3). Furthermore, plastic flow is not confined to the interacting asperities but it extends towards the subsurface. This leads to the nucleation of cracks, which propagate parallel to the surface and are ultimately responsible for the detachment of plate like wear debris particles of large size, through a mechanism called delamination wear [65].

At low temperatures, below M_d, the strain produced at the surface and subsurface of ASS sliders is sufficient to induce martensitic phase transformation, and it is well established that the formation of martensite has a significant effect in the wear phenomenon [52, 56, 57, 66]. The thickness of the work hardened and martensite layer depend on the material and the sliding conditions, namely load and sliding speed.

Some opposing effects have been reported for this hardened layer, based on two different mechanisms. On the one hand, martensite is said to increase the hardness of the substrate and, consequently, its wear resistance [57, 62, 67]. On the contrary, other authors have reported that the austenitic substrate, even after work hardening, is not strong enough to support the hard but brittle martensite surface layer,

leading to a high rate of fracture and formation of abrasive debris particles [56]. In such a scenario, the resilience and toughness of the material are of significant importance, and the ratio of hardness to elastic modulus has been reported to be a more appropriate index than the mere hardness, to rank the wear resistance [68, 69]. Best tribological performances have been reported for combinations of high surface hardness and relatively low elastic modulus, to reduce the tendency to plastic deformation and reduce the mismatch of properties, while keeping deformation within the elastic range.

Mild wear conditions are found at some higher sliding speeds and lower loads, as can be seen in the wear map in figure 2.1.5-2. The reduced wear rates are associated with the formation of a flat and smooth protective oxide layer on the surface [57-60], and the onset of a mechanism called oxidational wear [63]. A competition is established between the removal of the oxide layer through abrasion or flaking; and the reaction and passivation of the fresh metal surfaces exposed to the environment [70]. The former depends mainly on the load, whilst the latter is a function of the temperature and, consequently, the sliding speed. Under the right sliding conditions, a thin and tough oxide layer covers the surface uniformly and exerts good resistance to wear [57].

The ductility and resilience of the oxide layer are important to accommodate the deformation of the substrate [63]. In addition, the hardness and the elastic properties of the underlying material are critical to provide the necessary support to the layer of oxide. Under stable oxidational wear conditions, the oxide layer grows up to a critical thickness, at which it becomes unstable, and it finally flakes off by the propagation of fatigue cracks.

The stoichiometry of the oxide depends on the environment and the temperature of formation, i.e. the temperature at the sliding asperities, and its effect on the wear phenomenon is of significance [58]. At

low temperatures, below 300°C, α-Fe_2O_3 forms, whilst at temperatures between 450°C and 600°C Fe_3O_4 becomes stable and over 600°C FeO is found [71]; in the presence of moisture, these oxides may also form hydroxides [60, 72]. Once again, there are some controversial reports on the effect that each specific type of oxide has over wear rates and friction, but oxides are generally associated with mild wear regimes and detachment of fine debris particles [57, 59].

With regard to friction force, coefficients in the range 0.4 to 0.7 have usually been reported for a wide range of sliding conditions. An average coefficient of friction of 0.5 can be considered with fairly ample agreement [56, 60], although some variations and fluctuations in the friction force have also been mentioned [52]. The fluctuating nature of the friction force is well known [73], and it has been associated with the interaction of surface asperities [74], wear mode transitions, and formation, trapping and detachment of large wear debris particles [75]. It is interesting to note that discontinuities in the plastic deformation at the subsurface, such as twinning and phase transformations, would also yield fluctuations and variations in friction [56].

This succinct summary of the tribological properties of ASS was intended to provide a reference frame and introduce the basic principles of wear and friction under dry sliding in air. It is clear that the poor tribological performance of ASS represents a serious limitation for many applications, which demand excellent corrosion and wear resistance. Other stainless steels or non-ferrous alloys will continue to develop and might fill part of this gap, although this is usually achieved at the expense of toughness, corrosion resistance, ferromagnetism or cost. Surface engineering offers an alternative way to improve the tribological properties of ASS at the surface level, while keeping the traditional benefits of this material.

2. Surface engineering

2.1. Introduction and basic concepts

The wide use of surface treatments and coatings to combat wear was foreseen many years ago, based on the fact that the mere use of wear resistant bulk materials can be inappropriate and expensive [76, 77]. Furthermore, the increasing level of understanding of the importance of the surface properties and surface condition to the most common failure modes, i.e. wear, fatigue and corrosion, led to the recognition of surface engineering (SE) as a key technological area [78-80].

Several definitions have been proposed, usually implying the application of processes or treatments to deliberately modify the surface of engineering components, in order to attain adequate material properties for a given application, thus providing a cost effective enhancement in performance [81, 82]. This definition involves the concept of fitness-for-purpose [83] and it is generally accepted that SE can offer benefits such as [84]:

- Enhanced functional performance and higher productivity
- Use of cheaper substrate materials
- Provide flexibility to match substrate and surface properties for a particular application

It is of paramount importance to consider both the surface and the substrate when designing or selecting a SE treatment, as it has been pointed out by many authors [76-78, 82, 83]. The concentrated loads developed during the contact and slide of rough surfaces are of significance in tribological applications [85]. The strength of the substrate and the thickness of the coating or hardened layer define the load bearing capacity and fatigue response of the system, as shown in figure 2.2.1-1 [86-88]. A complete understanding of the behaviour of the substrate/surface system under the operating conditions is, thus, crucial.

SE can be described as an old and well known practice [83], and some examples of instructions for tempering and case hardening of metal weapons and tools have been quoted in the literature, dating back to 1400 BC [81]. The innovative aspect of SE is the design approach, and the increasing awareness of the importance of the surface properties and the surface condition to the performance of the interacting surfaces [78, 84]. In view of the increasingly demanding operating conditions and the requests to reduce production costs, many industrial sectors have turned their eyes to SE, making this a blooming area of technology.

The variety of SE treatments can be appreciated in figure 2.2.1-2. The ever wider range of options, and the absence of a comprehensive system for selection constitutes a great challenge for design engineers and the choice of a particular treatment is usually based on previous empirical experience rather than on a detailed or analytical study [76, 78, 89]. For the purpose of this review, the SE treatments will be classified, very broadly, into three groups [90]:

- Those which coat the substrate: PVD, CVD, thermal spraying, etc.
- Those which modify only the structure of the substrate: induction hardening, flame hardening and shot peening.
- Those which modify the chemical composition and the structure of the substrate: thermochemical, ion implantation, etc.

The ones of significance to this project are the thermochemical or diffusion hardening processes, and they will be treated in further detail in the next section.

Finally, the environmental impact of SE must be taken into account, in view of the increasingly stringent regulations, if not for our own sake. If the energy content of one particular material is taken as a

measure of its environmental friendliness (figure 2.2.1-3), it is evident that any additional process applied to it would increase its environmental footprint. However, if the increase in performance is significant enough, the trend is reversed. SE treatments can increase the life span of the components, reduce their size and weight, decrease energy losses associated with friction, minimise or even eliminate the use of polluting lubricating oils, among other environmental benefits [91].

2.2. Thermochemical and diffusion surface engineering treatments

Thermochemical treatments, sometimes referred to as case hardening or cementation, are based on the modification of the chemical composition of the substrate material. These treatments can be succeeded by a change in the structure through heat treatment. The formal definition available in BS EN 10052:1994 reads as follows [92]:

> *Thermochemical treatment: Heat treatment carried out in a medium suitably chosen to produce a change in the chemical composition of the base metal by exchange with the medium.*

In the case of diffusion treatment, the definition in that same standard is:

> *Diffusion treatment: Heat treatment or operation intended to cause the diffusion towards the interior of the ferrous product of elements previously introduced into the surface (for example, following carburising, boriding or nitriding).*

From these definitions it becomes clear that two main factors will govern the process, namely: the exchange or absorption reaction with the medium, and the diffusion in the metal [93]. As it is illustrated in figure 2.2.2-1, the medium will determine the way in which the diffusing elements are delivered to the

metal surface. A number of different media are available (solid, liquid, gas and plasma), and a detailed account of the media used for carburising will be given in a following section.

Once in the metal, the transport of the absorbed substance takes place by diffusion, and follows Fick's laws:

$$J = -D\frac{\partial C}{\partial x} \qquad (2.2\text{-}1)$$

$$\frac{\partial C}{\partial t} = D\frac{\partial^2 C}{\partial x^2} \qquad (2.2\text{-}2)$$

where J is the flux of diffusing substance, D is the diffusion coefficient, and $\partial C/\partial x$ is the concentration gradient [93, 94]. Therefore, the transport of the substance in solution is driven by its concentration gradient and the diffusion coefficient which, at the same time, depends on the temperature, the chemical composition and phase structure of the substrate. For a given alloy, kept at constant temperature in a medium with a consistent concentration of the substance of interest, the case depth will only depend on the time, according to equation (9):

$$x = a(Dt)^{1/2} = Kt^{1/2} \qquad (2.2\text{-}3)$$

where x is the case depth, a is a constant, D is the element diffusivity, t is the treatment time and K is a factor determined by a and D [93]. Higher treatment temperatures yield the same case depth in shorter time, although there are technical limitations related with life of the furnaces, and metallurgical considerations regarding the side effects of keeping the substrate material at high temperatures [94].

Consequently, diffusion treatments are slower when compared to other surface deposition techniques [77], and treatments as long as 72 hours are common practice in industry. On the other hand,

thermochemical treatments produce smooth case-core interfaces, which are beneficial for not only the wear and fatigue performance, but also the load bearing capacity [95].

The next section focuses on the application of thermochemical treatments on austenitic stainless steel substrates.

2.3. Low temperature thermochemical surface engineering of austenitic stainless steels

2.3.1. Rationale of low temperature treatments

As it has been mentioned in a previous section, the chemical composition of ASS makes them fully austenitic up to room temperature, and thus no phase transformation hardening takes place upon quenching. Consequently, SE treatments are an interesting alternative way to increase the surface hardness and improve the wear resistance. However, SE of ASS has traditionally been considered bad practice [30], as it poses two main problems: the passive oxide film and the precipitation of chromium carbides [96].

The passive chromium oxide film on ASS is stable under a wide range of conditions (figure 2.2.3-1) and isolates the substrate from the environment. This effect has been of interest for ASS components exposed to carburising gas mixtures, either in service [97, 98] or for SE purposes [99]. In the latter case, the oxide layer impairs diffusion of the hardening elements and, consequently, needs to be removed by applying some sort of surface activation process prior to the SE treatment [100, 101].

Furthermore, traditional SE treatments are conducted at high temperatures, around 500ºC - 600ºC in the case of nitriding, and 900ºC - 1000ºC for carburising [102, 103]. At these temperatures, and with increasing availability of nitrogen and carbon from the hardening medium, profuse precipitation of

chromium nitrides and carbides occurs, leading to a marked deterioration of the corrosion resistance of ASS. However, low temperature SE diffusion treatments with nitrogen and/or carbon have been reported to increase the surface hardness without affecting or even improving the corrosion resistance [103, 104].

It is nowadays widely accepted that hard, wear and corrosion resistant surface layers can be produced on ASS by means low temperature nitriding and/or carburising in a number of different media (salt bath, gas or plasma), each medium having its own strengths and weaknesses [105]. In order to retain the corrosion resistance of ASS, these processes are typically conducted at temperatures below 450ºC and 500ºC, for nitriding and carburising respectively (figure 2.2.3-2). The result is a layer of precipitation free austenite, supersaturated with nitrogen and/or carbon, which is usually referred to as *S-phase* or *expanded austenite* (EA) [105-109].

2.3.2. Metallurgical aspects of expanded austenite

There is general agreement in the literature regarding the thickness and the composition of EA layers. Maximum thicknesses in the order of 20 µm and 50 µm have been reported for nitriding and carburising respectively [107], with 20 at.% to 30 at.% of N and 5 at.% to 12 at.% of C correspondingly [109]. In the case of nitriding, the layer shows a steep gradient in composition (figure 2.2.3-3), with the associated abrupt change in properties, whilst the composition depth profile for the carburised layer is smoother [96, 105, 109]. The deviation of the carbon-depth profile in figure 2.2.3-3 compared to the typical profile shown in figure 2.2.2-1 is attributed to a variation of the diffusion coefficient with the carbon content [110].

On the other hand, there has been a strong disagreement with regard to the crystallographic structure of these carbon and nitrogen supersaturated layers [111-115]. The contradiction arises from a genuine difficulty in the identification of the X-ray diffraction (XRD) patterns, ascribed to the lattice strains and high density of crystallographic defects intrinsic to this layer of material. To this end, it is generally accepted that the so called S-phase is an integral part of the substrate with crystalline structure [111, 114]. The evidence indicates that this layer is single-phased, with the same fcc crystal structure of the parent austenite, although distorted as a result of a high content of interstitial elements in solution [112, 116]. Nevertheless other crystal structures have not been completely disregarded.

With regard to alloying elements, chromium has been considered crucial for the formation of EA, due to the very high chemical affinity with carbon and nitrogen [101, 106, 109, 117]. Therefore, interstitial C and N show a high probability to stay in the octahedral interstices of the fcc lattice, surrounding Cr substitutional atoms, which form trap sites of potential energy [101]. Molybdenum also seems to be beneficial to the kinetics of carburising, by delaying the precipitation of chromium carbides and thus allowing higher treatment temperatures [118], and by expanding the octahedral interstices in the fcc lattice [119].

From the thermodynamic point of view, EA is metastable and it will decompose into the stable austenite and carbide or nitride phases upon heat treatment [106, 108, 116, 120]. The incubation time for decomposition is temperature dependent, and nitrogen EA decays faster than carbon EA (figure 2.2.3-2), so that for prolonged service time, maximum operating temperatures in the order of 200ºC and 300ºC should be considered respectively. This metastable equilibrium or *paraequilibrium* is based on the fact that at the low temperatures at which the treatment is conducted, carbon and nitrogen exhibit diffusion rates significantly higher than the almost immobile substitutional elements, Cr and Ni. Under

such conditions, the precipitation of carbides and nitrides is suppressed, or delayed until large amounts of carbon and nitrogen are in solution [110, 117].

Detailed studies and observations with transmission electron microscopes (TEM) have revealed the precipitation of fine nitrides and needle-like carbides, especially in the outmost layer or close to structural defects in the microstructure [116, 121, 122]. Calculations of the volume misfit indicate that the strain energy associated with the precipitation of carbides contributes to keep the carbon in solution, although at high levels of supersaturation and expansion of the austenite cell, this energy barrier is significantly reduced [123].

The reported nitrides were of the MN type, while the carbides were of the M_5C_2 χ-kind (where M stands for metal and is most commonly Cr). In both cases, precipitation seems to follow a very specific and consistent orientation relationship with the austenitic phase [116, 121]:

$$\{001\}_{\gamma} \parallel \{001\}_{CrN}$$

$$\langle 001\rangle_{\gamma} \parallel \langle 001\rangle_{CrN}$$

$$\{111\}_{\gamma} \parallel \{001\}_{M_5C_2}$$

$$\langle 211\rangle_{\gamma} \parallel \langle 010\rangle_{M_5C_2}$$

Moreover, composition studies conducted on a scanning transmission electron microscope showed partitioning between the carbide and the austenitic phase of not only carbon, but nickel as well [123].

Summarising, the precipitation of nitrides or carbides takes place only after a relatively high level of supersaturation and expansion of the austenite has been reached, thus reducing the volume misfit strain energy barrier [123]. At the same time, the observed orientation relationship enables precipitation of needle-like carbides with highly coherent interfaces, minimising the long range transport of misfit dislocations and substitutional elements, mainly nickel.

2.3.3. Properties and applications of expanded austenite

Tensile tests have shown only minor differences between the untreated and treated ASS, some of the differences arising from the thermal cycle rather than the SE treatment itself [110, 124]. These differences can be summarised as a small reduction in the yield strength and in ductility, with a minor increase in the ultimate strength and elastic modulus; and they were attributed to the existence of high compressive residual stresses on the treated layer, and to a strain ageing effect produced at the treatment temperature.

The high compressive residual stresses present on the EA layers predicted obvious increases in the fatigue life and, in general, improvements of about 25% have been reported [125]. This is the result of a change in the failure mode, as the hard EA layer suppresses the alternating slip deformation at the surface [110, 124]. Consequently, the crack initiation site moves inwards, to the interface between the substrate and the EA layer, which can be explained by the strength-applied stress diagram in figure 2.2.1-1 [126]. It must also be noted that a minor increase in the notch sensitivity has also been reported for the low temperature carburised ASS [127].

The improvement in wear resistance is perhaps the most outstanding feature of EA. The degree of improvement depends on the sliding conditions, but volume losses between one and two orders of

magnitude lower than the untreated ASS are commonly reported for dry sliding [96, 125]. This improvement is attributed to the increased surface hardness, with a typical ratio 4:1 compared to the untreated ASS [128]. The EA layer prevents the surface from undergoing plastic deformation, and changes the wear mechanism from adhesion and abrasion, to a mild oxidational wear regime [128, 129]. However, under heavier loads, deformation of the subsurface occurs and leads to catastrophic failure, through propagation of subsurface cracks and spallation of the EA layer [130]. In this way, the carbon EA layers, being thicker and tougher than their nitrogen counterparts, show some advantage.

With regard to corrosion, the results vary significantly depending on the testing conditions. Surprisingly, most researchers found that low temperature nitriding and/or carburising do not harm the corrosion resistance of ASS, or even improve it. No conclusive explanation has been found for this improved corrosion behaviour, although it is clear that the benefit stands as long as nitrogen and carbon remain in solution and EA is free of precipitates [120]. In NaCl solutions, it is generally reported that EA remains passive under similar or wider range of potential compared to the untreated ASS, carbon EA showing a marginal advantage over nitrogen EA [96, 131, 132]. Similar or slightly higher initial current densities have usually been measured on EA, together with the absence of pitting potential, in contrast to what is usual for ASS [96, 125, 133]. Regarding repassivation, the evidence indicates that the passive film heals slower on EA than on ASS [132, 134].

This attractive combination of properties has caught the attention of both research and industrial fields, which is reflected in an increasing number of technical papers, reports, patents and processes. The applications include hydraulic pump components, valves, ball bearings, ferrules, etc. [135-143]. In the next section, some common processes to produce EA on ASS will be presented.

2.4. Common processes to produce expanded austenite

As it was previously mentioned, there are a number of different media capable of delivering carbon or nitrogen to enrich the surface of steel components, although not all of them are suitable for treating ASS or producing EA. Methods such as pack carburising and salt bath carburising or nitriding strongly depend on temperature to control the process driving reactions, and their effectiveness is low at the temperatures required to produce EA (T < 500ºC), especially in the case of carburising [88, 93]. Moreover, they have been widely superseded by gas media because of technical and environmental reasons.

Gas carburising with endothermic gas is, nowadays, the dominating carburising technology [144] and it has been successfully employed to produce EA [145, 146]. The main chemical reactions are as follows [93, 94]:

$$CH_4 \leftrightarrow (C) + 2H_2 \qquad (2.2\text{-}4)$$

$$2CO \leftrightarrow (C) + CO_2 \qquad (2.2\text{-}5)$$

$$CO + H_2 \leftrightarrow (C) + H_2O \qquad (2.2\text{-}6)$$

whilst the atmosphere control reactions are:

$$CO_2 + H_2 \leftrightarrow H_2O + CO \qquad (2.2\text{-}7)$$

$$CO_2 + CH_4 \leftrightarrow 2CO + 2H_2 \qquad (2.2\text{-}8)$$

$$H_2O + CH_4 \leftrightarrow CO + 3H_2 \qquad (2.2\text{-}9)$$

The carburising potential of the atmosphere (K_C) is usually controlled by reaction (2.2-6) according to the following equation:

$$K_C = \frac{p_{CO} p_{H_2}}{p_{H_2O}} \qquad (2.2\text{-}10)$$

where p_{CO}, p_{H2} and p_{H2O} are the partial pressures of each of the gases involved in the reaction.

There is some degree of secrecy about the available commercial processes to produce EA, but the vast majority of them are based on gaseous atmospheres containing CO [135, 145, 147]. The results are satisfactory, and the only drawback of these processes is the need for a prior surface activation to remove the passive oxide film, which is usually accomplished by using halogenated gases [100, 147, 148]. The low working pressures associated with vacuum carburising are known to remove the oxide layer from the treated components, although they require high temperatures to do so (900ºC to 1100ºC) and to activate the process reactions, i.e. thermal decomposition of the hydrocarbon gas under the catalytic effect of the hot steel surface [93, 149-152]. Another alternative is plasma SE, which removes the passive oxide film from the surface of ASS components through the sputtering action of highly active species present in the plasma [88]. Being the subject of this project, they will be treated in further detail in the next section.

2.5. Plasma surface engineering

Plasma surface engineering (PSE) is based on the abnormal glow discharge phenomenon that takes place on parts subjected to cathodic potential (several hundred volts), while being immersed in a low-pressure gas atmosphere (rough-medium vacuum) [153-157] (figure 2.2.5-1). Active species (i.e. excited or ionised atoms and molecules) are generated within the plasma and accelerated towards the cathodic worktable, where the parts to be treated are placed. While most of the energy involved in this process is released in the form of heat, a small part of it allows nitrogen and/or carbon species to be transferred to the solid state, through mechanisms that remain unclear.

It is custom to compare this plasma technology with gas or vacuum diffusion processes, although in PSE the reactions are under electric control, and the conventional equations to calculate the potential of the atmosphere do not entirely hold [152, 158]. The number of process variables increases: temperature, time, gas composition, pressure and flow rate, voltage, current, boost-diffusion cycle time and ratio, just to mention some. This larger number of relatively independent variables makes it more difficult to control and optimise the treatment, but also permits a higher degree of freedom when selecting the processing conditions.

As previously stated, the process variables are not completely independent of each other, and their interactions are of significant importance. The gas pressure affects the mean free path of the active species in the plasma [159, 160], and their kinetic energy is proportional to the acceleration produced in the cathode fall, i.e. the applied voltage [154, 155]. These two variables define, to some extent, the interaction between plasma and substrate, and the relative importance of some of the phenomena that take place during the process: sputtering, edge effect and ion implantation [161].

Plasma nitriding (PN) is usually performed in N_2-H_2 gas mixtures or NH_3. On the other hand, CH_4-H_2 mixtures are mainly used for plasma carburising (PC) purposes, although other carbon containing gases have proved to be useful in some cases [162]. The dilution of the gas is one of the variables that determine the flux of C or N transfer into the solid state, i.e. the rate of saturation of the surface [163]. Hydrogen additions are convenient for surface depassivation, especially when treating ASS. Moreover, the hydrogen content of the gas mixture also increases the tolerance of the process to possible air leaks in the chamber [164]. Small amounts of argon might be added to increase the sputtering effect and for surface activation [165].

The sputtering phenomenon is a very efficient heating mechanism, and it depends on the voltage and current density, the gas mixture and gas pressure, and even the shape of the components [166]. For treatments conducted at temperatures below 570ºC, sputtering can be the only source of heat, whilst additional heating is often required or convenient for higher temperatures [155, 167]. This is because in order to reach high temperatures by means of sputtering only, very high electric potentials are required, making the process unstable (arcing transition). However, it was found that much lower power densities are required for the activation of the treatment reactions, while the temperature can be reached using electric resistors, cathodic heaters or hollow cathodes [168, 169].

Decoupling temperature from electric plasma activation gives more freedom in the selection of the treatment conditions and better process stability and control [170-172]. Even though the activation provided by plasma during PSE is obviously responsible for the high rates of carbon and nitrogen mass transfer to the surface of the sample, the mechanisms involved are still not clear, and the models proposed in the literature have been severely disputed. Once the surface content reaches the saturation limit, the diffusion of N and C into the bulk material is a function of temperature, time and chemical driving force [163]. Depending on these three parameters, the final thickness of the alloyed layer and concentration gradient of the diffusing elements can vary from a few micrometers up to several hundreds of micrometers.

Direct current (DC) glow discharge thermochemical processes experienced a rapid uptake in industry in the 1970s and 1980s [161]. The advantages over conventional thermochemical treatments include: shorter cycle times, higher energy efficiency, lower gas consumption and environmental friendliness, just to mention some [156, 163, 170, 173, 174]. However, the higher equipment costs, the lack of thorough understanding of the process and such intrinsic problems of DC glow discharge plasma as

arcing, hollow cathode and edge effects were found to be difficult to solve, and thus a further spread of this technology has virtually stopped.

Moreover, the homogeneity of the temperature within the chamber was not satisfactory for some applications. Different methods were attempted in order to improve this aspect, making use of external heat sources like electric resistors or cathodic heaters [168]. These are metal sheets or meshes, subjected to cathodic potential, which are heated by the ionic bombardment and radiate heat to the rest of the chamber, thus heating the colder parts of the workload. A further improvement of this concept, together with the idea of post discharge plasma, became a novel plasma technology in 1999, named *active screen*. Active screen plasma (ASP) shows great potential to overcome the problems associated with DC plasma technology [175].

2.6. Active screen plasma technology

Among the plasma processes alternative to the DC technique, ASP is of particular interest due to the simplicity and effectiveness of its concept. In a conventional DC furnace, the worktable is negatively biased with respect to the wall of the chamber, which is earthed and plays the role of the anode in the electric circuit. If no supplementary heating elements are used, the workload needs to be subjected to relatively high electric potentials, in order to reach the treatment temperature by means of sputtering. The high electric potentials applied imply that the working condition moves closer to the arcing transition point in figure 2.2.5-1, and renders the treatment unstable, especially when the components are not completely free of grease, oxide scale or any other contaminant.

Moreover, components with complex geometries and of different sizes may not be heated uniformly, because of the distortion of the electric field in proximity of sharp edges [176]. The distortion of the

electric field affects the plasma and the plasma surface interactions, such as ionisation and sputtering, so that parts with small radius of curvature treated in DC furnaces are prone to the so called edge effect. The local temperatures developed at the edges can be much higher than in the rest of the component, causing changes in metallurgical structure and mechanical properties.

At the same time, hollow cathodes are the third type of defects frequently encountered in DC plasma treatments, and blind holes or dense work loads are vulnerable to this effect [169]. Hollow cathodes take place when two surfaces exposed to the plasma are separated by a certain distance, depending on the gas mixture, pressure and applied potential. These process variables define the thickness of the plasma sheath, as it will be explained in the next section. The overlapping of the plasma sheaths produces a peculiar electric field that traps electrons, which oscillate between the cathodic surfaces, increasing the ionisation events and producing a local increase in current density, with the consequent increase in temperature.

In the case of the active screen technology, the workload is surrounded by a mesh, which plays the role of the cathode (figure 2.2.6-1). The purpose of the mesh or active screen is twofold [177]:

- It radiates heat to the work load: the cage, being the cathode of the circuit, it is subjected to severe sputtering that increases its temperature; heat is thus transmitted to the workload by radiation and, to a lesser extent, by convection.
- It generates active species, principally excited neutral atoms and molecules, which are believed to be important for the treatment.

The worktable is electrically insulated, or subjected to a low negative bias to ease the flow of active species to the components [175]. In this way, sputtering does not take place on the surface of the

sample but on the mesh, and the workload is heated by radiation from the screen so that the temperature is more uniform and stable. Thereby, defects associated with direct exposure of the workload to highly negative potentials are reduced or eliminated. In practice, the AS technique has proved to be less sensitive to grease and rust on the treated parts [178]. From the aesthetic point of view, better surface qualities can be obtained, with complete absence of edge effects [179]. Finally, the local increases in temperature are reduced, producing more even hardening effects and properties [180].

Apart from its technological importance, AS has raised the unresolved issue of the nitriding and carburising mechanisms. Much work has been done on AS plasma nitriding (ASPN) in laboratory scale units, and it was concluded that the principal mass transfer mechanism involved sputtering of iron from the mesh, reaction of the iron atoms or particles with the active nitrogen in the plasma, and deposition of the iron nitrides on the worktable with subsequent decomposition and diffusion of free nitrogen [181-183]. However, the experience on industrial scale units has shown that other mechanisms and effects must be involved in the process [184, 185]. Furthermore, little work has been conducted up to date on active screen plasma carburising (ASPC).

It is evident that the mechanisms of plasma treatments pose a difficult challenge, which involves not only metallurgical aspects but also plasma-surface interactions and plasma physics. Therefore, the next section will introduce some basic but useful concepts of plasma physics and the plasma diagnostic techniques.

3. Fundamentals of plasma physics

3.1. Plasma

Plasma is usually known as *the fourth state of matter* and its inception requires a significant amount of energy, enough to break some atoms and molecules down into positive and negative particles, i.e. ions and electrons [186]. The amount of charged particles is balanced, so that the system remains electrically neutral. Contrary to the other phase changes, the transition of matter to the plasma state takes place gradually over a wide range of conditions, leading to different *degrees of ionisation* [187]. The energy required to ionise a gas can be applied to the system in the form of heat, although this is impractical due to the extremely high temperatures involved [188]. On the other hand, cold plasma can be produced by means of electric discharges, radio frequencies or microwave excitation of gases.

The study of electric discharges through gases dates back to the 18th century and involves famous researchers such as Faraday, Crookes, Thomson, Langmuir and Stark, just to mention some [186]. Although gases are good insulators under standard atmospheric conditions, they undergo ionisation when a strong electric field is applied, thus becoming electrically conductive [189]. A small fraction of charged particles from cosmic or natural radiation is normally present in the system. These particles are accelerated by the electric field and acquire sufficient energy to collide inelastically with gas molecules, ripping electrons or attaching to them to form positive and negative ions, respectively. Direct electron impacts can also excite the molecules to energy levels higher than the ground state but below the ionisation threshold.

Relatively few collisions occur in a cold plasma formed at low pressure, thus the system is not in local thermal equilibrium (LTE) [187]. This means that some highly energetic (fast or hot) particles coexist with others significantly less energetic (slow or cold) ones. The non-LTE is one of the most attractive

aspects of cold plasma and allows physico-chemical phenomena to take place in a wide range of conditions, far from equilibrium, depending on the gas composition, pressure, electromagnetic field, configuration and temporal behaviour of the discharge or excitation method.

Electrons are significantly lighter than neutral molecules or ions and, consequently, they are highly mobile. They respond faster than ions to fluctuations in electric and magnetic fields, and acquire higher energies. Even though most applications rely on the kinetics of ions, electrons are the primary agents in a plasma and their energy distribution is of significant importance [187, 190]. The energy or velocity of electrons is usually described by a Maxwellian distribution of the form:

$$f(v) = 4\pi n_e \left(\frac{m_e}{2\pi k_B T_e} \right)^{\frac{3}{2}} v^2 \exp\left(- \frac{m_e v^2}{2 k_B T_e} \right) dv \qquad (2.3\text{-}1)$$

where *f(v)* is the velocity distribution function according to Maxwell, n_e is the electron density, m_e is the electron mass, k_B is the Boltzmann constant, T_e is the characteristic electron temperature and *v* is the velocity [190]. Equation (2.3-1) represents a distribution where most electrons (bulk) have relatively low energies, whilst there is a small fraction (tail) of highly energetic electrons (figure 2.3.1-1).

The density of electrons, or other charged particles, is commonly described by the Boltzmann equation:

$$n_e = n_0 \exp\left(\frac{e \cdot \phi}{k_B T_e} \right) \qquad (2.3\text{-}2)$$

where n_e is the electron density in any position of potential Φ, n_0 is the electron density at a point of zero potential, *e* is the elementary charge, Φ is the potential at the position of interest, k_B is the Boltzmann constant and T_e is the electron temperature [191].

3.2. Electric breakdown

The electric brakedown of a gas at low pressure involves several steps, as it can be seen from figure 2.2.5-1. In the first regime, the gas is a good insulator and only the charged particles from background radiation carry a very small current [192]. When increasing the voltage, the current increases mainly through acceleration of these charged particles, until a saturation value is reached, depending on the gas composition and the pressure. If the voltage is raised further, the electrons gain sufficient energy to collide with the gas molecules inelastically, producing more electrons in an *avalanche effect*. This phenomenon defines the beginning of the Townsend discharges.

If the voltage is increased further, breakdown occurs and the current increases whilst the voltage can be reduced markedly. The electric breakdown of a gas is an irreversible process. The ion bombardment on the work table releases secondary electrons [190, 192], which subsequently multiply through the forementioned avalanche effect, thus increasing the availability of charge carriers considerably. This stage receives the name of *normal glow discharge*, due to the luminous phenomenon observed on the cathode (emission of light from the decay of excited and ionised atoms or molecules). The current density remains constant and any increase in current is a consequence of an increase in the area fraction of the cathode covered by the glow discharge [193].

Once the cathode is completely covered by the glow, a new discharge regime begins, named *abnormal glow discharge*. This is characterised by an increase in voltage with increasing current, the latter being a consequence of a higher current density as the whole surface of the cathode is already involved in the discharge [192, 193]. It is in this regime that PSE treatments are conducted, thus ensuring that all the surface of the cathode (i.e. all the components) are exposed to the glow and to the plasma-surface interactions. The selection of the current density, within the abnormal glow discharge range, depends on

the contribution ion bombardment makes to heating the cathode, and is limited by the onset of electric arcs. Arcing involves thermal emission of electrons from hot areas of the cathode, most frequently sharp asperities, although it also occurs on non-conductive pollution or dirt by the accumulation of electric charge [189, 190].

According to Paschen's law, for a given gas and electrode material, the breakdown voltage is a function of the pressure *p* and the distance between the electrodes *L* [192]. This correlation is illustrated in figure 2.3.1-2. On the left side of the minimum point ($pL < pL_{min}$), low pressure insulation occurs as a result of the low density of gas molecules and low frequency of ionising collision; whilst on the right side of the minimum point ($pL_{min} < pL$) high pressure insulation is a consequence of the higher energy losses experienced by electrons and ions in frequent collisions, mainly with neutral gas molecules [189]. Thus pL_{min} can be understood as the combination of pressure and distance between electrodes that yields the highest probability of ionisation and the largest amount of charge carriers.

3.3. Structure of the glow discharge

When a direct current (DC) glow discharge forms between two electrodes, the potential difference is concentrated close to the cathode, and several different regions are observed (figure 2.3.3-1) [187]. The first region in front of the cathode is the *Aston dark space*, a thin layer with a high density of electrons and very strong electric field, where electrons are still being accelerated and have not yet reached energy levels high enough to produce inelastic collisions with atoms and molecules, thus making this region appear dark [157]. Immediately next to the Aston dark space is the *cathode glow*, with a relatively high density of ions and, in some cases, excited atoms sputtered from the cathode, which account for the observed glow. The following is a relatively dark region called *cathode dark space*, although it is also

referred to as Crookes or Hittorf dark space. The electric field is moderate, and the space charge becomes positive as a consequence of the higher concentration of ions.

These regions are not always distinguishable and, in some cases, one of them may mask the others [157, 192]. In general, the space between the cathode surface and the end of the cathode dark space is called cathode region or sheath [187]. The difference in potential is mostly concentrated in this part of the discharge, and the thickness of the sheath will adjust itself to pL_{min}, following Pashen's law [157]. The electrons are accelerated across the sheath and acquire energy levels high enough as to excite and ionise gas molecules in the neighbouring area, called the *negative glow*, or even beyond.

The negative glow is relatively thick compared to the sheath, and is the brightest region of the discharge. Because of the high density of ions, the negative glow has a positive space charge, and the electric field in this region is relatively weak. The glow is more intense on the cathode side, where electrons are energetic enough to produce excitation and ionisation, and fades away towards the anode as the electrons slow down due to frequent collisions [157, 187]. The drop in the energy of electrons reduces the ionisation and excitation events and gives rise to another region, called Faraday dark space. The space charge in this region is small and the electric field is slightly negative.

The remaining space between the electrodes corresponds to a region of uniform glow called the *positive column* [157]. If the distance between electrodes is increased, the positive column lengthens while all the rest of the regions remain unchanged [192]. The electric field in the positive column is slightly negative and uniform to lead the electrons towards the anode, and the space charge can be considered quasi-neutral [187, 194]. Approaching the anode, a luminous region may be seen, called the anode glow, and immediately next to it a dark zone named anode dark space or anode sheath. The latter is the

result of the accumulation of electrons from the positive column next to anode, giving this region a characteristic negative space charge [157].

This brief summary on DC glow discharges serves as an introduction to the plasma diagnostic techniques of interest to this project, namely optical emission spectroscopy (OES) and electric probes, which will be explained in the following sections.

3.4. Plasma diagnostics

Plasma diagnostic techniques are of vital importance for the understanding, control and optimisation of plasma processes [195]. The working principles are varied (optic, electric or magnetic) and the information they obtain is often complementary, so that it is interesting to use more than one technique at the same time. The local disruption produced by the probes is critical and, although the devices and working principles are sometimes quite simple, the analysis of the signal usually raises difficulties [196].

The plasma parameters of significance to PSE processes can be summarised as follows [197]:

- Electron density and electron energy distribution (electron temperature)
- Type, density and energy of active species, i.e. ions, excited atoms and/or molecules.
- Electromagnetic fields, which define the movement, spatial distribution, and time response of the charged particles within the plasma.

Plasma diagnostic techniques have long been used to further understand the physics of plasma [198, 199]. In addition, once the underlying principles are known, they can also be used to provide real time information about the process, and to feed control systems [171, 200, 201]. Optical emission spectroscopy (OES) together with electric probes or collectors, are possibly the most extended plasma

diagnostic techniques. These methods are of importance to the present project and their basics will be briefly introduced in the next sections.

3.4.1. Optical emission spectroscopy

As it was stated in a previous section, inelastic collisions take place within the plasma, mainly through direct electron impact, producing ionisation and excitation of the gas atoms and molecules [194]:

$$e^-_{fast} + M \rightarrow M^+ + e^-_{slow} + e^-_{slow} \quad (2.3\text{-}3)$$

$$e^-_{fast} + M \rightarrow M^* + e^-_{slow} \quad (2.3\text{-}4)$$

where M is an atom or molecule and the superscripts $^+$ and * indicate the ionised and excited conditions respectively, e stands for electron and the subscripts *slow* and *fast* indicate the energy of the particle. It is evident that both M^+ and M^* are at higher energy levels than the atom or molecule at its ground state, i.e. its normal equilibrium condition. The energetic species M^+ and M^* have relatively short lifetimes and they experience decay processes, which frequently involve the emission of a photon to release the surplus energy [202]:

$$M^* \rightarrow M + h\upsilon \quad (2.3\text{-}5)$$

where $h\nu$ is the energy of the emitted photon, being h the Planck constant and ν the frequency of the photon. It is known from the atomic theory that the electron configuration and electronic energy levels are quantised, i.e. they do not assume any value, but certain allowed energy states [203]. Consequently, if the atomic and molecular energy states are quantised, the energy involved in their transitions must also be quantised; and this is the case of spontaneous emission, so that the energy of the photon $h\nu$ is quantised [131]:

$$\Delta E = E_k - E_i = h\nu \qquad (2.3\text{-}6)$$

where E_k is the energy level associated with the energetic states M^* or M^+, and E_i is the energy level at the ground state M, whilst $h\nu$ is the energy of the emitted photon.

In this way, each decay transition emits a photon with certain energy, i.e. at one particular frequency, giving rise to an emission pattern or spectrum, which can be used to identify the emitting species. Moreover, the intensity of every emission line is proportional to the number of molecules at each energy level, and the emission intensity has been used to correlate changes in the dominant ground state with a treatment parameter [197]. However, quantitative information and absolute concentrations are difficult or impossible to infer by this method.

The emission lines observed in atomic spectroscopy are due to the electronic transitions, i.e. changes in the electronic configuration of the excited atoms. In addition to this, polyatomic molecules show a more complex and finer structure, with different vibrational and rotational energy levels as a result of the relative movement of the atomic nuclei in the molecule [202]. Although interactions between electronic, vibrational and rotational energy levels exist, the energy difference is so large that, according to the Born-Oppenheimer approximation, each level can be considered separately and superimposed to the others, as shown in figure 2.3.4-1 and represented by the following equation [204]:

$$\Delta E = \Delta E_E + \Delta E_V + \Delta E_R \qquad (2.3\text{-}7)$$

where E_E, E_V and E_R are the electronic, vibrational and rotational energy levels respectively.

The emission lines are not sharp but diffuse, and usually called bands. The uncertainty principle proposed by Heisenberg indicates that each transition involves a slightly different energy, thus emitting photons at slightly different frequencies, which account for a *natural line broadening* [202]. The natural line width is insignificant compared to the effect of Lorentz and Doppler broadening. The former is a consequence of the collision of emitting species with other particles and the latter is associated with the motion of the species while emitting light [131]. Moreover, the experimental broadening of the equipment used to collect and analyse the light is often dominant.

The kit for spectroscopic observations typically includes an input optic device (telescope, collimator, or optical fibres), which gathers light (figure 2.3.4-2). Optical fibres are frequently used to feed the light into a monochromator, a polychromator or any similar equipment [205], where entrance slits or apertures define the throughput and bandpass of the system [206]. The light is thus focused onto a wavelength dispersing element, such as a grating or a prism, and a narrow range of wavelengths is reflected onto a detector, such as a silicon photodiode or a PMT [207]. The collected spectrum shows the intensity of the signal as a function of the wavelength, wavenumber or any equivalent scale.

OES is a popular diagnostic technique due to its simplicity, and also because it causes no disruption to the plasma. It provides useful information on the type and, to some extent, the population of active species in the plasma. High temperature optical fibres yield good spatial resolution, and have been used in optical pyrometers to collect light from specific areas of interest [208, 209]. Although valuable, the information obtained with OES is rather incomplete, and electric probes are necessary to obtain evidence on the energy and density of electrons [197]. This will be discussed in the next section.

3.4.2. Electric probes

In order to understand the information obtained from electric probe devices, it is useful to make some brief comments on the electric potential and mobility of charged particles in the plasma. It must be said that negative ions and double ionisation events are very scarce in the type of plasma of interest to this project, so that only electrons will be considered as negative charge carriers, and singly ionised atoms and/or molecules as positive charge carriers [191]. Moreover, the probability of electron-ion recombination in the volume (equation 2.3-8), i.e. the reverse of electron impact ionisation (equation 2.3-3), is rendered low by the necessary energy and momentum exchange among three particles [194]:

$$e^-_{slow} + e^-_{slow} + M^+ \rightarrow M + e^-_{fast} \qquad (2.3\text{-}8)$$

where *M* stands for atom or molecule and *e* for electron, while the fast and slow subscript indicates the energy or *temperature* of the particle. Volume recombination events are particularly unusual in gases at low pressure, thus most of the recombination processes occur at the wall of the vessel that confines the plasma, the latter acting as a third body.

As it was mentioned in a previous section, the potential between the electrodes is not evenly distributed, but it is related with the density of charged particles, according to Poisson's equation [210]:

$$\frac{d^2\phi}{dx^2} = \frac{4\pi e}{\varepsilon_0}\left(n_e - n_i\right) \qquad (2.3\text{-}9)$$

where Φ is the potential function, *x* is the distance from the cathode, *e* is the elementary charge, n_e and n_i are the density of electrons and ions respectively and ε_0 is the permittivity of the free space. In the

field free space within the plasma, where quasi-neutrality is maintained, the onset of a space charge by accumulation of ions is rapidly compensated and levelled by the highly mobile thermal electrons [191]. The accumulation of charges in the area surrounding the electrodes, the walls or any other foreign body immersed in the plasma, produces a shield that confines the perturbation to a distance λ_D, according to the Debye's equation [194]:

$$|\lambda_D| \approx \sqrt{\frac{\varepsilon_0 k_B T_e}{n_i e^2}} \qquad (2.3\text{-}10)$$

where λ_D is the distance of the perturbation or Debye length, ε_0 is the permittivity of the free space, k_B is the Boltzmann constant, T_e is the electron temperature, n_i is the ion density and e is the elementary charge.

The flow of ions and electrons is governed by diffusion and by the electric field drift, according to the following equation [194]:

$$\Gamma = -D\frac{\partial n}{\partial x} + n\mu E \qquad (2.3\text{-}11)$$

Where Γ is the flux of charges, D is the diffusion coefficient, n is the density of charges, x is the distance from the cathode, μ is the mobility of the charged particles and E is the electric field.

The flux of positive and negative charges out of the system must remain balanced in order to maintain its electric neutrality. Moreover, if an insulated electrode is immersed in the plasma, the same amount of positive and negative charges should arrive at its surface, so that no net flow of charges takes place [211]. However, as the electrons are highly mobile compared to the ions, the flux of electrons to any neutral surface exposed to the plasma would be larger than the flux of ions. Consequently, any foreign

body immersed in the plasma must develop a shield of negative potential in order to repel some of the electrons, and thus balance the flow of negative and positive charges. This potential is called *floating potential*, and depends on the type of gas, the pressure, and the electric discharge parameters.

Electric or electrostatic probes, frequently called *Langmuir probes or collectors*, are electrodes of known area and defined shape (figure 2.3.4-3), usually made of tungsten, molybdenum or graphite, and supported by an insulating ceramic or glass holder [196, 198]. The probes are immersed in the plasma and electrically biased, sweeping a range of electric potential with respect to the plasma [212]. The *I - U* curve is recorded and, providing the experimental settings and conditions are carefully selected and the correct model is used to evaluate the signal, it gives valuable information on the characteristic energy and density of electrons and ions [213].

Figure 2.3.4-4 shows the typical curve of a Langmuir probe. When the electrode is negatively biased, the electrons are repelled and only ions are allowed to arrive at the surface of the probe [211]. If the negative charge is not excessive, the ion flux is independent of the applied voltage, and it can be measured from this part of the curve, called *ion saturation region*. On the contrary, when the probe is positively biased, only electrons are allowed to reach the surface of the probe, thus the electron density can be calculated. This part of the curve is called *electron saturation region* [196]. Between these two extreme cases, the net flow of charge combines both electrons and ions, and the transition points give information on the electron and ion temperatures, T_e and T_i.

To this end, an improved version of the planar Langmuir probe or collector was designed to reduce the effect of deposition or pollution on the effective area of the electrode [214, 215]. The working principle is illustrated in figure 2.3.4-5. A capacitor is connected in series with the probe, and it is negatively biased,

or self-biased in case a radio frequency power supply is used [215-217]. The excitation or bias is then interrupted and the capacitor is left to discharge by the arrival of positive charges from the plasma, i.e. ions. The drain curve of the capacitor is recorded and gives very similar information to the ion saturation region of a conventional Langmuir probe, according to the following equation:

$$C \cdot \frac{dV}{dt} = \left[\Gamma_i - \Gamma_e\right] \cdot eA \qquad (2.3\text{-}12)$$

where C is the capacity connected to the probe, V is the potential across the capacitor, t is the time, Γ_i and Γ_e are the flux of ions and electrons respectively, e is the elementary charge and A the effective area of the probe.

This method is simple, and yields information with minimum signal post-processing. However, care should be exercised to avoid edge effects on the probe, and to apply the right level of bias to produce ion saturation, but not to disrupt the plasma conditions.

CHAPTER 3: EXPERIMENTAL PROCEDURES

1. Sample preparation

1.1. AISI 316 coupon samples

Coupon samples were cut from AISI 316 hot rolled bars (composition shown in table 3.1-1), using a high precision Struers Accutom-5 cutting machine, fitted with SiC cutting discs. The final dimensions of the samples were 25.4 mm in diameter and 6 mm in thickness. Both faces of the samples were wet ground with SiC grinding paper of grit #120 until flat, and one face was ground further up to grit #1200. Samples were then washed with soapy water and cotton, degreased with acetone in an ultrasonic bath for 10 minutes and dried with hot air.

Some samples were mirror polished with diamond pastes (6 μm and 1 μm) and colloidal silica suspension, on a Struers DAP-7 automatic polisher. The cleaning procedure after polishing was identical to the one described before.

Cross sections were cut from the samples with SiC cutting discs on a Struers Accutom-5 cutting machine, nickel plated when necessary, and mounted on conductive bakelite using MetPrep PA30 or Opal 400 mounting presses. The grinding, polishing and cleaning procedures were equivalent to the ones described before.

Whenever it was required, the microstructure was developed by means of an etching solution of composition 25 ml H_2O, 25 ml HNO_3 and 50 ml HCl. The sample of interest was immersed in the solution at room temperature for a few tens of seconds, and immediately rinsed with water and dried with hot air.

Small AISI 316 coupon samples, 2 mm in thickness and 10 mm in diameter were prepared for EBSD studies. The sample preparation procedure was equivalent to the one described before, with a careful final polishing with colloidal silica to obtain a smooth and stress-free surface.

1.2. Friction force samples

These samples were cut from an AISI 316 bar, 4½ inches (114.3 mm) in diameter, using an automatic cutting saw. Both faces were finely machined until flat and one face was wet ground with SiC grinding paper up to grit #1200. The final dimensions of the samples were: 114 mm in diameter and 12 mm in thickness, with a 16 mm through hole at its centre for holding purposes. The cleaning procedure after grinding was equivalent to the one described before.

1.3. Corrosion samples

Samples were produced from an AISI 316 bar, 10 mm in diameter, for immersion corrosion experiments. Rods 50 mm long were cut and an effective area 40 mm long and 8 mm in diameter was finely machined and dry ground with SiC emery paper up to grit #1200. A flange at one end of the rod (10 mm long and 10 mm in diameter) remained as rolled and was used for holding purposes (figure 3.1.3-1). These samples were subjected to the standard cleaning and degreasing procedures already explained.

1.4. Transmission Electron Microscopy (TEM) samples

Coupon samples were cut and back thinned with SiC grinding paper until less than 200 μm thick, leaving the treated surface untouched. Discs 3 mm in diameter were punched and further back thinned with emery paper, until they were between 50 μm and 80 μm in thickness. Dimpling was conducted from the back side of the sample in a South Bay Technology 515CE precision dimpling machine, using a

brass tool and 6 μm diamond paste with a 25 g load at a rotation speed of 140 rpm (14.66 s^{-1}), reaching a final thickness in the order of 10 μm to 20 μm.

Finally, the samples were mounted on copper discs, using a hot melt adhesive, and ion milled in a Gatan 691 Precision Ion Polishing System (PIPS) until perforation occurred. The two Ar guns were set at angles between 8º and 10º to ion mill the sample from a single side, i.e. the side opposite to the surface treated layer. The ion current was between 8 μA and 14 μA at 4 keV, and the sample was constantly rotated. Under these conditions, perforation happened within 2 hours. Samples were then removed from the holder and the remaining hot melt adhesive was cleaned using acetone.

Some powder samples and wear debris were also prepared for TEM observation. The sample preparation was, in these cases, very simple and consisted only in adding methanol to the glass container where the samples were kept. A pipette was then used to select particles of suitable size, which were deposited on a copper grid holder, 3 mm in diameter.

1.5. Residual Stresses (RS) bending thin disc samples

Thin discs, 25.4 mm in diameter and 0.5 mm in thickness, were cut from AISI 316 bars under carefully controlled conditions, in order to obtain flat and parallel surfaces. Both sides of the discs were wet ground with SiC paper, on a flat glass surface, up to grit #1200, and vibration polished with 6 μm diamond paste for several hours (approximately 12 hours), until no traces of the grinding marks could be observed. The previously described cleaning and degreasing procedures were applied and care was taken to avoid stresses that could bend the discs. Finally, the discs were identified and their thickness, roughness and flatness (in different directions) were measured in order to select the most suitable ones for the assessment of the residual stresses developed during the surface engineering treatment.

1.6. Other samples:

The sample preparation methods here explained cover most of the types of samples of significance to this project. Some other kinds of samples of different materials were eventually used: pure iron stripes, AISI 304 stripes, glass slides, copper coupons, just to mention some. The sample preparation procedures used in all these cases were very similar to the ones previously explained, and the particularities of each case will be explained when necessary.

2. Surface engineering plasma treatments: experimental procedures

Three different plasma furnaces were used for surface engineering treatments (figure 3.2.1-1):

- DC Klöckner Ionon 40 kVA unit for plasma carburising in DC and AS experimental arrangements
- DC Klöckner Ionon 60 kVA unit for plasma nitriding in DC and AS experimental arrangements
- AS Plasma Metal 75 kVA + 15 kVA industrial scale unit for AS plasma nitriding and carburising

The instrumentation was different for each furnace although, in general, it included mass flow meters to control the gas mixture and gas flow, two pressure gauges of different kinds (Penning, Pirani or Bourdon) to measure gas pressure, two K-type thermocouples protected by ceramic sheaths, and a pyrometer for verification (KIU-PM350).

With regard to the procedure for plasma treatments, it could be generally described as follows:

The samples to be treated were cleaned and placed on the work table inside the furnace. In some cases, a special holder or rig was required to keep the samples in position, for mechanical masking or to produce the desired arrangement inside the chamber. Once the samples were in place, a vacuum cleaner was used to remove dust particles that could have been deposited on the surface.

The chamber was then lowered and the ventilation valve closed. The cooling water began to circulate and the vacuum pump was turned on to evacuate the furnace, up to a vacuum level in the order of 1 Pa. Pure hydrogen gas was then fed into the chamber, and the main power supply was turned on to start the plasma.

During the initial stage, the electric power (current and voltage) and the gas pressure in the chamber were increased in steps, as a function of the temperature and the stability of the treatment (onset of arcing), and the limit of the heating stage was usually set at 300ºC. From this point onwards, the gas fed into the furnace was not pure H_2 any more, but the gas mixture selected for the treatment, i.e. N_2-H_2 for nitriding and CH_4-H_2 for carburising, or CH_4-H_2-N_2 for nitrogen enhanced carburising. All the remaining treatment conditions were automatically adjusted until the set point values could be reached (temperature, pressure, gas composition and bias[†]) and these set point values were kept stable throughout the duration of the treatment.

Once the treatment had finished, the feeding gas valve was closed and the chamber was evacuated. The samples were left to cool down, under the residual treatment gas pressure, until below 80ºC. The furnace was then ventilated and opened to remove the samples from the chamber. It was a normal practice to clean the samples with soapy water and cotton immediately after the treatment, and this will be considered the case unless otherwise mentioned.

The principal variables studied here were pressure and bias, although some other treatment conditions were also assessed, with regard to gas composition (N_2 enhanced carburising), treatment time and also active screen treatments with different arrangements (figures 3.2.1-2 and 3.2.1-3). The process

[†] Bias, as a set point, only applies to the active screen furnace and not to DC furnaces.

temperature, although of paramount importance for the diffusion treatment, has been already thoroughly studied, and it has been found to be limited by metallurgical aspects of the AISI 316 alloy, namely the formation conditions of expanded austenite and precipitation of secondary phases.

Therefore it was the objective of this study to optimise the plasma treatment conditions for a given treatment temperature in order to produce a thick and uniform expanded austenite layer on AISI 316 samples free from surface defects, such as edge effects and arcing damage; and to increase the understanding of the mechanisms of active screen treatments, and the main variables involved in the process (tables 3.2-1 to 3.2-4 and figure 3.2.1-4).

3. Characterisation techniques

3.1. Hardness

Low force hardness and micro hardness tests were conducted in a Mitutoyo MVK-H1 durometer fitted with Vickers or Knoop indenters. The load range was 10 g – 1000 g and calibration block #EP9716400 (757.3 $HMV_{0.3}$) was used to check the condition of the equipment before each measurement. The reported values are the average of at least six significative measurements and standards BS EN ISO 6507-1, 6507-2, 4516 and 4970 were taken as reference for these tests.

A Micro Materials nanotest system was used to conduct instrumented hardness tests and assess the mechanical properties of the outmost layer of treated samples (BS EN ISO 14577-1 and 14577-4). Eight indentations were conducted in each case under the testing conditions shown in table 3.3-1.

3.2. Roughness

Roughness measurements were conducted in a KozakaLab Surfcorder SE1700 stylus profilometer. Standards BS EN ISO 4287 and 1134-1 were taken as reference for these measurements. Different pick up settings were selected depending on the objective of the measurement (table 3.3-2).

3.3. Atomic Force Microscopy (AFM)

Contact mode atomic force microscopy was conducted in a Digital Instruments Dimension 3100 nanoscope, using Veeco NanoScope V.5.12r3 software and Veeco NP gold coated silicon nitride probes (table 3.3-3).

3.4. X-Ray Diffraction (XRD)

A Philips X'Pert diffractometer was used to obtain the X-ray diffraction patterns (table 3.3-4). The identification of the diffraction peaks was achieved by comparison with an XRD pattern database PANalytical X'Pert HighScore 1.0d.

3.5. Glow Discharge Optical Emission Spectroscopy (GDOES)

A Leco GDS-750 unit was used to obtain the composition-depth profiles of plasma surface treated samples. The method and measurement programme were calibrated using standard blocks of known composition, according to the instructions of the manufacturer.

3.6. Optical Microscopy (OM)

Optical metallographic observations were conducted in a Leica Leitz DMRX microscope equipped with a CCD camera for digital image acquisition.

3.7. Scanning Electron Microscopy (SEM)

Different scanning electron microscopes were used throughout the project, and for different purposes, depending on their strengths and availability:

- Philips XL30 – LaB_6 filament (SEI, BSE, EDX)
- Jeol 6300 – W filament (SEI, BSE)
- Jeol 6060 – W filament (SEI, BSE, EDX)
- Jeol 7000 – Field Emission Gun (SEI, BSE, EDX, EBSD)

3.8. Energy Dispersive X-Ray Spectroscopy (EDX)

Oxford Instruments Inca EDX detectors were used in all cases, controlled by means of Inca Energy software. The internal calibration standards were considered valid for the purpose of this project and only Ni or Co standards were used to correct the position of those reference peaks. The microscope settings were optimised for the analysis (acceleration voltage, spot size, working distance, etc.)

3.9. Electron Back Scattered Diffraction (EBSD)

Crystallographic orientation maps (COMs) were obtained on a Jeol 7000 FEG SEM fitted with an Oxford Instruments Inca Crystal Mk1 EBSD camera, at the general conditions listed in table 3.3-5. All the data were collected and analysed using Oxford Instruments Inca Crystal software for EBSD.

3.10. Transmission Electron Microscopy (TEM)

Two transmission electron microscopes were used in this project:

- Philips CM20 - LaB_6 filament
- FEI Tecnai F20 – FEG (EDX)

The micrographs and electron diffraction patterns (EDP) were obtained on Kodak SO-163 electron image film (3 ¼ in x 4 in), developed and digitalised with 300 dpi resolution.

4. Tribological properties: experimental procedures

4.1. Wear tests

A custom-made pin-on-disc wear testing apparatus was used to assess the wear resistance of treated and untreated samples (figure 3.4-1), and standard ASTM G99-05 was taken as a reference. Coupon samples, 25.4 mm in diameter and 6 mm in thickness with a surface finishing of SiC paper grit #1200, were rotated on a horizontal plane and worn against a steady WC-Co binder ball, 8 mm in diameter (table 3.4-1). The tests were conducted under dry conditions in laboratory air at room temperature; the relative humidity and room temperature were recorded for each test. The tests were 4.5 hours long, the applied load was 10 N (Hertzian contact stress 1.6 GPa) and the sliding speed 0.031 m/s, giving a total number of cycles of 17550 (for the coupon) or a sliding distance of 500 m (for the pin).

The matching surfaces were degreased with acetone, mounted on their respective holders and wiped again with a clean cloth with acetone, to remove any contaminants from their surfaces. The tribological couple was gently put into contact, and the load was applied 1 minute before sliding began. After the test, the samples were carefully removed from their respective holders and observed. The wear debris was collected for inspection and tested with a magnet. The profile of the wear track left on the tested samples was measured at not less than 6 different positions, by means of a KozakaLab Surfcorder SE1700 stylus profilometer (table 3.3-2). The obtained profile was integrated for the whole wear track and the total worn volume could be thus calculated.

4.2. Friction tests

The friction tests were conducted on a pin-on-disc custom-made machine, equipped with a 100 lb (45.36 kg) load cell and digital data acquisition card. Standard ASTM G115-04 was considered as a reference in this case. The AISI 316 discs, 114 mm in diameter and a surface finishing of SiC paper grit #1200, were mounted and rotated on a horizontal plane against a stationary 8 mm ball made of WC-Co, AISI 316 untreated or AISI 316 plasma carburised. Tests were conducted under dry conditions in laboratory air at room temperature, applying a load of 10 N and a sliding speed of 0.05 m/s. Several tests were conducted on each disc, so that the rotation speed was adjusted according to the diameter of the wear track in order to keep the sliding speed constant.

The matching surfaces were degreased with acetone and gently put into contact. The data collection started when the load was applied, 15 seconds before sliding began, and continued throughout the 10 minutes duration of the test, at a frequency of 1 data point per second. After the test, the samples were separated, removed from their holders and inspected. The wear debris was also collected and tested with a magnet.

5. Corrosion behaviour: experimental procedures

5.1. Corrosion tests in boiling acid solution

Immersion corrosion tests in different boiling acid solutions were conducted to assess the corrosion resistance of treated and untreated AISI 316 samples. The equipment consisted of a hot plate as heat source, a 1 litre volume cylindrical flask where the boiling acid and the samples were kept, a flask lid connected to a water coil condenser, and a vapour trap (figure 3.5-1).

To reveal the corrosion resistance of the tested samples under different conditions, various aqueous solutions were used following British Standards BS EN ISO 3651-1 and BS EN ISO 3651-2:

- 16% mass fraction H_2SO_4
- 16% mass fraction H_2SO_4 with 100 g/l $CuSO_4$ (BS 3651-2 Method A)
- 40% mass fraction H_2SO_4 with 25 g/l $Fe_2(SO_4)_3$ $5H_2O$ (BS 3651-2 Method C)
- 20% mass fraction HNO_3

The exposure times to the boiling acid varied from one hour up to 240 hours, the latter conducted in five periods of 48 hours each.

The samples to be tested were ultrasonically cleaned in acetone and weighed. The coupon samples were placed on glass Petri dishes to hold them and keep them separated from one another, and they were immersed in the acid solution at room temperature. The specimens were placed on top of copper coupons when copper contact was required (BS 3651-2 Method A). In the case of the rod cylindrical samples, an especial holder was designed and manufactured to hang the samples leaving only their effective area in contact with the acid.

Once the samples were placed in the flask, the solution was stirred with a magnetic follower, and heated up to its boiling point (record was kept of the heating time), and kept boiling for the entire testing time. Once the test had finished, the heat source was disconnected and the samples were immediately removed from the boiling solution, rinsed with water and ultrasonically cleaned with acetone. Mass loss measurements were thus conducted in an Avery Berkel analytical balance, with 0.1 mg accuracy.

5.2. Corrosion tests in acid at room temperature

These tests were conducted only with a 16% mass fraction H_2SO_4 aqueous solution at room temperature and only on coupon samples. The polished samples were masked with fast drying acrylic lacquer before being immersed in the acid solution for 120 hours at room temperature. After the test, the samples were removed from the acid, rinsed with water and cleaned with soapy water and acetone to remove the lacquer.

6. Plasma diagnostics – experimental procedures

6.1. Optical Emission Spectroscopy (OES)

OES spectra were first collected from outside the furnace, through a sight port window, using an Optronic Lab OL730Q telescope (table 3.6-1). The telescope was placed 80 cm away from the window and focused on the mesh of the active screen furnace, which resulted in a minimum source diameter of 20 mm approximately (figure 3.6-1). A cylindrical cone was made with white photographic cardboard panel, its internal surface being covered with an opaque black liner, and placed between the furnace and the telescope to reduce the stray light from reflections or other light sources. The use of such a cone also helped to align the telescope and to keep the measuring distance constant.

A 1000 μm core fibre optic cable fed the light into a Jobin Yvon Triax 180 spectrometer, with a 190 mm focal length and f/3.9 entrance aperture ratio (table 3.6-2). The optical arrangement consisted of entrance and exit slits, collimating and focusing mirrors, and a grating turret in a cross Czerny-Turner configuration. The turret was provided with two diffraction gratings, 150 and 1200 groves per millimetre, for collection of low and high resolution spectra respectively. The low resolution grating allowed a wavelength range of 1000 nm, while the high resolution grating admitted a total range of 0 nm to 1400 nm in steps of 100 nm. It must be mentioned that no signal could be collected below 250 nm, due to

absorption by the input optics and the air. The 1200 gr/mm grating yielded a spectral dispersion of 3.53 nm/mm and a spectral resolution of 0.3 nm at 500 nm.

A Jobin Yvon Spectrum ONE CCD thermoelectrically cooled detector head was used to measure the light intensity at different wavelengths. In all cases, sufficient time was given for the detector to reach the operating temperature before data collection (1 hour approximately). The CCD chip had a sensor array 1024 pixels wide and 256 pixels high, no binning was applied and a flush cycle was run before data acquisition, to reduce the noise. Data collection was controlled by a Jobin Yvon CCD-3000 unit, 16 bit ADC limit and 166 kHz conversion speed (table 3.6-3). The controller unit was operated from a PC using SpectraMax software for Windows.

The automated entrance and exit slits were kept at the same width for optimum throughput. The selected slit width was generally 0.04 mm for the measurements conducted with the telescope, and 0.08 mm for the spectra acquired with the optical fibre probe (method described below). The weaker signal obtained with the optical fibres was counterbalanced by the increased slit width, i.e. increased bandpass and throughput, although this also had an impact on the spectral resolution.

The system was calibrated, before each set of measurements, using the mercury green emission peak at 546.074 nm (NIST online database, Pearse and Gaydon reference book) from a commercial fluorescent lamp. In all cases, the Optronic Lab telescope was used to collect light from the lamp, and a calibration accuracy of ±0.005 nm was usually attained. The manufacturer's recommendations were followed to calibrate the spectrometer, and the conditions used are listed in table 3.6-4.

The positioning accuracy was found to be well within the ±0.3 nm pledged by the manufacturer, and the instrument calibration was not severely affected for one set of measurements, on condition that the grating turret was not rotated to change the dispersing element. Nonetheless, all the spectra were collected in the direction of increasing wavelength to minimise errors associated with clearances in the driving mechanism of rotation of the grating turret.

The collection of light from inside the furnace, or intrusive OES (IOES), was achieved by using high temperature resistant SiO_2 optical fibres, 100 / 110 μm core diameter, numerical aperture 0.22 and UV-Visible wavelength range (figure 3.6-1). A feedthrough was designed and manufactured to allow one single fibre to have one end inside the furnace and exposed to the plasma, and the other end plugged into the same Triax 180 spectrometer described before, by means of standard SMA connector (see appendix A for construction details).

These types of measurements were only conducted in the active screen unit and consisted of the standard heating stage, until the treatment conditions were reached. Next, spectra were collected sequentially under different treatment conditions, allowing sufficient time for the work table bias to reach stable values before each spectrum was acquired. Finally, an emission intensity map was produced with each set of measurements and each map was produced twice for verification purposes.

6.2. Ion Flux Probe (IFP)

A planar electric probe, similar to a planar Langmuir collector, was built to measure the characteristic parameters of the plasma in both DC and AS furnaces (refer to appendix B for construction details). Before each measurement, the active surfaces of the probe were polished with colloidal silica, cleaned with soapy water, ultrasonically cleaned with acetone and dried with hot air. The probe was then

mounted inside the chamber and connected with the measuring circuit placed outside the chamber, by means of a standard electrical feedthrough. All ceramic insulators were wet ground and washed before each experiment to eliminate the layer of conductive material deposited on them. Finally, the insulation and continuity were checked before each measurement.

A low noise Instek GPS-6010 DC power supply with variable output voltage (0 V to 60 V) was used to bias the probe. A Pico 2202 digital oscilloscope and 250 MHz oscilloscope probe, with an impedance of 50 MΩ and a X10 attenuation power, were used to acquire the drain curve of the tantalum capacitors connected in series with the probe (U_{MAX} = 63 V, C = 4.7 μF). The oscilloscope was connected to the USB port of a PC and the signal was monitored and stored in the hard drive of a PC using PicoScope 5.15.6 (32 bit) data collection software.

The experiments in the DC furnaces consisted of a standard heating stage until the selected treatment conditions were reached, followed by the data collection (approximately 1 hour) and the final cooling down cycle. Two measurements for each condition were conducted, including DC and AS arrangements, with standard carburising (CH_4-H_2) and nitriding (N_2-H_2) atmospheres, keeping temperature and pressure unchanged (figure 3.6-2).

The measurements conducted in the AS furnace consisted of the usual heating stage, followed by data collection in each of the treatment conditions of interest. A set of measurements in all the range of selected conditions demanded up to twelve hours, as it was necessary to wait for the furnace conditions to stabilise before collecting data. The whole range of conditions was divided into two parts, so that the insulating paper could be changed and the ceramic spacers cleaned. Several curves were collected for each condition, and the whole range of conditions was assessed up to three times.

The method of measurement consisted of charging the capacitor using the DC power supply, and subsequently connecting the capacitor to the probe with the active surface exposed to the plasma. The electric charge stored in the capacitor was such that the probe was biased to a potential some tens of volts more negative than its floating potential. This negative charge repelled electrons and, in some conditions, was enough to produce the so called ion saturation curve.

Under this condition, all the electrons were repelled and only the positive ions were allowed to reach the probe surface. Therefore, the drain curve of the capacitor provided information on the flow of positive ions to the probe. Once the negative potential dropped to low enough values, the high energy electrons managed to surmount the retarding potential and reached the surface of the probe. The arrival of both positive and negative charges to the probe produced a change in the discharge rate of the capacitor.

CHAPTER 4: RESULTS

1. Processing

AISI 316 samples were plasma treated in conventional DC furnaces, and these samples were adopted as bench markers for the treatments carried out in the active screen industrial scale unit. Different treatment conditions were explored in this AS furnace, in both nitriding and carburising atmospheres. As a first approach, it must be said that AS processes had to be conducted under different conditions from their DC counterparts (mainly, lower gas pressures), in order to obtain equivalent results. Furthermore, the working conditions used for ASPC and ASPN also differed, particularly with regard to the bias level (figures 4.1-1 and 4.1-2).

In these graphs, the bias is expressed in power units (kVA) for simplicity although, as it will be shown later, only by reporting both the electric potential and the current density can the conditions on the worktable be unambiguously defined. For one given power set point, the gas mixture and gas pressure determine, to a great extent, the combination of current density and electric potential on the worktable. The following equations were found to fit the data points with reasonable accuracy:

$$p = C \cdot P^{-k_3} \qquad (4.1\text{-}1)$$

$$C = k_1 e^{-k_2 i} \qquad (4.1\text{-}2)$$

$$i = -\frac{1}{k_2} \ln\left(\frac{p \cdot P^{k_3}}{k_1} \right) \qquad (4.1\text{-}3)$$

where i is the current in Amperes, p is the pressure in Pascals, P is the power applied on the work table in kVA and k_1, k_2 and k_3 are constants, for which values depend on the gas mixture (table 4.1-1).

A saturation limit is reached at low pressure and with high enough applied power, so that any further increase in the bias set point will not alter the actual parameters of the electric discharge. Under these conditions, the current density is self limited, and the electric potential is frequently very high (ca 900 V). If the gas pressure is increased, larger current densities can be drawn, and these are associated with lower electric potentials on the worktable. Furthermore, edge effects occur on samples treated above some current density threshold, so that the applied bias should be kept below a certain limit in order to retain the benefits of the AS method.

AS treatments conducted within the range of effective conditions, shown in figures 4.1-1 and 4.1-2, were less susceptible to process instabilities, and produced samples with homogeneous surface appearance. However, inadequate processing conditions also rendered AS treated samples inhomogeneous in morphology and properties. Figure 4.1-3 illustrates the arcing, hollow cathode and edge effects frequently observed on a DC worktable. At the same time, the damage these effects produce on treated components is apparent from figure 4.1-4, which also shows the comparatively improved surface quality obtained with AS.

Further studies within the range of effective treatment conditions revealed differences between the samples, particularly with regard to layer thickness. Figure 4.1-5 shows the layer thickness, measured from GDOES nitrogen or carbon composition profiles, as the size of the bubble superimposed on the map of treatment conditions presented before. It is evident from this figure that the optimum treatment conditions lay in the low pressure and moderate bias level for ASPC, and even lower pressure and bias level for ASPN. The layer thickness measured in each case is presented in tables 4.1-2 and 4.1-3, as a function of the pressure and the bias level set point.

Therefore, it is within this region of effective treatment conditions that most of the work on characterisation, wear and corrosion properties was conducted. The ASPC condition for maximum layer thickness was found at 125 Pa and 15% bias, while the parameters for minimum incidence of edge effect were 30 Pa and 5% bias. Samples treated under these two conditions were studied in particular and the results will be presented in the following sections.

However, it is timely to mention here that some differences in the mean residual stresses (RS) were evident from the bending of the ASPC treated thin discs. Figure 4.1-6 shows the typical profile of the RS discs, before and after treatment, collected with a stylus profilometer. The classic Stoney's formula and some modified formulas proposed by other authors were used to calculate the mean stress in the treated layer. The results show that the compressive residual stresses increased with the bias level and layer thickness (table 4.1-4). Although these results are by no means accurate, they are of use to reveal differences between the treatment conditions and to understand the behaviour of the samples in other tests.

2. Characterisation of plasma carburised AISI 316

AISI 316 samples plasma carburised in a DC furnace were adopted as bench markers for the treatments carried out under active screen arrangements. All the plasma carburising processes were conducted within the range of optimised conditions mentioned in the previous section. DC and AS treated samples showed the typical features and properties reported for carbon expanded austenite, as it will be shown in what follows.

Observation under the optical microscope revealed some changes in the microstructure after plasma carburising. The treated samples showed clear grain contrast due to slip bands, which appeared at

different orientations depending on the activated slip systems (figure 4.2-1). The slip bands can be clearly seen in the crystal orientation maps (COMs) obtained with EBSD on the same area of the sample before and after plasma carburising (figure 4.2-2). The EBSD pattern quality deteriorates after the plasma diffusion treatment, and this seems to be related with the high density of defects introduced into the crystal structure. The density of defects increases progressively as the layer grows with treatment time (figure 4.2-3)

The typical appearance of the treated layer can be seen from the cross section micrograph in figure 4.2-4. It consists of a white featureless layer which, in contrast to the substrate, is not affected by the etchant. This higher resistance to the etching agent can be considered as a first rough indication of some degree of increase in the corrosion resistance of the treated material.

With regard to morphology, a significant difference between DCPC and ASPC could be observed under SEM and AFM. Figure 4.2-5 shows the SEM high magnification micrographs, where some irregular morphology is seen on the surface of a DCPC sample, compared to the uniform appearance of the ASPC sample. This aspect was confirmed by AFM, as illustrated in figure 4.2-6, where the DCPC sample exhibits an uneven surface morphology in contrast to its ASPC counterpart.

The TEM studies conducted on the outmost layer of treated specimens revealed a slightly thicker oxide layer on the ASPC sample compared to the DCPC one (figure 4.2-7). A layer of particles was found to cover all the surface, and the typical morphology is shown in figure 4.2-8, together with the ring electron diffraction pattern (EDP) obtained on that same area. The particle size was between 25 nm and 30 nm for DCPC and between 30 nm and 40 nm for ASPC, whilst the indexing matched some iron and

chromium carbides of composition Fe_3C, Fe_2C_5 and $Cr_{23}C_6$ in both cases. Figure 4.2-9 shows the fcc diffraction pattern corresponding to austenite, which was obtained from the underlying material.

The XRD peaks shown in figure 4.2-10 were obtained from DCPC and ASPC samples and correlate with the austenite stick pattern in both cases. Only one additional diffraction peak of low intensity was found at 39.55º, which could be attributed to Hägg Carbide of composition Fe_5C_2. The peaks are sharp with a slightly asymmetric pseudo Voigt profile, and they exhibit order dependent widening compared to the untreated material. However, the reflections are shifted to lower angles, and the shifting varies with the 2θ angle. The analysis of this shifting and the calculated lattice parameters indicate that DCPC and ASPC produce the same degree of carbon supersaturation and lattice expansion (figure 4.2-11).

Figure 4.2-12 shows the typical GDOES composition-depth profiles for carbon, corresponding to DCPC and ASPC treated samples. As it is evident from this graph, there is a high degree of correlation between both curves in what concerns to the degree of carbon supersaturation, the composition profile, and also the layer thickness. A drop in carbon content is seen within the first 1 μm of the ASPC sample, which was found to match a small nitrogen peak. The active screen industrial scale unit was used for both plasma nitriding and plasma carburising, and it was not possible to remove all traces of nitrogen, even after several hours of consecutive carburising treatments.

With regard to hardness, figure 4.2-13 shows the Vickers microhardness values obtained on DCPC and ASPC samples using different loads, which serve as an indication of the load bearing capacity (LBC) of the treated layer. Once again there is a significant degree of correlation between both techniques. The ASPC samples showed some higher values at low indentation loads (25 g) which can be explained by

the nitrogen content of this outmost layer, and the slightly higher carbon content. On the other hand, the hardness of ASPC at 100 g indentation load was marginally lower than their DCPC counterparts.

The hardness values obtained with higher loads were virtually the same. However, some cracks were found inside and around the indentations conducted on DCPC specimens (figure 4.2-14). These cracks appeared at indentation loads higher than 500 g and are not considered as a failure of the treated layer, although they are an indication of a slight reduction in ductility.

The instrumented hardness tests conducted on AISI 316 untreated and plasma carburised samples confirmed a considerable increase in hardness and a small rise in the elastic modulus of the material after the plasma diffusion treatment. The curves in figure 4.2-15 illustrate the applied load against the displacement of the indentor, and the main results are summarised in table 4.2-1.

3. Study of the mechanisms of active screen plasma surface engineering

The set of experiments described in table 3.2-4 was conducted in order to understand the mechanisms involved in ASPC and the differences between the ASPC and the ASPN treatments. For the purpose of this assessment, ASPN was considered the yardstick for ASPC, as the former has been studied and discussed in further detail than the latter.

In first place, it must be said that the samples subjected to floating potential (i.e. arrangement C in figure 3.2.1-2) showed no hardening effect, and no signs of diffusion of carbon or nitrogen could be identified. Even though this evidence is of significance for the understanding of the mechanisms involved in active screen treatments, no further details will be given, since all the characterisation was identical to the untreated AISI 316 substrate.

On the other hand, DC and AS treated samples showed some hardening effect, although the results were dissimilar (arrangements A and B in figure 3.2.1-2). As the first approach, all DC treated samples, i.e. DCPN, DCPC and DCPCN, showed the characteristic edge effect; the ASPN and ASPCN samples had a very uniform surface appearance, whilst the ASPC sample exhibited a patchy morphology, which resembled the shape of the mesh used as active screen in this experiment (figure 4.3-1).

The XRD peaks shown in figure 4.3-2, for AISI 316 samples treated under different conditions, indicate that austenite is the only phase in all cases. However, the characteristic shifting and widening of the diffraction peaks of expanded austenite vary for each case. The shifting and widening is clearly seen after nitriding treatments (both DCPN and ASPN), whereas these effects are weaker on DCPC and DCPCN specimens, and almost no shifting or widening can be seen on ASPC and ASPCN samples.

The GDOES composition-depth profiles, obtained from this same set of samples, indicate the typical results after DC treatments: nitriding, carburising and N_2 enhanced carburising (figure 4.3-3). On the other hand, a significantly different response is once again evident after AS treatments. ASPN shows a similar nitrogen profile to DCPN, although the penetration depth was shallower; a similar result is observed for ASPCN, but the treated layer was significantly thinner in this case; finally the composition profile obtained from ASPC samples evidences very shallow carbon diffusion.

The LBC, assessed by means of Vickers microhardness at different indentation loads, confirmed the GDOES data (figure 4.3-4). The hardness values obtained for the nitrided test pieces were very high at low loads, and decreased rapidly at higher loads, with the onset of cracks around the indents (figure 4.3-5). On the other hand, the DCPC samples gave lower hardness values, with a gradual reduction, typical of the carbon diffusion profile; whilst its ASPC counterpart indicated little hardening effect. A similar

trend was observed on the DCPCN and ASPCN specimens, although the hardness results obtained on DCPCN show a plateau region, which also fits the GDOES composition profile.

As part of this set of experiments, AISI 304 stripes were treated in AS arrangements using a mesh with large holes, 25.4 mm in diameter. The hardness measurements conducted on these test pieces are shown in figure 4.3-6, and indicate an apparent difference between the areas uncovered (holes) and the areas covered by the cage in the case of nitriding. On the contrary, no differences are seen for carburising and N_2 enhanced carburising, in which virtually no hardening took place.

The roughness measurements performed on treated coupons showed some differences, as it can be seen from table 4.3-1, with DC treated samples showing consistently higher roughness values than their AS equals. A closer observation of AS treated specimens put into evidence the existence of a layer of deposited material on them. This was obvious on the copper coupons, some of which exhibited a silver colour after the treatment (figure 4.3-7).

SEM and AFM detailed studies showed a morphology analogous to the one described in the previous section, with particles of different sizes depending on the treatment conditions. In general, the ASPN samples appeared to be covered by a layer of fine particles, 50 nm to 100 nm in diameter, while the ASPC and ASPCN treated specimens showed a much coarser and irregular structure (figure 4.3-8).

The use of glass slides and copper substrates produced enough contrast with the deposition layer as to allow for some degree of identification of the present phases with XRD. Figure 4.3-9 shows the data collected from copper coupons and, in all cases, they show a perfect match with the peaks of the Cu standard. However, two small additional peaks at 41.69º and 44.89º can be seen after AS treatments, which could be attributed to Fe_xN and $(Fe, Cr)_xC_y$ respectively.

In the case of the glass slides, the deposition layer formed after ASPC and ASPCN was dusty, and did not resist the cleaning procedure, whilst the deposition produced by ASPN was surprisingly coherent and adherent (figure 4.3-10). The latter was analysed by means of XRD, and the diffraction peaks matched several Fe_xN compounds, and showed good agreement with the FeN pattern (figure 4.3-11). This finding is of relevance for the understanding of the mechanisms of active screen plasma surface engineering and will be discussed in the next chapter.

Finally, the mesh used for the experiments on the mechanisms of active screen plasma surface engineering was observed under the SEM and analysed by EDX to confirm its composition. The results proved that the mesh used for these experiments was AISI 304, and the typical micrograph and EDX spectrum are shown in figure 4.3-12. A similar analysis was conducted on the mesh of the AS industrial unit, and this was found to be made of low carbon steel (figure 4.3-13). In both cases, the deposited material found on the samples exhibits some interesting correlation with the material of the mesh.

4. Tribological properties

The wear resistance of AISI 316 untreated (UT), DC plasma carburised (DCPC) and active screen plasma carburised under two conditions (ASPC 125 Pa – 15% bias and ASPC 30 Pa – 5% bias) were compared. The treatment conditions selected for this assessment followed the same rationale mentioned in the section on processing, i.e. conditions of maximum layer thickness and minimum incidence of edge effect, respectively. Table 4.4-1 summarises the obtained results.

The appearance of the coupon samples after the wear tests evidences the difference in the wear response of the two materials (figure 4.4-1). The same is observed in the pictures of the counterpart WC-Co balls, in figure 4.4-2. It is also worth mentioning that a significant amount of wear debris was

produced during the wear test of the untreated material, in contrast with the very small amount found after the test in the case of all the treated samples. These three aspects of the wear tests will be described in further detail in what follows.

The measured wear volume indicated a marked improvement of all treated samples over the untreated AISI 316 substrate (figure 4.4-3). The worn volume of the expanded austenite was more than two orders of magnitude lower than that of the untreated AISI 316. On the other hand, no significant difference could be appreciated between the DCPC and the ASPC treated samples. All the treated samples exhibited wear properties typical for carbon expanded austenite.

A closer observation of the wear tracks under SEM revealed differences in morphology. The untreated AISI 316 suffered from abrasive and adhesive wear, while the treated samples developed a protective oxide layer. The difference in morphology can be appreciated in figure 4.4-4, and the composition of the oxide layer is evident from the EDX maps in figures 4.4-5 and 4.4-6. The layer is mainly formed by iron and chromium oxide, but some tungsten is also present (table 4.4-2). The latter evidences the transfer of material from the counterpart ball, and the formation of the so called third body during sliding. It is also interesting to note that nickel does not seem to follow the same pattern as chromium and iron.

Regarding the counterpart material, the size and shape of the wear scars on the WC-Co balls matched the width of the wear tracks left on coupon samples (figures 4.4-2 and 4.4-7). Detailed studies of the morphology and composition, under the SEM, revealed accumulation of material at the trailing edge (figure 4.4-8). This is more evident in the ball worn against the plasma carburised material. However, the SEM pictures and the EDX composition maps (figures 4.4-9 and 4.4-10) indicate that the amount of

material transferred from the coupon sample onto the counterpart ball is larger in the case of the untreated AISI 316. This is a clear evidence of severe adhesive wear of the untreated material.

The WC-Co balls worn against untreated AISI 316 showed a significant amount of iron and chromium on the wear scar. The oxygen signal was also strong, as the tests were conducted in laboratory air, and the high pressures and temperatures developed in the contact spots favoured oxidation (figure 4.4-9). On the other hand, the WC-Co balls worn against expanded austenite only displayed minor traces of iron oxide on the wear scar, and a small amount of material accumulated at the trailing edge (figure 4.4-10). It is evident that less material is transferred from the coupon sample onto the counterpart ball in this case.

With regard to the wear debris, obvious differences were found once again between the treated and the untreated specimens. The latter produced a significant amount of black debris during the sliding wear, and a simple test with a magnet revealed it responded to the magnetic field. Under the OM, the particles were 20 μm to 30 μm in size and metallic shiny (figure 4.4-11). The wear tests conducted on plasma carburised material produced small amounts of reddish-brown debris. This time, the particles were mostly non-magnetic, and only a few responded weakly to the magnetic field. OM observations showed the particles had a mean size of 10 μm with a plate-liked shape (figure 4.4-11).

The wear debris was observed under SEM and TEM in order to study their morphology and identify their nature. In both cases, the debris was found to be a conglomerate of smaller particles, but the particles were finer in the case of the plasma carburised material than in the untreated AISI 316 (figure 4.4-12). The ring electron diffraction patterns indicated possible martensite and magnetite matches for the untreated material (figure 4.4-13). This is in agreement with the appearance and magnetic properties

observed in the particles. On the other hand, the AISI 316 PC gave a possible haematite match, which once again correlates with the previous observations. However, an oxide of mixed nature must be present in this case, as the EDX spectrum exhibits the unequivocal presence of other alloying elements (figure 4.4-14). Table 4.4-3 summarises the findings on wear debris.

XRD was used to identify the phases present in the wear track of AISI 316 specimens. The intensity of the reflection shown in figure 4.4-15 is not considerable, but it fits the martensite pattern. In addition to this, microhardness measurements conducted on the wear track gave an average hardness of 560 $HMV_{0.01}$, which is significantly harder than the austenitic substrate. The hardness profile conducted on the cross section of the wear track clearly shows the hardening effect and, possibly, martensitic phase transformation (figure 4.4-16). Strain induced phase transformation is likely taking into account the severe deformation observed in the subsurface of the untreated material (figure 4.4-17).

EBSD phase and crystal orientation mapping gave some further evidence on the extent of the deformation and martensitic transformation. Figure 4.4-18 shows a similar SEM cross section image (without etching), and the EBSD map for austenite and martensite. These images show a 15 μm thick layer in which strain induced martensitic phase transformation took place, to some extent. Plastic deformation is evident up to a depth of 60 μm, and some degree of work hardening is also assumed to be associated with this phenomenon.

The study here presented indicates that work hardening took place during the wear tests of untreated AISI 316 against WC-Co. Moreover, evidence of strain induced martensitic transformation was found by means of TEM, XRD, EBSD and microhardness.

On the other hand, the same study conducted on the plasma carburised material yielded very different results. The electron diffraction pattern obtained with TEM did not match the martensite pattern; the XRD studies only showed reflections corresponding to austenite; and the microhardness profile conducted on the cross section was identical to a normal plasma carburised specimen. Only the EBSD orientation maps showed some evidence of deformation close to the surface (figure 4.4-19). However, this deformation was attributed not only to the shear stress of the wear test, but also to the distortion introduced by the carburising process itself.

The graphs in figure 4.4-20 show the friction signals obtained during sliding tests under similar conditions to the wear tests reported before. The results are summarised in table 4.4-4.

The AISI 316 UT couple (UT vs UT) produced an average coefficient of friction of 0.6 with fluctuations, in agreement with the literature. A large amount of wear debris was released during the tests, which was metallic in appearance, and magnetic. The WC-Co ball (UT vs WC) yielded lower friction coefficients, and left some stick-slip markings on the wear track and no significant debris; whilst the PC ball sliding on AISI 316 (UT vs PC) showed an intermediate behaviour in all these aspects. In general, the coefficient of friction clearly peaked when sliding started (μ_{static}), and subsequently decreased asymptotically to its steady sliding value ($\mu_{dynamic}$).

The friction signal for the AISI 316 untreated ball sliding against a PC disc (PC vs UT) exhibits significant instabilities with very high friction peaks. The peaks in the friction force correlated with intense noise during the test, and a considerable amount of black magnetic debris was produced. Both the WC and the PC balls sliding on PC discs (WC vs PC and PC vs PC) yielded lower coefficients of friction and produced small amounts of reddish brown wear debris, mainly non-magnetic (only some

particles responded to the magnet). The friction force displayed a relative maximum at the beginning of these tests, followed by a period of low friction and a final increase up to the final steady friction coefficient, which was higher than the initial relative maximum ($\mu_{static} < \mu_{dynamic}$).

5. Corrosion behaviour

The initial immersion corrosion tests conducted in a sulphuric acid solution (16% mass fraction) at room temperature produced very little corrosion in all the test pieces. The AISI 316 samples were found to change the appearance to a tarnished grey colour after only 10 minutes of exposure to the acid, while the PC samples retained their metallic shine throughout the experiment. OM and SEM observations of the corroded specimens revealed intense corrosion on MnS inclusions in the AISI 316 coupons, and failure of the outmost deposited layer of carbides in their ASPC equals (figure 4.5-1). The test was repeated with PC samples polished after treatment, on which no deposition layer remained, and no significant features or morphology could be observed in this case.

The tests conducted at boiling temperature in the same sulphuric acid solution (16% mass fraction) revealed clear differences between the specimens, as can be seen from figure 4.5-2. Corrosion was catastrophic on AISI 316, while the layer of EA was left virtually intact. The edges of DCPC 400 and ASPC 125 test pieces showed some contrast with the rest of the surface area, associated with some degree of edge effect. On the other hand, the ASPC 030 sample showed a very uniform surface appearance. The cross sections in figure 4.5-3 illustrate the different behaviour of the AISI 316 UT and AISI 316 PC (EA).

Detailed observation under SEM revealed some localised corrosion on the EA layer. The attack was particularly intense on MnS inclusions and, once the substrate was exposed, cavities of considerable

size were formed in the subsurface (figure 4.5-4). Some localised attack was also detected on slip bands, even in the early stages of the tests, although corrosion progressed slowly and the layer was still unbreached after 20 hours of exposure to this corrosive solution (figure 4.5-5). Finally, the grain boundaries were found to be vulnerable to localised corrosion, and this type of attack was clearly identified on samples exposed for 15 hours or longer periods of time (figure 4.5-6).

With regard to the preferential corrosion on slip bands and grain boundaries, it must be mentioned that these were observed more frequently on DCPC 400 and ASPC 125 samples than in the ASPC 030 ones, which were actually free from intergranular corrosion. In all cases, corrosion was more intense close to the edges of the samples, where the density of slip bands was higher and the grain boundaries appeared to be weaker. Once the layer of EA was breached, preferential dissolution of the substrate took place rapidly creating large subsurface pits, with some grain boundaries failing first (figure 4.5-7).

The tests performed on cylindrical specimens yielded similar results, with catastrophic corrosion of the AISI 316 substrate and mild corrosion of the treated samples, which took place, mainly, through defects in the EA layer (figure 4.5-8). The AISI 316 samples turned black after only a few minutes immersed in the corrosive solution, and a considerable amount of gas bubbles formed on their surface, which was attributed to the cathodic evolution of hydrogen. On the other hand, the PC samples retained their metallic appearance, although they became dull after the test. The evolution of hydrogen was not so profuse in these last cases.

The localised attack at the centre of the rods is noteworthy, and was attributed to the presence of MnS stringers; while the extended damage towards the edges of specimen DCPC 400 was believed to be a consequence of stronger edge effects produced by these treatment conditions. Finally, this tests also

provided quantitative data in the form of the average mass losses (3 samples per condition), which are shown in figure 4.5-9. The mass losses of all PC specimens were between 4 and 6 times lower than their untreated AISI 316 counterparts.

Corrosion tests conducted in H_2SO_4 16% solution with addition of $CuSO_4$ while in contact with metallic copper, produced very little corrosion of the AISI 316 substrate, though some degree of attack was found on defects of the EA layer. In this solution, the evolution of hydrogen was replaced by the cathodic reduction of copper ions, and no gas bubbles were seen to form on the surface of the test pieces. As it can be seen in figure 4.5-10, the edges of the specimens were more susceptible to localised corrosion, especially in the case of specimens DCPC 400 and ASPC 125, whereas their ASPC 030 and AISI 316 counterparts displayed very homogeneous appearances.

Closer observation with OM revealed preferential attack on slip bands in all the treated samples (figure 4.5-11). However, grains with higher density of slip bands were more severely attacked, so that corrosion was more extensive on DCPC 400 specimens, followed by ASPC 125 and ASPC 030. With regard to grain boundaries, even though no grains were dislodged and no severe intergranular corrosion was observed, some ditch type grain boundaries were seen on coupons DCPC 400 and ASPC 125; the edges of the samples were particularly vulnerable to this type of attack.

SEM and AFM studies of the corroded grain boundaries revealed they were the result of the coalescence of pits at the intersection of the slip bands with those grain boundaries, to form a continuous trench (figure 4.5-12). Moreover, EDX composition line scans provided some evidence of carbon enrichment in the area surrounding the trench, although this is not conclusive as no correlation could be found with carbide forming elements, particularly chromium (figure 4.5-13).

The gravimetric tests conducted on the test pieces corroded in boiling H_2SO_4 16% with $CuSO_4$ indicate very low mass losses, two orders of magnitude lower than the values reported for H_2SO_4 16% solution. Even though the figures are not conclusive, the corrosion factors in table 4.5-1 show a trend that is helpful to understand the results and rank the treatments according to their corrosion resistance.

Two other corrosive solutions were adopted in order to assess the susceptibility of the grain boundaries of the PC samples to localised attack: sulphuric acid 40% solution with iron sulphate, and nitric acid 20% solution. The former test was conducted for 24 hours and produced a very similar attack to the one observed with copper sulphate. Corrosion was more intense on defects in the EA layer, mainly slip bands, and some pits coalesced to produce more severe localised attack and form some ditch grain boundaries. The edge effect was revealed in the case of DCPC 400 and ASPC 125, while the ASPC 030 and AISI 316 exhibited a very even morphology.

In the case of nitric acid, the test was conducted for a total of 240 hours, in 5 periods of 48 hours in which the solution was renewed. The appearance of these samples differed slightly from previous tests, principally with regard to the attack on grain boundaries. As it can be seen from figure 4.5-14, the untreated AISI 316 suffered some mild attack and only the grain boundaries were developed after the test. On the other hand, all PC samples exhibited localised corrosion on slip bands and pits, which were larger and more numerous on the DCPC 400 specimens, followed by the ASPC 125 and the ASPC 030.

No grains were dislodged during the test, but ditch type grain boundaries were clearly observed under AFM, having a depth of, at least, 0.8 μm (figure 4.5-15). In these cases, the grain boundaries had the appearance of a continuos trench surrounding full grains, and no traces of primitive pits could be identified. Some severe localised corrosion was found in PC samples, which was attributed to the

presence of inclusions (figure 4.5-16). This type of attack was clearly present in all cases and, although it was not generalised, the depth of the pits was enough to be taken into consideration as a failure mode of the EA layer. In contrast, the corrosion rates calculated from gravimetric measurements indicate that the corrosion rate of the PC samples becomes comparable to the one of AISI 316 untreated substrate, after an initial period of high dissolution (figure 4.5-17).

6. Plasma diagnostics – Optical emission spectroscopy

The OES spectra collected with the telescope through the sight port of the furnaces were useful to identify the most common active species involved in electric discharges through different gas mixtures, i.e. CH_4–H_2, CH_4–N_2–H_2 and N_2–H_2. The spectra in figures 4.6-1 to 4.6-3 show some of the differences. The signals collected through the sight port for DC and AS experimental arrangements were virtually identical, although the emission intensity was slightly higher in the AS setting, due to the hollow cathodes formed on the mesh.

In the case of plasma carburising (CH_4–H_2), the spectrum was very scarce in peaks, and only the atomic hydrogen Balmer series could be seen. The H_α at 656.125 nm dominated this wavelength range, and only some weak H_2 and CH^+ peaks completed the spectrum. For the nitrogen enhanced plasma carburising (CH_4–N_2–H_2), the addition of only 1% N_2 changed the shape of the spectra in a considerable way, and the CN (violet system) and N_2^+ (first negative system) bands were clearly present, although the H_α line remained to be the most intense. Finally, the spectra for plasma nitriding were dominated by the N_2^+ (first negative system) bands which, under some conditions, were even more intense than the H_α emission line. Some NH, hydrogen and nitrogen peaks completed the spectra.

The study of OES emission spectra under different active screen conditions was found difficult to conduct with this experimental arrangement, i.e. from outside the furnace. When measurements were done through the sight port, the telescope was focused on the active screen itself (the mesh), which is designed to form hollow cathodes. These hollow cathodes changed their position, quantity and intensity depending on the treatment conditions and, as a result, they also made the collected OES signal erratic. In conclusion, no clear correlation could be observed between these emission spectra and the AS treatment conditions.

The optical fibres used to probe the AS industrial unit yielded optical signal directly from the worktable, which was found to vary consistently with the treatment conditions, although this was achieved at expense of signal intensity and signal-to-noise ratio. Therefore, only the strongest emission lines and bands could be used for this purpose, and the H_α and H_β peaks of the Balmer series at 656.125 nm and 486.003 nm respectively, were selected in the case of plasma carburising‡, whilst the N_2^+ emission band at 391.44 nm was chosen for the assessment of plasma nitriding. The emission intensity was recorded, for each gas mixture, at different working pressures and bias levels, and the information was consolidated in graphs of the kind shown in figure 4.6-4.

The OES maps thus obtained exhibit increasing intensity with increasing level of bias, and this intensity is higher in the low pressure region. As it was mentioned in a previous section, low working pressures imposed a limitation on the level of bias and, consequently, on the emission intensity. Increasing the gas pressure allowed a further increase in the applied bias, and the emission intensity responded accordingly. However, this was true only until some pressure threshold was reached, and the relative maximum in emission intensity was found to agree with the conditions identified for maximum layer

‡ The use of the H emission lines was justified because atomic hydrogen is a by-product of the decomposition of the methane molecule and trials showed some sensitivity of peaks in the Balmer series to the amount of CH_4 in the gas mixture. Nevertheless, the identification of clear and strong carbon containing species would of course be of interest.

thickness. Once the pressure threshold was exceeded, the emission intensity fell even for very high levels of bias; this point was found at higher pressures for ASPC than for ASPN (figure 4.6-5).

The optical signal was plotted against different electric parameters and some trends were revealed, depending on the gas pressure and the gas mixture (figure 4.6-6). The emission intensity plotted as a function of the bias voltage showed some quadratic trend at high pressure, while the data points obtained at low pressure deviated from this line. Both ASPC and ASPN exhibited very similar responses to the electric potential of the worktable. The emission intensity was found to vary linearly with the electric current, although the slope was affected by the gas pressure and, furthermore, a clear breaking point was found in ASPN, whereas this was not visible for ASPC. Finally, the emission intensity showed considerable correlation with the bias power applied on the work table, with slight changes in slope for ASPC and a clear breaking point for ASPN.

7. Plasma diagnostics – Ion flux probe

The use of the IFP under AS arrangements inside a DC furnace indicated a strong electrostatic coupling with the active screen electric input. This was concluded from the oscillations in the floating potential (FP) of the electrostatic probe, which perfectly matched the electric input characteristics of each furnace (figure 4.7-1); while the same experiments conducted in conventional DC arrangements showed only background noise on the FP electric signal. Figure 4.7-2 shows the differences in FP between the DC and AS arrangements, which was seen to depend on the gas mixture and gas pressure used for the experiment. In addition, the flux of ions was measured and the obtained results indicate appreciably higher values in the case of the AS setting, although it must be said that these figures bare considerable error.

A similar type of analysis was conducted inside the AS industrial unit, and the oscillation in the FP of the electrostatic probe was once again in agreement with the power input of the furnace (figure 4.7-3). The average value of the FP was also found to vary with the treatment conditions, shifting to more negative values with increasing bias and pressure (figure 4.7-4). However, a limitation imposed on the applied bias was once again found at low gas pressure, and the FP values were observed to remain constant or even decrease slightly once this bias saturation level was reached. Unfortunately, only a reduced range of treatment conditions could be assessed because of limitations in the probe and the measuring circuit.

An attempt was made to calculate the ion flux from the drain curve of the capacitor of the IFP measuring circuit. Figure 4.7-5 shows the drain curves obtained with the worktable under floating potential for ASPC and ASPN at different gas pressures. The different responses were clear, and the capacitor was drained several times faster in the low pressure range, indicating a higher rate of arrival of positive charges onto the effective surface area of the probe. Some measurements were also conducted under normal treatment conditions, although the range was seriously restricted by limitations of the probe and the measuring circuit, and the errors make these figures unreliable. In general, it can be said that the calculated ion fluxes increased with bias and decreased with gas pressure (figure 4.7-6).

CHAPTER 5: INTERPRETATION AND DISCUSSION

1. Active screen processing conditions

The current-voltage characteristic curves obtained in the AS furnace indicate a non-linear relationship typical of abnormal glow discharges, with the current density increasing more rapidly at higher pressures (figure 5.1-1) [190, 192]. The two constraints found in the operating conditions, namely the onset of edge effects and the current saturation, are relatively well known phenomena.

The edge effect is a result of the local increase in the electric field, and the consequent higher ionisation rate and higher current density [218]. This obviously declines when lower electric potentials are applied, although it has also been reported that low pressure discharges are less sensitive to concentration of electric field on sharp edges [219].

The current saturation can be attributed to a low density of charge carriers and to technical limitations of the power supply. In the plasma, the density of electrons is approximately the same as the density of ions ($n_e \approx n_{+)}$, and the current density can be expressed as [220]:

$$j = en_e \mu_e E = \sigma E \qquad (5.1\text{-}1)$$

where j is the current density, e is the elementary charge, n_e is the electron density, μ_e is the electron mobility, σ is the conductivity of the weakly ionised gas, and E is the electric field. The value of E is defined by the potential delivered by the power supply (U_{MAX} = 926 V for the AS furnace) and the distance between the electrodes in the furnace, which impose the first limitation.

The conductivity of the ionised gas (σ) is a function of the density of charged particles and, consequently, of the frequency of ionising collisions. A coefficient α is widely used to express the number of ionising collisions undergone by one electron in a 1 cm trajectory along the electric field *E*. This is defined by the following equation [220]:

$$\frac{\alpha}{p} = Ae^{\left(-\frac{B}{E/p}\right)} \qquad (5.1\text{-}2)$$

where α is Townsend first ionisation coefficient, *p* is the gas pressure, *A* and *B* are gas constants and *E* is the electric field between the electrodes. A reduction in the pressure increases the E / p ratio and the mean energy acquired by electrons between collisions, but it also reduces the probability of collision with gas molecules, which defines the second constraint for equation 5.1-1.

Equation 5.1-2 resembles the experimental relation 4.1-2. Even though no clear physical meaning could be attributed to each one of the constants, term *C* seems to account for the *avalanche effect*, while the term on power *P* varies as σE (equation 4.1-1).

With regard to the bias, it is interesting to note that the real applied power differed from the bias set point (figure 5.1-2). The deviations were considerable and erratic, although it can be said that at low pressures there was a trend towards higher power levels than the set point, while at high pressures the tendency was inverted. The data points for bias current, plotted against bias set point, lay in a straight line, so that the control system is believed to calculate the bias from the current measured on the work table (figure 5.1-3). This deviation is not considered to be of fundamental importance as long as it is considered in the analysis.

No meaningful correlation could be found between the bias set point or the bias current and the optimum treatment conditions at 125 Pa and 15% bias for ASPC, and 75 Pa and 10% bias for ASPN. However, the applied power exhibits a very similar trend and the optimised treatment conditions correspond to maxima in the applied power (figure 5.1-4). This is not surprising taking into account that the electron density increases with the applied power [221]. At low pressure, the bias current saturates and the power is thus limited, but higher power can be applied at moderate pressures. For current densities low enough to avoid edge effects, the maximum applied power corresponds to the optimum condition.

The optimised conditions for ASPC and ASPN also show some qualitative agreement with the Paschen curves reported for pure H_2[§] and 25% N_2 – 75% H_2 [220, 222]. Pure H_2 breaks down at higher potentials and values of $p \cdot L$ (pressure x distance between electrodes) compared to the 25% N_2 – 75% H_2 mixture. Furthermore, the ratio pL_{H2} / $pL_{N2\text{-}H2}$ from the cited references gives an average value of 1.46, while the ratio of optimum pressures for this project p_{ASPC} / p_{ASPN} yields 1.66, which is in reasonable agreement. This is a rather speculative interpretation, although it seems sensible to think of the optimum working conditions found in this project as those closest to the point of highest ionisation efficiency, i.e. the minimum in the Paschen curve [189].

Unfortunately, the full Paschen curves could not be obtained in the present project, thus only very general conclusions can be drawn. In view of the experimental evidence, the curves are expected to show a minimum breakdown potential in the region of the optimum treatment conditions reported here, while they would be shifted to lower potentials and lower $p \cdot L$ values compared to the conventional DC discharges, due to the additional influx of electrons from the metallic mesh of the AS furnace [223, 224].

§ The 3% CH_4 content of the gas mixture used for ASPC does not significantly affect the plasma physicochemistry, so that it will be considered as pure H_2 for the purpose of this analysis.

In this regard, a comparison of the discharge parameters in DC and AS furnaces, making use of the similarity relations [157], indicated the presence of additional charge carriers [190], i.e. the AS furnace draws larger current and power than the DC furnace for similar discharge conditions (table 5.1-1).

Finally, figure 5.1-5 shows the same I-V characteristic curves of figure 5.1-1, but this time it includes the value of E / p, represented in the size of the bubble. It is clear from this graph that electrons acquire significantly larger energies in the low pressure side of the range of assessed conditions, which accounts for the increased efficiency of the plasma treatment observed in this same pressure region.

2. Carbon expanded austenite

2.1. Layer growth kinetics

The results obtained by means of DCPC and ASPC showed substantial agreement in terms of layer thickness, although differences were found depending on the ASPC treatment conditions (table 4.1-2). An estimation of the carbon diffusivity was obtained making use of the following equation:

$$x = a(Dt)^{1/2} = Kt^{1/2} \qquad (5.2\text{-}1)$$

where x is the layer thickness, a is a constant, D is the carbon diffusivity, t is the treatment time, and K is the product of a and D. The obtained values are listed in table 5.2-1 and they are in substantial agreement with the values reported in the literature [118, 119, 225].

The measurements of layer thickness conducted after different treatment times gave some information regarding the growth kinetics, as it is illustrated in figure 5.2-1. The data points obtained in this project are plotted together with those reported by Y. Sun [118] and M. Tsujikawa et al. [119, 225]. The former

reported a linear dependence of layer thickness with the square root of time (equation 5.2.2) and interpreted it as a proof of the dominance of atomic diffusion mechanism.

$$x = 3.80 + 5.95 \cdot t^{1/2} \qquad (5.2\text{-}2)$$

On the other hand, the data reported by Tsujikawa et al. [119, 225] show a quadratic dependence of layer thickness with the square root of time, which agrees with the data points obtained in this project. This trend has also been identified by other authors [226, 227] who attributed the deviation to the sputtering of substrate material by highly energetic ions from the plasma.

One additional outcome of these assumptions is the existence of some incubation time for the layer growth. The linear dependence reported by Sun has a non-zero ordinate at origin, which was considered to be the consequence of adding methane to the gas mixture during the heating stage. In contrast, the quadratic dependence found in this project, and also reported by Tsujikawa, indicates some time will elapse before the layer starts growing, and this feature is of significance in order to understand the mechanisms involved in the treatment.

To this end, it is generally accepted that expanded austenite forms under a metastable equilibrium of carbon in austenite, sometimes referred to as paraequilibrium (PE) [110, 122, 147]. Leaving aside some discussion on terminology [228-230], paraequilibrium can be defined as a kinetically constrained equilibrium, in which the substitutional atoms are virtually immobile in front of the interstitial atoms [231, 232]. Other authors have interpreted PE as a complete trapping of interstitials in the substitutional lattice [233] and, in the particular case of expanded austenite, the chromium content of the alloy seems to play a fundamental role in trapping C and N interstitials [101].

Other trapping mechanisms of interstitial elements have been reported, which include interaction with crystal defects [234]. Maalekian et al. [235] have recently studied the influence of a heavily dislocated crystal structure on the distribution of carbon in martensitic steel, and Heure et al. [236] conducted internal friction studies on ASS gas carburised at low temperature and concluded that the obtained results were consistent with multicarbon interstitial-vacancy complexes. In the present study, COMs were obtained on the same areas of a sample after different treatment times. Figure 5.2-2 shows the average EBSD pattern quality and the carbon content from GDOES profiles, obtained after each treatment. The pattern quality is sensitive to defects in the crystal structure [237] and a qualitative correlation can be seen, although this evidence is not solid enough to draw conclusions.

2.2. Microstructure evolution

With regard to the microstructure, comparative studies conducted on AISI 316 after DCPC and ASPC showed equivalent results. Figure 4.2-1 illustrates the change observed on the microstructure of AISI 316 after PC. The presence of slip bands has been previously reported [135, 238-240] and it is a clear indication of plastic deformation of the surface layer under the high compressive stresses developed upon the expansion of the austenite lattice. Contrary to what Xu et al. have reported [241], very short incubation times were necessary in the present case, and slip lines were found in AISI 316 samples after only 1 hour of plasma carburising treatment at 450ºC. The density of slip bands and the height of the steps were observed to increase with treatment time.

The strain is obviously unevenly distributed, and depends on the crystallographic orientation of the grains, relative to the stress plane [242]. In this way, some grains show no signs of deformation, while others show one or two sets of parallel slip lines, i.e. one or two slip systems have been activated. Moreover, a higher density of slip bands is seen close to the grain boundaries, whereas the central

region of the grain remains relatively unaffected (figure 5.2-3). This is the result of the stress concentration and generation of dislocations at certain regions of the microstructure [243-245].

The rotation of the crystallographic structure upon plastic deformation is known to affect the texture of ASS [246] and the anisotropic strain produced during plasma or ion beam surface treatments has been found to produce rotation of the crystallographic planes of single crystal and polycrystalline samples [247-249]. Several authors conducted XRD texture studies on plasma nitrided samples, and reported differences in the pole figures obtained before and after the surface treatment [113, 250, 251]. Figure 5.2-4 shows the results obtained on PC samples in this project, which show good agreement with the results reported by Mändl et al. [250].

The crystallographic structure of carbon and nitrogen EA has been extensively studied by means of TEM and XRD, and there is a significant body of literature and discussion in this regard [106, 111, 114-116, 252]. TEM studies provide extremely useful but also very localised information, and in the case of XRD it is difficult to establish the individual contribution of different effects (residual stresses, dislocations or stacking faults) [112, 114]. Therefore, an attempt was made to use EBSD and AFM to provide complementary information on the microstructure of EA.

The slip bands in figure 5.2-5 exhibit some 40 nm steps, which are considerably larger than the 10 nm limit reported for approximately 45% deformation in a similar material under tension [253]. The number of emerged crystallographic planes can be estimated taking into account the relationship:

$$h = n\vec{z} \cdot \vec{b} \qquad (5.2\text{-}3)$$

where *h* is the height of the step, *n* is the number of planes, $\vec{z}$ is the vector normal to the surface and $\vec{b}$ the Burgers vector for the dislocations. Computations for the most common steps, about 30 nm in height, yielded some 100 planes. Slipping was assumed to take place mainly along the {111} <110> path, as this is known to be the main slip system in AISI 316 [242, 245, 246, 253].

The deformation mechanism proposed in [253] implies that the balance between the internal friction necessary to move dislocations and the external applied stress (or the local stress field at a given stress raising point) is reached at maximum deformation steps of 10 nm, equivalent to 52 emerging dislocations. Consequently, if a direct comparison is considered valid, larger stress levels must have been reached in the present project or the additional amount of dislocations generated by the plasma diffusion treatment changed the equilibrium point.

The slip system activated in each grain, by the compressive plane stress developed during PC, depends on the crystallographic orientation, as it can be seen in figure 5.2-6. Grains with one of the {111} planes parallel to the surface are more prone to cross slip, although the angle of cross slip in some grains indicate that sliding could have taken place on {100} or {110} planes, when their orientation was suitable. The domains formed on cross slip, i.e. the chessboard like sub-grain arrangement [245], would play a role of significance in the distortion and broadening of the XRD peaks, and could eventually develop a deformation texture [246]. Although the inverse pole figures obtained with EBSD showed some changes after the PC treatment, no consistent trend was observed.

The sub-grain structures are clearly visible after plasma carburising, and some sub-grain boundaries can be seen from the line scans shown in figure 5.2-7. Moreover, the misorientation map also exhibits signs of distortion (figure 5.2-8), and the grains with high density of slip bands also show large levels of

misorientation within the grain. It is speculated here that the small domains formed by cross slip rotate upon deformation and they are thus responsible for the misorientation observed within the grains [246]. The AFM scans also indicate that these domains do not remain plane, but they are tilted during sliding (figure 5.2-5). The changes in the colour orientation code of the EBSD COMs (sample normal direction) indicate rotation of the crystallographic planes. Although attempts were made to quantify this rotation, the results were not consistent.

The orientation relationship of grain boundaries was also affected by the plastic deformation, and the change in $\Sigma 3$ CSL grain boundaries is illustrated in figure 5.2-9. The degradation of CSL grain boundaries with increasing strain has also been reported in [245], and it was found to be a consequence of the rotation of the crystallographic planes away from the original CSL orientation relationship. Some CSL were seen to degrade faster, presumably because those grains were suitably oriented for deformation and rotation. However, this trend extended rapidly towards all the microstructure and grain boundaries at longer treatment times and, consequently, larger strains.

2.3. Residual stresses (RS)

The assessment of residual stresses developed on AISI 316 PC samples has long been attempted, as it has a considerable influence on the performance of this material. Several methods have been used to measure residual stresses, and XRD is among the most accepted ones. Unfortunately, it was not possible to use the XRD d-sin$^2\psi$ technique in this project, so alternative methods were used. However, some comments will be made with regard to the XRD results obtained in the θ-2θ geometry.

After plasma carburising, the XRD austenite peaks were found to be consistently shifted to lower 2θ angles and broadened, the latter effect increased with the reflection order. There exist a number of

different causes which could be responsible for these effects, and the determination of their individual contributions usually involves some assumptions [249, 254]. Stacking faults and microstrains are thought to be the main reasons for the peak broadening [107, 112], together with a reduction in the size of the diffracting domains as a result of the considerable plastic deformation undergone during PC [255, 256]. The peaks are broadened very nearly symmetrically, so that twin faults seem to play only a minor role [257-259].

The peak shifting can be associated with the high density of dislocations, twins and stacking faults, and also with the level of residual elastic strains, i.e. residual stresses [107, 114, 257-259]. It is once again difficult to separate the contribution made by each of these effects, but the XRD diffraction peaks (figure 4.2-10) and the plot of a_{hkl} vs $\cos\theta \cdot \cot\theta$ (figure 4.2-11) are consistent with an uneven lattice expansion (table 5.2-2) and the presence of high compressive residual stresses [107, 112, 114]. An attempt was made to estimate the residual stress by using the method proposed by Wagner et al. [259]. This method uses second order reflections to separate the contribution made by stacking faults and residual stresses to the peak shifting. Thereby, the maximum residual stress estimated in this way was -1.98 GPa (refer to Appendix C for details on this calculation).

The XRD measurements of residual stresses conducted by Sun et al. [254] on carbon EA yielded average values in the order of -0.3 GPa to -1.5 GPa within the layer, with maximum compressive residual stresses at the surface between -1.5 GPa and -3.5 GPa. These values were compared with the maximum compressive residual stress from the expansion produced by the carbon content of EA, calculated to be as high as -10 GPa, and plastic deformation was proposed to account for the partial relaxation of such enormous residual stresses.

In this project, modified Stoney's formulas were used to calculate the residual stresses developed during PC, from the curvature of thin discs. Calculations yielded values of compressive residual stresses in the order -0.4 GPa to -0.8 GPa, which are in considerable agreement with the average residual stresses reported in [254]. The theory of thin plates and shells [260-262] was used to analyse the bending discs further (refer to appendix C for details on these calculations). The average residual stress obtained was -0.770 GPa, which is very close to the value obtained with the Stoney's formula.

However, this calculation assumes a constant residual stress profile within the EA layer, which is far from the real case. If the stress distribution is approximated by a triangular distribution (figure 5.2-10), and reducing the moments to the layer-core interface, it yields a value of residual stresses at the surface of -1.155 GPa. Furthermore, this triangular distribution of residual stresses is still fictitious. If the hardening effect is considered to be a function of the carbon content of the EA, it is thus sensible to assume that the residual stresses profile will be similar to the carbon-depth profile obtained from GDOES. Figure 5.2-10 shows the distribution which, for the same input data used previously, gives a maximum residual stress at the surface of -1.22 GPa.

These levels of stress are obviously higher than the yield stress of AISI 316 (240 MPa) so that a significant degree of strain hardening must have taken place. It would be thus reasonable to presume that the residual stresses are distributed according to the strain hardened profile [263]. Microhardness tests are sensitive to residual strain [264, 265] and indentations conducted at different loads provide information from different layers of material, depending on the penetration depth. The ratio of indentation diagonal (D) to penetration depth (h) can be estimated to be approximately 7:1 [266]; and empirical evaluations have shown that the contribution made by the first layers of underlying material up to a depth equal to $3 \cdot h$ accounts for the 44% of the measured hardness [267].

Figure 5.2-11 shows hardness profiles calculated from LBC Vickers microhardness experiments, considering the hardness values represent a layer of material equal to 1, 2 and 3 times the indentation depth h. The hardness profile vs 3h is in reasonable agreement with the Knoop hardness profiles, except for the outmost layer, where errors are known to increase for hardness measurements conducted on cross sections. Considering a distribution of residual stresses equivalent to the curve hardness vs 3h, the maximum compressive stress at the surface is found to be -1.61 GPa, in order to produce the same bending moment as in the previous cases (figure 5.2-10).

The values of residual stresses obtained with this method are in surprisingly good agreement with the ones measured by XRD. However, it must be said that the former method is expected to yield lower values than the latter. The reason for this is that the bending discs give information about the residual stresses of the first kind or macrostresses, whereas XRD measures microstresses [268].

Finally, the curves obtained by instrumented indentations will be briefly discussed from the point of view of the residual stresses present on the samples. The indentations are affected by the presence of residual elastic stresses and residual plastic strains, especially in the case of a material that work hardens [269-271], and the shifting of the curves obtained from EA are consistent with the presence of high compressive residual stresses (figure 4.2-15).

Unfortunately, the methodology used to estimate the residual stresses usually requires imaging the indentation marks, and also the determination of some experimental coefficients, which could not be done during this project. However, an attempt was made to calculate the residual stresses following the methodology proposed in [272]. This method assumes the elastic response of the material is not affected by the residual stresses, and so the shadowed area in figure 5.2-12 would represent the elastic

energy contribution of the residual stresses. Making use of some geometrical considerations with regard to the indentor, the residual stresses can be calculated as follows:

$$\sigma_{residual} = \frac{P_1 - P_2}{2\pi \tan^2 \alpha h^2} \qquad (5.2\text{-}4)$$

where P_1, P_2 and h are obtained from figure 5.2-12 and α is an experimental coefficient. Substituting the values in table 5.2-3, one obtains a residual stress of -9.57 GPa. This compares favourably with the maximum theoretical stress of -10 GPa calculated by Sun et al. from the carbon content of EA, although such a high level of stress is highly unlikely. The coefficient α could be a source of error, as this is experimentally determined and the same value of α as in [272] was used in this calculation, without further consideration. The method could thus yield some interesting results, although further consideration of the experimental constants is necessary.

3. Tribological properties

3.1. Wear of AISI 316 untreated substrate

The evidence obtained on AISI 316 samples agrees with the results reported in the literature [52, 56, 57, 60, 61]. The rough appearance of the wear track (figure 4.4-4), the large size, shape and metallic nature of the debris (figure 4.4-11) [273], the occurrence of strain induced martensitic transformation (figure 4.4-15) and the severe plastic deformation of the subsurface (figure 4.4-17) are all signs of severe wear [274]. The plastic deformation of the subsurface and the formation of a fine microstructure in the severely distorted layer of material are characteristic features of this wear regime. Moreover, the EBSD COM revealed that this layer of material develops a strong deformation texture showing {111} or {100} planes parallel to the surface (figure 5.3.1-1) [275, 276]

According to the theory of adhesive wear, the plastic flow of the subsurface is a result of the adhesion between asperities at the sliding surfaces [62]. At the same time, some loose particles may become embedded in one of the surfaces, and produce deformation and abrasion on the opposite surface [277]. The theory of adhesive wear is useful to explain such phenomena as subsurface deformation, transfer of material to the counterpart slider and friction. However, this theory has been extensively challenged because it fails to elucidate the mechanism of detachment of wear particles [274].

The theory of delamination has been developed to describe wear under conditions of subsurface plastic flow [65, 278], and accounts for the formation of plate like wear debris particles, similar to the ones found in this project [75]. The theory predicts the formation of subsurface voids, which would coalesce to form cracks and, ultimately, to detach metallic debris particles. Although this theory has been extensively used to analyse wear of metals [75, 274, 275, 279], other authors have questioned its fundamentals, i.e. the nucleation of cracks in a region of the substrate which is essentially subjected to high compressive stresses [280, 281]. These same authors proposed an alternative mechanism of wear known as ratchetting.

According to the ratchetting wear mechanism, the fractures nucleated in the substrate are of ductile nature, as a result of the severe plastic strain imposed by sliding. If the loads are low and the yield point of the material is not exceeded, i.e. within the elastic range, the failure mechanism is most probably one of high cycle fatigue [281]. On the contrary, if the yield threshold is exceeded, plastic deformation takes place and accumulates in the subsurface region after each loading cycle. Consequently, the total strain accumulated in the subsurface, after a number of loading cycles, exceeds the strain produced by each individual loading cycle [280, 282] (figure 5.3.1-2). The latter scenario would lead to failure through a low cycle fatigue mechanism, called ratchetting wear [281].

In both cases, i.e. delamination and ratchetting, the plastic flow accumulated in the subsurface plays a fundamental role in the wear process. The understanding of the wear mechanisms of AISI 316 helps to identify the cause of the significant increase in wear resistance observed after low temperature plasma carburising. This will be further discussed in the following section.

3.2. Tribological properties of the expanded austenite layer

The plasma carburised specimens showed a significant improvement in tribological performance when compared with the untreated AISI 316 (figures 4.4-1 and 4.4-3). Moreover, clear evidence of oxidational wear mechanism was obtained from the appearance of the wear track (figures 4.4-4 to 4.4-6), the appearance of the wear debris particles (figures 4.4-11 and 4.4-12) and their nature (figures 4.4-13 and 4.4-14).

Close observation of the wear tracks produced on PC specimens showed brittle failure of the outmost layer of carbides (figure 5.3.2-1). This was very clear on samples with a thin EA layer, in which the brittle carbide layer had very little or no support from the substrate [283]. On the other hand, the failure of the outmost layer of carbides is not so clearly seen on specimens with thick EA layers. The carbides are obviously removed upon wear, as the EA layer exhibits a very smooth surface with no signs of the original particulate morphology (figure 5.3.2-2), but no evidence of spalling could be found on the sides of the wear track. This can be attributed to the support provided by the underlying EA. In any case, the outmost layer of deposited carbides does not seem to play a significant role in the wear resistance of EA.

It is important to note that very little plastic strain is seen in the subsurface of worn PC specimens (figure 4.4-19). The deformation is mainly elastic, and plastic strain is only confined to the surface. The ratio of

elastic modulus to hardness (table 4.2-1) reflects this change, as it dropped from 105.75 for the untreated substrate to 20.48 for the plasma carburised layer. Therefore, according to the theory of ratchetting, the failure mode would change from low cycle fatigue (ratchetting) to high cycle fatigue [281]. The predominance of this wear mode depends on contact mechanics considerations [85], namely the normal load, the friction force and the roughness of the sliding surfaces. The maximum load a specimen can bear without undergoing plastic deformation is a function of the EA layer thickness, and failure of plasma carburised components has been reported at high loads, induced by the plastic deformation of the underlying substrate material [129, 130].

In the case of a thick enough EA layer, or a low enough normal load, the stresses developed in the subsurface are within the elastic range, and the wear process is limited to the surface of the specimen, where a layer of oxide forms. The formation of this layer of oxides on the tribosurface is an indication of a mild wear mode, which is commonly called oxidational wear [284]. The flow of heat is of significant importance to this wear mechanism, as it defines the formation of the oxide layer. Additionally, different types of oxide will be stable depending on the flash temperature, i.e. the temperature developed at the contacting asperities [63]. In this way, haematite (α-Fe_2O_3) is reported to be the stable oxide at temperatures below 300ºC, whereas magnetite (Fe_3O_4) is stable between 450ºC and 600ºC [58, 71, 284]. Regardless of the type of oxide, oxidational wear is a mechanism of mild wear.

The formation of the layer of oxide is thus of interest, in view of its relevance to the wear process, and figure 5.3.2-3 shows the genesis of this layer. In the first place, small fragments are deformed under the stress developed during sliding. It is important to note that these fragments may include WC particles pulled out from the counterpart ball, as a result of the abrasion of the Co binder (figure 5.3.2-4) [285]. The fragments are subsequently compacted, to form a coherent layer, although the morphology of the

original particles is still visible on the oxide glaze (figure 5.3.2-5). Moreover, some fractures propagate along the original deformation lines, as it is shown in figure 5.3.2-6. The development of fractures perpendicular to the sliding direction is the first step in the detachment mechanism. The schematic in figure 5.3.2-7 shows the different steps of nucleation and propagation of cracks until the final detachment of wear fragments.

These observations are in agreement with the literature on wear of EA [128] and also with the oxidational wear mechanism proposed in [59, 63, 284]. Furthermore, the layer of oxide, i.e. the existence of a layer of material which is different from the original materials involved in the wear process, is usually mentioned in the specialised literature as *the third body*. A further development of the third body concept in tribological systems has been presented in [286] and involves a state of equilibrium between competing mechanisms of detachment of particles from the surfaces and ejection of particles from the contact region. In this way, the protective oxide layer is thought to grow up to a critical thickness at which it becomes unstable and brakes.

Figure 5.3.2-8 illustrates the effect of the oxide layer thickness. Even though previous illustrations clearly showed oxide particles underwent deformation during sliding, the thick oxide glaze was found to fracture, in a way that resembled a brittle solid [274]. Consequently, the tough and thin oxide layer seems to grow throughout the sliding process until a relatively thick oxide glaze forms, which finally fails under the sliding asperities in a brittle manner. The role of the supporting layer must not be overseen, and the mechanical properties of the underlying EA are of fundamental importance to support the protective oxide layer, which would otherwise fail.

Therefore, the function of the layer of expanded austenite in the wear mechanism is, at least, twofold: it reduces the plastic deformation of the subsurface and confines it to the surface, and it provides a convenient support to the protective layer of oxides. Moreover, if a wear mechanism of abrasion or microabrasion is taken into consideration, a third function can be added to the protective role of the EA layer. In this case, the hardness ratio of the abrasive particles to the sliding surface is of importance [129]. The principal abrasive particles in the system are Fe_3O_4 or α-Fe_2O_3 oxides (400-750 HV) [72, 274]. Thus, the cause of improvement becomes apparent as the hardness of the sliding surface is increased from 200 HV to 800-900 HV, which is comparable or even higher than the abrasive particles.

With regard to friction, the interpretation of the friction force and friction coefficient is not unequivocal and, additionally, there is a large scatter in the friction data reported in the literature for EA [141, 287-290]. The results obtained in this project are in reasonable agreement with those reported in [128], i.e. the EA layer exhibits some higher coefficient of friction compared to the untreated AISI 316 substrate. This is consistent with the presence of a layer of rhombohedral α-Fe_2O_3 oxide, which is hard and abrasive when compared to the more ductile cubic oxides, Fe_3O_4 and FeO [72, 291]. In addition, the coefficient of friction increases with sliding distance until it reaches its steady state value, which could be interpreted as an increase of the contact area upon the growth of the oxide layer [292]. Once the steady condition is reached, the noise in the friction signal is a result of deformation processes, debris detachment and debris ejection events [56].

4. Corrosion behaviour

4.1. Corrosion behaviour of AISI 316 untreated substrate in different acid solutions

The resistance of AISI 316 to sulphuric acid solutions is limited, and it mainly depends on the temperature and concentration of acid in solution [30, 31, 37, 293]. In the particular case of the 16%

sulphuric acid solution at room temperature, the corrosion rate of this alloy is nil or very low, and the attack is only concentrated on weak points in the microstructure, especially MnS stringers (figure 4.5-1) [38]. However, on increasing the temperature of the solution up to its boiling point, the rapid evolution of hydrogen makes AISI 316 active and severe corrosion occurs (figures 4.5-3 and 4.5-8) [2].

Addition of oxidising agents, such as Fe^{3+} and Cu^{2+} cations, substitute hydrogen in the cathodic reactions, and consequently stabilise the passive film. This extends the range of corrosion resistance of ASS to higher temperatures or higher acid concentrations [31]. From the electrochemical point of view, the potential of stainless steel in these sulphuric acid solutions, with respect to a saturated calomel electrode, has been reported to change accordingly (figure 5.4.1-1) [2, 37].

With regard to nitric acid, AISI 316 is generally passive under a wide range of conditions [37]. However, highly oxidising solutions can produce transpassive corrosion, which is particularly intense at grain boundaries (figure. 4.5-14) [294]. This type of attack develops sensitised grain boundaries, although it also affects unsensitised boundaries to a lesser extent [2, 295].

4.2. Corrosion behaviour of carbon expanded austenite: outmost layer

The PC samples exposed to sulphuric acid 16% solution at room temperature exhibited very little corrosion, and only the outmost layer of material was found to fail (figure 4.5-1). This early stage of corrosion was confirmed during the tests conducted at boiling temperature, in which some material was found to peal off the surface of the samples after only a few minutes of exposure. SEM and TEM studies showed that the recovered fragments were of a similar nature to the outmost layer of material previously studied (figure 5.4.2-1). The XPS analysis of this outmost layer yielded C, Cr, O and Fe peaks (figure

5.4.2-2), in agreement with the literature [36, 296]. Unfortunately, extensive use of XPS was not possible during this project.

Further experiments conducted with polished samples, in sulphuric acid solution at room temperature, showed good corrosion resistance in all cases. This clearly indicates that the corrosion resistance is not a result of the deposition layer of carbides, nor of a thicker oxide layer formed upon plasma treatment (figure 4.2-7). In a similar way as it was reported in [297], the primitive oxide layer was removed after only a few minutes of exposure to the boiling solution of sulphuric acid. Thus, the carbon expanded austenite was found to be corrosion resistant itself, and the passive film must have been formed, in-situ, during the test.

The corrosion resistance of carbon, nitrogen and carbon-nitrogen expanded austenite has been reported at length [96, 125, 132-134, 298-304]. Most of the evidence is in the form of polarisation curves obtained in NaCl solutions and, in general, authors report:

- A shift of the corrosion potential in the noble direction
- Extended range for passivity
- Complete suppression of pitting, even at very high anodic potentials
- In some cases or under some conditions, considerably lower current densities

This description is in agreement with the results obtained in this project for corrosion in boiling sulphuric acid solutions, namely: reduced evolution of hydrogen, extended range of passivity and lower corrosion rates. However, the underlying passivation mechanism is still an open question.

An electrochemical study of surface modified ASS with nitrogen and carbon reported benefits in terms of corrosion resistance, but the experimental details are sparse [305]. The reported mechanism of dissolution of nitrogen and alkalisation can not explain the good response of the carburising layers [306] cited in [307]. More recent studies have proposed different mechanisms of passivation, including salt passive films [308, 309], hydrated oxides [307], modification of the semiconductor characteristics of the passive film [303] or even the same corrosion mechanism as in the untreated substrate [304]. Unfortunately this remains unclear.

4.3. Defects in the expanded austenite layer [310]

In reducing solutions, under cathodic potentials (figure 5.4.1-1), the improvement in corrosion resistance is significant. The evolution of hydrogen is not so readily observed after immersion, and the expanded austenite clearly shows a wider window of passivity, when compared to the untreated AISI 316 substrate (figure 4.5-8 and 4.5-9). The improvement is limited by the susceptibility of EA layers to localised corrosion on weak points of their structure (figures 4.5-4 to 4.5-6). These are clearly developed in more oxidising environments, such as sulphuric acid solutions with Fe^{3+} and Cu^{2+} additions, and also in nitric acid solutions (figures 4.5-11 and 4.5-14). The latter solutions shift the potential of ASS in the anodic direction and render it passive, so that very mild or negligible general corrosion of the grain surface occurs, whilst the dissolution of susceptible areas is accelerated, thus increasing contrast [295].

Elongated MnS stringers reaching the surface are known to diminish the corrosion resistance of surface alloyed ASS [142], and the attack progresses very rapidly after immersion in the boiling sulphuric acid solution (figure 4.5-4). The presence of slip bands evidences plastic deformation taking place during the treatment as a result of very high compressive stresses developed by the expansion of the austenite [238]. These defects, together with some susceptible grain boundaries, are preferential sites for

precipitation of carbides (see next section) and they provide channels for the corrosive medium to reach the substrate, where subsurface pits are formed (figures 4.5-5 and 4.5-6) [311].

Consequently, it can be said that corrosion of PC specimens is controlled by the density of defects in the expanded austenite layer. Figure 5.4.3-1 shows a schematic of the failure modes observed on treated samples. The most intense attack takes place on MnS inclusions, but localised corrosion also occurs on slip bands and grain boundaries. Corrosion progresses at a continuous rate, depending on the type of defect, until the substrate material is exposed. At this stage, a rapid anodic dissolution of the substrate takes place and subsurface pits of significant size are formed. In areas where the density of defects is high, the subsurface pits coalesce and the expanded austenite layer flakes off. In applications involving corrosion-wear, the formation of cavities in the subsurface layer would significantly affect the performance of the components [312, 313].

The density of slip bands and of susceptible grain boundaries is higher at the edges than in the central area of the specimens (figure 5.4.3-2). Furthermore, the density of these defects increases with the applied power (i.e. ASPC 030, ASPC 125 and DCPC 400 in increasing order). This is attributable to the strong plasma-surface interactions developed on sharp edges, and the associated local increase in current density and temperature. The bias levels, thus the power and current densities, selected for each ASPC treatment account for the observed differences in corrosion performance. In this way, low bias levels produce uniform surface morphologies on the treated samples and, consequently, a more even and predictable corrosion behaviour is observed. On the other hand, high bias levels and, ultimately, DCPC produce edge effects, and the consequent uneven or localised corrosion.

4.4. Effect of deformation and precipitation of carbides

The slip bands observed on the PC samples are non-equivocal evidence of plastic deformation taking place during the treatment, presumably due to the high residual stresses developed upon the expansion of the austenite unit cell. The dislocation walls so formed can become subgrain boundaries (figure 5.2-7) [245]. Moreover, due to the constraints imposed by the neighbouring grains, plastic deformation usually implies some degree of rotation of the crystallographic planes, as it has been reported in deformation studies conducted in ASS [242], and also for EA [247-249]. This rotation has a significant effect on the type of grain boundaries and can, eventually, lead to the development of a deformation texture [245, 246]. Finally, precipitation of carbides is also affected by deformation structures and grain boundary characteristics [20, 24, 314]. All these features —namely crystallographic texture, grain boundary characteristics and precipitation of carbides— have a marked effect on the corrosion properties of ASS and will be discussed below.

The effect of crystallographic texture on the corrosion resistance of ASS was reported in [44], where closely packed crystallographic planes were found to favour the formation of the passive film, and reduce the amount of sites for localised corrosion, with the consequent increase in corrosion resistance. In this project, even though deformation took place, no significant deformation texture seems to have developed (figure 5.4.4-1). The changes in the inverse pole figures obtained on untreated AISI 316 and on PC showed no consistent trend, so that texture can not be considered to contribute significantly to the corrosion resistance of EA. Furthermore, the quantity of favourable sites for localised corrosion is greatly increased in EA layers.

With regard to the grain boundaries, several studies have recently reported improvements in corrosion resistance of ASS through an increase in the number fraction of special grain boundaries and a

reduction in the connectivity of random grain boundaries [45, 46, 315]. However, the trend observed in this project is towards a degradation of CSL orientation grain boundaries (figure 5.4.4-2), which are converted into stepped boundaries as reported in [245]. This supports the results reported in [316], where an increase in corrosion resistance was obtained by increasing the frequency of random grain boundaries. The postulated mechanism is related to the flux of chromium and the precipitation of carbides of small size only, which will be discussed in what follows.

Precipitation of chromium carbides is of significant importance to the corrosion resistance of ASS since it produces a depletion of chromium in the surrounding areas, and the consequent weakening of the passive film. This process is mainly dependent on the diffusion of chromium and, consequently, on temperature [314], thus sharp corners are more susceptible to exhibit precipitates due to the edge effect developed on them (figure 5.4.4-3). However, the deformation structures have been found to play an important role in carbide precipitation and the high energy grain boundary ledges produced on intersection of grain boundaries with slip bands, or even the intersection of two slip bands seem to offer favourable sites for precipitates [19, 314, 317, 318]. Moreover, recent studies have reported early stages of precipitation at temperatures as low as 250ºC [319]. With regard to carbon expanded austenite, precipitation of small needles of M_5C_2 carbides have been reported to be favoured at crystallographic defects, where diffusion of substitutional elements (mainly Cr and Ni) requires minimum energy [121, 123].

In this project, evidence of carbides has been obtained by means of XRD, TEM (figure 4.2-8) and EDX (figure 4.5-13). Furthermore, the selective attack observed in corrosion experiments is consistent with the type of sensitisation reported in [320] associated with precipitation at deformation structures. Given the high carbon content of the EA, the presence of favourable sites renders precipitation of carbides

highly probable [20, 24]. However, the low temperature at which the treatment is conducted only allows short range diffusion of substitutional elements, so that the chromium depletion is of a local nature, thus severe intergranular corrosion is avoided.

5. Plasma diagnostics: Optical Emission Spectroscopy (OES)

5.1. Plasma chemistry

The spectra in figures 4.6-1 to 4.6-3 show the typical optical emission peaks obtained for gas mixtures corresponding to nitriding, carburising and nitrogen enhanced carburising. Although the existence of N and C containing species is essential for these surface treatments, the presence of other species — either as pollutants, as by-products of a primary reaction, or as intentional additions to the gas mixture— can have a non-trivial effect in the physicochemistry of plasma. Some of these reactions are considered of importance for the interpretation of the OES results obtained in this project and will be discussed in the following paragraphs.

Plasma nitriding in N_2-H_2 and in N_2-H_2-Ar gas mixtures have been extensively studied and a large amount of evidence has been gathered [165, 321-327]. The effect of Ar and H in depassivation and surface activation is usually highlighted. In the case of Ar, this is achieved through increased sputtering power of the gas mixture, whereas H increases the chemical etching of O species. Moreover, the dissociation of N_2 is increased with small additions of H_2 (less than 1%), which was attributed to the strong interaction (population and depopulation) between vibrational levels of both molecular gases [328-331]. The electric parameters of the discharge also vary with increasing H_2 content of the gas mixture, and a minimum in discharge impedance is found around 75% N_2 − 25% H_2.

In the case of carburising, there is significantly less information available [332], although the CH_4-H_2 and CH_4-H_2-Ar plasmas have been extensively studied for deposition of diamond-like carbon [333-338]. In these studies, atomic H has been clearly identified as a by-product of the decomposition of the CH_4 molecule. In addition, a role of significance has been assigned to atomic H in the dissociation of CH_4 [336, 337]. Depending on the gas pressure and gas temperature, dehydrogenation of methane by H atoms competes or even dominates over electron impact dissociation.

The hydrogen abstraction efficiencies of CO and OH have been reported to be even higher than atomic H [338, 339]. Bearing in mind these same principles, and due to technical limitations to do experiments with other gases (CO, CO_2 or O_2), small additions of N_2 were used. Contrary to what could be expected from the dissociation enthalpies listed in table 5.5-1 [340], a strong interaction between N and C is evident from the relatively high activity of CN groups in figure 4.6-2. The interaction between C and N to form CN species has also been reported in [341], and this mechanism would involve a chemical driving force, similar to the one reported in [339] for dissociation of CH_4 with small additions of CO. This result highlights the importance of chemical interaction between the species present in the plasma phase.

5.2. Emission intensity maps

The emission intensity maps obtained by means of the optical fibre probe yielded good information on the plasma under different treatment conditions (figure 4.6-5). The selection of the emission bands used for the purpose of the emission intensity maps was very much influenced by the signal-to-noise ratio. However, there are good reasons to correlate these bands with the N and C activity in the plasma. In the case of nitriding, transition N_2^+ ($B^2\Sigma_u^+ - X^2\Sigma_g^+$) is usually the most intense, with a band head at 391.44 nm [342, 343]. Moreover, this so called *first negative system* of N_2 has been related to

vibrational metastable states [344], which are believed to play a significant role in the stepwise dissociation of molecular nitrogen, in view of the high energy required for direct dissociation [345, 346].

The emission intensity is known to increase with the electron density (n_e) and the electron temperature (T_e) and, as a consequence, the emission intensity increases with the power (figure 4.6-6) [347]. The electron temperature is particularly important, assuming that ionisation takes place mainly through single collisions with energetic electrons. However, for a molecular gas, and in particular for N_2, step ionisation from excited levels must also be considered [348-351]. An example of stepwise excitation proceeds as follows:

$$e^- + N_2(X) \rightarrow e^- + e^- + N_2^+(X) \qquad (5.5\text{-}1)$$

$$e^- + N_2^+(X) \rightarrow e^- + N_2^+(B) \qquad (5.5\text{-}2)$$

where *X* indicates the ground state and *B* the excited state, and this or similar mechanisms would be of importance at high electron densities and low electron temperatures. This is believed to be the case at the high pressure range assessed in this project (P > 250 Pa), where the electron temperature has been reported to drop due to the increasing number of collisions, and the electron energy distribution function shows a significantly smaller high energy tail [222, 352-356].

Figure 5.5.2-1 illustrates the relative increase in the emission intensity of the nitrogen first negative system, with respect to the hydrogen Balmer series, at increasing gas pressure in ASPN conditions. Considering the energy required for direct electron impact excitation of H_α and N_2^+ are 12.74 eV [346] and 18.5 eV [357] respectively, it seems plausible that, in the high pressure range, the N_2^+ is being populated through stepwise ionisation, which lowers the energy threshold to 10.5 eV [357]. Moreover, these changes in the electron energy distribution function (EEDF) and the ionisation processes with gas

pressure could also account for the different trends observed in the emission intensity with respect to discharge electric parameters (figure 4.6-6).

In the case of ASPC, the absence of intense peaks corresponding to C containing species limits the analysis to the hydrogen Balmer series. As it was mentioned in section 5.1 of this chapter, atomic hydrogen is not only a by-product of the decomposition of the methane molecule, but it also plays an active role in the dehydrogenation of CH_X groups. Therefore, its study could be considered to represent, to some extent, the C activity in the plasma. Nevertheless, the study of CH_X emission peaks in the vacuum UV region of the spectrum, or in absorption, would be of interest [358].

The intensity maps obtained under carburising atmospheres (figure 4.6-5) exhibit one interesting feature: in the low pressure region, the emission intensity was found to increase with the applied bias up to a maximum value, near the current saturation region, followed by a marginal decrease on further increasing the bias. This was contrary to the expectations, as higher applied power was supposed to yield higher emission intensity. The trend was initially considered an experimental error, but the same phenomenon was observed on repetition of the experiment in CH_4-H_2 gas mixtures, although it was not so evident or not observable at all, in N_2-H_2. A possible explanation for this phenomenon became apparent from the results of the ion flux probe, discussed in the next section.

6. Plasma diagnostics: Ion flux probe (IFP)

The flux of ions measured in the AS industrial furnace under both nitriding and carburising atmospheres shows the same trend, i.e. the ion flow increases with the bias level, and decreases with gas pressure (figures 4.7-5 and 4.7-6). The effect of bias seems self-evident, as an increase in the negative potential applied to the worktable increases the electric field, thus the ion drift. In the case of pressure, two

different effects merge together: the reduction in the ion mobility on increasing pressure, and the changes in the EEDF which affect the production of ions, as discussed in the previous section [220].

The trend followed by the floating potential of the probe (i.e. the potential at which equal number of electrons and ions arrive at the probe, thus yielding zero net current) is noteworthy. The floating potential initially dropped to more negative values when bias was applied, followed by a reverse in the trend on further increasing the bias, and this behaviour was clearer in CH_4-H_2 than in N_2-H_2 gas mixtures (figure 4.7-4). Although the phenomenon was initially considered an artefact, its resemblance to the OES observations raised doubts.

On further analysing the OES and IFP signals and the electric parameters of the AS furnaces during the experiments, it was found that the reduction in emission intensity and the shifting of the floating potential to more positive values, correlated with considerable reductions in the power applied to the mesh of the AS furnace. This reduction was imposed by the automatic control system of the furnace in order to keep the temperature stable, to compensate for the increasing power applied on the worktable. In view of these observations, the cathodic mesh in the AS furnace could be considered an additional source of electrons, similar to the triode discharges reported in [359-361].

With regard to the measurements conducted with the electric probe in DC and AS experimental arrangements inside a conventional DC furnace, similar trends were observed: the AS arrangement produced larger ion fluxes, and changed the floating potential (figure 4.7-2). However, the latter varied depending on the gas mixture. For the carburising atmosphere, the floating potential dropped to more negative values, whereas under nitriding atmospheres the potential shifted in the positive direction.

Considering that the same gas mixture, the same gas pressure, and the same electric discharge parameters were applied in both the DC and the AS experiments, the electron temperature is thought to remain constant. Therefore, the differences may be attributed to an increase in the electron density, which is, once again, consistent with the results reported for triode discharges [359-361]. In the particular case of nitrogen containing atmospheres, higher electron densities would render step ionisation processes more profuse, thus increasing the density of ions and shifting the floating potential to more positive values (i.e. less negative floating potentials are required to balance the flow of electrons and ions).

However, there is an additional factor that should be considered in the case of an AS furnace, namely the geometry of the cathodic mesh. The mesh in an AS arrangement is negatively biased and it surrounds the workload, so that there is an electric field which tends to confine electrons within the operative volume of the furnace. This concept is by no means new, and there is a large body of literature on the electrostatic confinement of plasma in a variety of ways, and using different electrode arrangements [221, 223, 362-367].

A considerable increase in the plasma density is reported by confining charged particles, as the path of electrons from the cathode to the anode is extended due to reflections on the cathodic surfaces [223, 362]. The confinement effect is restricted to the low energy electrons (*slow* or *cold* electrons), whilst the high energy electrons (*fast* or *hot* electrons) would escape the trapping electric field [366]. The dimension and the geometry of the chamber are of significant importance in this regard. Furthermore, the confinement is consistently reported to be more effective in the low pressure range [221, 363, 365], in which the negative glow extends to fill the whole volume within the confining field.

The creation of a uniform negative glow throughout the operating volume of the furnace is of interest because it is in this region of the gas discharge where the active species are produced. Therefore, the high electron density developed inside the mesh of an active screen furnace facilitates the creation of active species. Furthermore, the electron density has already been proposed as a parameter to predict and control the carbon potential of the plasma [171]. Consequently, the parameters of the electric discharge affect the chemistry of the gas (increase activity through ionisation), and this, at the same time, affects the parameters of the electric discharge (changes in EEDF observed in molecular gases). As a result, both parameters should be considered together [368].

It is thus proposed that the AS arrangement contributes to the creation of additional primary electrons and confinement of charged particles within the operative volume of the chamber, yielding plasma conditions more suitable for nitriding and carburising. The electric parameters applied on the workload can be thus controlled independently to produce the required degree of ion bombardment on the components [359-361, 369].

7. Mechanisms of active screen plasma surface engineering

It is convenient to begin the discussion on the mechanisms of active screen plasma surface engineering by talking about nitriding, as this has been more extensively studied than carburising. The evidence found in the former will be comparatively discussed with respect to the latter.

7.1. Active screen plasma nitriding (ASPN)

One of the most interesting findings of the experiments on the mechanisms of active screen plasma surface engineering is the layer of material deposited on the ASPN treated samples (figure 4.3-7). This deposition layer covered the AS plasma nitrided specimens with a morphology that depended on the

treatment conditions and the crystallographic orientation (figures 5.7.1-1 and 5.7.1-2) [370]. The glass slides were especially useful for XRD studies (figures 4.3-10), and the pattern shows a very clear coincidence with Fe_XN nitrides and a remarkable correlation with FeN (figure 4.3-11). This experimental finding is of significance considering that the deposition layer has been deemed in the literature as one of the fundamental mechanisms of active screen plasma nitriding [181-183].

The sputtering and redeposition mechanism was first proposed by Kölbel and has been supported and reviewed by several authors ever since [154, 159, 160, 371, 372]. The model attributes the nitriding mechanism to iron atoms which are sputtered from the specimen, and subsequently react with the nitrogen in the plasma. Unstable FeN nitrides would thus be redeposited on the specimen surface, and would decay into lower $Fe_{2-3}N$ and Fe_4N nitrides, releasing nitrogen atoms free to diffuse (figure 5.7.1-3). In the case of active screen plasma nitriding, the mesh was proposed to be the source of sputtered iron atoms [181-183], in view of the absence of ion bombardment or sputtering on specimens treated at floating potential [179].

Further evidence on the importance of the transferred material is apparent from the results obtained under an AS arrangement using a mesh with big holes. In the case of ASPN, the area of the sample covered by the mesh exhibited significant hardening effect, while the area under the hole showed little signs of nitriding (figure 4.3-6). The appearance of both areas of the sample is very similar, and only a minor change in the metallic shine is observed, the area covered by deposited material being dull grey, whereas the area under the hole retained its metallic shine. In terms of composition, the EDX analysis of the deposited material revealed alloying elements such as Cr and Ni in addition to Fe (figure 5.7.1-4), in agreement with the composition of the AISI 304 mesh (figure 4.3-12).

Sputtering of material from the mesh and its subsequent deposition on the treated specimens has been extensively discussed and reported in the literature on active screen plasma nitriding [180, 373-376]. To this end, and given the evidence produced during this project, sputtering and deposition is an irrefutable fact, although its relevance for the treatment is still an open question, and it has been seriously confronted [185, 377]. The results obtained in this project indicate that the treatment conditions for the thickest deposition layer of iron nitride differ from those ones for the thickest layer of nitrogen expanded austenite (figure 5.7.1-5). Indeed, the very concept of active screen plasma nitriding was not developed on the theory of sputtering and redeposition, but on the post-discharge nitriding, i.e. the generation of active species on the mesh and their transfer to the worktable through a carefully designed gas flow [177].

From the experience gathered in this project, the contribution made by the gas flow to the transfer of active species from the mesh towards the worktable is arguable. This is evident considering that experiments conducted inside DC furnaces have been widely successful without introducing any special modifications in the gas flow [180-183, 374, 378]. Furthermore, experimental arrangements with plate lids, which severely restrict gas flow, have produced similar or even better results than those with mesh lids [182, 378]. In addition, the distance active species can travel as such, is limited due to their considerably short lifetimes. This was observed in the experiments conducted without a lid in [182] and also in the experiments conducted in this project using a mesh with big holes, in which the hardening effect was limited to regions of the specimens lying in proximity to the active screen mesh (figure 4.3-6).

Consequently, the post-discharge mechanism seems to be limited to relatively small scales and, in fact, it has been found difficult to produce satisfactory hardening in large scale active screen units without applying some level of bias on the treated components [184, 185, 377, 379]. Nevertheless, the

relevance of the mesh as a source of active species deserves further attention. In this project, the efficiency of the plasma treatment showed a substantial degree of correlation with the optical emission intensity of active species. At the same time, the emission intensity was affected by the electric discharge conditions on the mesh. Consequently, the influence of the mesh on the treatment becomes apparent, and it is here proposed that the role played by the mesh in an AS furnace is threefold: it radiates heat, it is an additional source of electrons in a similar way to a triode discharge; and it confines electrons within the operative volume of the furnace.

These last two roles of the mesh in an AS furnace are not mutually exclusive, but synergetic. The beneficial effect of an additional source of electrons has been reported in experiments conducted in triode discharges [359-361] and was discussed in a previous section. However, it has also been noted that the plasma density is not uniform in these arrangements [380]. On the contrary, the geometrical arrangement of active screen furnaces produces an even distribution of electrons around the workload. Furthermore, under suitable conditions, the confining negative electric field generated by the mesh would also contribute to produce a higher electron density and more uniform distribution of electrons and, as a consequence, a more uniform plasma density [223, 362, 363].

The theory is consistent with the results obtained in this project, and those ones reported in the literature on active screen [185], triode discharges [359, 360] and electrostatic confinement of plasmas [223, 362, 363]. The additional electrons provided by the mesh allow operating the furnace at lower pressures, at which the electrostatic confinement is also more effective. The higher electron density implies an increased number of collisions with gas molecules, which will eventually lead to a larger number of active species and a higher plasma density. This can finally be translated into an increased plasma reactivity and nitriding power.

A final comment should be made on the need to apply bias in large scale active screen units [184, 185, 379]. This issue recalls the ancient discussion on the effect of ions versus the role of neutrals in plasma nitriding [381-383]. The equipment used in this project did not allow for a complete decoupling of the voltage and current discharge characteristics of the worktable, which are related with the ion energy and ion flux. Therefore, the results are not conclusive, although there is a clear increase in the hardening effect and the EA layer thickness with both increased voltage and current, i.e. with increased applied power.

Even though it was possible to nitride samples at floating potential, this condition did not produce the thickest layer of EA. Furthermore, the adhesion of the deposition layer was not satisfactory and the layer of iron nitrides was found to peel off in some regions (figure 5.7.1-6). It can be thus concluded that a small level of bias is not only desirable, but also necessary to optimise the treatment conditions. The deposition layer seems to be beneficial, but it is not the only mechanism operating in ASPN treatments. The evidence indicates that the active species in the plasma are of fundamental importance to control the nitriding potential. Therefore, the optimisation of the treatment would require uncoupling the plasma generation and heat source from the treated components [361, 380], and carefully selecting the discharge conditions applied on the worktable, in order to favour the plasma-surface interactions, which are of complex nature [323].

7.2. Active screen plasma carburising (ASPC)

The results obtained for AS plasma carburising indicate similar trends to AS plasma nitriding, although the operating mechanisms are clearly different (figure 4.3-10). The first significant distinction observed is the complete absence of a coherent and dense deposition layer. The glass slides treated in ASPC conditions only exhibited some fine powder on their surfaces which, according to the EDP obtained in

TEM studies, was identified as Fe_3C (figure 5.7.2-1). Further characterisation of this material was only possible from the deposition film grown on the walls of the furnace —i.e. on the anodic walls lying some 100 mm in front of the cathodic mesh— after several consecutive carburising treatments. The morphology is obviously coarser (figure 5.7.2-2), but it is clearly formed by conglomeration of smaller particles, and the XRD result indicates a very good correlation with the Fe_3C pattern.

A thin layer of carbides was found on ASPC treated AISI 316 samples (figure 4.2-8), and it has been reported in the literature [384]. However, the role of these carbides in the mechanism of plasma carburising treatments seems to be negligible. Therefore, plasma carburising seems to arise as a result of the step decomposition of the methane molecule according to the following reactions [163, 385]:

$$e^- + CH_4 \rightarrow CH_3^+ + H + 2e^- \qquad (5.7\text{-}1)$$

$$e^- + CH_3 \rightarrow CH_2^+ + H + 2e^- \qquad (5.7\text{-}2)$$

$$e^- + CH_2 \rightarrow CH^+ + H + 2e^- \qquad (5.7\text{-}3)$$

$$e^- + CH \rightarrow C^+ + H + 2e^- \qquad (5.7\text{-}4)$$

The ions would thus be adsorbed at the cathodic surface and would release C atoms free to diffuse into the bulk material. The fact that CH and C ions or excited species were not abundant in the OES spectra, collected during the ASPC treatments, leads to the assumption that CH_X species with $x > 1$ would be responsible for the hardening effect. This assumption implies that a significant amount of hydrogen is adsorbed with the carbon, which was suggested in [386] and confirmed in [387].

The quantity of reports on plasma carburising is sparse, although there is a high degree of agreement in the evidence. In general, the carburising is attributed to reactions under electric control, which

emphasises the importance of plasma activation and plasma reactivity [155, 332, 388]. A direct correlation between ions and excited species, and the carbon mass flow has been established; moreover, the electron density has been proposed as a convenient variable to control the carbon potential of the plasma [171]. All this evidence is in favour of the model proposed for AS plasma surface engineering, in which higher electron densities would increase the number of collisions and the plasma reactivity.

However, this explanation is not completely satisfactory in view of the difficulty to produce hardening on samples left at floating potential. This was initially thought to be a consequence of the presence of passivating oxide at the surface of AISI 316 specimens. Therefore, some experiments were conducted applying a surface activation stage at the beginning of the treatment, consisting of bombardment of the surface with argon ions, but the results were equally negative. Furthermore, the high hydrogen content of the gas mixture is supposed to chemically etch the oxides formed on stainless steel samples, and to increase the tolerance of the treatment to residual oxygen gas [388]. Nevertheless, the results were negative in all the attempts, thus it can be concluded that the application of bias is essential for ASPC. The equipment used in this project did not allow for an independent selection of potential and current, but the hardening effect was found to increase with both, i.e. with the applied power.

This need for ion bombardment to produce hardening in H_2-CH_4 gas mixtures does not weaken the potential benefits offered by the AS technique. The uncoupling of the plasma and heat sources from the treated components, provides an additional degree of freedom to optimise the treatment. Furthermore, the possibility to increase the electron density, the plasma density and the plasma uniformity within the operative volume of the furnace, is clearly an interesting feature of AS. Finally, the transfer of material

from the mesh onto the worktable was negligible in the case of ASPC, compared to ASPN. This discards the sputtering and redeposition as a main mechanism for ASPC.

CHAPTER 6: SUMMARY AND CONCLUSIONS

The evidence produced throughout this project and the discussion presented in the last chapter can be summarised as follows:

I. Active screen plasma processing:

1. It is possible to generate carbon expanded austenite in austenitic stainless steel using active screen plasma technique.
2. Based on systematic experimental work, effective AS processing windows have been identified to produce carbon and nitrogen expanded austenite equivalent to conventional DC treatments.
3. Optimal treatment conditions for maximum layer thickness and no incidence of edge effect were identified at 125 Pa and 15% bias for ASPC, and 75 Pa and 10% bias for ASPN.
4. The surface quality of active screen treated samples could be significantly improved compared to the DC counterparts. Defects such as edge effects, hollow cathodes and arcing were minimised or eliminated.

II. Characterisation of carbon expanded austenite produced on AISI 316:

5. The layer of carbon expanded austenite produced in the active screen furnace was equivalent to the one obtained in DC furnaces in terms of layer thickness, composition, phase constitution and hardness. Improved surface quality was consistently obtained under the right AS treatment conditions.
6. The microstructure of the treated material was severely deformed and distorted. Degradation of the CSL boundaries took place, with a trend towards a randomisation of the grain boundaries.

7. The residual stresses developed in the plasma carburised layers were measured and the maximum compressive residual stresses were calculated to be in the order of -1.6 GPa. Residual stresses were found to increase with the ion bombardment and the layer thickness.

III. Tribological properties of carbon expanded austenite:

8. Under the conditions assessed in this project, plasma carburised AISI 316 exhibited a resistance to wear two orders of magnitude higher than the untreated material.
9. The dominant wear mechanisms were found to be changed from severe adhesive and delamination wear for the untreated AISI 316, to mild oxidational wear for the plasma carburised material.
10. The carbon expanded austenite can avoid subsurface plastic deformation, increase resistance to abrasion by hard particles or asperities, and provide support to the protective oxide layer.
11. The coefficient of friction exhibited by carbon expanded austenite was higher than the untreated AISI 316 under the sliding conditions used in this project.

IV. Corrosion behaviour of carbon expanded austenite:

12. Plasma carburised AISI 316 showed higher corrosion resistance than the untreated AISI 316 in boiling 16% sulphuric acid solutions. Furthermore, active screen plasma carburising produced greater improvement than DC treatments through the elimination of edge effects.
13. The outer layer of carbides played no protective role against corrosion, but it failed shortly after being immersed in acid solutions. The improved corrosion resistance was attributed to the carbon expanded austenite itself.

14. The failure of the carbon expanded austenite in a corrosive environment was defect controlled. The weak points of the microstructures include: MnS inclusions, deformation slip bands and grain boundaries. Sharp edges were particularly susceptible areas to develop the latter two defects.

V. Plasma diagnostic techniques:

15. Optical emission spectroscopy, in the UV-visible range, was a valuable technique to identify active species in N_2-H_2 gas mixtures, although it was severely limited in the case of diluted CH_4-H_2 atmospheres.
16. The emission intensity of nitrogen ionic species and hydrogen atomic species showed a considerable correlation with the treatment effectiveness. Therefore, the intensity maps obtained with the optical fibre probe were useful to identify the optimum range of treatment conditions.
17. The interpretation of the ion flux probe signal indicates that the plasma inside an active screen furnace was considerably affected by the electric parameters applied on the cathodic mesh. The flow of ions increased with increasing bias and decreased with increasing gas pressure.

VI. Mechanisms of active screen plasma surface engineering:

18. Sputtering and redeposition was found to be a mechanism of significance for active screen plasma nitriding, although the active plasma species and some moderated ion bombardment were necessary for treatment optimisation.
19. Ion bombardment was a necessary condition for active screen plasma carburising. The activation provided by the plasma was of importance for the decomposition of methane, whereas sputtering and redeposition played no role in this case.
20. The role of the cathodic mesh in an active screen furnace seems threefold: it radiates heat, it is an additional source of electrons in a similar way to a triode discharge; and it confines low energy

electrons within the operative volume of the furnace in a manner that resembles an electrostatic confinement of the plasma.

CHAPTER 7: PROPOSALS FOR FUTURE WORK

The present project contributed to the understanding of active screen plasma processing, the characterisation of carbon expanded austenite, its tribological properties and corrosion behaviour. Evidence was produced on the mechanisms involved in the active screen plasma treatments, and the diagnostic techniques allowed some basic characterisation of the plasma. From the results obtained in this project, the following topics are suggested for future studies:

- The metallic mesh of AS furnaces may be replaced by other electrode arrangements, which could be equally or even more effective in producing additional electrons and plasma confinement, and show further flexibility and simplicity, e.g. segmented hollow cathodes.

- Plasma diagnostic with optical fibre assisted OES and electric probes provide useful and complementary information about the plasma. Further improvements of these techniques would be valuable, for example to produce spatial distribution maps of active species, electron density and electron temperature inside the AS furnace.

LIST OF REFERENCES

1. Ashby, M. F.: *Materials selection in mechanical design*, 2nd Ed. (1999) Oxford, Butterworth Heinemann

2. Streicher, M. A.: *Stainless steels: past, present and future* in 'The metallurgical evolution of stainless steel' 1st Ed. (1979) London, The Metals Society, 442-475

3. Keown, S. R.: *The history of alloy steels with special reference to Sheffield contributions*, Perspectives in Metallurgical Development (1984) Sheffield, The Metals Society, 36-46

4. Bhadeshia, H. and Honeycombe, R.: *Steels: microstructures and properties*, 3rd Ed. (2006) London, Butterworth-Heinemann

5. Pickering, F. B.: *Introduction: The metallurgical evolution of stainless steel* in 'The metallurgical evolution of stainless steel' 1st Ed. (1979) London, The Metals Society, 1-42

6. Pickering, F. B.: *Physical metallurgical development of stainless steel*, Stainless Steel '84 (1984) Göteborg, London Institute of Metals, 2-28

7. Oshima, T., Habara, Y. and Kuroda, K.: *Efforts to save nickel in austenitic stainless steels*, ISIJ International (2007) 47, *3,* 359-364

8. British Standard DPC 08/30166437 DC, 2008, "Stainless steels: chemical composition", BSI, London, www.bsi-global.com

9. Voronenko, B. I.: *Austenitic-ferritic stainless steel: a state-of-the-art review*, Metal Science and Heat Treatment (1997) 39, *9-10,* 428-437

10. *New 200-series steels: An opportunity or a threat to the image of stainless steel?*, International Stainless Steel Forum (2005) *November,* 1-14

11. Shanina, B. D., Gavriljuk, V. G., Berns, H. and Schmalt, F.: *Concept of a new high-strength austenitic stainless steel*, Steel Research (2002) 73, *3,* 105-113

12. Leslie, W. C. and Hornbogen, E.: *Physical metallurgy of steels* in 'Physical metallurgy' 4th Ed. (1996) Oxford, Elsevier North Holland, 1556-1620

13. Handbook Committee, A. S. M.: *Metals Handbook Vol 8: Metallography, structures and phase diagrams*, 8th Ed. (1973) Novelty, Ohio, ASM American Society for Metals

14. Marshall, P.: *Austenitic stainless steel: microstructure and mechanical properties*, 1st Ed. (1984) London, Elsevier Applied Science Publishers

15. Villanueva, D. M. E., Junior, F. C. P., Plaut, R. L. and Padilha, A. F.: *Comparative study on sigma phase precipitation of three types of stainless steels: austenitic, superferritic and duplex*, Materials Science and Technology (2006) 22, *9,* 1098-1104

16. Angel, T.: *Formation of martensite in austenitic stainless steels* in 'The metallurgical evolution of stainless steel' 1st Ed. (1953) London, The Metals Society, 402-412

17. Kirk, D. and Payne, N. J.: *Transformations induced in austenitic stainless steels by shot peening*, The 7th International conference on shot peening (1999) Warsaw, Poland, Institute of Precision Mechanics, 15-22

18. Fang, X. F. and Dahl, W.: *Strain hardening and transformation mechanism of deformation-induced martensite transformation in metastable austenitic stainless steels*, Materials Science and Engineering A: Structural Materials: Properties, Microstructure and Processing (1991) A141, 189-198

19. Hong, H. U., Rho, B. S. and Nam, S. W.: *Correlation of the M23C6 precipitation morphology with grain boundary characteristics in austenitic stainless steel*, Materials Science and Engineering A: Structural Materials: Properties, Microstructure and Processing (2001) A318, 285-292

20. Trillo, E. A. and Murr, L. E.: *A TEM investigation of M23C6 carbide precipitation behaviour on varying grain boundary misorientations in 304 stainless steels*, Journal of Materials Science (1998) 33, *5,* 1263-1271

21. Bruemmer, S. M. and Charlot, L. A.: *Development of grain boundary chromium depletion in type 304 and 316 stainless steel*, Scripta Metallurgica (1986) 20, 1019-1024

22. Jack, D. H. and Jack, K. H.: *Carbides and nitrides in steel*, Materials Science and Engineering (1973) 11, 1-27

23. Sourmail, T.: *Precipitation in creep resistant austenitic stainless steels*, Materials Science and Technology (2001) 17, *1,* 1-14

24. Trillo, E. A. and Murr, L. E.: *Effects of carbon content, deformation and interfacial energetics on carbide precipitation and corrosion sensitization in 304 stainless steel*, Acta Materialia (1999) 47, *1,* 235-245

25. Williams, T. M.: *Precipitation in neutron-irradiated type 316*, Stainless Steel '84 (1984) Göteborg, London Institute of Metals, 403-412

26. Padilha, A. F., Escriba, D. M., Materna-Morris, E., Rieth, M. and Klimenkov, M.: *Precipitation in AISI 316L(N) during creep tests at 550 and 600 C up to 10 years*, Journal of Nuclear Materials (2007) 362, 132-138

27. Farrar, R. A.: *Influence of microsegregation on phase transformations and properties of type 316 weld metals at elevated temperatures*, Stainless Steel '84 (1984) Göteborg, London Institute of Metals, 336-342

28. Sourmail, T. and Bhadeshia, H.: *Modelling simultaneous precipitation reactions in austenitic stainless steels*, Computer Coupling of Phase Diagrams and Thermochemistry (2003) 27, *2,* 169-175

29. Slattery, G. F. and O'riordan, P.: *Microstructural transformations in stress relieved type 316 stainless steel weld metal*, Metallography (1980) 13, 59-70

30. Handbook Committee, A. S. M.: *The selection of stainless steel for atmospheric and marine corrosion service* in 'Metals Handbook Vol 1: Properties and selection of metals' 8th Ed. (1961) Novelty, Ohio, American Society for Metals, 552-576

31. Davis, J. R.: *Atmospheric and aqueous corrosion* in 'ASM Speciality Handbook: Stainless steels' 1st Ed. (1996) Materials Park, Ohio, ASM International, 133-153

32. Evans, U. R.: *The passivity of metals: Part I - The isolation of the protective film*, Journal of Chemical Society (1927) *May,* 1020-1040

33. Vernon, W. H. J., Wormwell, F. and Nurse, T. J.: *The surface film on chromium-nickel 18-8 stainless steel*, Metallurgia (1944) 31, *181,* 19-22

34. Dye, T. G., Fursey, A., Lloyd, G. O. and Robson, M.: *Stripping thin oxide films from metals*, Journal of Physics E: Scientific Instruments (1968) 1, *2,* 463-464

35. Sudesh, T. L., Wijesinghe, L. and Blackwood, D. J.: *Characterisation of passive films on 300 series stainless steels*, Applied Surface Science (2006) 253, 1006-1009

36. Montemor, M. F., Simoes, A. M. P., Ferreira, M. G. S. and Da Cuhna Belo, M.: *The role of Mo in the chemical composition and semiconductive behaviour of oxide films formed on stainless steels*, Corrosion Science (1999) 41, 17-34

37. Sedriks, A. J.: *Corrosion of stainless steels*, 1st Ed. (1979) New York, John Wiley and sons

38. Sedriks, A. J.: *Metallurgical aspects of passivation of stainless steels*, Stainless Steel '84 (1984) Göteborg, London Institute of Metals, 125-133

39. Brandis, H. and Kiesheyer, H.: *Influence of chromium and molybdenum on chloride corrosion of stainless steels*, Stainless Steel '84 (1984) Göteborg, London Institute of Metals, 217-221

40. Dayal, R. K., Parvathavarthini, N. and Raj, B.: *Influence of metallurgical variables on sensitisation kinetics in austenitic stainless steels*, International Materials Review (2005) 50, *3,* 129-155

41. Matula, M., Hyspecka, L., Svoboda, M., Vodarek, V., Dagbert, C., Galland, J., Stonawska, Z. and Tuma, L.: *Intergranular corrosion of AISI316L steel*, Materials Characterization (2001) 46, *2-3,* 203-210

42. Barbi, N. C. and Judd, G.: *Microstructure and microsegregation effects in the intergranular corrosion of austenitic stainless steel*, Metallurgical Transactions A: Physical Metallurgy and Materials Science (1972) 3, *11,* 2959-2964

43. Brandon, D. G., Ralph, B., Ranganathan, S. and Wald, M. S.: *A field ion microscope study of atomic configuration at grain boundaries*, Acta Metallurgica (1964) 12, *7,* 813-821

44. Ravi Kumar, B., Singh, R., Mahato, B., De, P. K., Bandyopadhyay, N. R. and Bhattacharya, D. K.: *Effect of texture corrosion behaviour of AISI 304L stainless steel*, Materials Characterization (2005) 54, *2,* 141-147

45. Tsurekawa, S., Nakamichi, S. and Watanabe, T.: *Correlation of grain boundary connectivity with grain boundary character distribution in austenitic stainless steel*, Acta Materialia (2006) 54, *13,* 3617-3626

46. Michiuchi, M., Kokawa, H., Wang, Z. J., Sato, Y. S. and Sakai, K.: *Twin-induced grain boundary engineering for 316 austenitic stainless steel*, Acta Materialia (2006) 54, *19,* 5179-5184

47. Randle, V.: *Twinning-related grain boundary engineering*, Acta Materialia (2004) 52, *14,* 4067-4081

48. Rohrer, G. S., El Dasher, B. S., Miller, H. M., Rollett, A. D. and Saylor, D. M.: *Distribution of grain boundary planes at coincident site lattice misorientations*, Interfacial Engineering for Optimized Properties III (2004) San Francisco, CA, USA, Materials Research Society, 265-275

49. Brandon, D. G.: *The structure of high angle grain boundaries*, Acta Metallurgica (1966) 14, *11,* 1479-1484

50. Reed, B. W., Minich, R. W., Rudd, R. E. and Kumar, M.: *The structure of the cubic coincident site lattice rotation group*, Acta Crystallographica A: Foundations of Crystallography (2004) A60, 263-277

51. Chivers, T. C.: *Nuclear tribology: a personal perspective*, Tribology International (1986) 19, *5,* 225-233

52. Smith, A. F.: *The friction and sliding wear of unlubricated 316 stainless steel at room temperature in air*, Wear (1984) 96, *3,* 301-318

53. Lim, S. C. and Ashby, M. F.: *Wear mechanism maps*, Acta Metallurgica (1987) 35, *1,* 1-24

54. Ashby, M. F. and Lim, S. C.: *Wear mechanism maps*, Scripta Metallurgica et Materialia (1990) 24, 805-810

55. Lim, S. C., Ashby, M. F. and Brunton, J. H.: *Wear rate transitions and their relationship to wear mechanisms*, Acta Metallurgica (1987) 35, *6,* 1343-1348

56. Hsu, K.-L., Ahn, T. M. and Rigney, D. A.: *Friction, wear and microstructure of unlubricated austenitic stainless steels*, Wear (1980) 60, *1,* 13-27

57. Dumbleton, J. H. and Douthett, J. A.: *The unlubricated adhesive wear resistance of metastable austenitic stainless steel containing silicon*, Wear (1977) 42, *2,* 305-332

58. Allen, C. B., Quinn, T. F. J. and Sullivan, J. L.: *The oxidational wear of high chromium ferritic steel on austenitic stainless steel*, Transactions of the ASME Journal of Tribology (1985) 107, *2,* 172-179

59. Smith, A. F.: *The influence of surface oxidation and sliding speed on the unlubricated wear of 316 stainless steel at low load*, Wear (1985) 105, *2,* 91-107

60. Smith, A. F.: *The friction and sliding wear of unlubricated 316 stainless steel in air at room temperature in the load range 0.5 - 90N*, Wear (1986) 110, *2,* 151-168

61. Smith, A. F.: *The sliding wear of 316 stainless steel in air in the temperature range 20-500C*, Tribology International (1985) 18, *1,* 35-43

62. Archard, J. F. and Hirst, W.: *The wear of metals under unlubricated conditions*, Proceedings of the Royal Society of London A: Mathematical and physical sciences (1956) 236, *1206,* 397-410

63. Quinn, T. F. J.: *Review of oxidational wear. Part I: The origins of oxidational wear*, Tribology International (1983) 16, *5,* 257-271

64. Sarkar, A. D.: *Friction and wear*, 1st Ed. (1980) London, Academic press

65. Suh, N. P.: *An overview of the delamination theory of wear*, Wear (1977) 44, *1,* 1-16

66. Zandrahimi, M., Reza Bateni, M., Poladi, A. and Szpunar, J. A.: *The formation of martensite during wear of AISI304 stainless steel*, Wear (2007) 263, *1-6,* 674-678

67. *Wear resistant surfaces in engineering*, 1st Ed. (1986) London, Great Britain Department of Trade and Industry, H.M.S.O

68. Leyland, A. and Matthews, A.: *On the significance of the H/E ratio in wear control: a nanocomposite coating approach to optimised tribological behaviour*, Wear (2000) 246, *1-2,* 1-11

69. Leyland, A. and Matthews, A.: *Design criteria for wear-resistant nanostructured and glassy-metal coatings*, Surface and Coatings Technology (2004) 177-178, 317-324

70. Lancaster, J. K.: *The formation of surface films at the transition between mild and severe metallic wear*, Proceedings of the Royal Society of London A: Mathematical and physical sciences (1963) 273, *1355,* 466-483

71. Sakrani, S. B. and Sullivan, J. L.: *Iron oxide films in tribological surfaces of alloy steel*, Third International Conference on Thin Film Physics and Applications (1998) Shanghai, China, SPIE - The International Society for Optical Engineering, 175-179

72. Godfrey, D.: *Iron oxides and rust (hydrated iron oxides) in tribology*, Lubrication Engineering (1999) 55, *2,* 33-38

73. Rabinowicz, E.: *Friction fluctuations* in 'Fundamentals of friction: macroscopic and microscopic processes' 1st Ed. (1992) London, Kluwer Academic Publishers, 25-34

74. Stolarski, T. A.: *Basic principles of tribology: friction* in 'Tribology in machine design' 1st Ed. (1999) Oxford, Butterworth Heinemann, 13-19

75. Barwell, F. T.: *The contribution of particle analysis to the study of wear of metals*, Wear (1982) 90, *1,* 167-181

76. Smart, R. F.: *Selection of surfacing treatments*, Tribology International (1978) 11, *2,* 97-104

77. Hurricks, P. L.: *Some aspects of the metallurgy and wear resistance of surface coatings*, Wear (1972) 22, *3,* 291-319

78. Bell, T.: *Surface engineering: its current and future impact on tribology*, Journal of Applied Physics (1992) 25, *1A,* A297-A306

79. Roberts, W. H.: *Some current trends in tribology in the UK and Europe*, Tribology International (1986) 19, *6,* 295-311

80. Whelan, R. C., Howlett, S., Keown, S. R. and Vaughan, D. A. J.: *The CEST surface engineering initiative* in 'Surface engineering and heat treatment: past, present and future' 1st Ed. (1991) London, The Institute of Metals,

81. Bell, T.: *Surface engineering: past, present and future*, Surface Engineering (1990) 6, *1,* 31-40

82. Jacobs, M. H.: *Surface engineering of materials*, Materials and Design (1993) 14, *1,* 33-37

83. Strafford, K. N. and Subramanian, C.: *Surface engineering: an enabling technology for manufacturing industry*, Journal of Materials Processing Technology (1995) 53, 393-403

84. Roberts, W. H.: *Surface engineering and tribology in general engineering* in 'Surface engineering and heat treatment: past, present and future' 1st Ed. (1991) London, The Institute of Metals,

85. Bhushan, B.: *Contact mechanics of rough surfaces in tribology: multiple asperity contact*, Tribology Letters (1998) 4, *1,* 1-35

86. Priestner, R. and Priestner, D. M.: *Importance of substrate in surface engineering*, Surface Engineering (1991) 7, *1,* 53-59

87. Mao, K., Sun, Y. and Bell, T.: *Contact mechanics of engineering surfaces: state of the art*, Surface Engineering (1994) 10, *4,* 297-306

88. Thelning, K. E.: *Steel and its heat treatment*, 2nd Ed. (1984) London, Butterworths

89. Syan, C. S., Matthews, A. and Swift, K. G.: *Knowledge-based expert systems in surface coating and treatment selection for wear reduction*, Surface and Coatings Technology (1987) 33, 105-115

90. Elliot, T. L.: *Surface hardening*, Tribology International (1978) 11, *2,* 121-125

91. James, A. S., Thomas, K., Mann, P. and Wall, R.: *The role and impacts of surface engineering in environmental design*, Materials and Design (2005) 26, *7,* 594-601

92. British Standard EN 10052:1994, "Vocabulary of heat treatment terms for ferrous products", BSI, London, www.bsi-global.com

93. Committee on gas carburizing, A. S. M.: *Carburizing and carbonitriding*, 1st Ed. (1977) Metals Park, Ohio, American Society for Metals

94. Parrish, G. and Harper, G. S.: *Production gas carburising*, 1st Ed. (1985) Oxford, Pergamon

95. Sun, Y. and Bell, T.: *Plasma surface engineering of low alloy steel*, Materials Science and Engineering A: Structural Materials: Properties, Microstructure and Processing (1991) A140, 419-434

96. Sun, Y., Li, X. and Bell, T.: *Low temperature plasma carburising of austenitic stainless steels for improved wear and corrosion resistance*, Surface Engineering (1999) 15, *1,* 49-54

97. Yin, R.: *Carburization of 310 stainless steel exposed at 800-1100C in 2% CH4/H2 gas mixture*, Corrosion Science (2005) 47, 1896-1910

98. Christ, H. J.: *Experimental characterization and computer based description of the carburization behaviour of the austenitic stainless steel AISI 304L*, Materials and Corrosion (1998) 49, *4,* 258-265

99. Ueda, Y., Kanayama, N., Ichii, K., Oishi, T. and Miyake, H.: *Effect of nitrogen on the plasma (ion)-carburized layer of high nitrogen austenitic stainless steel*, Surface and Coatings Technology (2005) 200, *1-4,* 521-524

100. Somers, M., Christiansen, T. and Ller Per, M.: *Case-hardening of stainless steel* European Patent 1521861 (2004) EU

101. Parascandola, S., Moller, W. and Williamson, D. L.: *Successful nitriding of austenitic stainless steel: the diffusion mechanism of nitrogen and the role of the surface oxide layer*, Stainless Steel 2000 (2000) Osaka, Maney - IofM - IFHTSE - JSHT, 201-214

102. Ueda, Y., Kanayama, N., Ichii, K., Oishi, T. and Miyake, H.: *Metallurgical characteristics of the plasma (ion)-carburized layer of austenitic stainless steel SUS 316L*, Surface and Coatings Technology (2005) 193, *1-4,* 50-54

103. Zhang, Z. L. and Bell, T.: *Structure and corrosion resistance of plasma nitrided stainless steel*, Surface Engineering (1985) 1, *2,* 131-136

104. Bell, T. and Sun, Y.: *Process for the treatment of austenitic stainless steel articles* UK Patent 9715180.7 (1998) UK

105. Bell, T.: *Surface engineering of austenitic stainless steel*, Surface Engineering (2002) 18, *6,* 415-422

106. Li, X. Y.: *Low temperature plasma nitriding of 316 stainless steel - Nature of S-phase and its thermal stability*, Surface Engineering (2001) 17, *2,* 147-152

107. Sun, Y., Li, X. and Bell, T.: *Structural characteristics of low temperature plasma carburised austenitic stainless steel*, Materials Science and Technology (1999) 15, *10,* 1171-1178

108. Li, X. Y., Thaiwatthana, S., Dong, H. and Bell, T.: *Thermal stability of carbon S phase in 316 stainless steel*, Surface Engineering (2002) 18, *6,* 448-452

109. Christiansen, T. and Somers, M.: *Characterisation of low temperature surface hardened stainless steel*, Struers Journal of Materialography (2006) 9, 1-17

110. Michal, G. M., Ernst, F., Kahn, H., Cao, Y., Oba, F., Agarwal, N. and Heuer, A. H.: *Carbon supersaturation due to paraequilibrium carburization: stainless steels with greatly improved mechanical properties*, Acta Materialia (2006) 54, *6,* 1597-1606

111. Fewell, M. P., Mitchell, D. R. G., Priest, J. M., Short, K. T. and Collins, G. A.: *The nature of expanded austenite*, Surface and Coatings Technology (2000) 131, *1-3,* 300-306

112. Christiansen, T. and Somers, M.: *On the crystallographic structure of S-phase*, Scripta Materialia (2004) 50, 35-37

113. Marchev, K., Hidalgo, R., Landis, M., Vallerio, R., Cooper, C. V. and Giessen, B. C.: *The metastable m phase layer on ion-nitrided austenitic stainless steels Part 2: crystal structure and observation of its two-directional orientation anisotropy*, Surface and Coatings Technology (1999) 112, *1-3,* 67-70

114. Sun, Y., Li, X. Y. and Bell, T.: *X-ray diffraction characterisation of low temperature plasma nitrided austenitic stainless steels*, Journal of Materials Science (1999) 34, *19,* 4793-4802

115. Mingolo, N., Tschiptschin, A. P. and Pinedo, C. E.: *On the formation of expanded austenite during plasma nitriding of an AISI 316L austenitic stainless steel*, Surface and Coatings Technology (2006) 201, *7,* 4215-4218

116. Li, X. Y.: *Characterisation of low temperature plasma nitrided austenitic stainless steel*, PhD thesis (1999) Metallurgy and Materials - The University of Birmingham

117. Sun, Y. and Bell, T.: *Low temperature plasma nitriding characteristics of precipitation hardening stainless steel*, Surface Engineering (2003) 19, *5,* 331-336

118. Sun, Y.: *Kinetics of low temperature plasma carburizing of austenitic stainless steels*, Journal of Materials Processing Technology (2005) 168, 189-194

119. Tsujikawa, M., Noguchi, S., Yamauchi, N., Ueda, N. and Sone, T.: *Effect of molybdenum on hardness of low-temperature plasma carburized austenitic stainless steel*, Surface and Coatings Technology (2007) 201, *9-11,* 5102-5107

120. Li, X. Y. and Dong, H.: *Effect of annealing on corrosion behaviour of nitrogen S phase in austenitic stainless steel*, Materials Science and Technology (2003) 19, *10,* 1427-1434

121. Ernst, F., Cao, Y. and Michal, G. M.: *Carbides in low-temperatue-carburized stainless steel*, Acta Materialia (2004) 52, *6,* 1469-1477

122. Cao, Y., Ernst, F. and Michal, G. M.: *Colossal carbon supersaturation in austenitic stainless steels carburized at low temperature*, Acta Materialia (2003) 51, *14,* 4171-4181

123. Ernst, F., Cao, Y., Michal, G. M. and Heuer, A. H.: *Carbide precipitation in austenitic stainless steel carburized at low temperature*, Acta Materialia (2007) 55, *6,* 1895-1906

124. Tokaji, K., Kohyama, K. and Akita, M.: *Fatigue behaviour and fracture mechanism of a 316 stainless steel hardened by carburizing*, International journal of fatigue (2004) 26, 543-551

125. Thaiwatthana, S., Li, X. Y., Dong, H. and Bell, T.: *Comparison studies on properties of nitrogen and carbon S phase on low temperature plasma alloyed AISI 316 stainless steel*, Surface Engineering (2002) 18, *6,* 433-437

126. Ceschini, L. and Minak, G.: *Fatigue behaviour of low temperature carburised AISI 316L austenitic stainless steel*, Surface and Coatings Technology (2007) 202, *9,* 1778-1784

127. Akita, M. and Tokaji, K.: *Effect of carburizing on notch fatigue behaviour in AISI 316 austenitic stainless steel*, Surface and Coatings Technology (2006) 200, *20-21,* 6073-6078

128. Qu, J., Blau, P. J. and Jolly, B. C.: *Tribological properties of stainless steel treated by colossal carbon supersaturation*, Wear (2007) 263, *1-6,* 719-726

129. Sun, Y. and Bell, T.: *Dry sliding wear resistance of low temperature plasma carburised austenitic stainless steel*, Wear (2002) 253, *5-6,* 689-693

130. Sun, Y. and Bell, T.: *Effect of layer thickness on the rolling-sliding wear behavior of low-temperature plasma-carburized austenitic stainless steel*, Tribology Letters (2002) 13, *1,* 29-34

131. Martin, W. C. and Wiese, W. L.: *Atomic, molecular, and optical physics handbook* in 2.1st Ed. (2002) Gaithersburg, NIST,

132. Thaiwatthana, S., Li, X. Y., Dong, H. and Bell, T.: *Corrosion wear behaviour of low temperature plasma alloyed 316 austenitic stainless steel*, Surface Engineering (2003) 19, *3,* 211-216

133. Aoki, K. and Kitano, K.: *Surface hardening for austenitic stainless steels based on carbon solid solution*, Surface Engineering (2002) 18, *6,* 462-464

134. Dong, H., Qi, P.-Y., Li, X. Y. and Llewellyn, R. J.: *Improving the erosion-corrosion resistance of AISI 316 austenitic stainless steel by low-temperature plasma surface alloying with N and C*, Materials Science and Engineering A: Structural Materials: Properties, Microstructure and Processing (2006) 431, 137-145

135. Farrell, K., Specht, E. D., Pang, J., Walker, L. R., Rar, A. and Mayotte, J. R.: *Characterization of a carburized surface layer on an austenitic stainless steel*, Journal of Nuclear Materials (2005) 343, 123-133

136. Tanaka, S., Ueda, K., Mitamura, N. and Oohori, M.: *The development of an austenitic stainless steel bearing with high corrosion resistance and high non-magnetic property*, Journal of ASTM International (2006) 3, *2,* 1-7

137. Bos, M. J.: *Case hardening of austenitic stainless steel pump components*, World Pumps (1998) March, 30-34

138. Ceschini, L., Lanzoni, E., Sambogna, G., Bordiga, V. and Schild, T.: *Tribological behaviour and corrosion resistance of Kolsterized AISI 316L austenitic stainless steel: existing applications in the automotive industry*, Journal of ASTM International (2006) 3, *2,* 1-9

139. Williams, P. and Marx, S.: *Low temperature case hardening processes* US Patent 6,093,303 (2000) United States of America

140. Bell, T. and Sun, Y.: *Process for the treatment of austenitic stainless steel articles* US Patent 6,238,490 (2001) United States of America

141. Ueda, N., Yamauchi, N., Sone, T., Okamoto, A. and Tsujikawa, M.: *DLC film coating on plasma-carburized austenitic stainless steel*, Surface and Coatings Technology (2007) 201, *9-11,* 5487-5492

142. van der Jagt, R. H., Kolster, B. H. and Gillham, M. W. H.: *Anti-wear/corrosion treatment of finished austenitic stainless steel components: the Hardcor process*, Materials and Design (1991) 12, *1,* 41-46

143. Lebrun, J. P., Poirier, L., Hertz, D. and Lincot, C.: *Environmentally friendly low temperature plasma processing of stainless steel components for nuclear industry*, Stainless Steel 2000 (2000) Osaka, Maney - IofM - IFHTSE - JSHT, 361-375

144. Grafen, W. and Edenhofer, B.: *New developments in thermo-chemical diffusion processes*, Surface and Coatings Technology (2005) 200, *5-6,* 1830-1836

145. Christiansen, T. and Somers, M.: *Low temperature gaseous nitriding and carburising of stainless steel*, Surface Engineering (2005) 21, *5-6,* 445-455

146. Somers, M. and Christiansen, T.: *Kinetics of microstructure evolution during gaseous thermochemical surface treatment*, Phase Equilibria and Diffusion (2005) 26, *5,* 520-528

147. Michal, G. M., Ernst, F. and Heuer, A. H.: *Carbon paraequilibrium in austenitic stainless steel*, Metallurgical Transactions A: Physical Metallurgy and Materials Science (2006) 37A, *6,* 1819-1824

148. Aoki, K., Shirahata, T., Tahara, M. and Kitano, K.: *Low temperature gas carburising for austenitic stainless steels: the NV-Pionite process*, Stainless Steel 2000 (2000) Osaka, Maney - IofM - IFHTSE - JSHT, 389-405

149. Kula, P., Pietrasik, R. and Dybowski, K.: *Vacuum carburizing - Process optimization*, Journal of Materials Processing Technology (2005) 164-165, 876-881

150. Ryzhov, N. M., Smirnov, A. E., Fakhurtdinov, R. S., Mulyakaev, L. M. and Gromov, V. I.: *Special features of vacuum carburizing of heat-resistant steel in acetylene*, Metal Science and Heat Treatment (2004) 46, *5-6,* 230-235

151. Birch, B. J. and Ellis, B.: *Twenty five years of vacuum heat treatment* in 'Surface engineering and heat treatment: past, present and future' 1st Ed. (1991) London, The Institute of Metals,

152. Hoffmann, F. and Clausen, B.: *Low pressure carburizing with and without plasma assistance*, ASTRA (2004) Hyderabad, India, International Advanced Research Centre for Powder Metallurgy and New Materials (ARCI),

153. Berghaus, B.: *Method of ionitriding objects made of iron and steel* GB Patent 1202810 (1968) UK

154. Edenhofer, B.: *Physical and metallurgical aspects of ionitriding - Part 1*, Heat Treatment of Metals (1974) *1,* 23-28

155. Booth, M., Farrell, T. and Johnson, R. H.: *Theory and practice of plasma carburising*, Materials and Design (1984) 5, *3,* 139-148

156. Grube, W.: *Direct-current glow discharge furnace for high-rate carburizing*, Journal of Vacuum Science and Technology (1979) 16, *2,* 335-338

157. Reece Roth, J.: *Industrial plasma engineering II*, 1st Ed. (1997) London, IOP Publishing

158. Jacobs, M. H. and Law, T. J.: *Plasma carburising: operating theory and practice with a large industrial unit*, Heat Treatment of Metals (1984) 3, 56-66

159. Wells, A. and Strydom, I. l. R.: *Sputtering and redeposition of cathode material during plasma nitriding*, Surface Engineering (1986) 2, *4,* 263-267

160. Ruset, C., Ciuca, S. and Grigore, E.: *The influence of the sputtering process on the constitution of the compound layers obtained by plasma nitriding*, Surface and Coatings Technology (2003) 174-175, 1201-1205

161. Edenhofer, B.: *Physical and metallurgical aspects of ionitriding - Part 2*, Heat Treatment of Metals (1974) *2,* 59-67

162. Haruman, E., Bell, T. and Sun, Y.: *Compound layer characteristics resulting from plasma nitrocarburising in atmospheres containing carbon dioxide gas additions*, Surface Engineering (1992) 8, *4,* 275-282

163. Edenhofer, B., Conybear, J. G. and Legge, G. T.: *Opportunities and limitations of plasma carburising*, Heat Treatment of Metals (1991) 18, *1,* 6-12

164. Maliska, A. M., Egert, P., de Souza, A. R., Speller, C. V. and Klein, A. N.: *Influence of oxygen in a plasma nitriding process*, Journal of Materials Science (1997) 32, *23,* 6375-6382

165. Avni, R. and Spalvins, T.: *Nitriding mechanisms in Ar-N2, Ar-N2-H2 and Ar-NH3 mixtures in DC glow discharges at low pressures (less than 10 torr)*, Materials Science and Engineering (1987) 95, 237-246

166. Ruset, C.: *The influence of pressure on temperature uniformity in the plasma nitriding process*, Heat Treatment of Metals (1991) 18, *3,* 81-84

167. Hick, A. J.: *The industrial application of ionic carburising*, Heat Treatment of Metals (1984) 3, 56-66

168. Rembges, W. and Oppel, W.: *Process control of plasma nitriding and plasma nitrocarburizing in industry*, Surface and Coatings Technology (1993) 59, *1-3,* 129-134

169. Janosi, S., Kolozsvary, Z. and Kis, A.: *Controlled hollow cathode effect: New possibilities for heating low-pressure furnaces*, Metal Science and Heat Treatment (2004) 46, *7-8,* 310-316

170. Hombeck, F. and Bell, T.: *Environmentally harmless plasma thermochemical processes*, Surface Engineering (1991) 7, *1,* 45-52

171. Okumiya, M., Tsunekawa, Y., Matsumoto, T., Tanaka, K. and Nagai, T.: *Carbon content control in plasma carburizing using process parameter and probe methods*, Surface and Coatings Technology (2003) 174-175, 1171-1174

172. Staines, A. M. and Bell, T.: *Technological importance of plasma-induced nitrided and carburized layers on steel*, Thin Solid Films (1981) 86, *2-3,* 201-211

173. Bell, T., Sun, Y. and Suhadi, A.: *Environmental and technical aspects of plasma nitrocarburising*, Vacuum (2000) 59, *1,* 14-23

174. Bell, T. and Dearnley, P. A.: *Environmental issues in surface engineering and related industrial sectors*, Surface Engineering (1994) 10, *2,* 123-128

175. Georges, J.: *Nitriding process and nitriding furnace therefor* US Patent 5,989,363 (1999) United States of America

176. Alves Jr., C., de Araujo, F. O., Ribeiro, K. J. B., da Costa, J. A. P., Sousa, R. R. M. and de Sousa, R. S.: *Use of cathodic cage in plasma nitriding*, Surface and Coatings Technology (2006) 201, *6,* 2450-2454

177. Georges, J.: *Industrial thermochemical treatments and plasma nitriding* (2002) http://www.plasma-metal.lu, 13 July 2008

178. Li, C. X., Dong, H. and Bell, T.: *A feasibility study of plasma nitriding of steel with an oxide layer on the surface*, Journal of Materials Science (2006) 41, *18,* 6116-6118

179. Li, C. X., Georges, J. and Li, X. Y.: *Active screen plasma nitriding of austenitic stainless steel*, Surface Engineering (2002) 18, *6,* 453-458

180. de Sousa, R. R. M., de Araujo, F. O., Ribeiro, K. J. B., Mendes, M. W. D., da Costa, J. A. P. and Alves Jr., C.: *Cathodic cage nitriding of samples with different dimensions*, Materials Science and Engineering A: Structural Materials: Properties, Microstructure and Processing (2007) 465, 223-227

181. Zhao, C., Li, C. X., Dong, H. and Bell, T.: *Study on the active screen plasma nitriding and its nitriding mechanism*, Surface and Coatings Technology (2006) 201, *6,* 2320-2325

182. Li, C. X., Bell, T. and Dong, H.: *A study of active screen plasma nitriding*, Surface Engineering (2002) 18, *3,* 174-181

183. Zhao, C., Li, C. X., Dong, H. and Bell, T.: *Study of the active screen plasma nitriding*, Transactions of Materials and Heat Treatment (2004) 25, *1,* 330-333

184. Hubbard, P., Dowey, S. J., Doyle, E. and McCulloch, D.: *Influence of bias and in situ cleaning on through cage (TC) or active screen plasma nitrided (ASPN) steels*, Surface Engineering (2006) 22, *4,* 243-247

185. Spies, H.-J., Le Thien, H. and Biermann, H.: *Verhalten von Staehlen beim Plasmanitrieren mit einem Aktivgitter (Behaviour of steels in active screen plasma nitriding)*, HTM Z. Werkst. Warmebeh. Fertigung (2005) 60, *4,* 1-8

186. D'Agostino, R., Favia, P., Oehr, C. and Wertheimer, M. R.: *Low temperature plasma processing of materials: past, present and future*, Plasma Processes and Polymers (2005) 2005, *2,* 7-15

187. Bogaerts, A., Neyts, E., Gijbels, R. and van der Mullen, J.: *Gas discharge plasmas and their applications*, Spectrochimica Acta B: Atomic Spectroscopy (2002) 57, *4,* 609-658

188. Sree Harsha, K. S.: *Principles of vapor deposition of thin films*, 1st Ed. (2006) London, Elsevier

189. Kuffel, E., Zaengl, W. S. and Kuffel, J.: *Chapter 5: Electrical breakdown in gases* in 'High voltage engineering fundamentals' 2nd Ed. (2000) Oxford, Elsevier Newnes, 281-366

190. Druyvesteyn, M. J. and Penning, F. M.: *The mechanism of electrical discharges in gases of low pressure*, Reviews of Modern Physics (1940) 12, *April 1940,* 87-174

191. Langmuir, I.: *Electrical discharges in gases at low pressures*, Journal of the Franklin Institute (1932) 214, 275-298

192. Sree Harsha, K. S.: *Chapter 4: Cold plasma discharges* in 'Principles of vapour deposition of thin films' 1st Ed. (2006) London, Elsevier, 259-365

193. Morse, P. M.: *A theory of the electric discharge through gases*, Physical review (1928) 31, 1003-1017

194. Braithwaite, N. S.: *Introduction to gas discharges*, Plasma Sources Science and Technology (2000) 9, *4,* 517-527

195. ITER: *Measurement of plasma parameters*, Nuclear Fusion (1999) 39, *12,* 2541-2575

196. Demidov, V. I., Ratynskaia, S. V. and Rypdal, K.: *Electric probes for plasmas: the link between theory and instrument*, Review of Scientific Instruments (2002) 73, *10,* 3409-3439

197. Hancock, G.: *Diagnostic of active species in plasmas*, Surface and Coatings Technology (1995) 74-75, 10-14

198. Mott-Smith, H. M. and Langmuir, I.: *The theory of collectors in gaseous discharges*, Physical review (1926) 28, 727-763

199. Found, C. G. and Langmuir, I.: *Study of a neon discharge by the use of collectors*, Physical review (1932) 39, 237-253

200. Cooke, K. E., Goodyear, A., Hampshire, J. and Teer, D. G.: *An investigation of an industrial coating environment with planar probe technology*, Surface and Coatings Technology (2004) 188-189, 750-755

201. Al-Kuzee, J., Matsuura, T., Goodyear, A., Nolle, L., Hopgood, A., Picton, P. and Braithwaite, N. S.: *Intelligent control of low pressure plasma processing*, 29th Annual Conference of the IEEE Industrial Electronics Society (2003) Roanoke, VA, USA, IEEE, 1932-1937

202. Modest, M. F.: *Chapter 10: Radiative properties of molecular gases* in 'Radiative heat transfer' 2nd Ed. (2003) London, Academic Press, 288-360

203. Halliday, D. and Resnick, R.: *Fisica: parte II (Physics: part II)*, 2nd Ed. (1977) Buenos Aires, John Wiley and Sons

204. Svanberg, S.: *Atomic and molecular spectroscopy: basic aspects and practical applications*, 3rd Ed. (2001) New York, Springer

205. Olesik, J. W.: *ICP-OES* in 'Encyclopedia of materials characterization' 1st Ed. (1992) London, Butterworth-Heinemann, 633-644

206. Harrison, G. R., Lord, R. C. and Loofbourow, J. R.: *Practical spectroscopy*, 2nd Ed. (1948) New York, Prentice Hall

207. Optronic Laboratories Application Note A14: *Spectroradiometry Methods* (1998)

208. Polk, J. E., Marrese-Reading, C. M., Thornber, B., Dang, L., Johnson, K. L. and Katz, I.: *Scanning optical pyrometer for measuring temperatures in hollow cathodes*, Review of Scientific Instruments (2007) 78, *9,* 0931011-0931018

209. Korotchenko, V. and Matthews, A.: *Substrate temperature monitoring in plasma assisted processes*, Vacuum (1986) 36, *1-3,* 61-65

210. Langmuir, I.: *The interaction of electron and positive ion space charges in cathode sheaths*, Physical review (1929) 33, 954-967

211. Langmuir, I.: *The pressure effect and other phenomena in gaseous discharges*, Journal of the Franklin Institute (1923) 196, 751-762

212. Swift, J. D. and Schwar, M. J. R.: *Electrical probes for plasma diagnostics*, 1st Ed. (1970) London, Iliffe Books Ltd

213. Loeb, L. B.: *Fundamental processes of electrical discharge in gases*, 1st Ed. (1939) London, Chapman and Hall

214. Booth, J. P. and Braithwaite, N. S.: *Method and device for measuring an ion flow in a plasma* US Patent 5,936,413 (1999) United States of America

215. Braithwaite, N. S., Booth, J. P. and Cunge, G.: *A novel electrostatic probe method for ion flux measurements*, Plasma Sources Science and Technology (1996) 5, *4,* 677-684

216. Braithwaite, N. S. J., Sheridan, T. E. and Boswell, R. W.: *Transient RF self-bias in electropositive and electronegative plasmas*, Journal of Applied Physics (2003) 36, *22,* 2837-2844

217. Booth, J. P., Braithwaite, N. S. J., Goodyear, A. and Barroy, P.: *Measurements of characteristic transients of planar electrostatic probes in cold plasmas*, Review of Scientific Instruments (2000) 71, *7,* 2722-2727

218. Boeuf, J. P.: *A two dimensional model of DC glow discharges*, Journal of Applied Physics (1988) 63, *5,* 1342-1349

219. Spyrou, N., Peyrous, R., Soulem, N. and Held, B.: *Why Paschen's law does not apply in low pressure gas discharges with inhomogeneous fields*, Journal of Physics D: Applied Physics (1995) 28, *4,* 701-710

220. Raizer, Y. P.: *Gas discharge physics*, 1st Ed. (1997) London, Springer

221. Toader, E. I., Graham, W. G., Mahony, C. M. O. and Steen, P. G.: *Characterization of a high density direct current reflex discharge plasma source operating in Ar and N2*, Review of Scientific Instruments (2002) 73, *8,* 2974-2980

222. Meek, J. M. and Craggs, J. D.: *Electrical breakdown of gases*, 1st Ed. (1953) Oxford University Press

223. Metel, A.: *Plasma immersion ion implantation based on glow discharge with electrostatic confinement of electrons*, Surface and Coatings Technology (2002) 156, *1-3,* 38-43

224. Lisovskiy, V. A., Yakovin, S. D. and Yegorenkov, V. D.: *Low pressure gas breakdown in uniform DC electric field*, Journal of Applied Physics (2000) 33, *21,* 2722-2730

225. Tsujikawa, M., Egawa, M., Ueda, N., Okamoto, A., Sone, T. and Nakata, K.: *Effect of molybdenum and copper on S-phase layer thickness of low-temperature carburized austenitic stainless steel*, Surface and Coatings Technology (2008) 202, *22-23,* 5488-5492

226. Williamson, D. L., Wilbur, P. J., Fickett, F. R. and Parascandola, S.: *Role of ion-beam processing time in the formation and growth of the high-nitrogen phase in austenitic stainless steel*, Stainless Steel 2000 (2000) Osaka, Maney - IofM - IFHTSE - JSHT, 333-352

227. Moller, W., Parascandola, S., Telbizova, T., Gunzel, R. and Richter, E.: *Surface processes and diffusion mechanisms of ion nitriding of stainless steel and aluminium*, Surface and Coatings Technology (2001) 136, *1-3,* 73-79

228. Hillert, M. and Agren, J.: *Reply to comments on "On the definition of paraequilibrium and orthoequilibrium"*, Scripta Materialia (2005) 52, 87-88

229. Speer, J. G., Matlock, D. K., DeCooman, B. C. and Schroth, J. G.: *Comments on "On the definitions of paraequilibrium and orthoequilibrium" by M. Hillert and J. Agren, Scripta Materialia, 50, 697-9 (2004)*, Scripta Materialia (2005) 52, 83-85

230. Hillert, M. and Agren, J.: *On the definitions of paraequilibrium and orthoequilibrium*, Scripta Materialia (2004) 50, 697-699

231. Enomoto, M. and Aaronson, H. I.: *Derivation of general conditions for paraequilibrium in multi-component systems*, Scripta Metallurgica (1985) 19, 1-3

232. Ghosh, G. and Olson, G. B.: *Simulation of paraequilibrium growth in multicomponent systems*, Metallurgical Transactions A: Physical Metallurgy and Materials Science (2001) 32A, *3,* 455-467

233. Aziz, M. J.: *Model for solute redistribution during rapid solidification*, Journal of Applied Physics (1982) 53, *2,* 1158-1168

234. Wert, C. A. and Frank, R. C.: *Trapping of interstitials in metals*, Annual Reviews of Materials Science (1983) 13, 139-172

235. Maalekian, M. and Kozeschnik, E.: *A thermodynamic model for carbon trapping in lattice defects*, Computer Coupling of Phase Diagrams and Thermochemistry (2008) 32, *4,* 650-654

236. Heuer, A. H., Ernst, F., Kahn, H., Avishai, A., Michal, G. M., Pitchure, D. J. and Ricker, R. E.: *Interstitial defects in 316L austenitic stainless steel containing "colossal" carbon concentrations: An internal friction study*, Scripta Materialia (2007) 56, 1067-1070

237. Zaefferer, S.: *The electron backscatter diffraction technique - a powerful tool to study microstructures by SEM*, JEOL News (2004) 39, *1,* 10-15

238. Yu, Z. W., Wang, L., Xu, X. L. and Gao, Y. Z.: *In situ SEM and AFM observations of surface morphology of plasma nitrided layer of austenitic stainless steel*, Materials Science and Technology (2005) 21, *8,* 921-924

239. Borgioli, F., Fossati, A., Galvanetto, E., Bacci, T. and Pradelli, G.: *Glow discharge nitriding of AISI 316L austenitic stainless steel: influence of treatment pressure*, Surface and Coatings Technology (2006) 200, *18-19,* 5505-5513

240. Sun, Y. and Haruman, E.: *Influence of processing conditions on structural characteristics of hybrid plasma surface alloyed austenitic stainless steel*, Surface and Coatings Technology (2008) 202, *17,* 4069-4075

241. Xu, X., Yu, Z., Wang, L., Qiang, J. and Hei, Z.: *Phase depth distribution characteristics of the plasma nitrided layer on AISI 304 stainless steel*, Surface and Coatings Technology (2003) 162, *2-3,* 242-247

242. Monteiro, S. N.: *Influence of grain orientation on the dislocation substructure in austenitic stainless steel*, Metallurgical Transactions A: Physical Metallurgy and Materials Science (1975) 6, *4,* 938-940

243. Byun, T. S.: *On the stress dependence of partial dislocation separation and deformation microstructure in austenitic stainless steel*, Acta Materialia (2003) 51, *11,* 3063-3071

244. Lee, E. H., Byun, T. S., Hunn, J. D., Yoo, M. H., Farrell, K. and Mansur, L. K.: *On the origin of deformation microstructures in austenitic stainless steel - Part 1: Microstructures*, Acta Materialia (2001) 49, *16,* 3269-3276

245. Cizek, P., Whiteman, J. A., Rainforth, W. M. and Beynon, J. H.: *EBSD and TEM investigation of the hot deformation substructure characteristics of a type of 316L austenitic stainless steel*, Journal of Microscopy (2004) 213, 285-295

246. Donadille, C., Valle, R., Dervin, P. and Penelle, R.: *Development of texture and microstructure during cold-rolling and annealing of fcc alloys: example of an austenitic stainless steel*, Acta Metallurgica (1989) 37, *6,* 1547-1571

247. Abrasonis, G., Riviere, J. P., Templier, C., Declemy, A., Pranevicius, L. and Milhet, X.: *Ion beam nitriding of single and polycrystalline austenitic stainless steel*, Journal of Applied Physics (2005) 97, *8,* 8353101-8353110

248. Abrasonis, G., Riviere, J. P., Templier, C., Declemy, A., Muzard, S. and Pranevicius, L.: *A comparative study of ion beam nitriding of single-crystalline and polycrystalline 316L austenitic stainless steel*, Surface and Coatings Technology (2005) 196, *1-3,* 262-266

249. Riviere, J. P., Templier, C., Declemy, A., Redjdal, O., Chumlyakov, Y. and Abrasonis, G.: *Microstructure of expanded austenite in ion-nitrided AISI 316 single crystals*, Surface and Coatings Technology (2007) 201, *19-20,* 8210-8214

250. Mandl, S. and Rauschenbach, B.: *Anisotropic strain in nitrided austenitic stainless steel*, Journal of Applied Physics (2000) 88, *6,* 3323-3329

251. Marchev, K., Landis, M., Vallerio, R., Cooper, C. V. and Giessen, B. C.: *The m-phase layer on ion nitrided austenitic stainless steel (III): an epitaxial relationship between the m-phase and the parent phase and a review of structural identifications of this phase*, Surface and Coatings Technology (1999) 116-119, 184-188

252. Ichii, K. and Fujimura, K.: *Structure of the ion-nitrided layer of 18-8 stainless steel*, Stainless Steel 2000 (2000) Osaka, Maney - IofM - IFHTSE - JSHT, 13-22

253. Frechard, S., Martin, F., Clement, C. and Cousty, J.: *AFM and EBSD combined studies of plastic deformation in a duplex stainless steel*, Materials Science and Engineering A: Structural Materials: Properties, Microstructure and Processing (2006) A 418, 312-319

254. Sun, Y. and Chin, L. Y.: *Residual stress evolution and relaxation in carbon S-phase layers on AISI 316 austenitic stainless steel*, Surface Engineering (2002) 18, *6,* 443-447

255. Wagner, C. N. J.: *X-ray study of low-temperature cold work in silver and aluminum*, Acta Metallurgica (1957) 5, *9,* 477-482

256. Paterson, M. S.: *X-ray diffraction by face-centered cubic crystals with deformation faults*, Journal of Applied Physics (1952) 23, 805-811

257. Mikkola, D. E. and Cohen, J. B.: *Effects of thermal-mechanical treatments on faulting in some fcc alloys*, Journal of Applied Physics (1962) 33, *3,* 892-898

258. Adler, R. P. I. and Wagner, C. N. J.: *X-ray diffraction study of the effects of solutes on the occurrence of stacking faults in silver-base alloys*, Journal of Applied Physics (1962) 33, *12,* 3451-3458

259. Wagner, C. N. J., Baisseau, J. P. and Aqua, E. N.: *X-Ray diffraction study of plastically deformed copper*, Transactions of the Metallurgical Society of AIME (1965) 233, *7,* 1280-1286

260. Timoshenko and Woinowsky-Krieger: *Theory of plates and shells*, 2nd Ed. (1959) London, McGraw Hill

261. Sglavo, V. M., Bonafini, M. and Prezzi, A.: *Procedure for residual stress profile determination by curvature measurements*, Mechanics of Materials (2005) 37, *8,* 887-898

262. Roll, K.: *Analysis of stress and strain distribution in thin films and substrates*, Journal of Applied Physics (1976) 47, *7,* 3224-3229

263. Loh, N. L. and Siew, L. W.: *Residual stress profiles of plasma nitrided steels*, Surface Engineering (1999) 15, *2,* 137-142

264. Johnson, K. L.: *The correlation of indentation experiments*, Journal of Mechanics and Physics of Solids (1969) 18, *2,* 115-126

265. Richer, G. C.: *Indentation hardness*, Metallurgia (1945) 31, *186,* 296-299

266. British Standard EN ISO 4516:2002, "Metallic and other inorganic coatings - Vickers and Knoop microhardness tests", BSI, London, www.bsi-global.com

267. Buckle, H.: *Use of the hardness test to determine other material properties* in 'The science of hardness testing and its research applications' Ed. (1971) Metals Park, Ohio, American Society for Metals, 453-494

268. van Houtte, P. and de Buyser, L.: *The influence of crystallographic texture on diffraction measurements of residual stress*, Acta Metallurgica et Materialia (1993) 41, *2,* 323-336

269. Doerner, M. F. and Nix, W. D.: *A method for interpreting the data from depth-sensing indentation instruments*, JOurnal of Materials Research (1986) 1, *4,* 601-609

270. Suresh, S. and Giannakopoulos, A. E.: *A new method for estimating residual stresses by instrumented sharp indentation*, Acta Materialia (1998) 46, *16,* 5755-5767

271. Carlsson, S. and Larsson, P. L.: *On the determination of residual stress and strain fields by sharp indentation testing - Part I: theoretical and numerical analysis*, Acta Materialia (2001) 49, *12,* 2179-2191

272. Wang, Q., Ozaki, K., Ishikawa, H., Nakano, S. and Ogiso, H.: *Indentation method to measure the residual stress induced by ion implantation*, Nuclear Instruments and Methods in Physics Research B: Beam Interactions with Materials and Atoms (2006) 242, *1-2,* 88-92

273. Stachowiak, G. P. and Podsiadlo, P.: *Automated classification of wear particles based on their surface texture and shape features*, Tribology International (2008) 41, *1,* 34-43

274. Hutchings, I. M.: *Tribology: Friction and wear of engineering materials*, 1st Ed. (1992) London, Arnold

275. Rigney, D. A. and Glaeser, W. A.: *The significance of near surface microstructure in the wear process*, Wear (1978) 46, *1,* 241-250

276. Rigney, D. A. and Hirth, J. P.: *Plastic deformation and sliding friction of metals*, Wear (1979) 53, *2,* 345-370

277. Glaeser, W. A.: *Friction and wear*, IEEE Transactions on parts, hybrids and packaging (1971) PHP 7, *2,* 99-105

278. Suh, N. P.: *The delamination theory of wear*, Wear (1973) 25, *1,* 111-124

279. Straffelini, G., Trabucco, D. and Molinari, A.: *Sliding wear of austenitic and austenitic-ferritic stainless steels*, Metallurgical Transactions A: Physical Metallurgy and Materials Science (2002) 33A, *3,* 613-624

280. Kapoor, A., Johnson, K. L. and Williams, J. A.: *A model for the mild ratchetting wear of metals*, Wear (1996) 200, *1-2,* 38-44

281. Johnson, K. L.: *Contact mechanics and the wear of metals*, Wear (1995) 190, *2,* 162-170

282. Kang, G.: *Ratchetting: recent progresses in phenomenon observation, constitutive modeling and application*, International journal of fatigue (2008) 30, 1448-1472

283. Podgornik, B. and Vizintin, J.: *Influence of substrate treatment on the tribological properties of DLC coatings*, Diamond and Related Materials (2001) 10, *12,* 2232-2237

284. Quinn, T. F. J.: *Physical analysis for tribology*, 1st Ed. (1991) Cambridge University Press

285. Shipway, P. H. and Hogg, J. J.: *Dependence of microscale abrasion mechanisms of WC-Co hardmetals on abrasive type*, Wear (2005) 259, *1-6,* 44-51

286. Fillot, N., Iordanoff, I. and Berthier, Y.: *Wear modeling and the third body concept*, Wear (2007) 262, *7-8,* 949-957

287. Li, C. X. and Bell, T.: *Sliding wear properties of active screen plasma nitrided 316 austenitic stainless steel*, Wear (2004) 256, *11-12,* 1144-1152

288. Foerster, C. E., Serbena, F. C., da Silva, S. L. R., Lepienski, C. M., de M. Siqueira, C. J. and Ueda, M.: *Mechanical and tribological properties of AISI 304 stainless steel nitrided by glow discharge compared to ion implantation and plasma immersion ion implantation*, Nuclear Instruments and Methods in Physics Research B: Beam Interactions with Materials and Atoms (2007) B257, *1-2,* 732-736

289. Manova, D., Hirsch, D., Richter, E., Mandl, S., Naumann, H. and Rauschenbach, B.: *Microstructure of nitrogen implanted stainless steel after wear experiment*, Surface and Coatings Technology (2007) 201, *19-20,* 8329-8333

290. Sun, Y. and Kappaganthu, S. R.: *Effect of nitrogen doping on sliding wear behaviour of stainless steel coatings*, Tribology Letters (2004) 17, *4,* 845-850

291. Vergne, C., Boher, C., Gras, R. and Levaillant, C.: *Influence of oxides on friction in hot rolling: Experimental investigations and tribological modelling*, Wear (2006) 260, *9-10,* 957-975

292. Persson: *Dry friction dynamics* in 'Sliding friction: physical principles and applications' 1st Ed. (1998) Berlin, Springer, 367-385

293. Monypenny, J. H. G.: *Stainless iron and steel*, 3rd Ed. (1951) London, Chapman and Hall

294. Fauvet, P., Balbaud, F., Robin, R., Tran, Q. T., Mugnier, A. and Espinoux, D.: *Corrosion mechanisms of austenitic stainless steels in nitric media used in reprocessing plants*, Journal of Nuclear Materials (2008) 375, 52-64

295. Streicher, M. A.: *General and intergranular corrosion of austenitic stainless steels in acids*, Journal of The Electrochemical Society (1959) 106, *3,* 161-180

296. Castle, J. E. and Clayton, C. R.: *The use of x-ray photo-electron spectroscopy in the analysis of passive layers on stainless steel*, Corrosion Science (1977) 17, 7-26

297. Shieu, F. S., Deng, M. J. and Lin, S. H.: *Microstructure and corrosion resistance of a type 316L stainless steel*, Corrosion Science (1998) 40, 1267-1279

298. Thaiwatthana, S., Li, X. Y., Dong, H. and Bell, T.: *Mechanical and chemical properties of low temperature plasma surface alloyed 316 austenitic stainless steel*, Surface Engineering (2002) 18, *2,* 140-144

299. Li, C. X. and Bell, T.: *Corrosion properties of active screen plasma nitrided 316 austenitic stainless steel*, Corrosion Science (2004) 46, 1527-1547

300. Spies, H.-J., Eckstein, C. and Zimdars, H.: *Structure and corrosion behaviour of stainless steels after plasma and gas nitriding*, Surface Engineering (2002) 18, *6,* 459-461

301. Nosei, L., Farina, S., Avalos, M., Nachez, L., Gomez, B. J. and Feugeas, J.: *Corrosion behaviour of ion nitrided AISI 316L stainless steel*, Thin Solid Films (2008) 516, *6,* 1044-1050

302. Sun, Y.: *Enhancement in corrosion resistance of austenitic stainless steel by surface alloying with nitrogen and carbon*, Materials Letters (2005) 59, 3410-3413

303. Martin, F. J., Lemieux, E. J., Newbauer, T. M., Bayles, R. A., Natishan, P. M., Kahn, H., Michal, G. M., Ernst, F. and Heuer, A. H.: *Carburization-induced passivity of 316L austenitic stainless steel*, Electrochemical and Solid-State Letters (2007) 10, *12,* C76-C78

304. Nikam, V. V., Reddy, R. G., Collins, S. r., Williams, P. C., Schiroky, G. H. and Henrich, G. W.: *Corrosion resistant low temperature carburized SS 316 as bipolar plate material for PEMFC application*, Electrochimica Acta (2008) 53, 2743-2750

305. Leitao, E., Silva, R. A. and Barbosa, M. A.: *Electrochemical impedance spectroscopy of nitrogen and carbon sputter coated 316L stainless steel*, Corrosion Science (1997) 39, 333-338

306. Baba, H., Kodama, T. and Katada, Y.: *Role of nitrogen on the corrosion behavior of austenitic stainless steels* Corrosion Science (2002) 44, 2393-2407

307. Kuczynska-Wydorska, M. and Flis, J.: *Corrosion and passivation of low temperature nitrided AISI 304L and 316L stainless steel in acidified sodium sulphate solution*, Corrosion Science (2008) 50, 523-533

308. Flis, J. and Kuczynska, M.: *Effect of low temperature plasma nitriding on corrosion of 304L stainless steel in sulfate and chloride solutions*, Journal of The Electrochemical Society (2004) 151, *11,* B573-B580

309. Flis, J., Kuczynska-Wydorska, M. and Flis-Kabulska, I.: *The effect of molybdenum on corrosion of low temperature nitrided stainless steel in sulphate-chloride solution*, Journal of Solid State Electrochemistry (2006) 10, 689-695

310. Corujeira Gallo, S. and Dong, H.: *Corrosion behaviour of direct current and active screen plasma carburised AISI 316 stainless steel in boiling sulphuric acid solutions*, Corrosion Engineering Science and Technology (2009) Article in Press

311. Picard, S., Memet, J. B., Sabot, R., Grosseau-Poussard, J. L., Riviere, J. P. and Meilland, R.: *Corrosion behaviour, microhardness and surface characterisation of low energy, high current ion implanted austenitic stainless steel*, Materials Science and Engineering A: Structural Materials: Properties, Microstructure and Processing (2001) A303, 163-172

312. Dearnley, P. A.: *Corrosion wear response of S phase coated 316L*, Surface Engineering (2002) 18, *6,* 429-432

313. Dong, H., Sun, Y. and Bell, T.: *Enhanced corrosion resistance of duplex coatings*, Surface and Coatings Technology (1997) 90, *1-2,* 91-101

314. Murr, L. E., Advani, A., Shankar, S. and Atteridge, D. G.: *Effects of deformation (strain) and heat treatment on grain boundary sensitization and precipitation in austenitic stainless steels*, Materials Characterization (1990) 39, *2-5,* 575-598

315. Bi, H. Y., Kokawa, H., Wang, Z. J., Shimada, M. and Sato, Y. S.: *Suppression of chromium depletion by grain boundary structural change during twin-induced grain boundary engineering of 304 stainless steel*, Scripta Materialia (2003) 49, 219-223

316. Wasnik, D. N., Kain, V., Samajdar, I., Verlinden, B. and De, P. K.: *Resistance to sensitization and intergranular corrosion through extreme randomization of grain boundaries*, Acta Materialia (2002) 50, *18,* 4587-4601

317. van Aswegen, J. S. T., Honeycombe, R. W. K. and Warrington, D. H.: *Precipitation on stacking faults in Cr-Ni austenitic steels*, Acta Metallurgica (1964) 12, *1,* 1-13

318. Parvathavarthini, N., Dayal, R. K. and Gnanamoorthy, J. B.: *Influence of prior deformation on the sensitization of AISI type 316LN stainless steel*, Journal of Nuclear Materials (1994) 208, 251-258

319. Wasnik, D. N., Dey, G. K., Kain, V. and Samajdar, I.: *Precipitation stages in a 316L austenitic stainless steel*, Scripta Materialia (2003) 49, 135-141

320. Kiuchi, K., Kikuchi, M. and Kondo, T.: *A new type of low temperature sensitization of austenitic stainless steels enhanced with defect-solute interactions*, Journal of Nuclear Materials (1991) 179-181, 481-484

321. Figueroa, C. A., Weber, S., Czerwiec, T. and Alvarez, F.: *Oxygen, hydrogen, and deuterium effects on plasma nitriding of metal alloys*, Scripta Materialia (2006) 54, 1335-1338

322. Baldwin, M. J., Haydon, S. C. and Fewell, M. P.: *Metastable states and nitriding plasmas*, Surface and Coatings Technology (1997) 97, *1-3,* 97-101

323. Walkowicz, J.: *On the mechanisms of diode plasma nitriding in N2-H2 mixtures under DC-pulsed substrate biasing*, Surface and Coatings Technology (2003) 174-175, 1211-1219

324. Rusnak, K. and Vicek, J.: *Emission spectroscopy of the plasma in the cathode region of N2-H2 abnormal glow discharges for steel surface nitriding*, Journal of Physics D: Applied Physics (1993) 26, *4,* 585-589

325. Ricard, A.: *Production of active plasma species for surface treatments*, Journal of Physics D: Applied Physics (1997) 30, *16,* 2261-2269

326. Ricard, A., Czerwiec, T., Belmonte, T., Bockel, S. and Michel, H.: *Detection by emission spectroscopy of active species in plasma-surface processes*, Thin Solid Films (1999) 341, *1-2,* 1-8

327. Walkowicz, J., Smolik, J. and Miernik, K.: *Research on physico-chemical bases of the ion nitriding process control with the use of plasma spectroscopic diagnostics*, Vacuum (2000) 56, *1,* 63-69

328. Loureiro, J. and Ricard, A.: *Electron and vibrational kinetics in an N2-H2 glow discharge with application to surface processes*, Journal of Physics D: Applied Physics (1993) 26, *2,* 163-176

329. Ferreira, C. M., Gordiets, B. F. and Tatarova, E.: *Kinetic theory of low-temperature plasmas in molecular gases*, Plasma Physics and Controlled Fusion (2000) 42, *12B,* B165-B188

330. Bastien, F., Wu, J. H., Goguillon, P. and Marode, E.: *Mechanism of a nitrogen abnormal glow discharge. Computation and measurements of the spatial light distribution*, Journal of Physics D: Applied Physics (1990) 23, *7,* 813-822

331. Gordiets, B. F., Ferreira, C. M., Pinheiro, M. J. and Ricard, A.: *Self-consistent kinetic model of low-pressure N2-H2 flowing discharges: I. Volume processes*, Plasma Sources Science and Technology (1998) 7, *3,* 363-378

332. Rie, K.-T., Menthe, E. and Wohle, J.: *Optimization and control of a plasma carburizing process by means of optical emission spectroscopy*, Surface and Coatings Technology (1998) 98, *1-3,* 1192-1198

333. Pastol, A. and Catherine, Y.: *Optical emission spectroscopy for diagnostic and monitoring of CH4 plasmas used for a-C.H deposition*, Journal of Physics D: Applied Physics (1990) 23, *7,* 799-805

334. Catherine, Y., Pastol, A., Athouel, L. and Fourrier, C.: *Diagnostics of CH4 plasmas used for diamond-like carbon deposition*, IEEE Transactions on Plasma Science (1990) 18, *6,* 923-929

335. Schulz-von der Gathen, V., Ropcke, J., Gans, T., Kaning, M., Lukas, C. and Dobele, H. F.: *Diagnostic studies of species concentrations in a capacitively coupled RF plasma containing CH4-H2-Ar*, Plasma Sources Science and Technology (2001) 10, *3,* 530-539

336. Heintze, M., Magureanu, M. and Kettlitz, M.: *Mechanism of C2 hydrocarbon formation from methane in a pulsed microwave plasma*, Journal of Applied Physics (2002) 92, *12,* 7022-7031

337. Menningen, K. L., Childs, M. A., Toyoda, H., Ueda, Y., Anderson, L. W. and Lawler, J. E.: *CH3 and CH densities in a diamond growth DC discharge*, Contributions to Plasma Physics (1995) 35, *4-5,* 359-373

338. Wolden, C. A. and Gleason, K. K.: *On the pressure limits of diamond chemical vapor deposition*, Diamond and Related Materials (1996) 5, *12,* 1503-1508

339. Teii, K., Ito, H., Hori, M., Takeo, T. and Goto, T.: *Kinetics and role of C, O, and OH in low-pressure nanocrystalline diamond growth*, Journal of Applied Physics (2000) 87, *9,* 4572-4579

340. Atkins, P. W.: *Phisical chemistry*, 3rd Ed. (1986) Oxford University Press

341. Escobar-Alarcon, L., Arrieta, A., Camps, E., Romero, S., Muhl, S. and Camacho-Lopez, M. A.: *a-CN thin film properties as a function of laser ablation plasma parameters*, Diamond and Related Materials (2007) 16, *4-7,* 1291-1294

342. Walkowicz, J., Supiot, P., Smolik, J. and Grushin, M.: *The influence of the N2-H2 mixture composition on the spectroscopic and temporal behaviour of glow discharge characteristics in pulse-supplied nitriding processes*, Surface and Coatings Technology (2004) 180-181, 407-412

343. Cleugh, D.: *Plasma species analysis for in situ assessment of surface treatments*, Surface Engineering (2002) 18, *2,* 133-139

344. Kim, Y. M., U., K. J. and Han, J. G.: *Investigation on the pulsed DC plasma nitriding with optical emission spectroscopy*, Surface and Coatings Technology (2002) 151-152, 227-232

345. Kim, Y.-K., Baek, J.-M. and Lee, K.-H.: *Plasma diagnostics of pulsed d.c. glow discharge combined with ICP for deep nitriding process*, Surface and Coatings Technology (2001) 142-144, 321-327

346. Kulakowska-Pawlak, B. and Zyrnicki, W.: *Spectroscopic investigations into plasma used for nitriding processes of steel and titanium*, Thin Solid Films (1993) 230, *2,* 115-120

347. Hugon, R., Henrion, G. and Fabry, M.: *Diagnostics of a DC pulsed-plasma assisted nitriding process*, Surface and Coatings Technology (1993) 59, *1-3,* 82-85

348. Behringer, K. and Fantz, U.: *Spectroscopic diagnostics of glow discharge plasmas with non-Maxwellian electron energy distributions*, Journal of Physics D: Applied Physics (1994) 27, *10,* 2128-2135

349. Richard, A., Hubert, J. and Michel, H.: *Correlations between active plasma species and steel surface nitriding in microwave post-discharge reactors*, Plasma Technology (1992)

350. Herion, G., Hugon, R., Fabry, M. and Scherentz, V.: *Reactivity of a DC-pulsed plasma: plasma diagnostics and nitrided sample analysis*, Surface and Coatings Technology (1997) 97, *1-3,* 729-733

351. Petitjean, L. and Ricard, A.: *Emission spectroscopy study of N2-H2 glow discharge for metal surface nitriding*, Journal of Applied Physics (1984) 17, *5,* 919-929

352. Lombardi, G., Hassouni, K., Benedic, F. and Mohassed, F.: *Spectroscopic diagnostics and modeling of Ar/H2/CH4 microwave discharges used for nanocrystalline diamond deposition*, Journal of Applied Physics (2004) 96, *11,* 6739-6751

353. Gordillo-Vazquez, F. J., Camero, M. and Gomez-Aleixandre, C.: *Spectroscopic measurements of the electron temperature in low pressure radiofrequency Ar/H2/C2H2 and Ar/H2/CH4 plasmas used for the synthesis of nanocarbon structures*, Plasma Sources Science and Technology (2006) 15, *1,* 42-51

354. Boffard, J. B., Lin, C. C. and DeJoseph Jr., C. A.: *Application of excitation cross sections to optical plasma diagnostics*, Journal of Physics D: Applied Physics (2004) 37, *12,* 143-161

355. Ljepojevic, N. N. and Labat, J. M.: *Selfconsistent calculation of the hydrogen plasma parameters. I. Stationary plasmas*, Journal of Physics D: Applied Physics (1982) 15, *4,* 621-629

356. Langmuir, I. and Jones, H. A.: *Collisions between electrons and gas molecules*, Physical review (1928) 31, 357-404

357. Hugon, R., Fabry, M. and Henrion, G.: *The influence of the respective durations of the discharge and the afterglow on the reactivity of a DC pulsed plasma used for iron nitriding*, Journal of Applied Physics (1996) 29, *3,* 761-768

358. Herzberg, G.: *Molecular spectra and molecular structure: III. Electronic spectra and electronic structure of polyatomic molecules*, 1st Ed. (1966) London, van Nostrand Company

359. Leyland, A., Fancey, K. S., James, A. S. and Matthews, A.: *Enhanced plasma nitriding at low pressures: a comparative study of DC and RF techniques*, Surface and Coatings Technology (1990) 41, *3,* 295-304

360. Leyland, A., Fancey, K. S. and Matthews, A.: *Plasma nitriding in a low pressure triode discharge to provide improvements in adhesion and load support for wear resistant coatings*, Surface Engineering (1991) 7, *3,* 207-215

361. Michel, H., Czerwiec, T., Gantois, M., Ablitzer, D. and Ricard, A.: *Progress in the analysis of the mechanisms of ion nitriding*, Surface and Coatings Technology (1995) 72, *1-2,* 103-111

362. Andreu, J., Sardin, G., Esteve, J. and Morenza, J. L.: *Electrostatic confinement effects on a hot cathode DC glow discharge in silane*, Journal of Physics D: Applied Physics (1987) 20, *11,* 1479-1483

363. Spielman, R. B., DeGroot, J. S. and Rasmussen, D. A.: *An improved low-pressure DC discharge*, Journal of Applied Physics (1976) 47, *5,* 1909-1911

364. Rozsa, K., Janossy, M., Bergou, J. and Csillag, L.: *Noble gas mixture CW hollow cathode laser with internal anode system*, Optics communications (1977) 23, *1,* 15-18

365. Arslanbekov, R. R., Kudryavtsev, A. A. and Movtchan, I. A.: *Cage discharge: theory and experiment*, IEEE Transactions on Plasma Science (1996) 24, *3,* 1079-1094

366. Arslanbekov, R. R., Kudryavtsev, A. A. and Tobin, R. C.: *On the hollow-cathode effect: conventional and modified geometry*, Plasma Sources Science and Technology (1998) 7, *3,* 310-322

367. Major, F. G., Gheorghe, V. N. and Werth, G.: *Charged particle traps: physics and techniques of charged particle field confinement*, 1st Ed. (2004) Berlin, Springer

368. Ingram, S. G. and Braithwaite, N. S. J.: *Ion and electron energy analysis at a surface in an RF discharge*, Journal of Physics D: Applied Physics (1988) 21, *10,* 1496-1503

369. Muratore, C., Walton, S. G., Leonhardt, D., Fernsler, R. F., Blackwell, D. D. and Meger, R. A.: *Effect of plasma flux composition on the nitriding rate of stainless steel*, Journal of Vacuum Science and Technology (2004) A22, *4,* 1530-1535

370. Kuppusami, P., Sundararaman, D. and Raghunathan, V. S.: *Comparative study of plasma nitriding behaviour of a type 316 stainless steel and a microalloyed steel*, Surface Engineering (1993) 9, *2,* 137-141

371. Wells, A. and Strydom, I. l. R.: *Influence of sputtering and redeposition on compound layer growth during plasma nitriding*, Surface Engineering (1988) 4, *1,* 55-59

372. Korhonen, A. S., Molarius, J. M. and Sulonen, M. S.: *Plasma processing in nitrogen containing atmospheres: 10 years' development*, Surface Engineering (1988) 4, *1,* 44-50

373. Hubbard, P., McCulloch, D. G., Doyle, E. D., Dowey, S. J. and Georges, J. N.: *A fundamental contribution to a study of the active screen plasma nitriding process*, IFHTSE (2006) Vienna, Austria,

374. de Sousa, R. R. M., de Araujo, F. O., Ribeiro, K. J. B., Dumelow, T., P., d. C. J. A. and Alves, C. J.: *Ionic nitriding in cathodic cage of AISI 420 martensitic stainless steel*, Surface Engineering (2008) 24, *1,* 52-56

375. Ahangarani, S., Sabour, A. R. and Mahboubi, F.: *Surface modification of 30CrNiMo8 low-alloy steel by active screen setup and conventional plasma nitriding methods*, Applied Surface Science (2007) 254, *5,* 1427-1435

376. Cleugh, D.: *Effects of Rare Earth additions on plasma nitriding of EN40B steel*, PhD thesis (2003) Metallurgy and Materials - University of Birmingham

377. Doyle, E., Dowey, S., Hubbard, P. and McCulloch, D.: *A study of key processing parameters in the active screen plasma nitriding (ASPN) of steels*, IFHTSE (2005) Riva-Del Garda, Italy,

378. Ahangarani, S., Mahboubi, F. and Sabour, A. R.: *Effects of various nitriding parameters on active screen nitriding behaviour of a low alloy steel*, Vacuum (2006) 80, *9,* 1032-1037

379. Doyle, E., Wong, Y., Dowey, S., Cairney, J. and Munroe, P.: *Nitriding response of high speed steels using active screen plasma nitriding (ASPN)*, IFHTSE (2005) Riva-Del Garda, Italy,

380. Czerwiec, T., Michel, H. and Bergmann, E.: *Low-pressure, high-density plasma nitriding: mechanisms, technology and results*, Surface and Coatings Technology (1998) 108-109, 182-190

381. Hudis, M.: *Study of ion-nitriding*, Journal of Applied Physics (1973) 44, *4,* 1489-1496

382. Tibbets, G. G.: *Role of nitrogen atoms in "ion-nitriding"*, Journal of Applied Physics (1974) 45, *11,* 5072-5073

383. Brokman, A. and Tuler, F. R.: *A study of the mechanisms of ion nitriding by the application of a magnetic field*, Journal of Applied Physics (1981) 52, *1,* 468-471

384. Li, J. L., O'Keefe, T. J. and James, W. J.: *Iron carbide films formed by plasma deposition and plasma carburizing*, Materials Science and Engineering B: Solid-State Materials for Advanced Technology (1990) B7, 15-23

385. Edenhofer, B., Grafen, W. and Muller-Ziller, J.: *Plasma-carburising - A surface heat treatment process for the new century*, Surface and Coatings Technology (2001) 142-144, 225-234

386. Lampe, T., Eisenberg, S. and Laudien, G.: *Compound layer formation during plasma nitriding and plasma nitrocarburising*, Surface Engineering (1993) 9, *1,* 69-76

387. Li, S. and Manory, R. R.: *Comparison of compound layer nucleation mechanisms in plasma nitriding and nitrocarburizing: the effect of CHn species*, Journal of Materials Science (1999) 34, *5,* 1045-1049

388. Jauberteau, I., Cinelli, M. J., Cahoreau, M., Jauberteau, J. L. and Aubreton, J.: *Expanding microwave plasma for steel carburizing: role of the plasma impinging species on the steel surface reactivity*, Journal of Vacuum Science and Technology (2000) A18, *1,* 108-114

Table 2.3-1: Typical commercial ASS compositions [4]

AISI type / Element	Composition [wt%]						
	301	302	304	310	316	321	347
C	0.15 max	0.08 max	0.08 max	0.25 max	0.08 max	0.08 max	0.08 max
N	0.03	0.03	0.03	0.03	0.03	0.03	0.03
Cr	16-18	17-19	18-20	24-26	16-18	17-19	17-19
Ni	6-8	8-10	8-12	19-22	10-14	9-12	9-13
Mo					2-4		
Ti						5x %C	
Nb							10x %C
Mn	1.50	1.50	1.50	1.50	1.50	1.50	1.50

Table 2.3-2: Tentative list of precipitates significant to ASS [23]

Precipitate	Structure	Parameters [nm]	Composition
NbC	fcc	a = 0.447	NbC
NbN	fcc	a = 0.440	NbN
TiC	fcc	a = 0.433	TiC
TiN	fcc	a = 0.424	TiN
Z phase	tetragonal	a = 0.3037, c = 0.7391	CrNbN
$M_{23}C_6$	fcc	a = 1.057 – 1.068	$Cr_{16}Fe_5Mo_2C_6$ (e.g.)
M_6C	diamond cubic	a = 1.062 – 1.128	$(FeCr)_{2\ 1}Mo_3C$, Fe_3Nb_3C, M_6S
σ phase	tetragonal	A = 0.880, c = 0.454	Fe – Ni – Cr – Mo
Laves phase	hexagonal	a = 0.473, c = 0.772	Fe_2Mo, Fe_2Nb
χ phase	bcc	a = 0.8807 – 0.8878	$Fe_{36}Cr_{12}Mo_{10}$
G phase	fcc	a = 1.12	$Ni_{16}Nb_6Si_7$, $Ni_{16}Ti_6Si_7$

Table 3.1-1: Commercial specification and chemical composition of the samples

Element	C	Cr	Fe	Mn	Mo	N	Ni	S	P	Si
Commercial specification	0.08 max	16.00 18.00	balance	2.00 max	2.00 3.00	0.10 max	10.00 14.00	0.03 max	0.04 max	0.75 max
Samples	0.06	17.20	66.90	1.30	2.20	-	11.70	0.014	0.026	0.60

Table 3.2-1: DC carburising and nitriding treatment conditions

Treatment	Temperature	time	Gas composition			Pressure
			H_2	N_2	CH_4	
DC Nitriding	400ºC	10 h	75%	25%	-	500 Pa
DC Carburising	450ºC	10 h	97%	-	3%	500 Pa

Table 3.2-2: ASPC assessed treatment conditions

T = 450°C t = 10 h Gas = H_2-3%CH_4		Pressure range [Pa]				
		30	80	125	250	400
Bias level [%]	0	•		•		•
	5	•	•	•	•	•
	10	•		•	•	
	15	•	•	•	•	•
	20	•		•		
	25	•	•			

$$Bias[\%] = \frac{Applied \cdot power[kVA]}{15kVA} \cdot 100$$

Table 3.2-3: ASPN assessed treatment conditions

T = 400°C t = 10 h Gas = H_2-25%N_2		Pressure range [Pa]					
		30	75	100	125	150	250
Bias level [%]	0	•					
	5	•					
	10		•	•	•	•	•

$$Bias[\%] = \frac{Applied \cdot power[kVA]}{15kVA} \cdot 100$$

Table 3.2-4: Active screen mechanisms: assessed treatment conditions

T = 450°C / 420°C P = 400 Pa t = 10 h		Pressure range [Pa]			
		DC	FP	AS_{sh}	AS_{bh}
Treatment	Carburising	•	•	•	•
	N_2 enhanced carburising	•	•	•	•
	Nitriding	•	•	•	•

Notation: DC - Direct Current; FP - Floating Potential; AS_{sh} - Active Screen mesh with small holes (Ø= 8mm); AS_{bh} – Active Screen mesh with large holes (Ø= 25.4mm)

Table 3.3-1: Instrumented hardness settings

Variable	Value
Type of experiment	Depth vs. Load
Type of indentor	Berkovich pyramid
Initial load	0.01 mN
Maximum load	200.00 mN
Loading rate	5 mN/s
Dwell at maximum load	5 s
Displacement between indents	x=25 μm, y=15 μm
Thermal drift correction	Enabled

Table 3.3-2: Stylus profilometer settings for different measurements

Parameter	Roughness	Wear track	RS bending discs
Filter	Gaussian	2CR	2CR
λ_c	0.8 mm	2.5 mm	0.8 mm
E length / S length	5.0 mm	2.5 mm	25.0 mm
R speed = M speed	0.5 mm	0.5 mm	0.5 mm
Standard	ISO / BS	ANSI / JIS 82	ANSI / JIS 82
Data	R_a / R_y / R_z	PPFL	PPFL
Tip radius	2 µm	2 µm	2 µm

Table 3.3-3: AFM settings

Tip	
Height	2.5 µm - 3.5 µm
Front and side angles	35°
Tip radius	20 nm
Cantilever	
Material	Silicon nitride
Top layer	Au (60 nm)
Shape	Triangular
Length	180 µm
Width	33 µm
Elastic constant	0.12 N/m

Table 3.3-4: XRD settings

Variable	Value
Scan – Detector arrangement	θ - 2θ
Step size [2θ]	0.02°
Scan step time [s]	1.00 s
Scan type	Continuous
Anode material	Cu
Generator settings	40 kV, 40 mA
Used wavelength ($K_{\alpha 1}$)	1.540 Å

Table 3.3-5: SEM and EBSD camera settings for COM

Microscope	
Acceleration Voltage	20 kV
OL Aperture	3
Probe current	110 µA (12)
Working distance	15 mm
Tilt angle	70º
Map	
Crystal map size	512 pixels x 512 pixels
EBSD Camera	
Acquisition mode	Live
Sensitivity	High
Integration time*	54 ms
Video gain*	8
Background	
Average frames	10
Smooth filter size	11 x 11
Background correction	Division
Solver set up	
Minimum indexed bands	4
Maximum solution error	5
Depth of search for solution	Optimum
Hough resolution	High accuracy
Filter size	9 (Def)
Detect minimum number of bands	5
Hough radius	48
Min relative intensity	0.10
Reflective planes	37
Texture	{001} <110>

* The values here reported are approximate as these parameters are sample sensitive, and were altered in each case.

Table 3.4-1: Composition and properties of WC-Co binder bearing balls used for wear and friction tests

Composition	
Tungsten Carbide	93 - 95%
Cobalt	5 - 7%
Typical properties	
Hardness	90.5 - 91.5 HRA
Transverse Rupture Strength @ 20°C	2600 N/mm^2
Fracture Toughness Kc @ 20°C	12 $MN/m^{1/2}$
Compressive Strength @ 20°C	6200 N/mm^2
Poisson's Ratio	0.22
Magnetic Properties	Slightly Magnetic

Table 3.6-1: Optronic Labs OL 730-9Q reflex telescope - Technical specifications

Variable	Value
Lens type	Fused silica
Focal length	203 mm
Clear aperture	Φ = 60 mm
Focus (nominal)	85 cm to ∞
Field of view apertures	1.5, 3 and 5 mm
Field of view at ∞ (nominal)	0.5º, 1.0º and 1.5º
Minimum source diameter @ 85 cm	20 mm approximately
Wavelength range	250 nm - 2500 nm

Table 3.6-2: Jobin Yvon Triax 180 monochromator - Technical specifications

Variable	Value
Focal length	190 mm
Entrance aperture ratio	f / 3.9
Grating size	50 mm x 50 mm
Image magnification at exit	1.00
Scanning range*	0 nm - 1400 nm
Spectral dispersion*	3.53 nm / mm
Spectral resolution*	0.3 nm @ 500 nm
Wavelength positioning accuracy	+ / - 0.3 nm
Wavelength repeatability	0.06 nm
Wavelength drive step size*	0.06 nm

*with 1200 gr/mm grating

Table 3.6-3: Jobin Yvon Spectrum ONE detector and CCD 3000 controller unit specifications

Variable	Value
Detector type	CCD
Sensor array	1024 pixels x 256 pixels
Cooling method	Thermoelectric (Peltier)
Operating temperature	-30ºC
ADC limit	16 bit
Controller speed	166 kHz

Table 3.6-4: OES calibration conditions

Variable	Value
Integration time	0.1 s
Slit width	0.013 mm
Grating	1200 gr/mm
Dark offset CCD correction	Enabled

Table 4.1-1: Constants of equations (4.1-1) to (4.1-3) depending on the gas mixture

Gas mixture	k_1	k_2	k_3
3% CH_4 - 97% H_2	89.04	0.3182	1.45
25% N_2 - 75% H_2	82.22	0.3357	1.72

Table 4.1-2: ASPC layer thickness (GDOES) after treatment under different conditions

ASPC T = 450°C, t = 10 h 3%CH_4 – 97%H_2		Pressure [Pa]				
		30	80	125	250	400
Bias level [%]	0	0.5 µm		0.5 µm		0.5 µm
	5	14.0 µm		16.5 µm	2.0 µm	0.5 µm
	10	14.0 µm		17.0 µm	9.0 µm	
	15	14.0 µm	16.0 µm	20.0 µm	13.0 µm	0.75 µm
	20	14.0 µm		16.0 µm		
	25	14.0 µm	18.0 µm			

$$Bias[\%] = \frac{Applied \cdot power[kVA]}{15kVA} \cdot 100$$

Table 4.1-3: ASPN layer thickness (SEM) after treatment under different conditions

ASPN T = 400°C, t = 10 h 25%N_2 – 75%H_2		Pressure [Pa]					
		30	75	100	125	150	250
Bias level [%]	0	6.2 µm					
	5	6.5 µm					
	10		6.6 µm	5.8 µm	5.2 µm	5.4 µm	5.0 µm

$$Bias[\%] = \frac{Applied \cdot power[kVA]}{15kVA} \cdot 100$$

Table 4.1-4: Mean residual stresses measured from the bending of thin discs after ASPC

Condition	Layer thickness	Disc thickness	Maximum Deflection	Radius of curvature	Stoney [BS]	Mèzin et al	Wang et al
P030B05	14 µm	515 µm	45 µm	1.7921 m	-0.489 GPa	-0.533 GPa	-0.311 GPa
P125B15	20 µm	530 µm	90 µm	0.8962 m	-0.725 GPa	-0.815 GPa	-0.485 GPa

Note: Refer to appendix C for details on these calculations

Table 4.2-1: Instrumented indentation results from AISI 316 UT and AISI 316 PC samples

Sample	Maximum depth [nm]		Plastic depth [nm]		Hardness [GPa]		Elastic Modulus [GPa]		E/H
	Average	Std. dev.	Average	Std. dev.	Average	Std. dev.	Average	Std. dev.	
AISI 316	2,156.97	41.79	2,093.27	42.68	1.95	0.08	206.22	6.64	105.75
ASPC	1,030.46	23.96	881.72	23.77	10.54	0.59	215.91	11.97	20.48

Table 4.3-1: Roughness measured on Cu samples after treatment under different conditions

Ra [um]	DC	AS
Nitriding	0.310 µm	0.139 µm
Carburising	0.232 µm	0.187 µm
N_2 enhanced carburising	0.234 µm	0.175 µm

Table 4.4-1: Assessed conditions and summary of pin-on-disc wear results

Sample label	Pressure	Bias	Roughness	Hardness	Theoretical worn volume*	Measured worn volume
AISI 316	N/A	N/A	0.0801 µm	200.20 $HMV_{0.025}$	3.1924 mm^3	2.7130 mm^3
DCPC 400	400 Pa	N/A	0.0837 µm	837.37 $HMV_{0.025}$	0.0075 mm^3	0.0052 mm^3
ASPC 125	125 Pa	15%	0.0772 µm	866.54 $HMV_{0.025}$	0.0150 mm^3	0.0059 mm^3
ASPC 030	30 Pa	5%	0.0716 µm	857.05 $HMV_{0.025}$	0.0120 mm^3	0.0054 mm^3

*Note: the theoretical worn volume was calculated, assuming that no significant wear of the pin took place, using the following equation:

$$V = 2\pi R\left[r^2 \sin^{-1}\left(\frac{d}{2r}\right) - \left(\frac{d}{4}\right)\left(4r^2 - d^2\right)^{\frac{1}{2}}\right]$$

Table 4.4-2: Composition of wear debris (EDX) for AISI 316 UT and AISI 316 PC

Element	AISI 316	AISI 316 PC (oxide layer)
C [wt%]	7.4	1.5
O [wt%]	39.2	43.0
Cr [wt%]	9.7	10.0
Mn [wt%]	0.9	0.8
Fe [wt%]	35.8	34.0
Co [wt%]	0.4	0.2
Ni [wt%]	5.7	6.2
Mo [wt%]	0.7	0.6
W [wt%]	0.2	3.7

Table 4.4-3: Summary of results obtained on the wear debris

Wear debris	Colour	Size	Magnetic	Possible phases	
AISI 316 PC	Red / Orange	< 20 µm	No	α-Fe_2O_3	Haematite
AISI 316 UT	Black	> 20 µm	Yes	Fe_3O_4	Magnetite
				$C_{0.05}Fe_{1.95}$	Martensite

Table 4.4-4: Summary of friction results

Disc	Hardness	Roughness	Average coefficient of friction		
	[$HMV_{0.05}$]	Ra [µm]	AISI 316 ball	WC-Co ball	ASPC ball
AISI 316 UT	311.3	0.292	0.61	0.40	0.55
ASPC	837.7	0.278	1.06	0.63	0.80

Table 4.5-1: Corrosion factor for corrosion tests in boiling 16% H_2SO_4 with $CuSO_4$ for 20 hours

Samples	Corrosion factor*
DCPC 400	5.14
ASPC 125	4.29
ASPC 030	3.67

*Note: the corrosion factor was calculated according to the following equation:

$$CF = \frac{\Delta M_{treated}}{\Delta M_{AISI316}}$$

Table 5.1-1: Electric parameters in DC and AS furnaces under similar discharge conditions

Furnace	Pressure	Current	Voltage	Power
DC	400 Pa	5.0 A	550 V	2.75 kVA
AS	150 Pa	6.0 A	540 V	3.24 kVA
DC	125 Pa	2.0 A	800 V	1.60 kVA
AS	50 Pa	2.2 A	896 V	1.97 kVA

Table 5.2-1: Carbon diffusivity calculated from different treatment conditions

Treatment 450ºC – 3%CH_4	Carbon diffusivity K [cm^2 / s]
DCPC	$1.11 \cdot 10^{-10}$
ASPC P125B15	$1.11 \cdot 10^{-10}$
ASPC P030B05	$5.44 \cdot 10^{-11}$

$$x = a(Dt)^{1/2} = Kt^{1/2}$$

Table 5.2-2: Lattice expansion measured on EA from the XRD peak shift

hkl	EA lattice expansion
111	2.34%
200	3.32%
220	2.53%
311	3.02%
222	2.61%

Table 5.2-3: Parameters used for estimation of residual stresses from the instrumented indentation test

Variable	Symbol	Value
Maximum applied load	P_1	200 mN
Load at intersection point B	P_2	40 mN
Experimental constant	α	65.3º
Depth of residual indentation	h	750 nm

*Note: Refer to figure 5.2-12 for details on the variables

Table 5.5-1: Bond enthalpies [kJ / mol] [340]

	H	C	N	O
H	436			
C	412	348 (i)		
		612 (ii)		
		518 (a)		
N	388	305 (i)	163 (i)	
		613 (ii)	409 (ii)	
		890 (iii)	945 (iii)	
O	463	360 (i)		146 (i)
		743 (ii)		497 (ii)

Reference: (i) single bond, (ii) double bond, (iii) triple bond, (a) aromatic

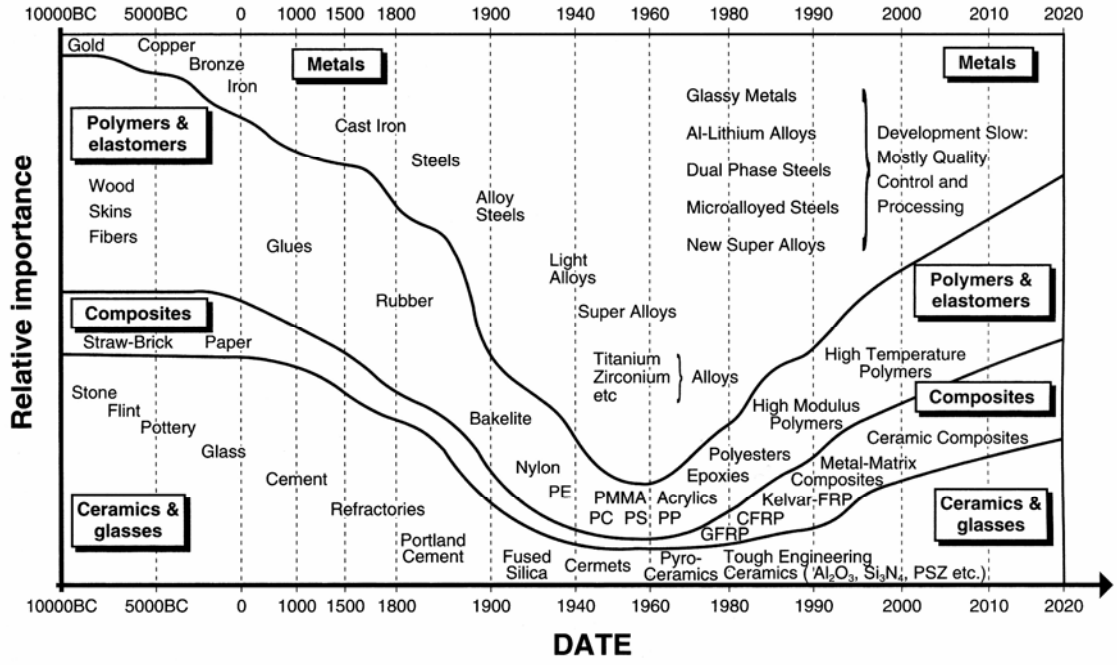

Figure 2.1.1-1: Historical evolution of materials and their relative importance [1]

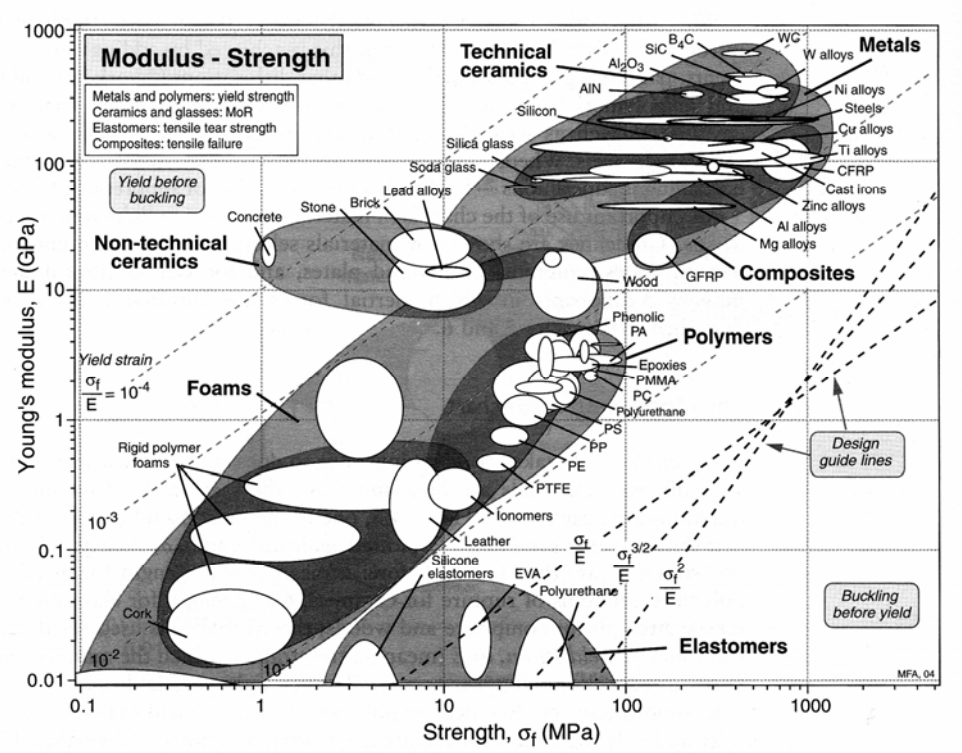

Figure 2.1.1-2: Young's modulus - Strength materials selection chart [1]

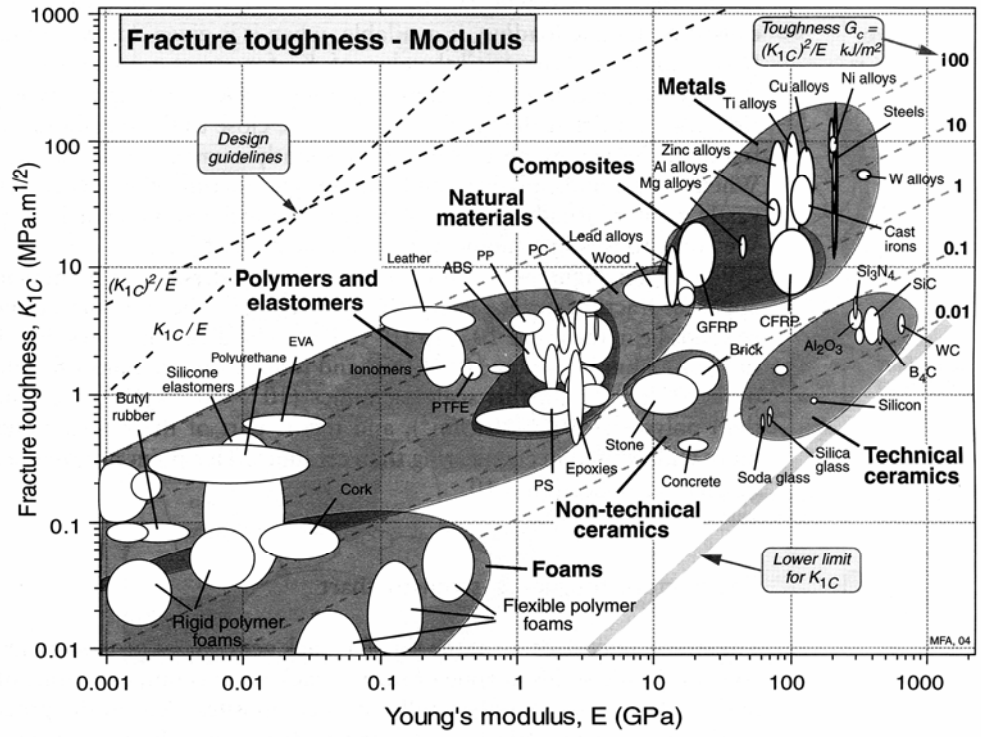

Figure 2.1.1-3: Fracture toughness – Young's modulus materials selection chart [1]

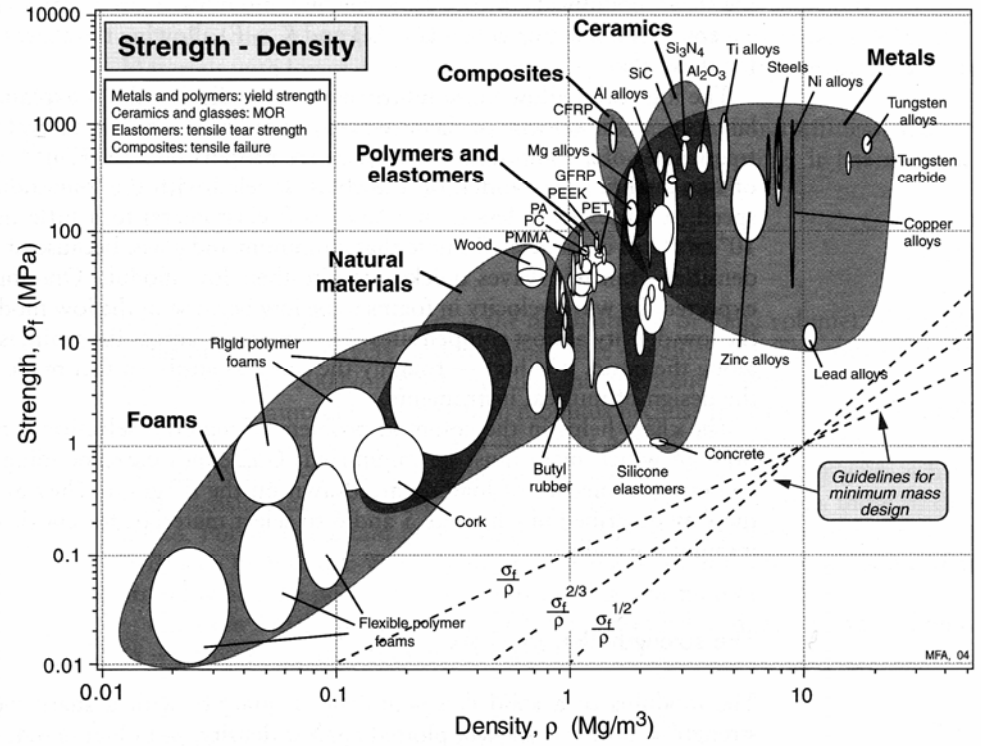

Figure 2.1.1-4: Strength - Density materials selection chart [1]

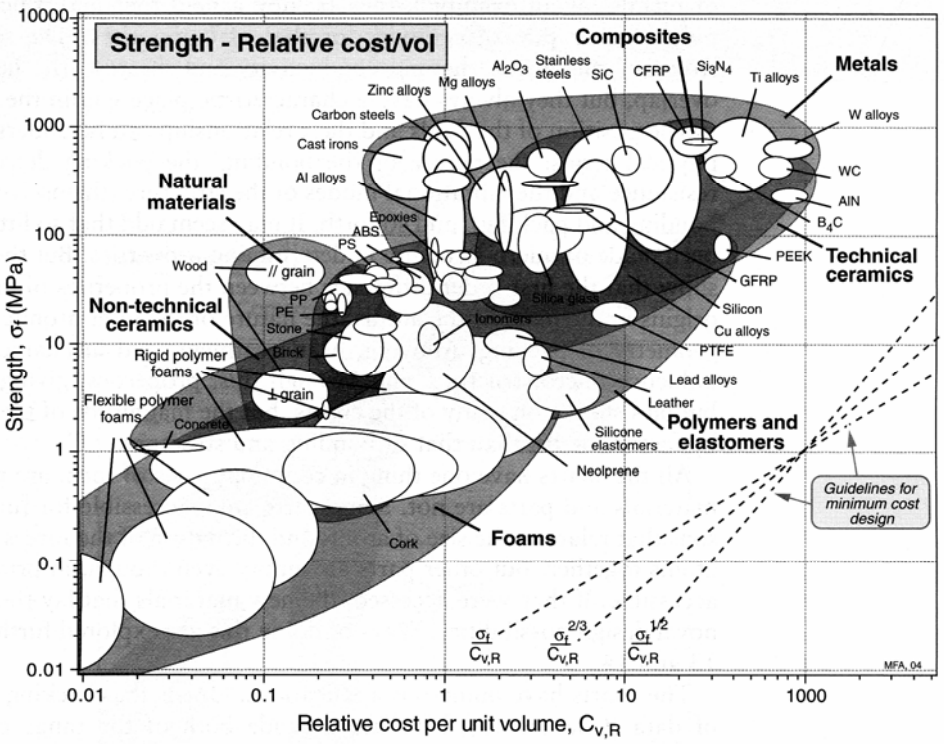

Figure 2.1.1-5: Strength - Relative cost materials selection chart [1]

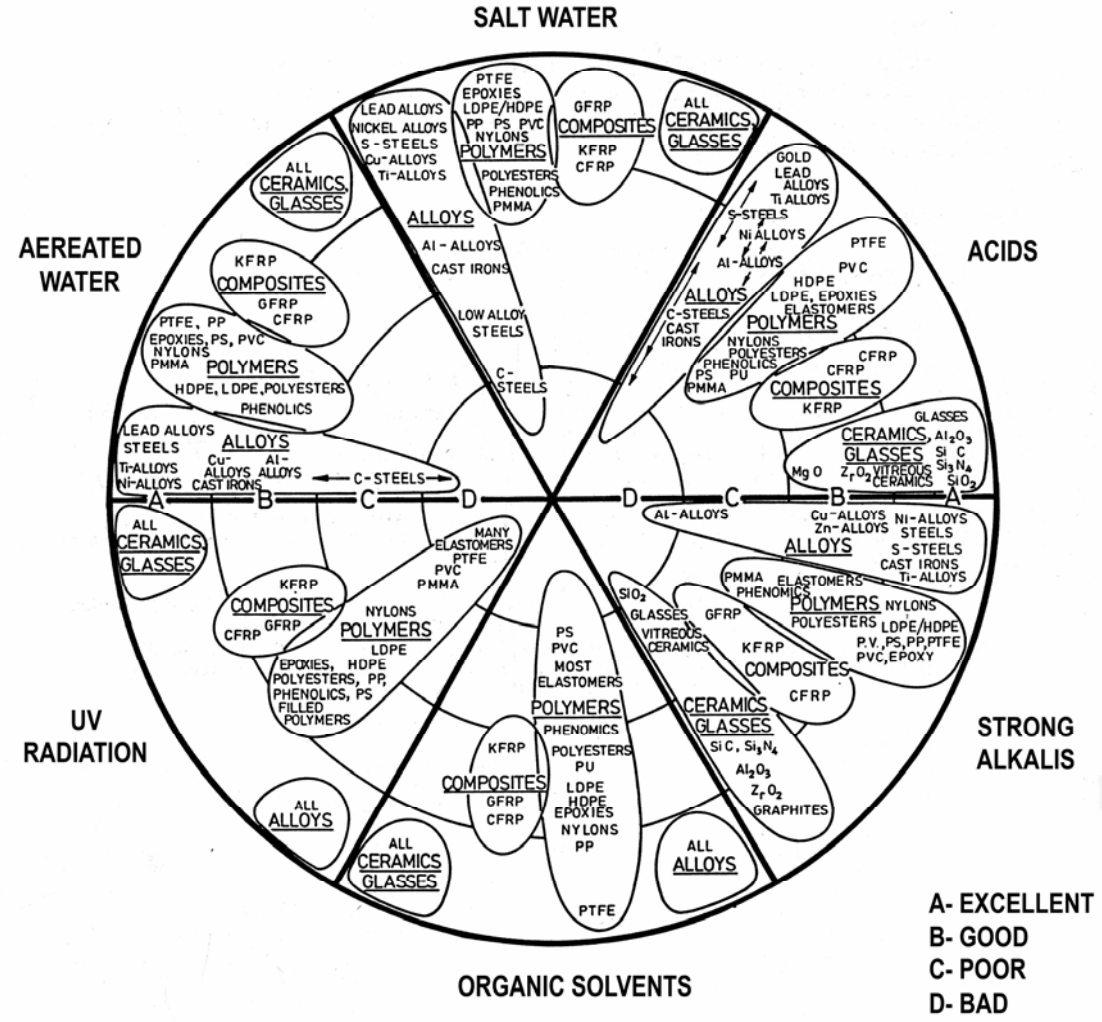

Figure 2.1.1-6: Corrosion resistance materials selection chart [1]

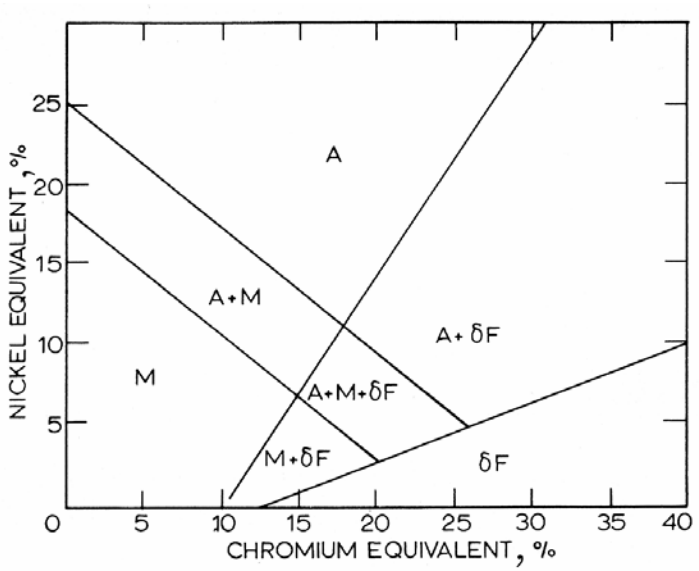

A = austenite; M = martensite; δF = delta ferrite

Figure 2.1.2-1: Schaeffler diagram for stainless steel classification [5]

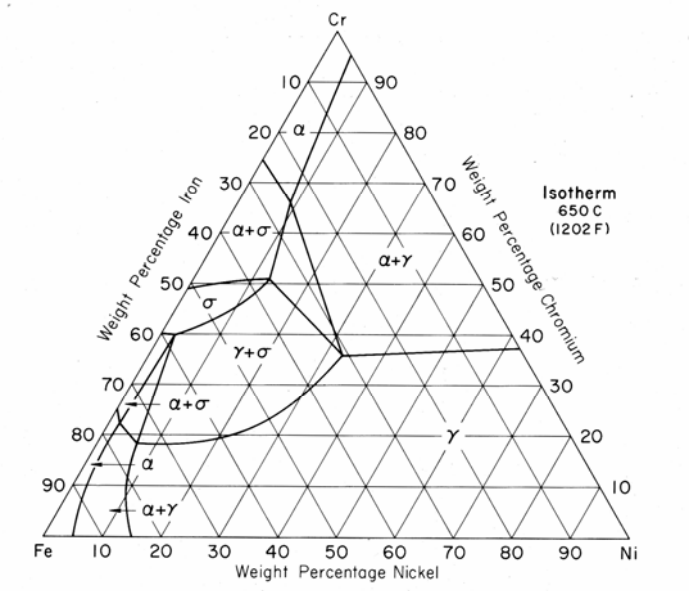

Figure 2.1.3-1: Fe-Cr-Ni ternary phase diagram [13]

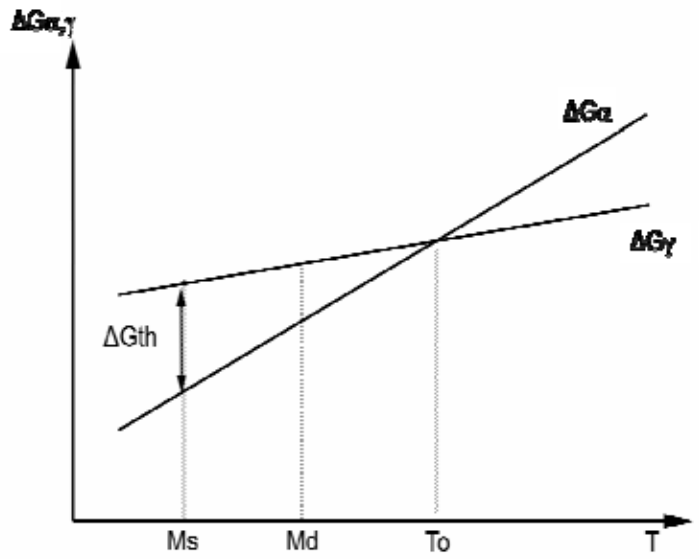

Figure 2.1.3-2: Schematics of Ms and Md for martensitic transformation in ASS [18]

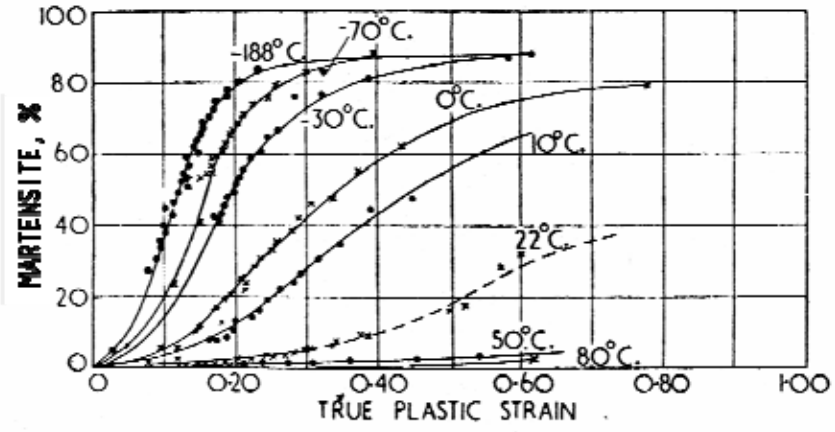

Figure 2.1.3-3: Stress induced martensitic transformation of ASS at different temperatures [16]

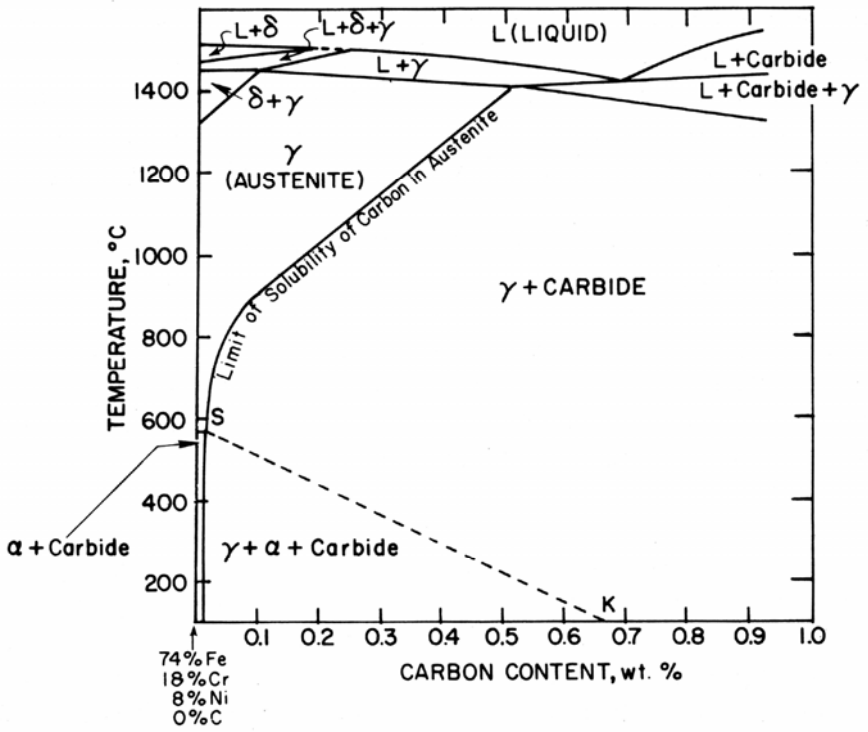

Figure 2.1.3-4: Solubility of carbon in austenitic stainless steel 18/8 [37]

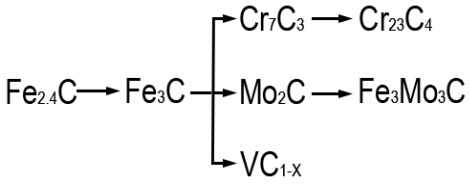

Figure 2.1.3-5: Reference carbide precipitation sequence [22]

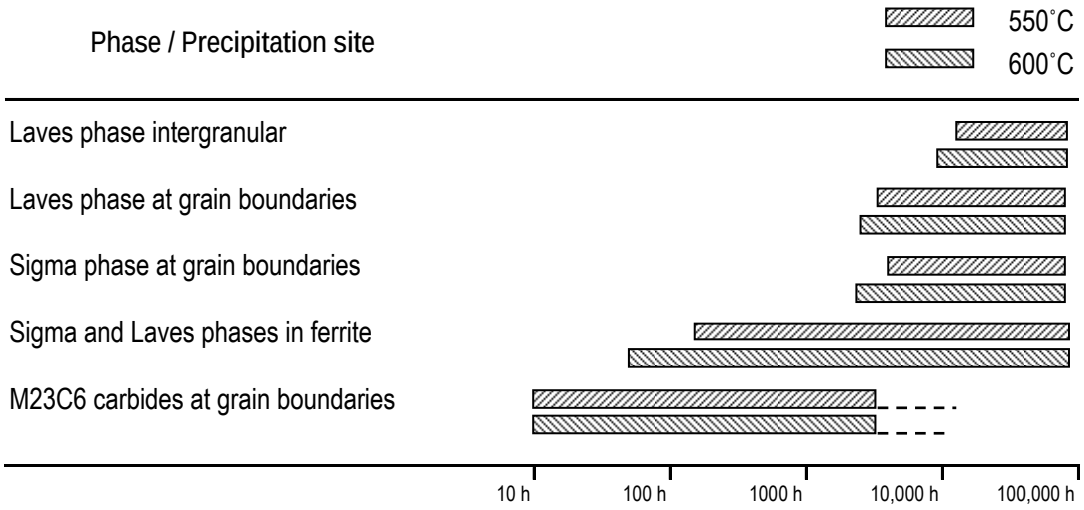

Figure 2.1.3-6: Ageing times for phase precipitation in AISI 316 at 550ºC and 600ºC [26]

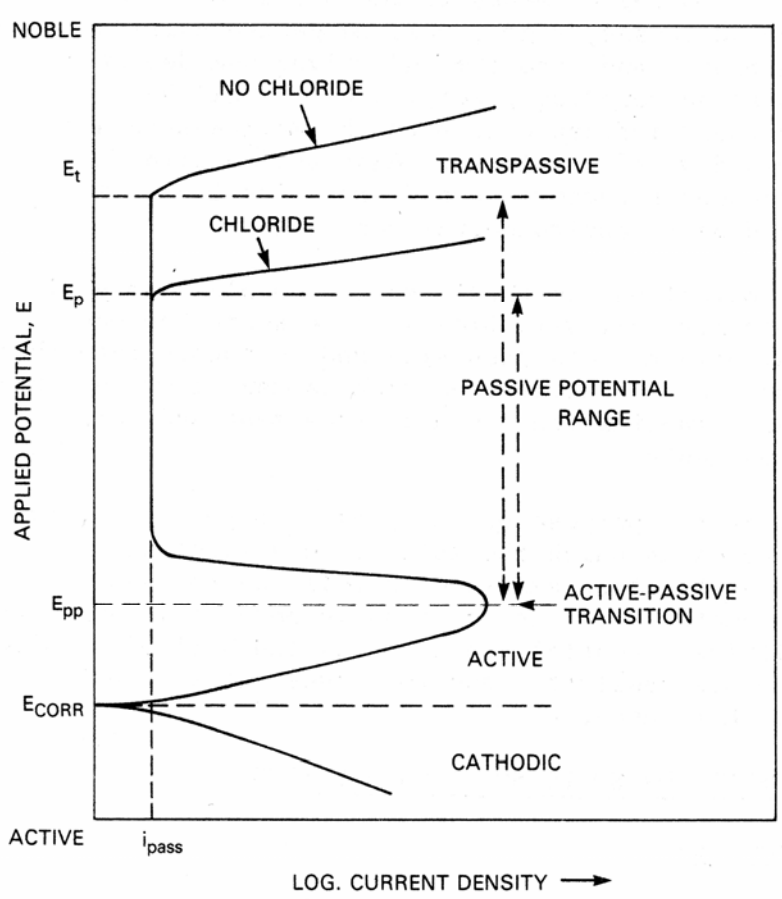

Figure 2.1.4-1: Schematics of polarisation curve of ASS in sulphuric acid [38]

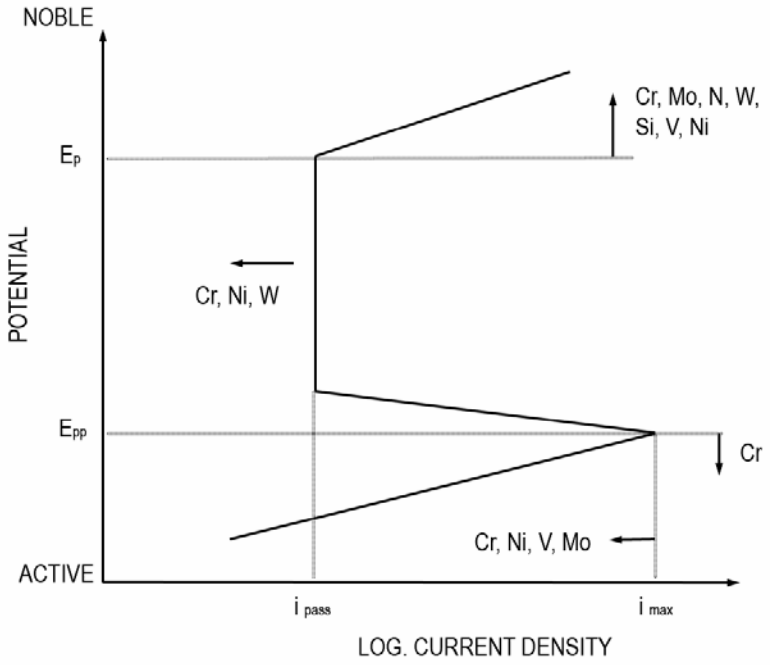

Figure 2.1.4-2: Effect of alloying elements on the polarisation curve of ASS [38]

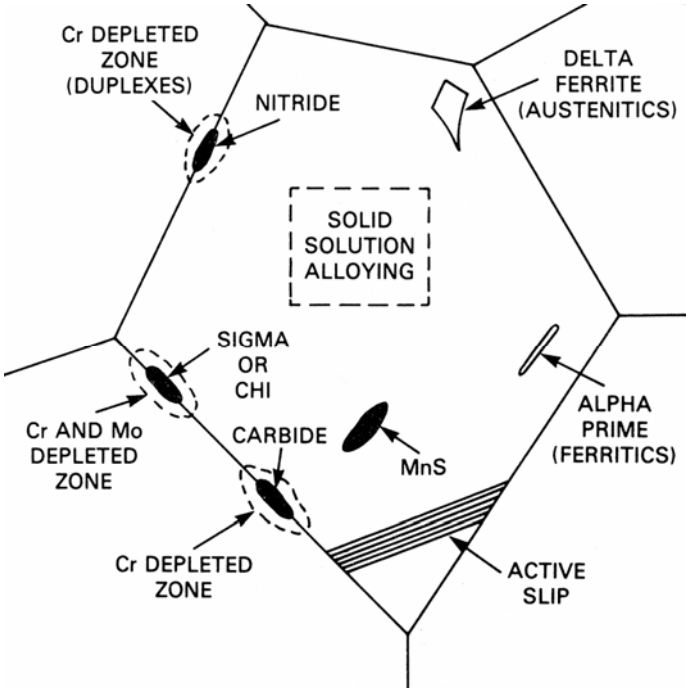

Figure 2.1.4-3: Metallurgical features detrimental to the corrosion resistance of ASS [38]

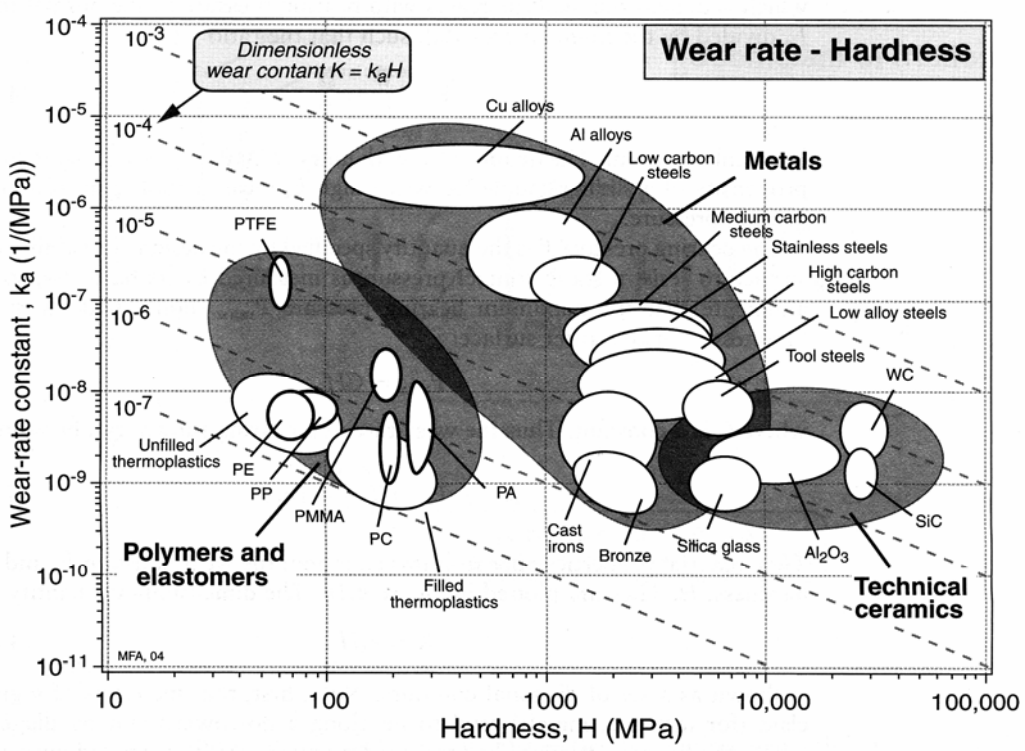

Figure 2.1.5-1: Wear resistance materials selection chart [1]

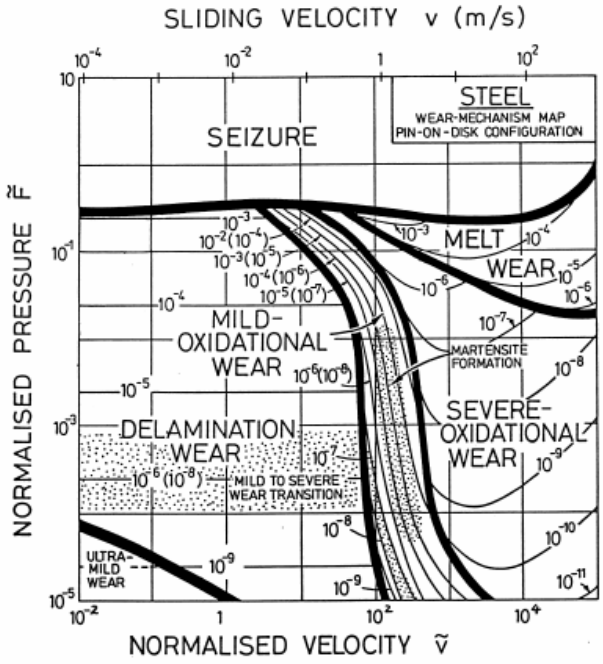

Figure 2.1.5-2: Wear rate transitions [55]

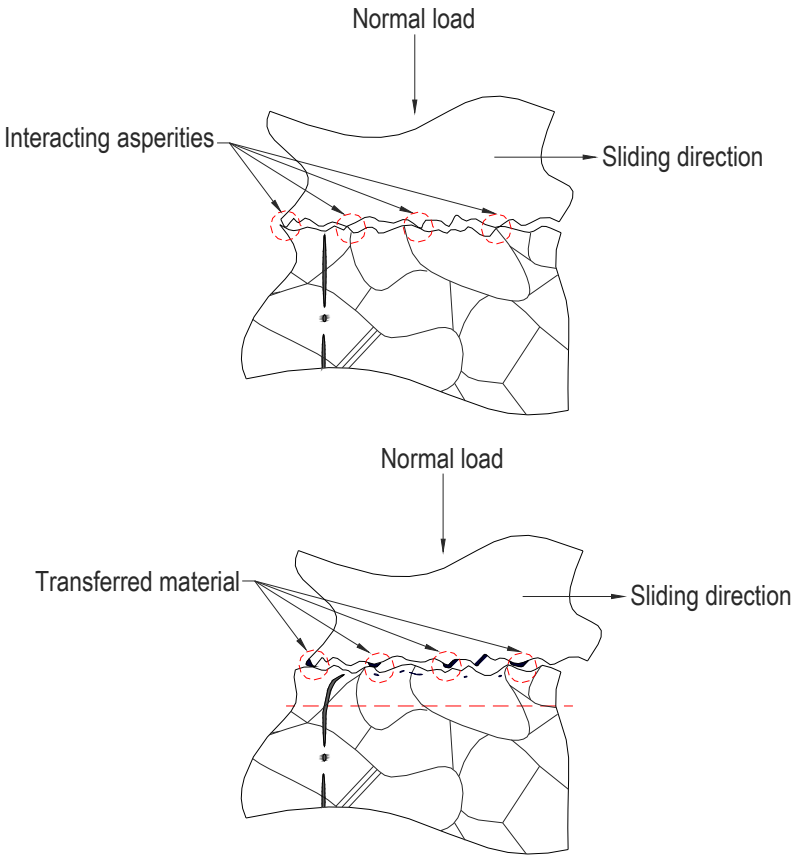

Figure 2.1.5-3: Transfer of material between interacting asperities and deformation of the subsurface

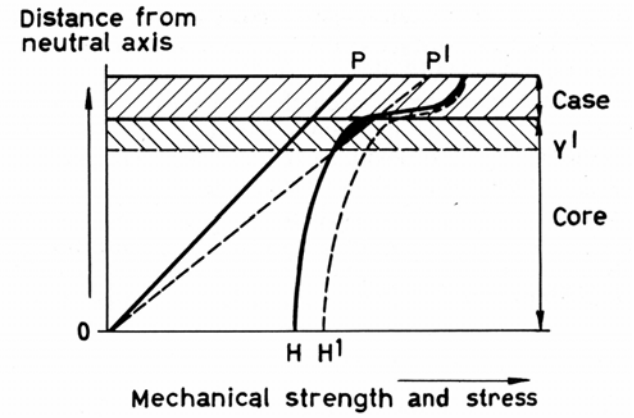

Figure 2.2.1-1: Schematic of the stress and mechanical strength diagram for a cross section of a surface engineered component between the neutral axis and the surface [88]

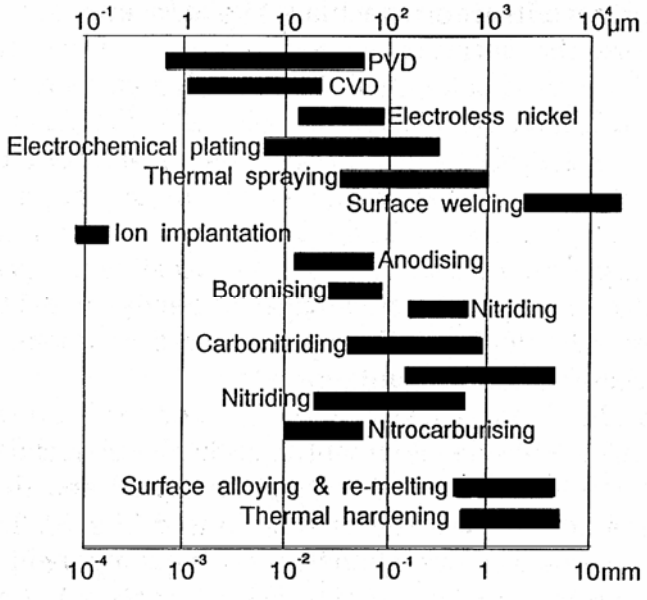

Figure 2.2.1-2: Typical thickness obtained with surface engineering processes [81]

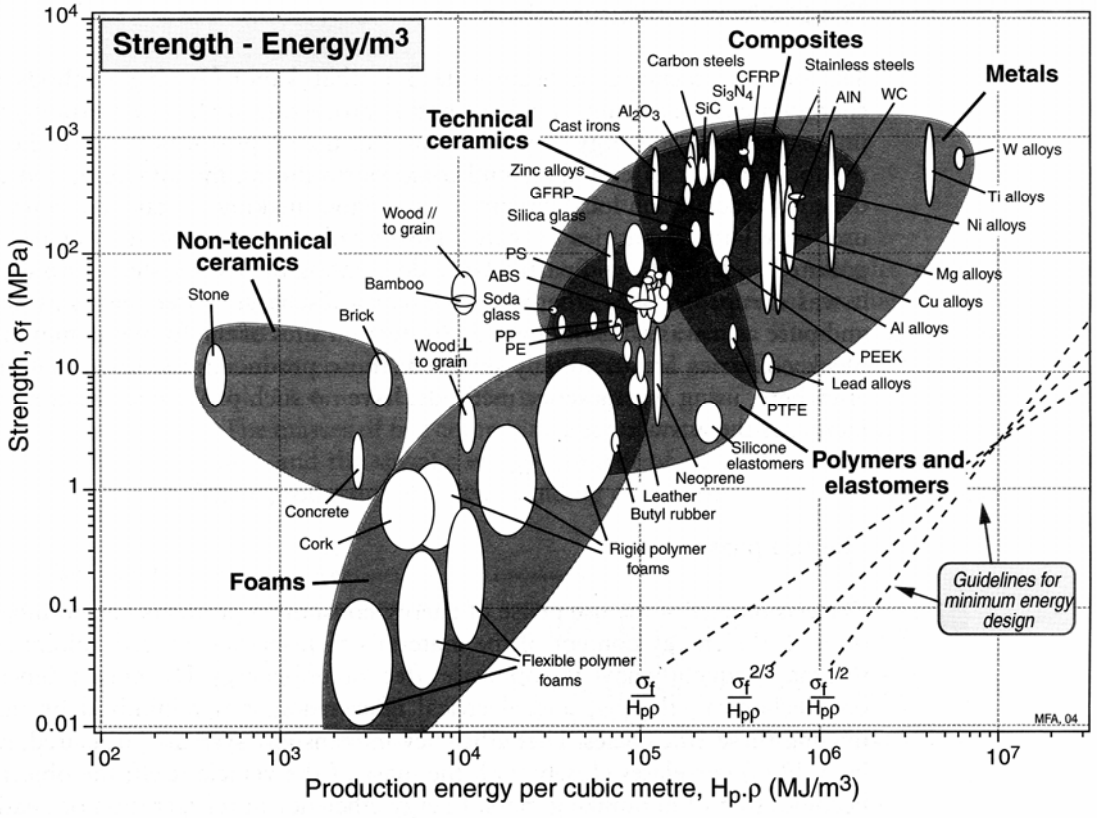

Figure 2.2.1-3: Energy content vs strength chart for different materials [1]

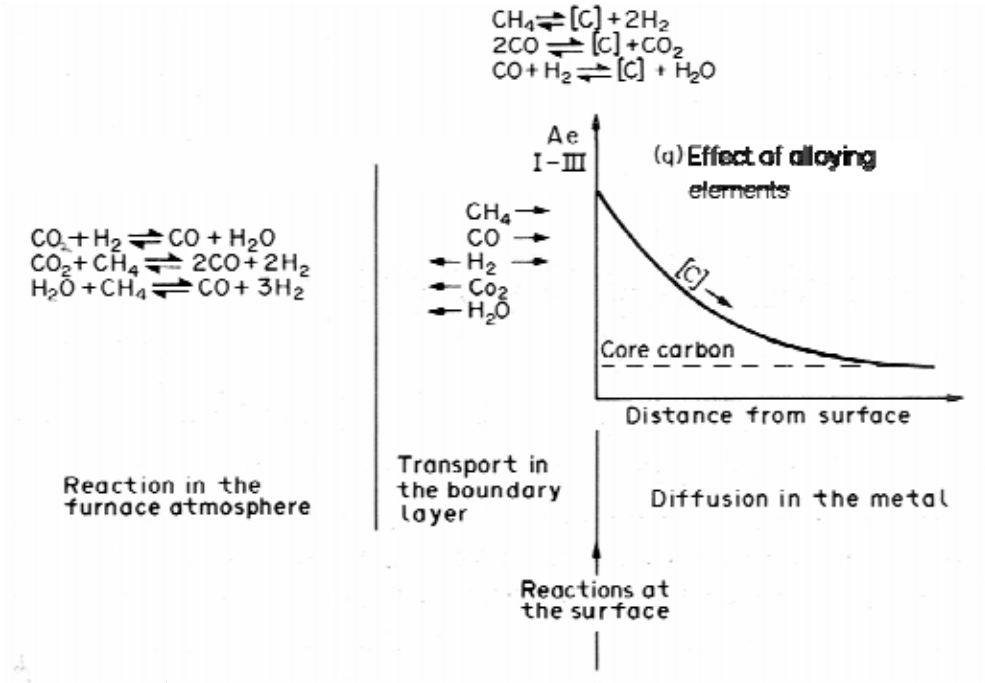

Figure 2.2.2-1: Schematic representation of the reaction steps in gas carburising [94]

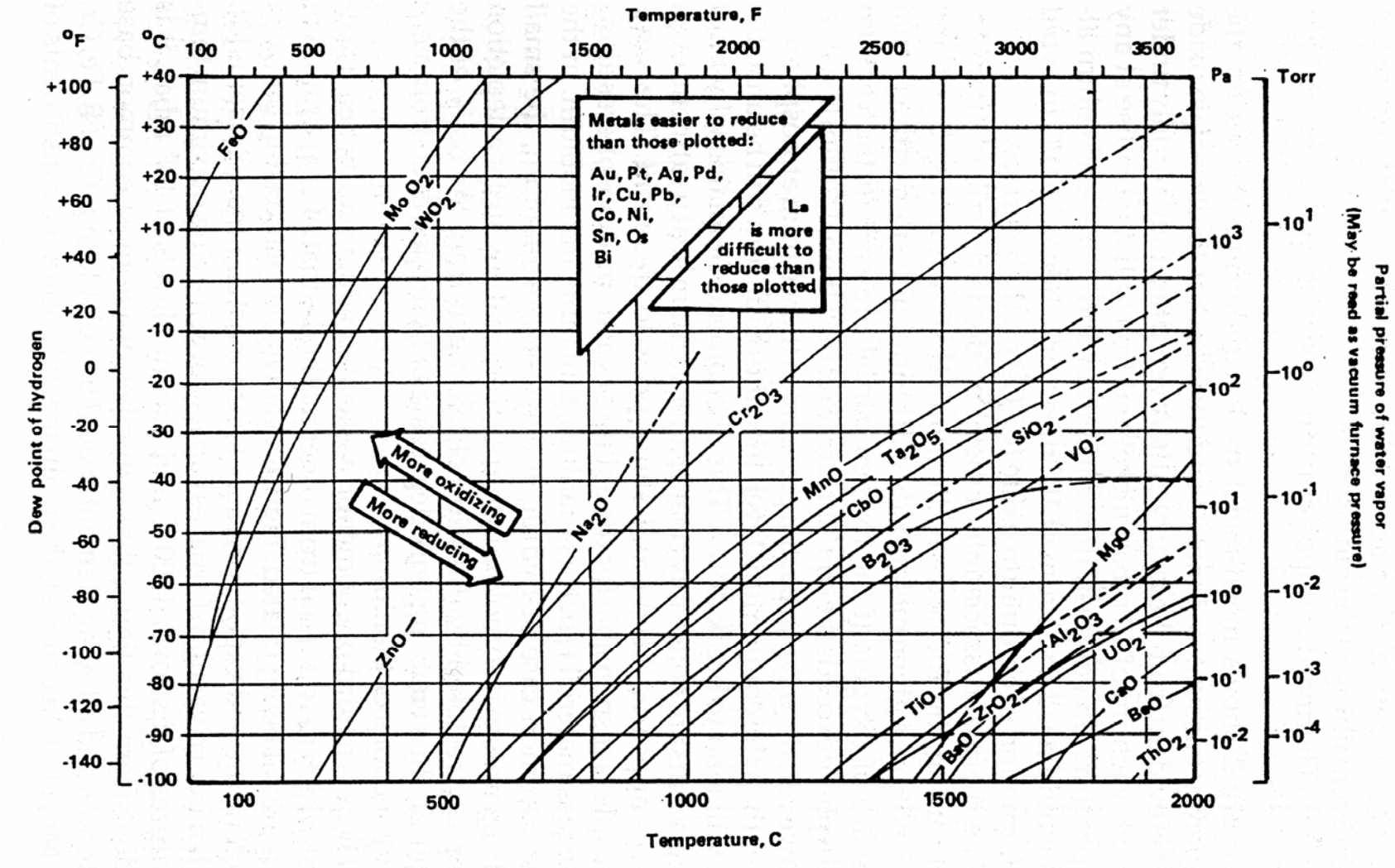

Figure 2.2.3-1: Metal-metal oxide equilibrium curves in hydrogen atmospheres [151]

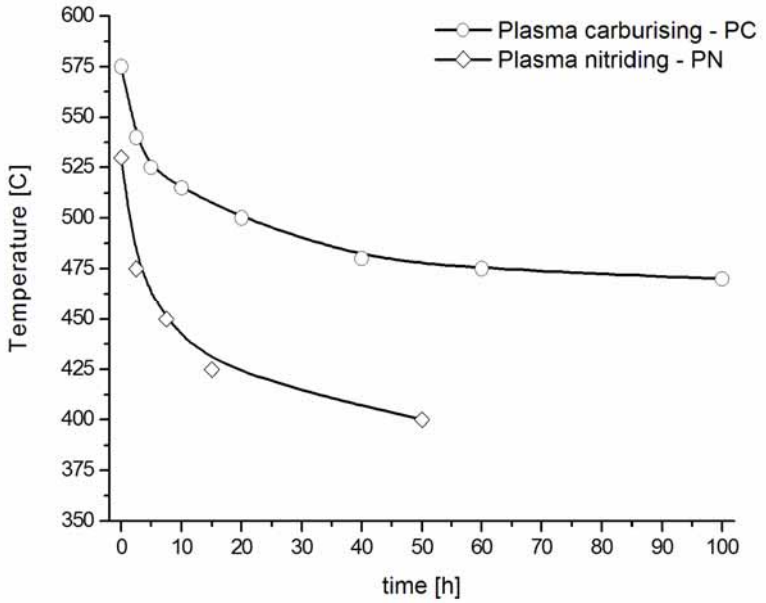

Figure 2.2.3-2: Threshold Temperature-time curves to produce precipitation free microstructures upon plasma nitriding (PN) and plasma carburising (PC) on AISI 316 [105]

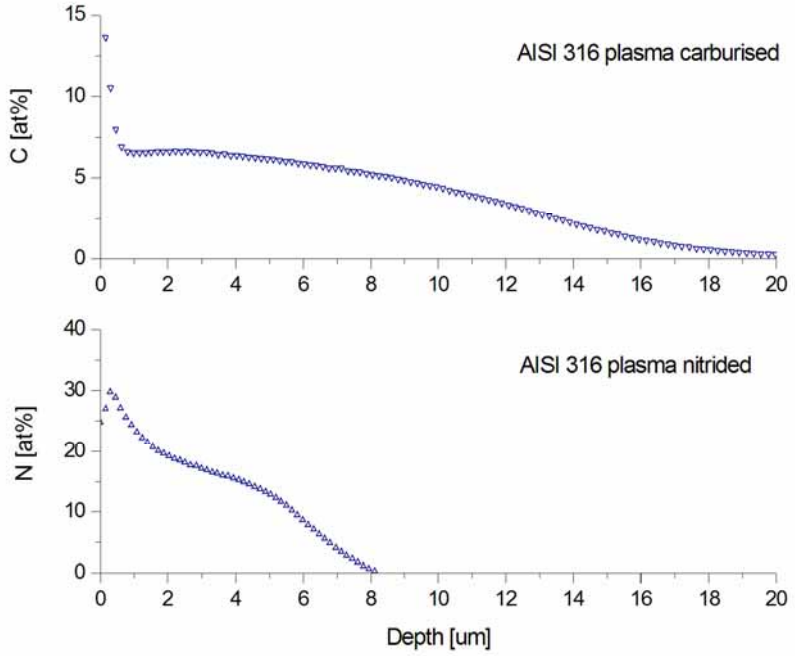

Figure 2.2.3-3: GDOES composition depth profile of AISI 316 plasma carburised and nitrided

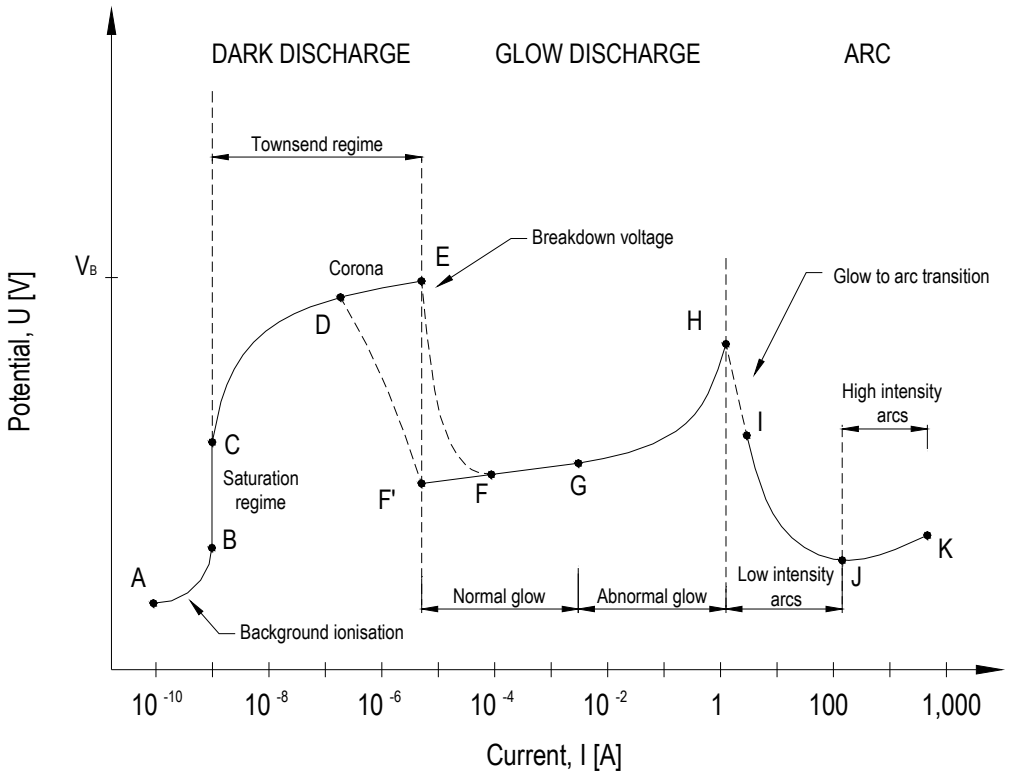

Figure 2.2.5-1: Current - voltage characteristic curve for DC plasma [157]

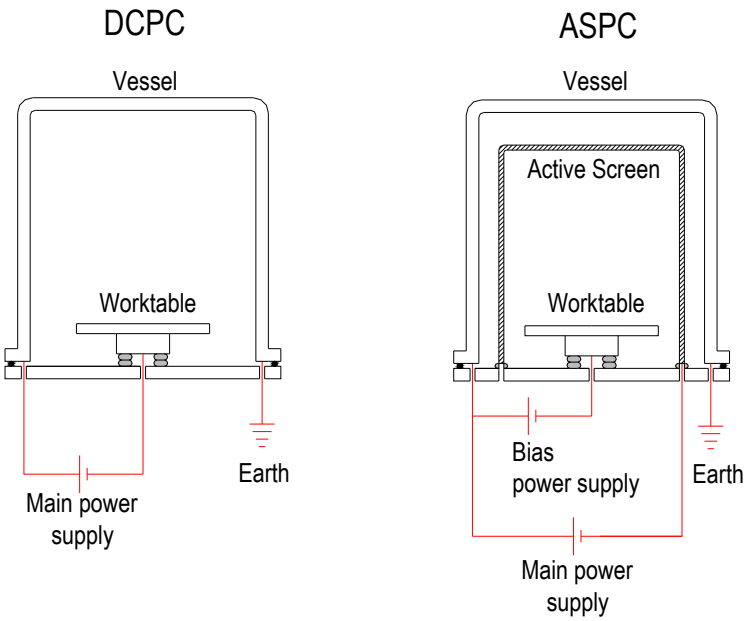

Figure 2.2.6-1: DC and AS furnaces for plasma carburising (DCPC and ASPC)

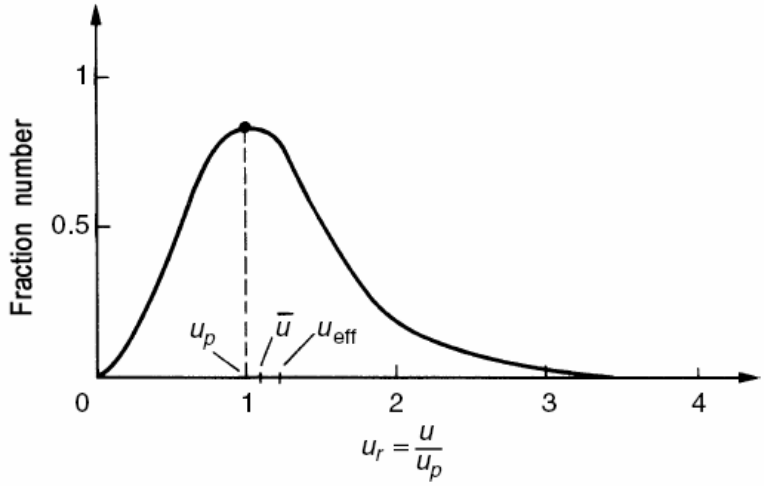

Figure 2.3.1-1: Maxwell electron energy distribution function – u_p: most probable velocity, ū: average velocity, u_{eff}: r.m.s. velocity [189]

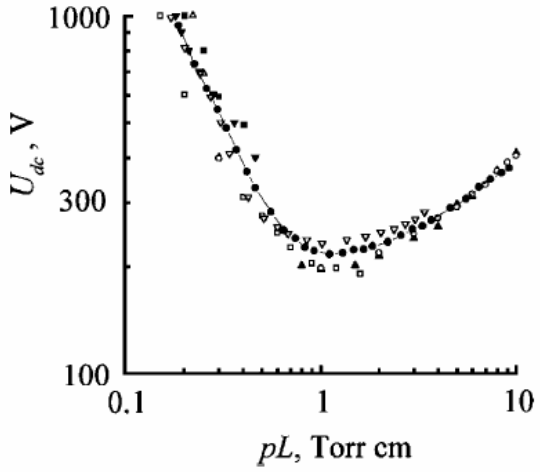

Figure 2.3.1-2: Typical Pashen curve [224]

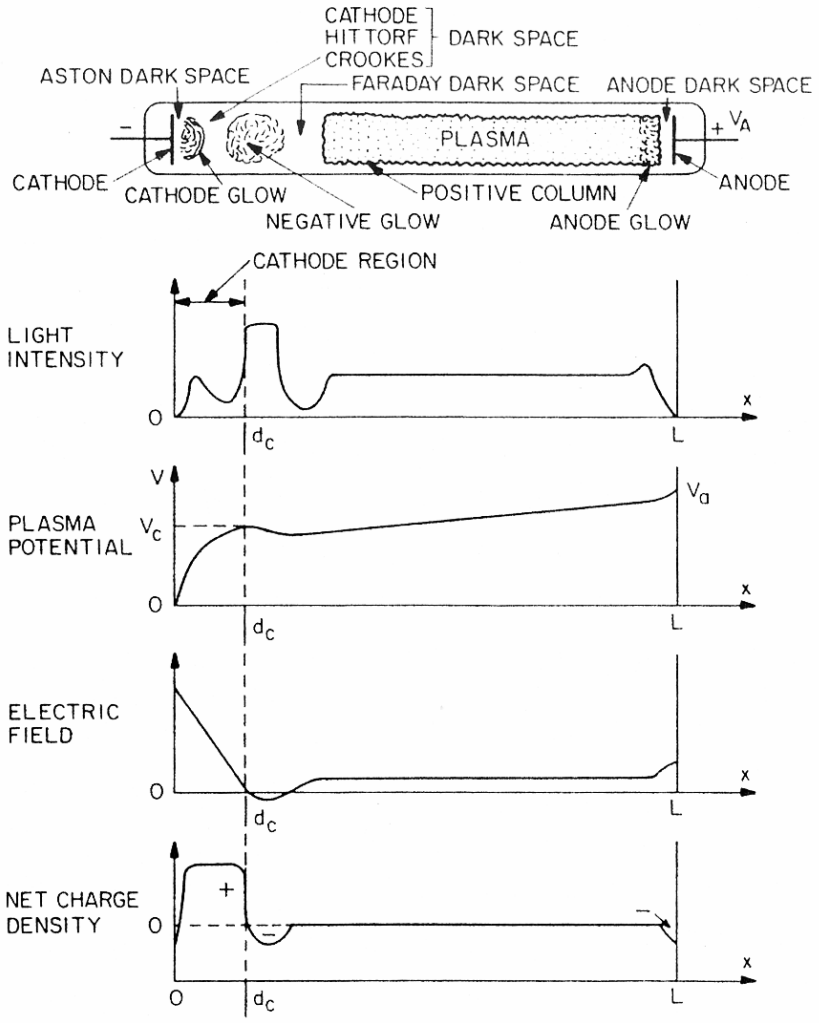

Figure 2.3.3-1: Structure of the glow discharge [157]

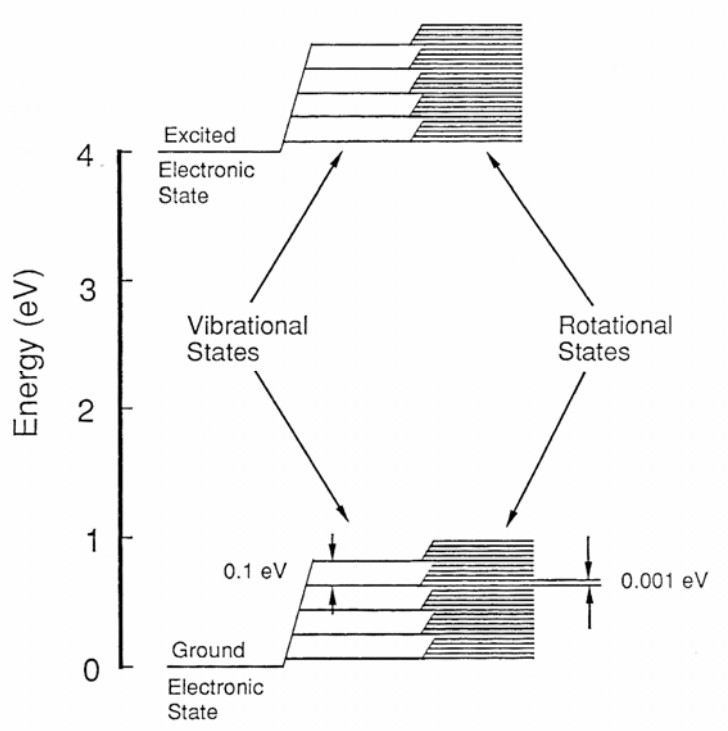

Figure 2.3.4-1: Diagram of electronic, vibrational and rotational energy levels of a molecule [204]

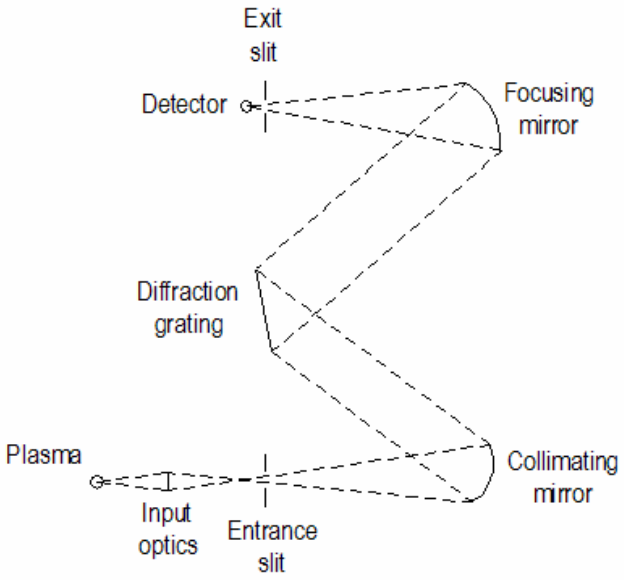

Figure 2.3.4-2: Typical OES equipment [205]

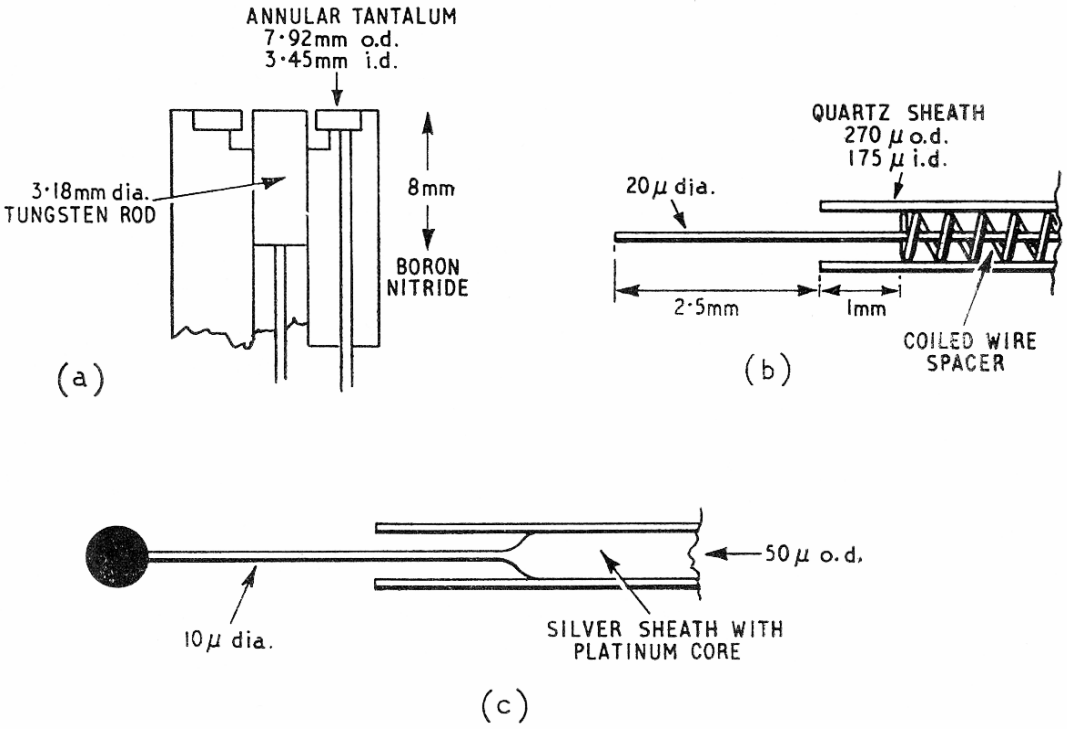

Figure 2.3.4-3: Typical electric probes – (a) plane, (b) cylindrical, (c) spherical [212]

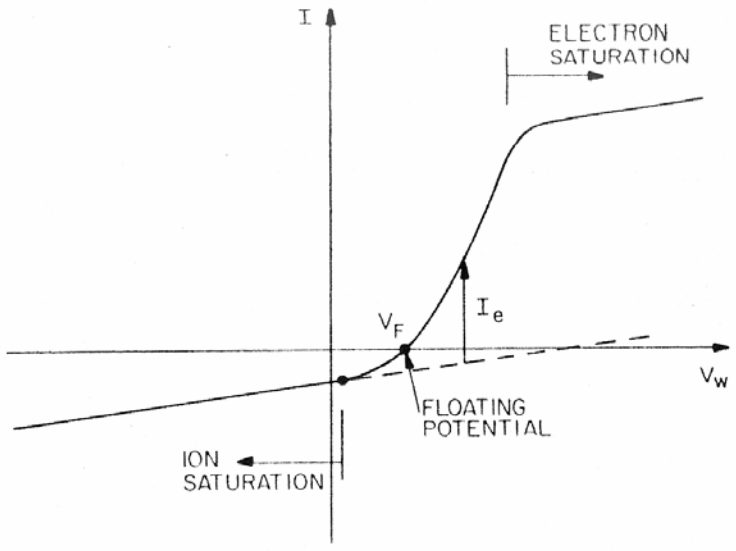

Figure 2.3.4-4: typical current voltage curve obtained with an electric probe [157]

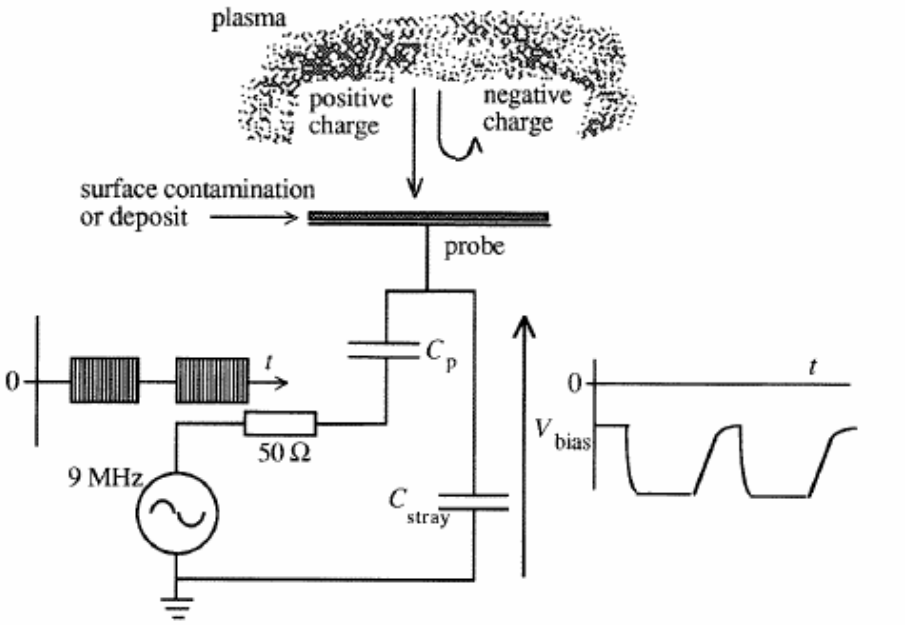

Figure 2.3.4-5: Ion flux probe [215]

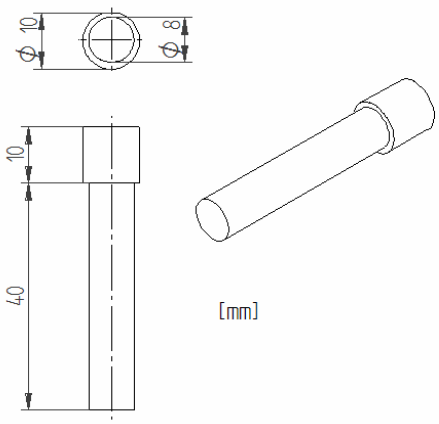

Figure 3.1.3-1: Schematics of corrosion samples

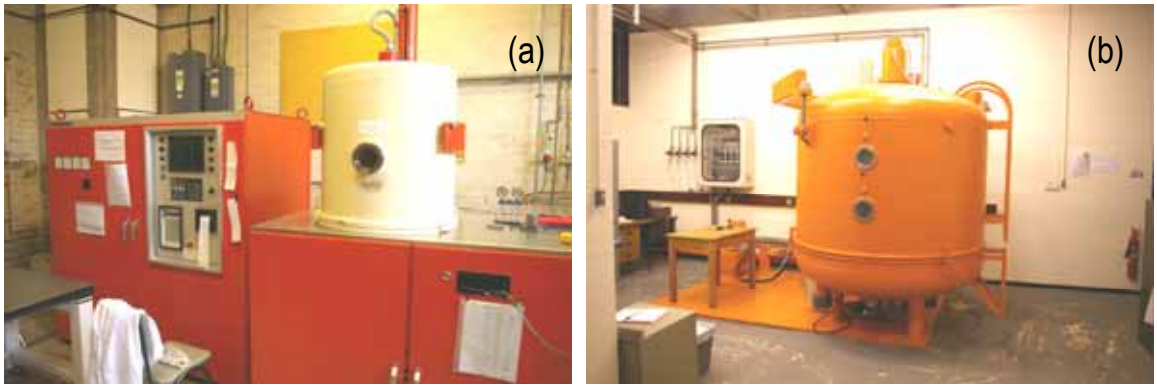

Figure 3.2.1-1: (a) Klöckner Ionon DC furnace and (b) Plasma Metal active screen industrial unit

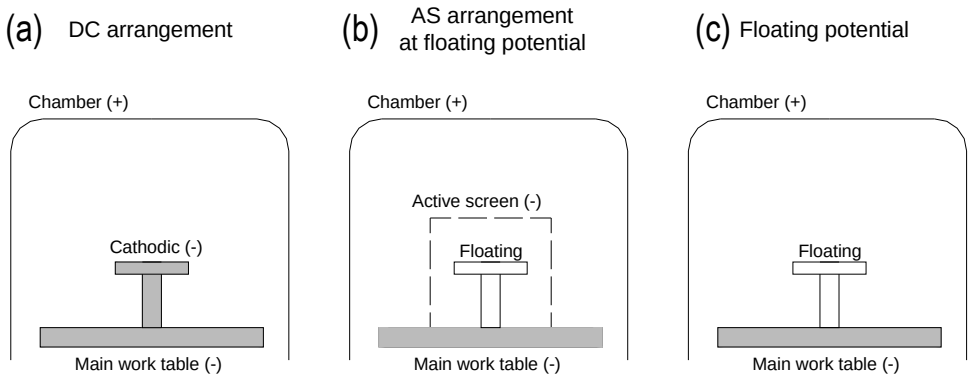

Figure 3.2.1-2: (a) DC, (b) AS and (c) FP arrangements inside a conventional DC plasma furnace used to study the mechanisms of active screen plasma treatments.

Figure 3.2.1-3: DC, AS_{sh}, AS_{bh}, and FP arrangements inside a conventional DC plasma furnace used to study the mechanisms of active screen plasma treatments.
DC: direct current; AS: active screen; FP: floating potential; AS_{sh}: AS mesh with small holes (Ø = 8 mm), AS_{bh}: AS mesh with large holes (Ø = 25.4 mm)

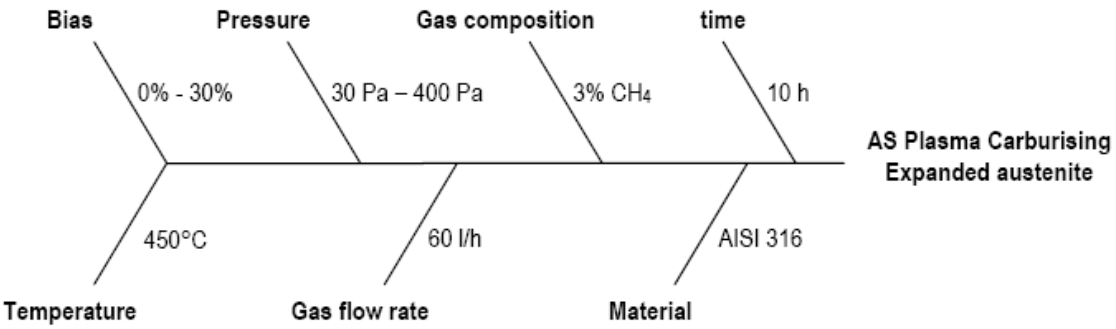

Figure 3.2.1-4: Fish bone diagram of the treatment conditions involved

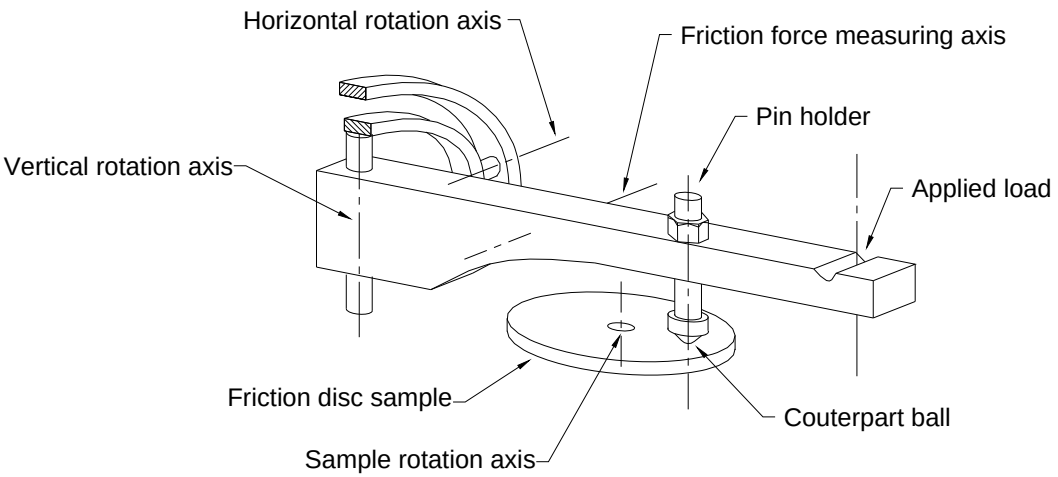

Figure 3.4-1: Schematics of the pin-on-disc apparatus used for wear and friction tests

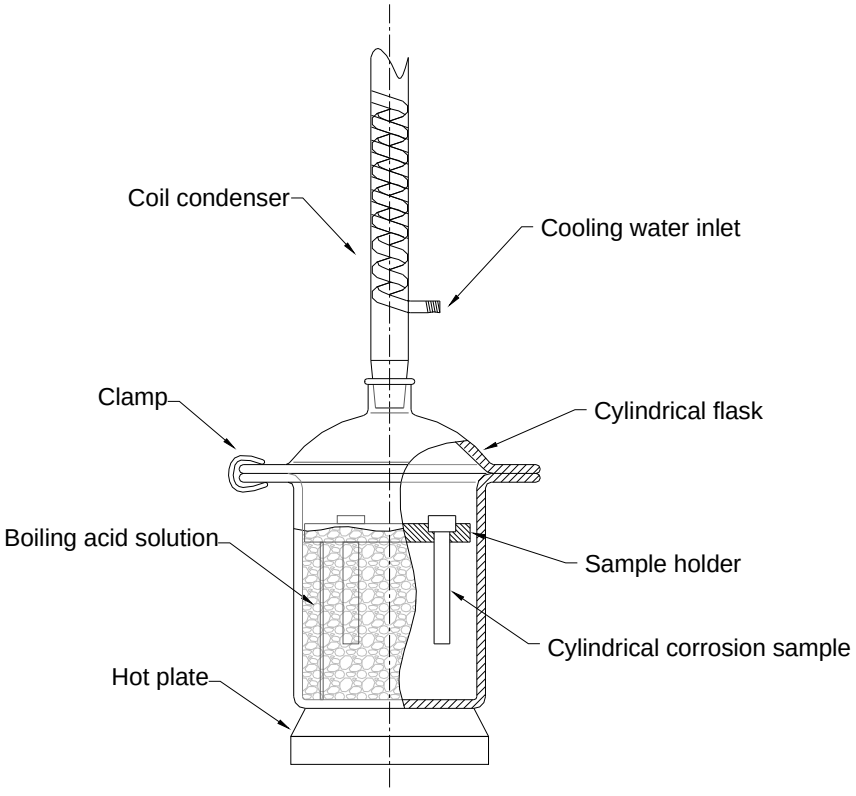

Figure 3.5-1: Schematics of the apparatus used for immersion corrosion in boiling acid solutions

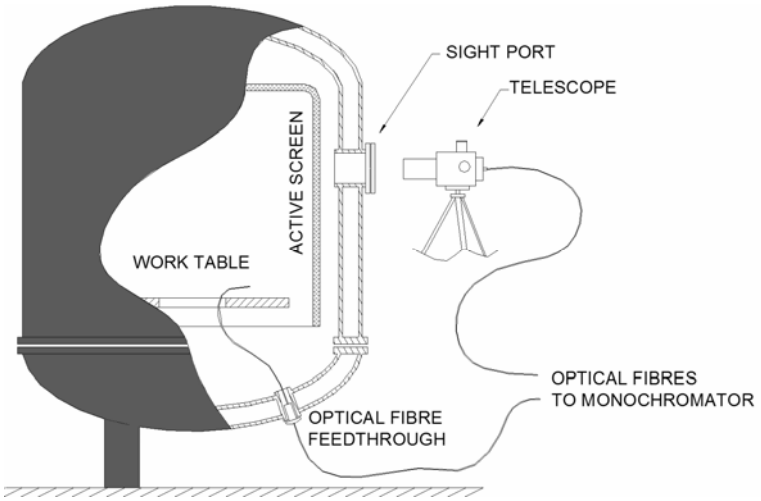

Figure 3.6-1: Experimental arrangement used for OES (telescope) and IOES (optical fibre probe)

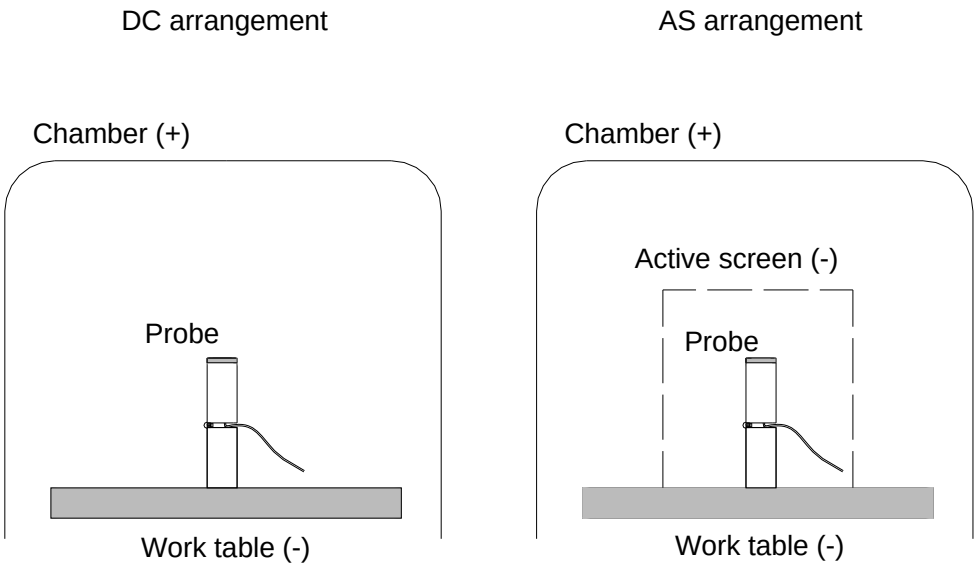

Figure 3.6-2: DC and AS experimental arrangements used for IFP measurements

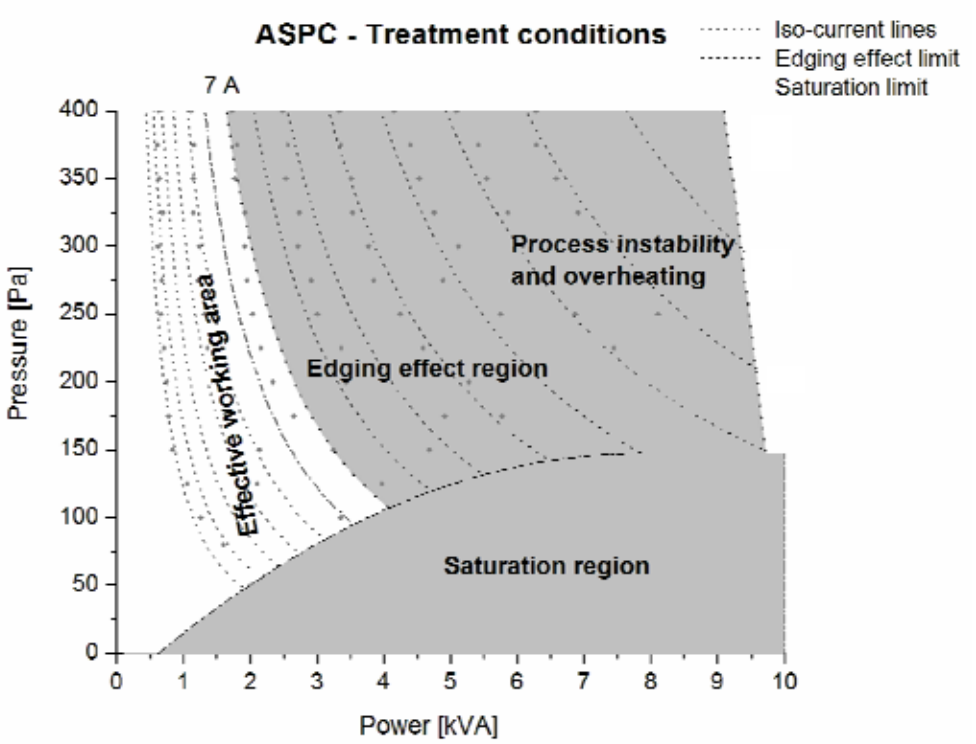

Figure 4.1-1: ASPC processing conditions on the work table

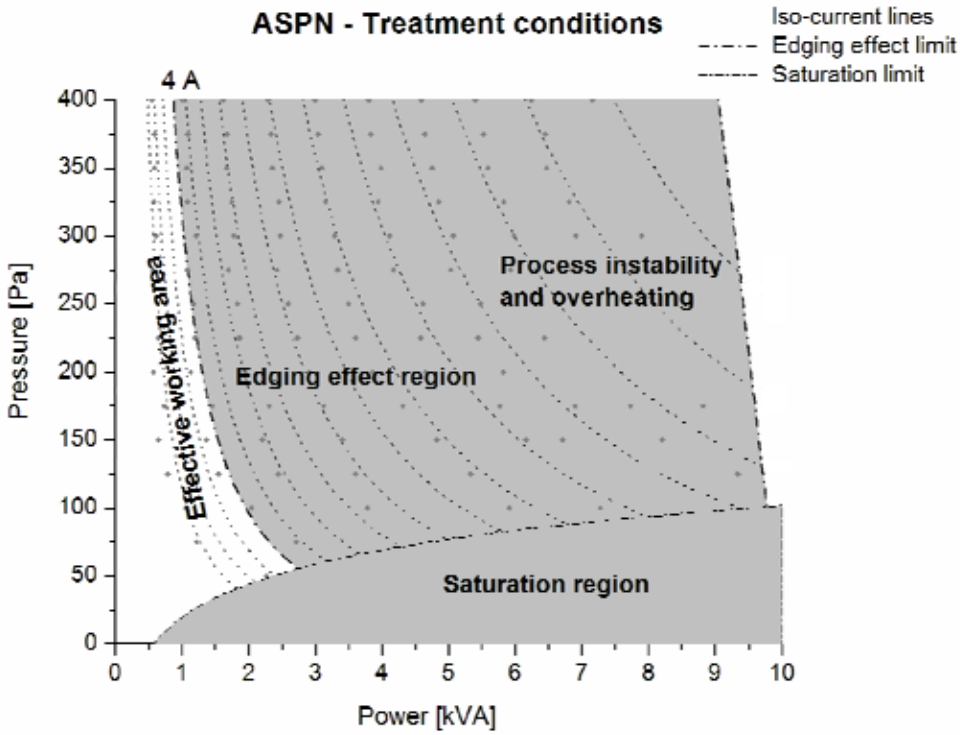

Figure 4.1-2: ASPN processing conditions on the work table

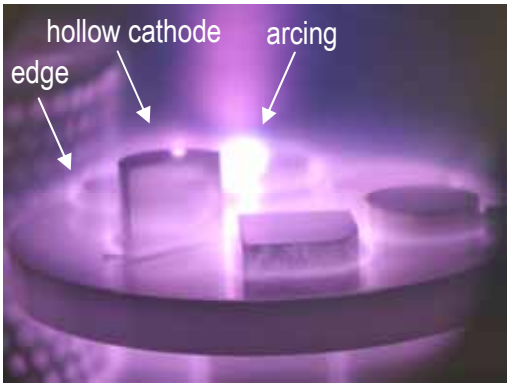

Figure 4.1-3: Samples in a DC conventional treatment, showing arcing on a dirty or rusty specimen, and hollow cathode effect on a sample with a blind hole.
An Active Screen experimental arrangement is also seen on the left side of the same picture.

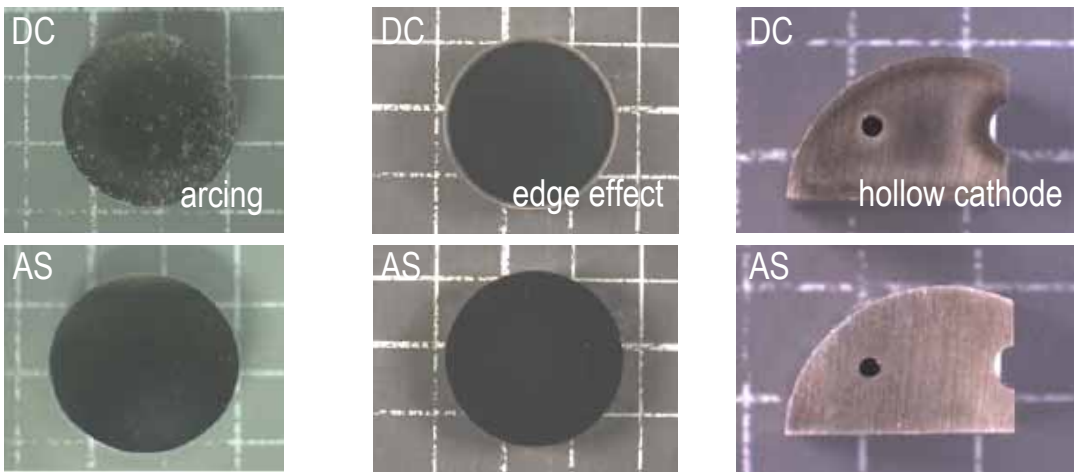

Figure 4.1-4: Surface damage by process instabilities in DC conventional treatments

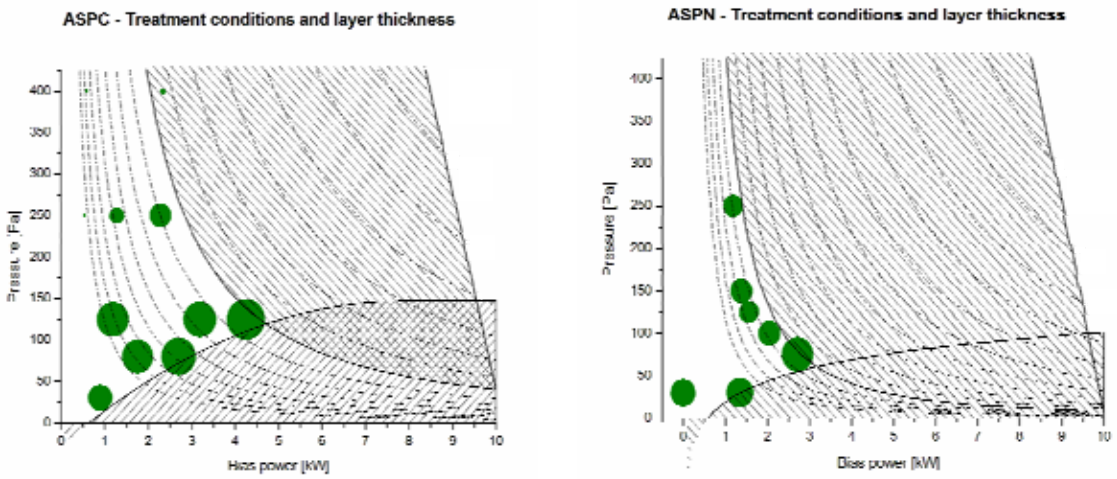

Figure 4.1-5: Layer thickness (size of the bubble) superimposed on the map of treatment conditions for ASPC and ASPN

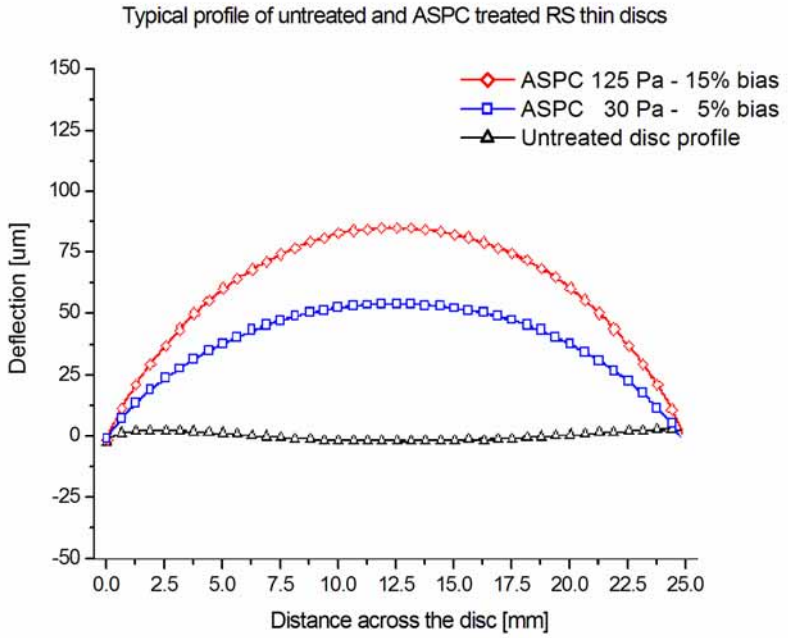

Figure 4.1-6: Typical profile of the thin discs used for the assessment of residual stresses

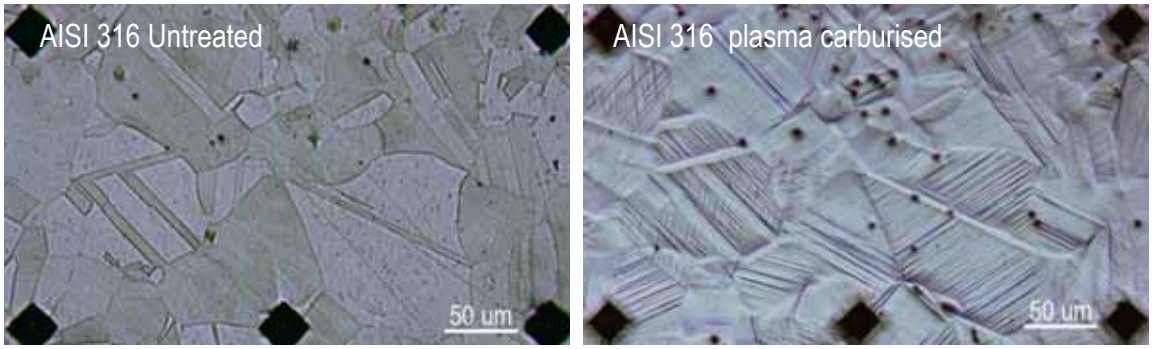

Figure 4.2-1: Optical micrographs of the same area before and after plasma carburising

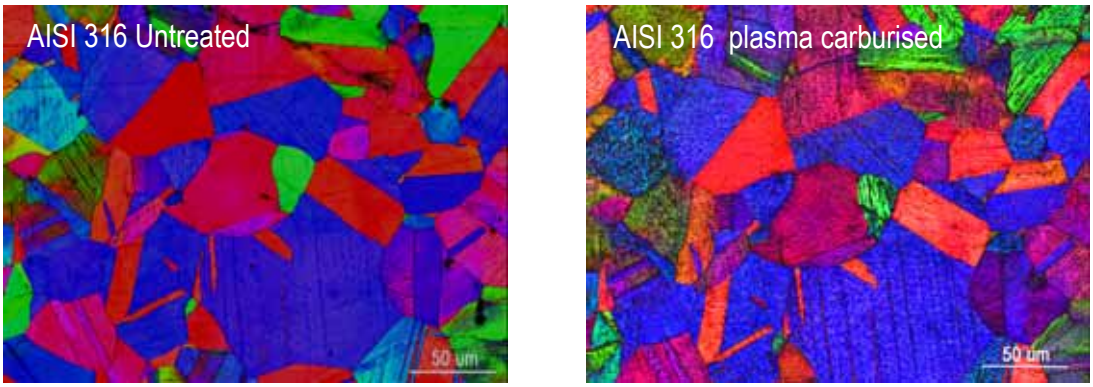

Figure 4.2-2: EBSD Crystal Orientation Maps of the same area before and after plasma carburising

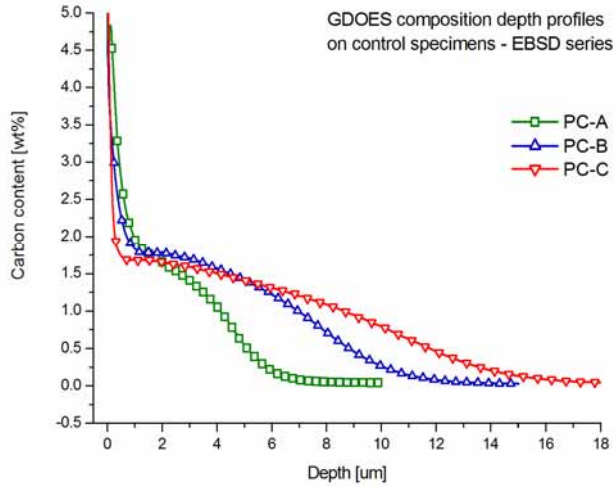

Figure 4.2-3: GDOES composition-depth profiles for different treatment times: (A) 1 hour, (B) 3 hours and (C) 6 hours

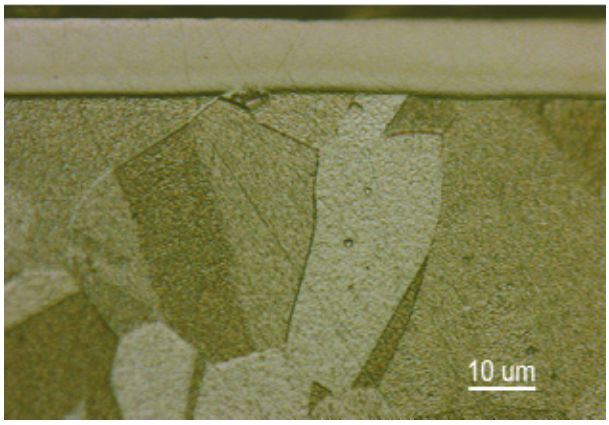

Figure 4.2-4: Typical cross section micrograph of an AISI 316 plasma carburised specimen

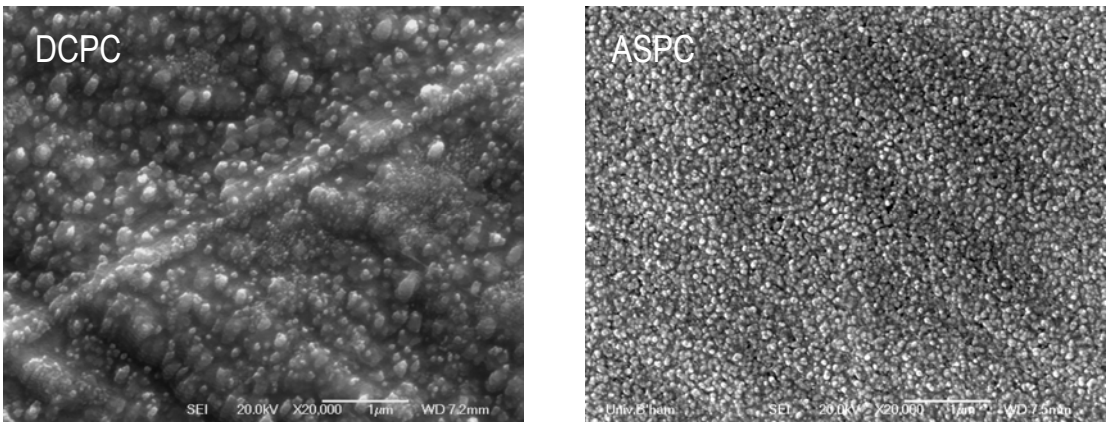

Figure 4.2-5: SEM micrographs of DCPC and ASPC treated samples

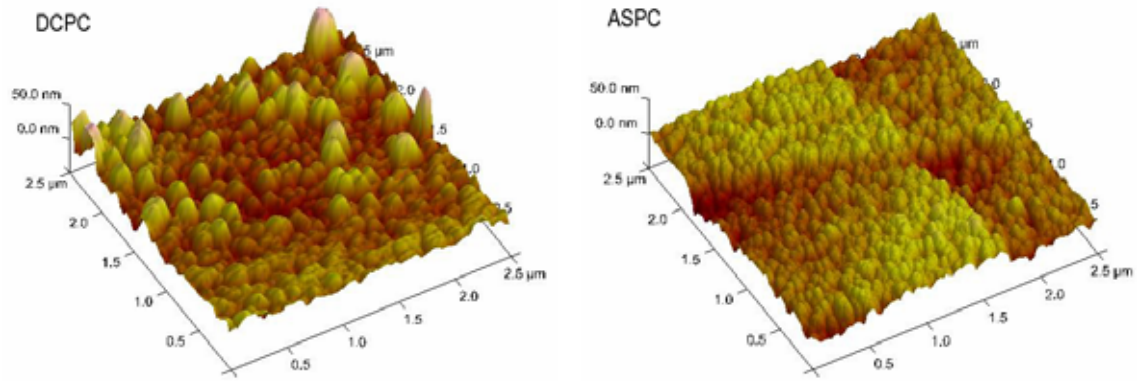

Figure 4.2-6: AFM images of DCPC and ASPC treated samples

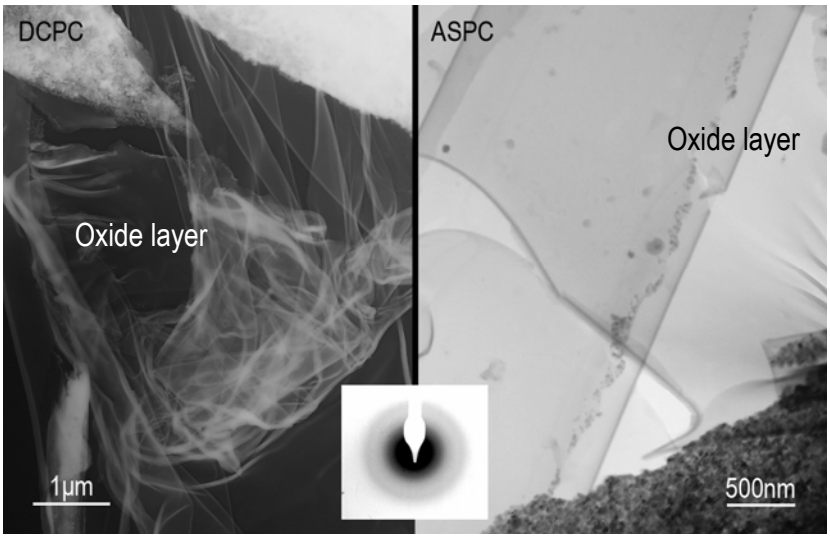

Figure 4.2-7: TEM micrograph and diffraction pattern (amorphous) of the oxide layer on DCPC and ASPC samples (top view)

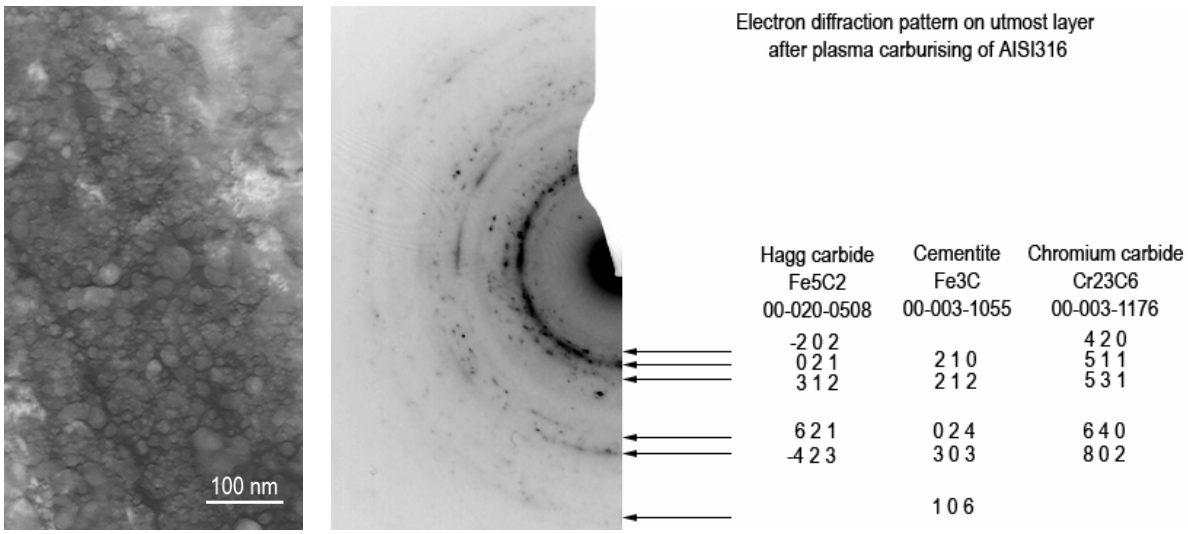

Figure 4.2-8: TEM micrograph and ring electron diffraction pattern on a plasma carburised specimen

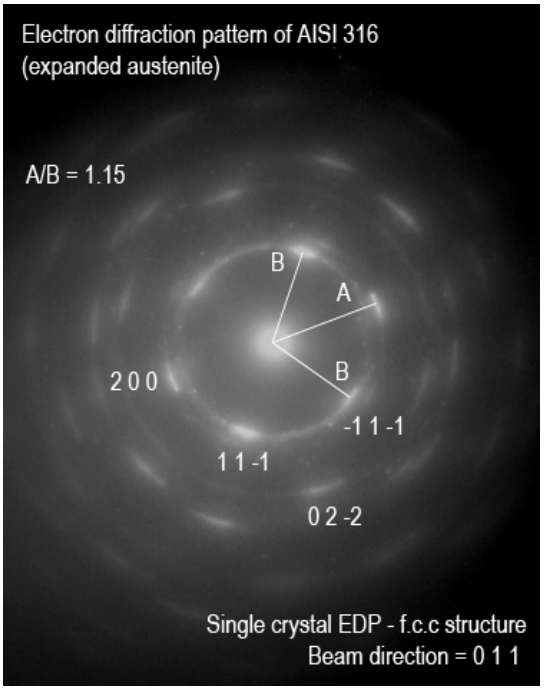

Figure 4.2-9: Electron diffraction pattern of the carbon expanded austenite on a plasma carburised specimen

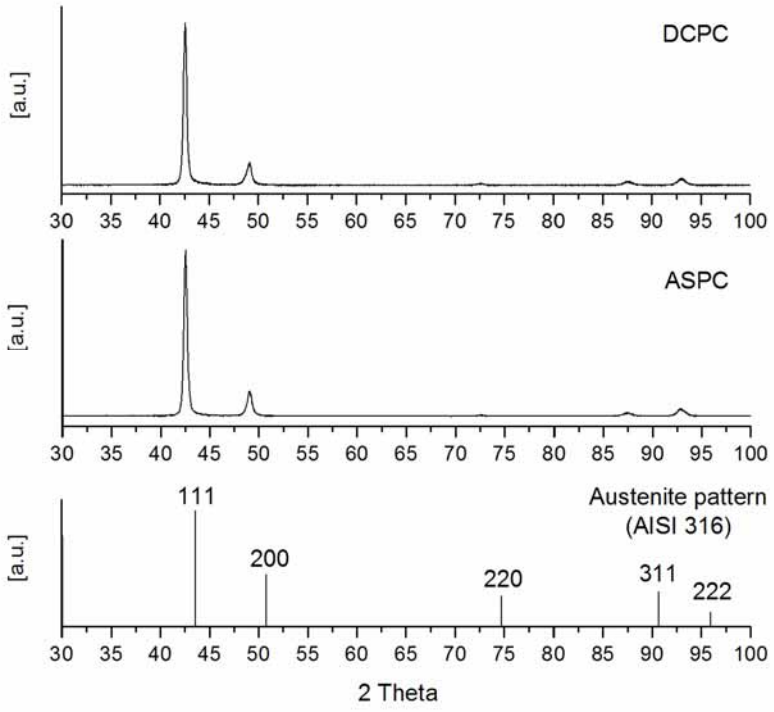

Figure 4.2-10: XRD pattern obtained on DCPC and ASPC, and austenite reference pattern

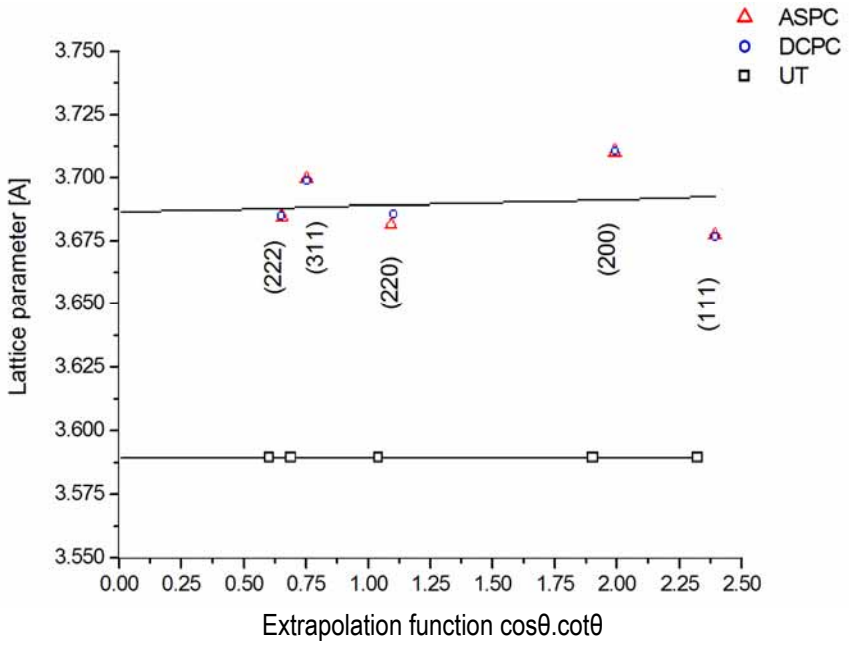

Figure 4.2-11: Lattice parameter a_{hkl} vs cosθ.cotθ of expanded austenite and AISI 316 UT

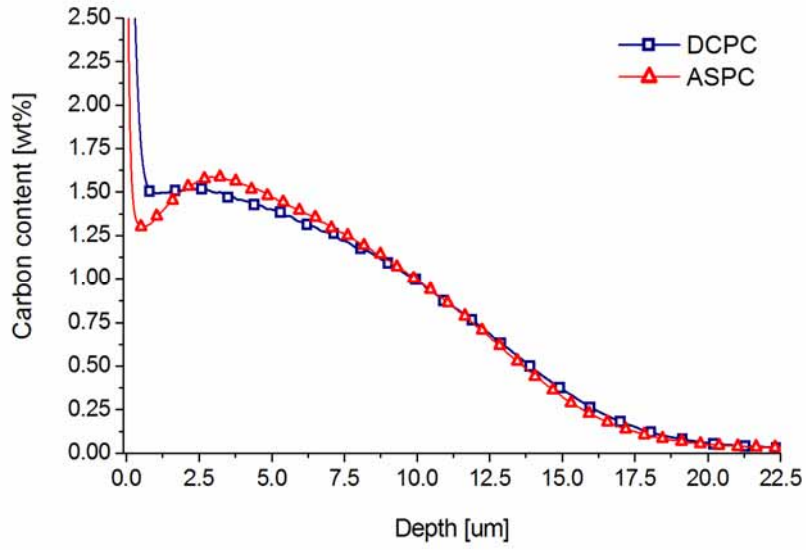

Figure 4.2-12: GDOES composition-depth profile of DCPC and ASPC treated samples

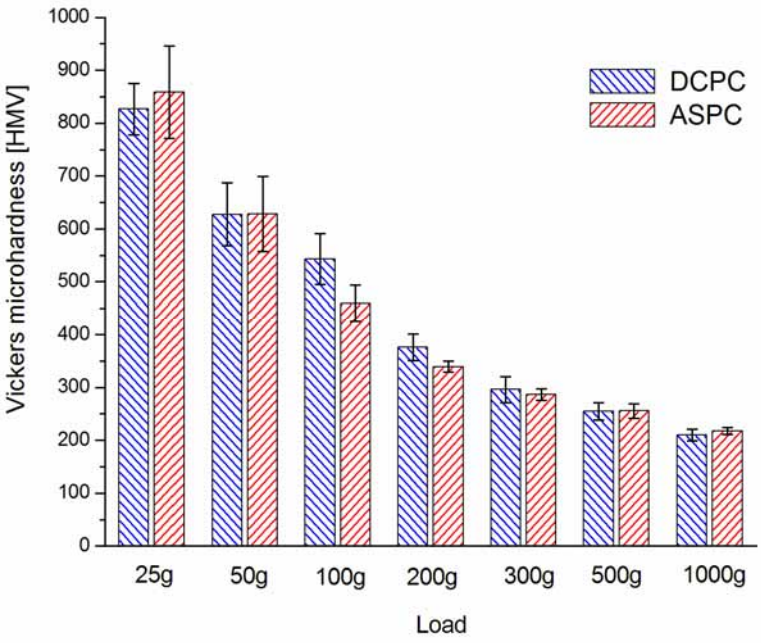

Figure 4.2-13: Load bearing capacity (LBC) of DCPC and ASPC treated samples

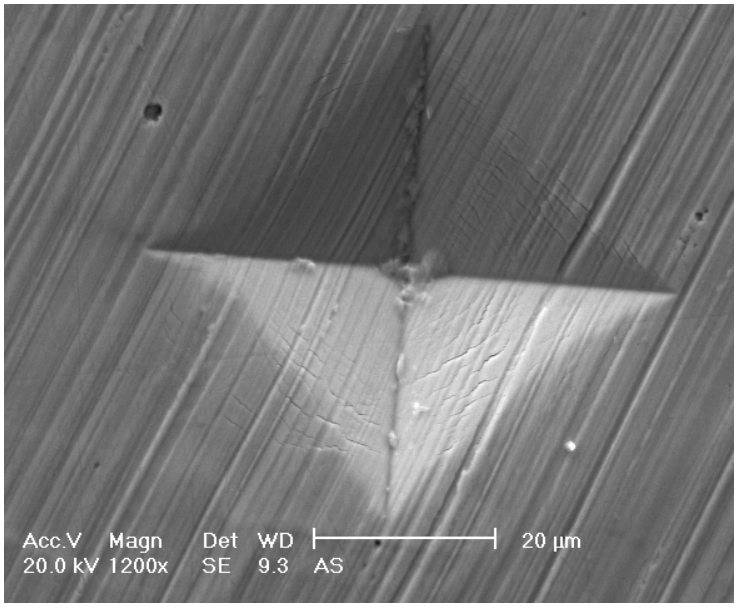

Figure 4.2-14: Cracks inside a low-force (500g) Vickers indentation on a DCPC sample

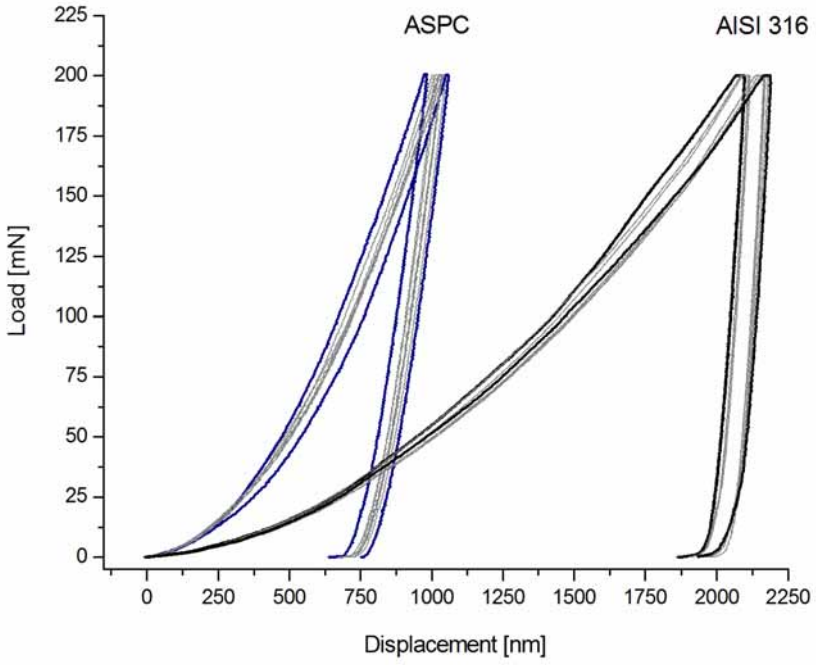

Figure 4.2-15: Instrumented hardness on AISI 316 untreated and ASPC treated samples

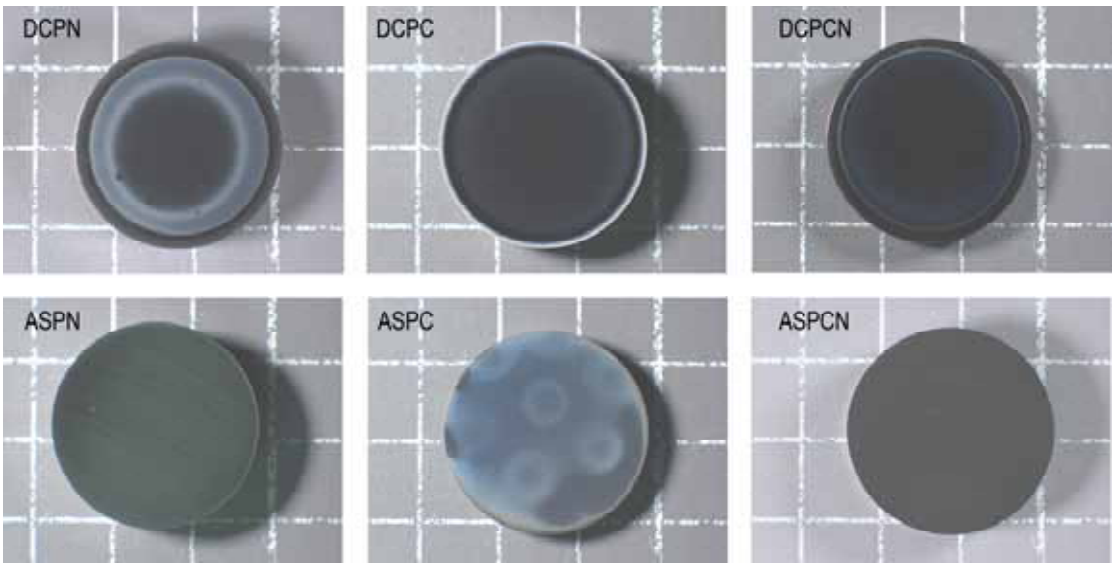

Figure 4.3-1: Appearance of the samples treated under DC and AS arrangements in nitriding, carburising and nitrogen enhanced carburising atmospheres

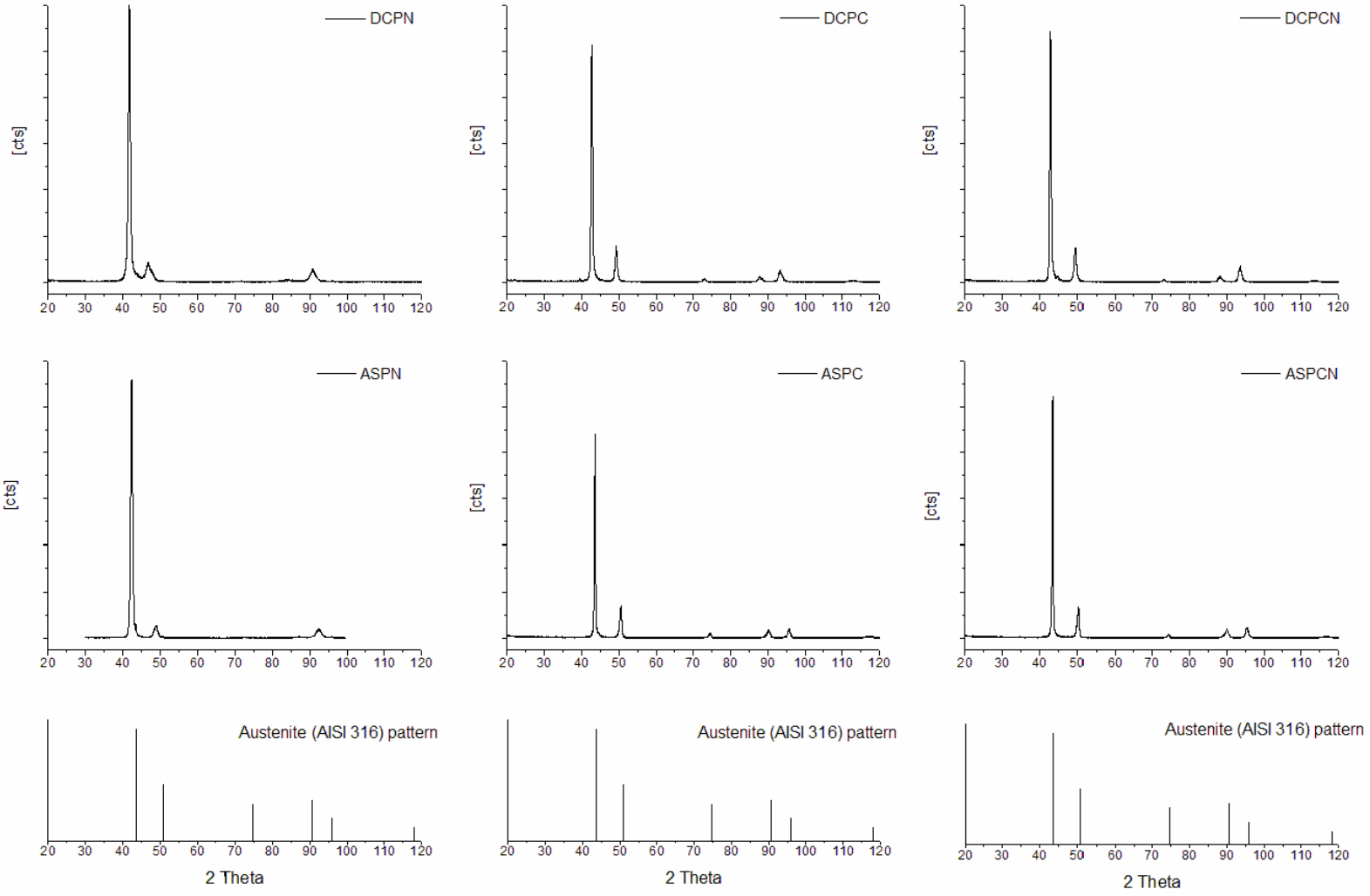

Figure 4.3-2: XRD patterns of AISI 316 treated under DC and AS arrangements in nitriding, carburising and N_2 enhanced carburising atmospheres

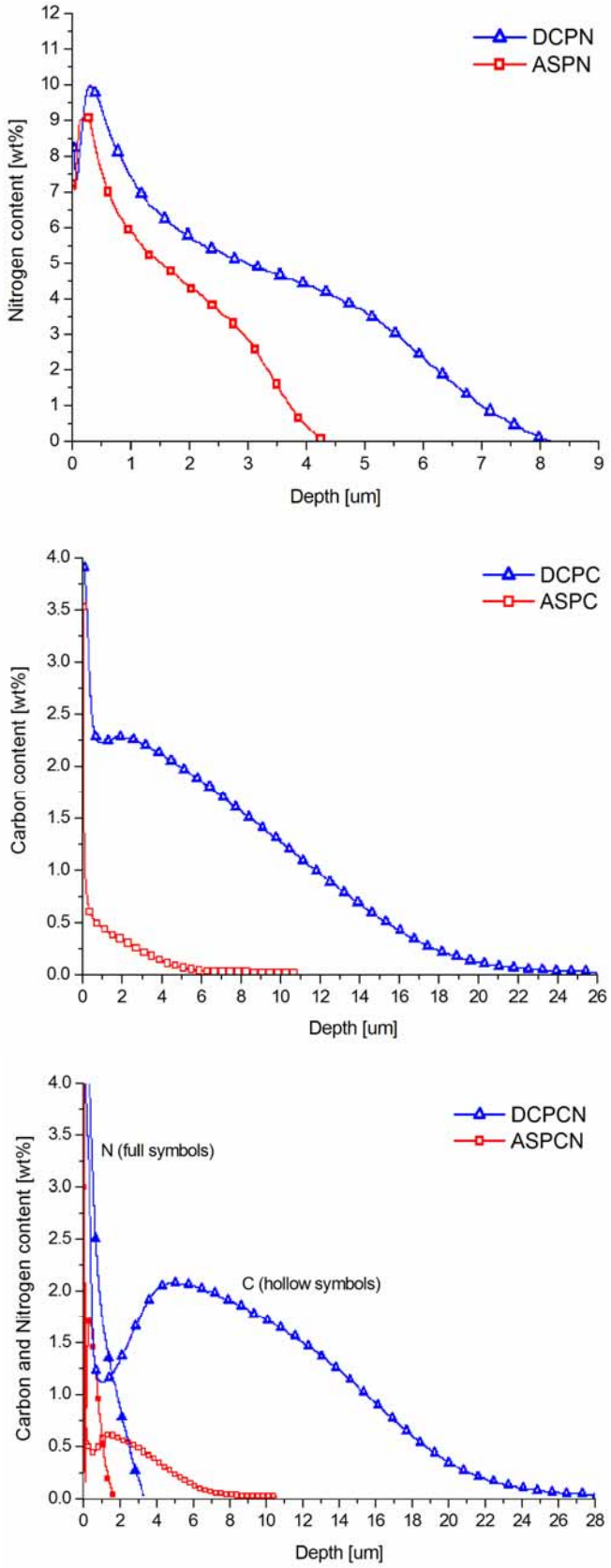

Figure 4.3-3: GDOES composition-depth profiles of samples treated under DC and AS arrangements in nitriding, carburising and N_2 enhanced carburising atmospheres

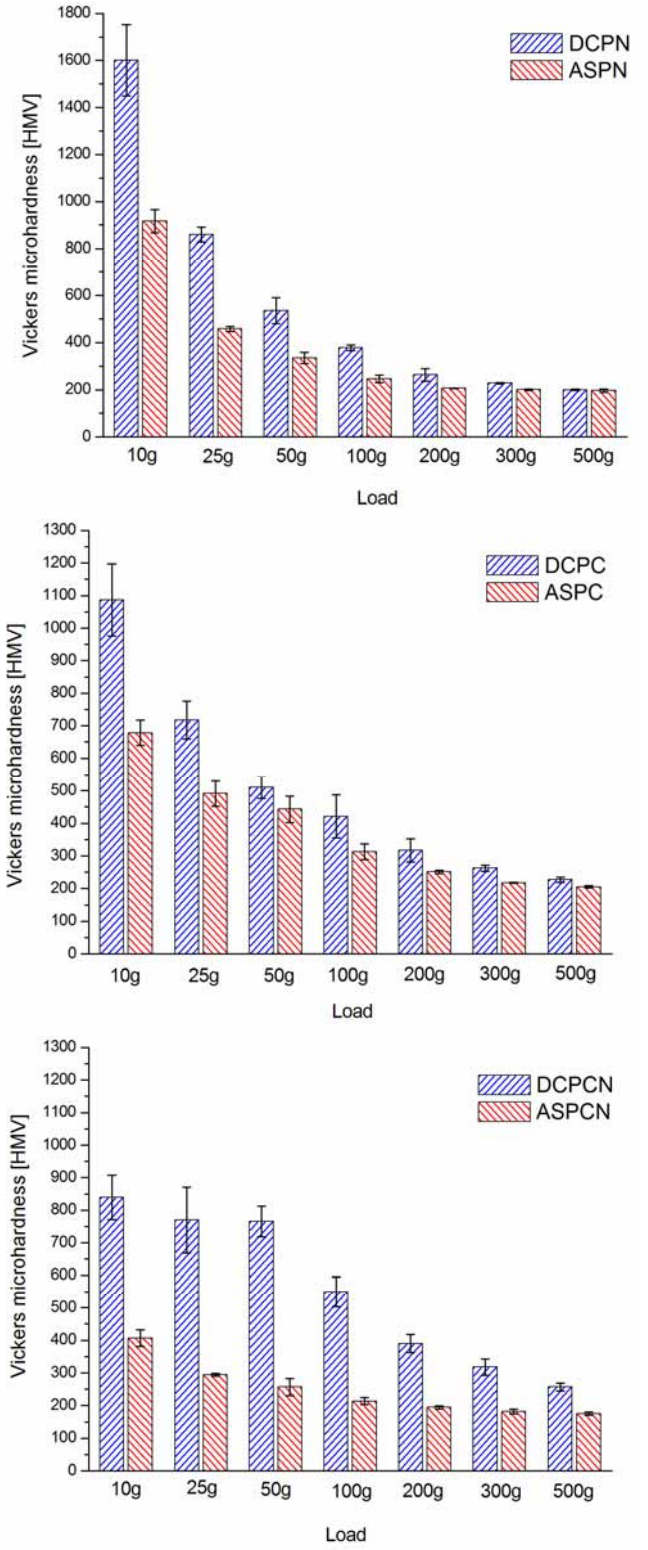

Figure 4.3-4: Load bearing capacity (LBC) of samples treated under DC and AS arrangements in nitriding, carburising and N_2 enhanced carburising atmospheres

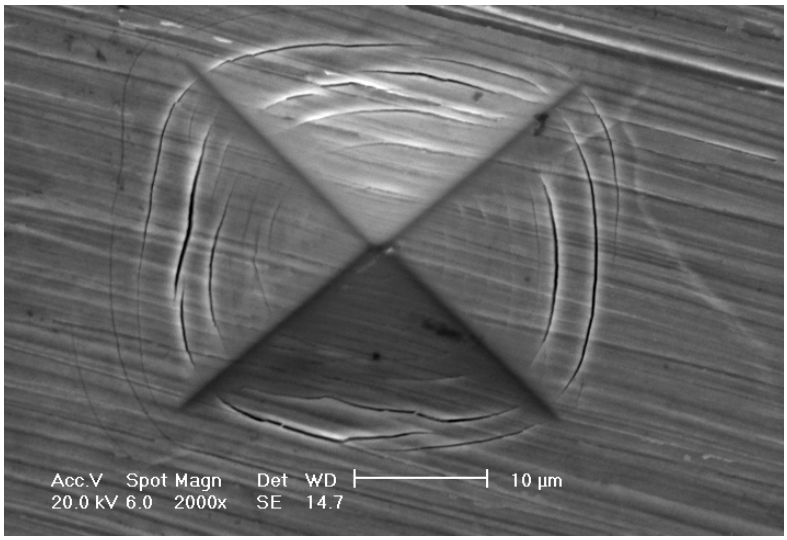

Figure 4.3-5: Optical micrograph of a hardness indent on one AISI316 sample after ASPN

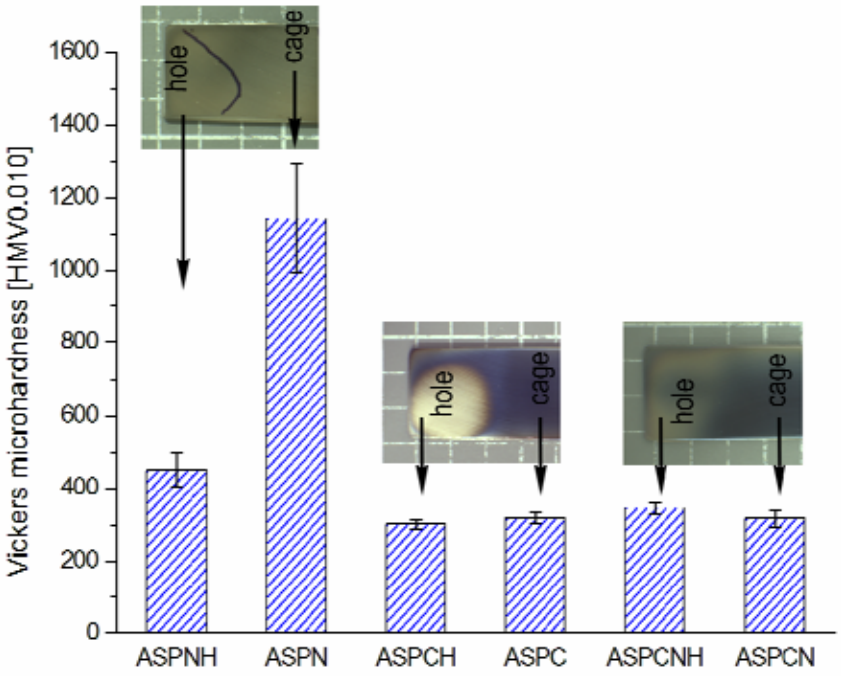

Figure 4.3-6: Vickers microhardness tests on different parts of the AISI304 stripe specimens treated in an AS arrangement with big holes in the mesh

AS: Active screen, PN: plasma nitriding, PC: plasma carburising, PCN: nitrogen enhanced carburising, H: hole area

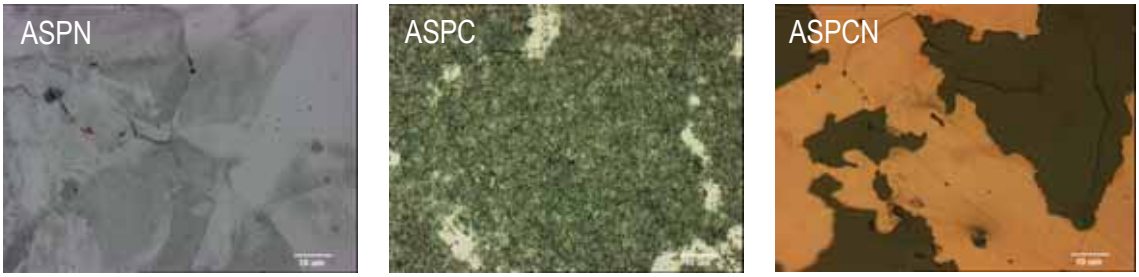

Figure 4.3-7: Optical micrographs of the deposition layer on ASPN, ASPC and ASPCN copper samples

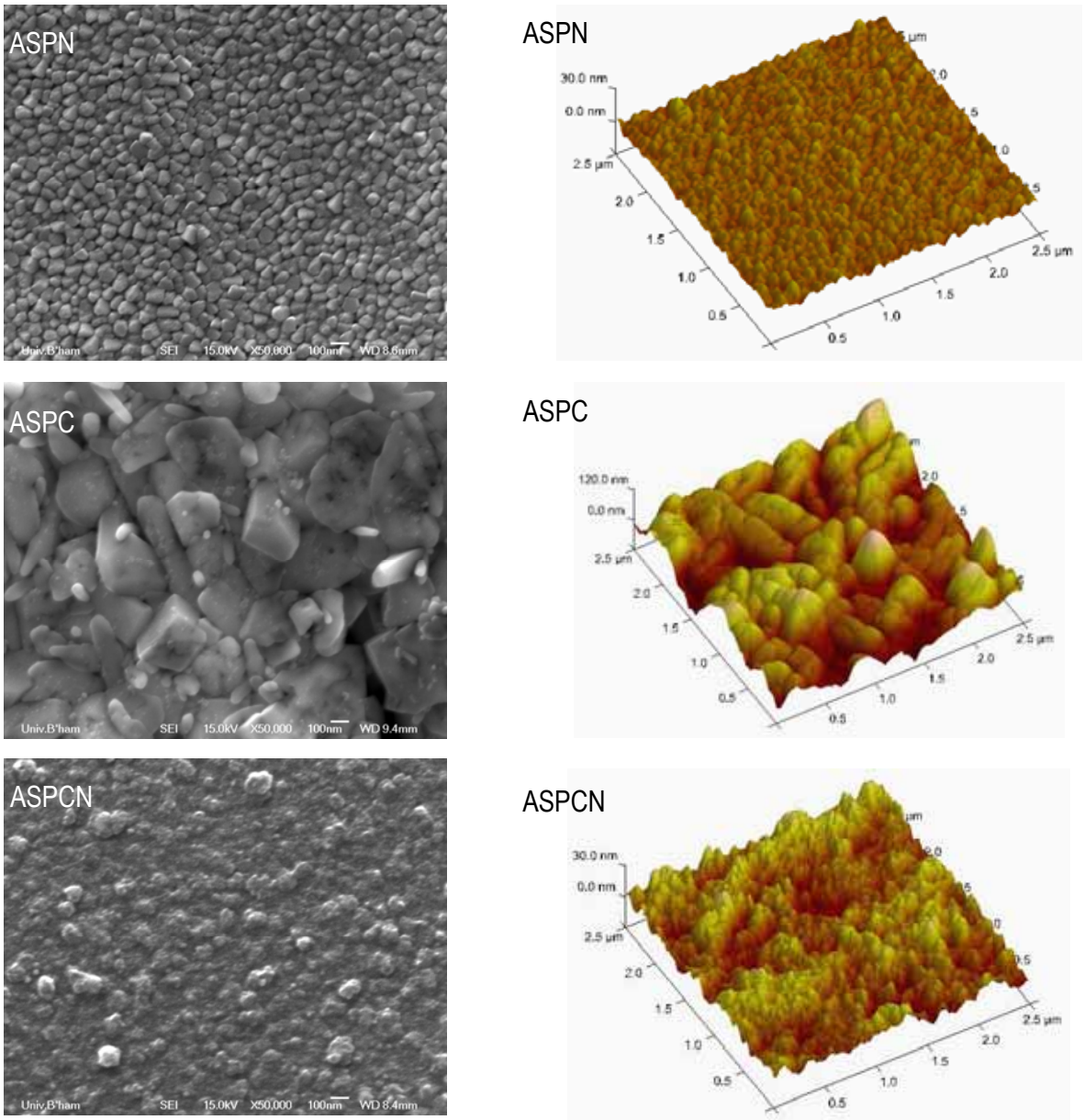

Figure 4.3-8: Morphology of AS nitrided, carburised and N_2 enhanced carburised samples observed under SEM and AFM

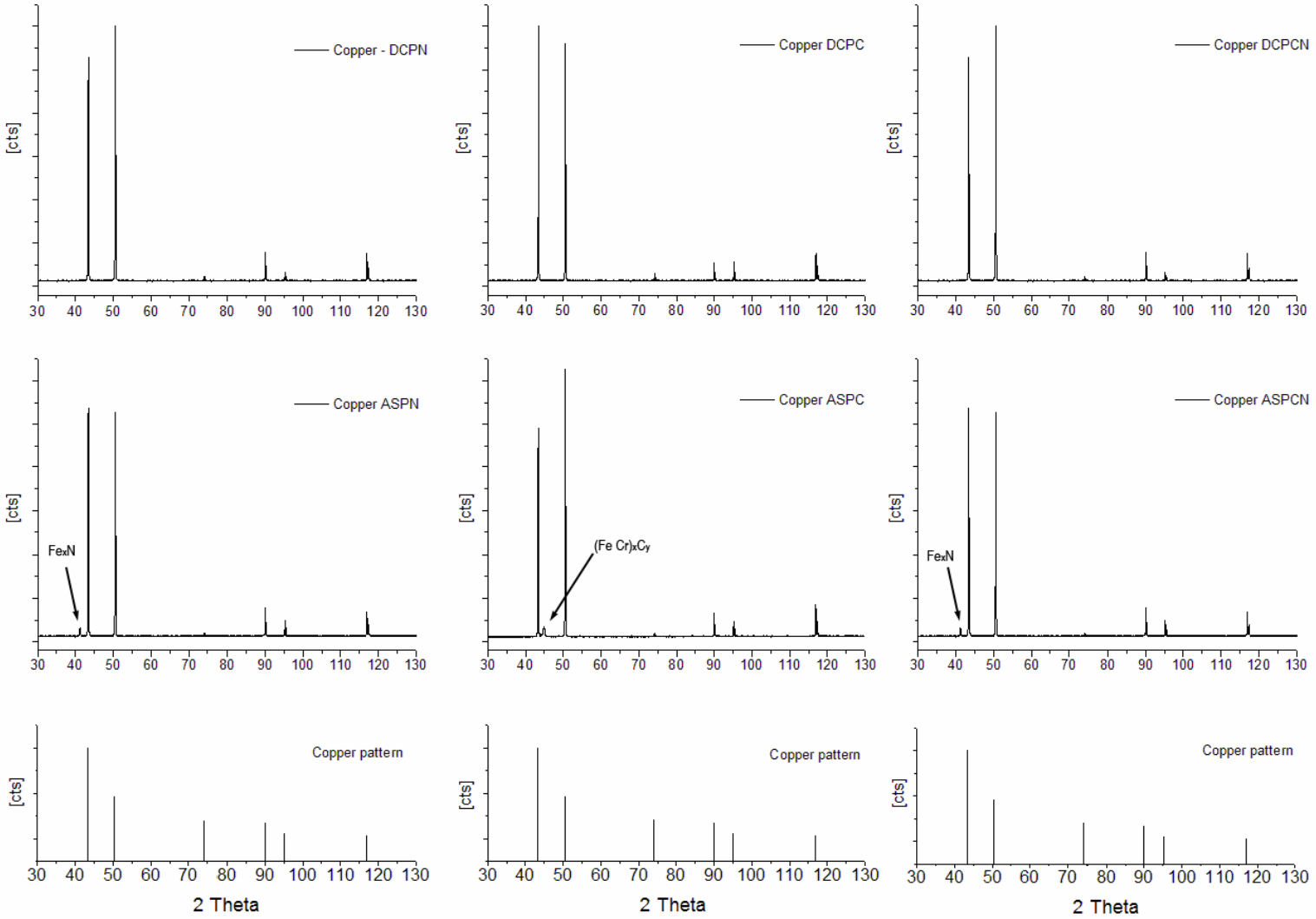

Figure 4.3-9: XRD patterns of copper samples treated under DC and AS arrangements in nitriding, carburising and N_2 enhanced carburising atmospheres

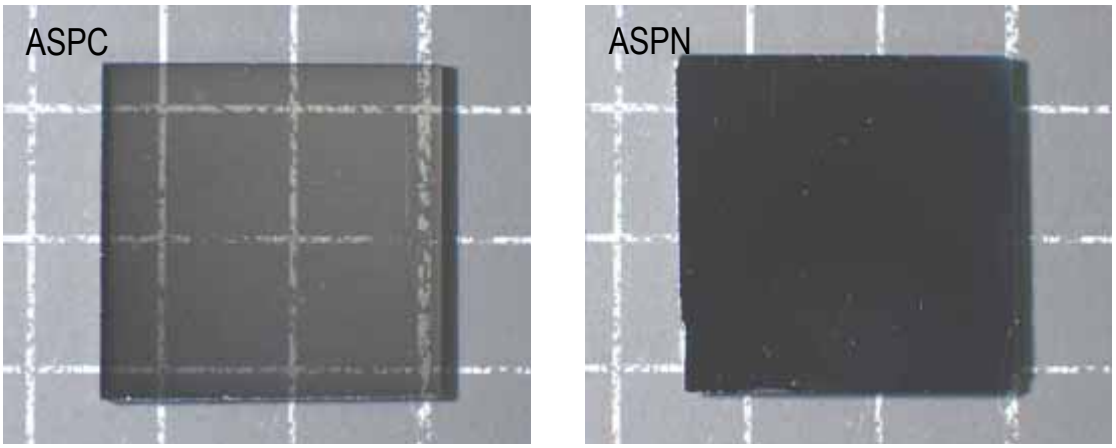

Figure 4.3-10: ASPC and ASPN treated glass slides

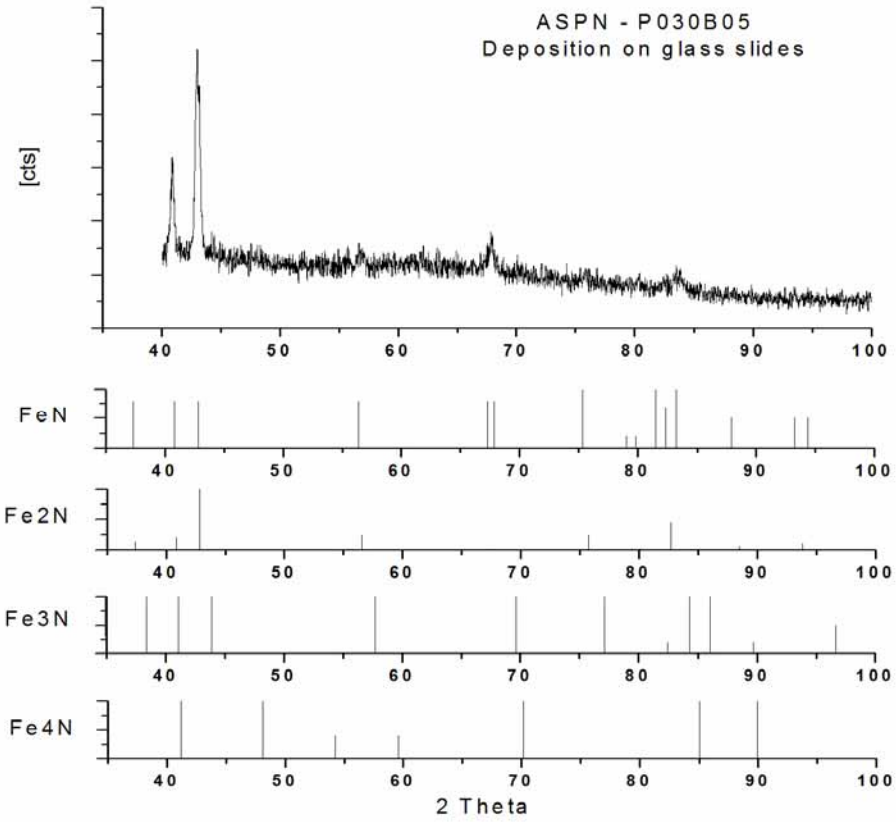

Figure 4.3-11: XRD peaks of the deposition layer on ASPN treated glass slides

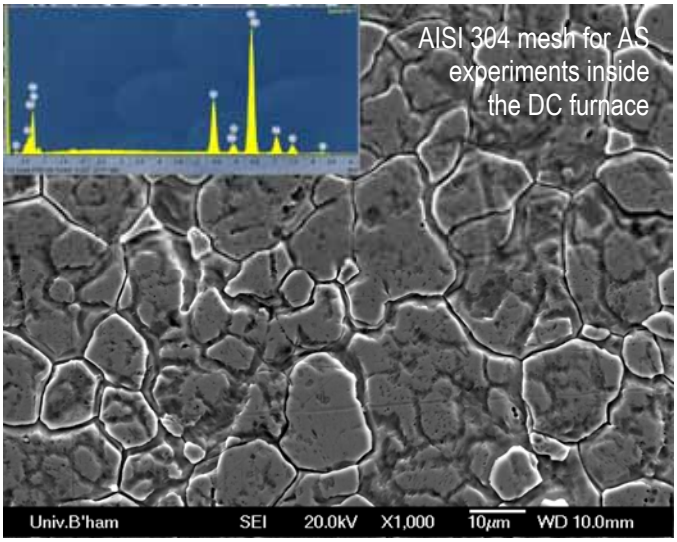

Figure 4.3-12: Micrograph and EDX spectrum of the mesh material used in the AS experimental settings inside DC furnaces.

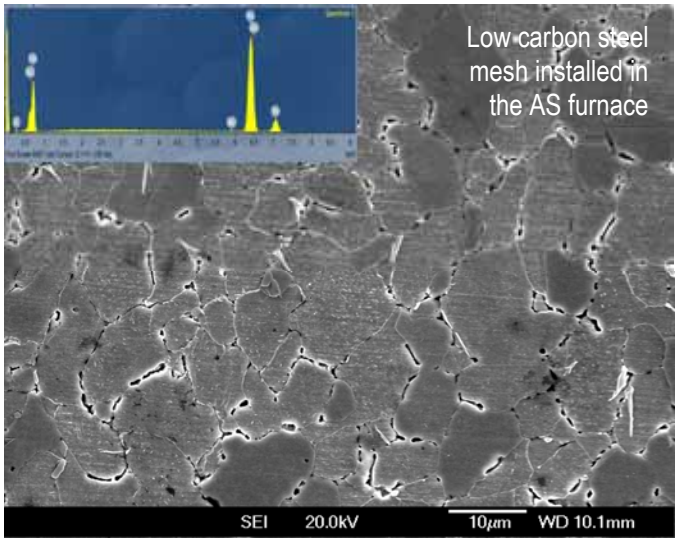

Figure 4.3-13: Micrograph and EDX spectrum of the mesh material used in the AS industrial unit

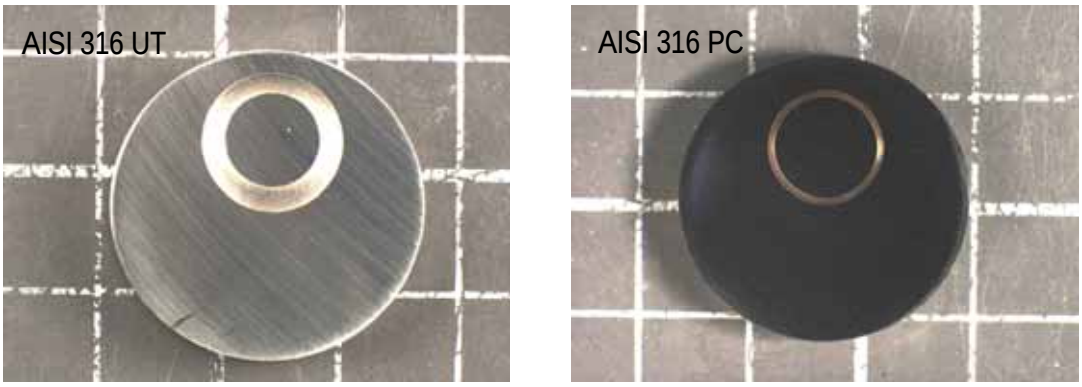

Figure 4.4-1: Typical appearance of the wear tracks on AISI 316 UT and AISI 316 PC

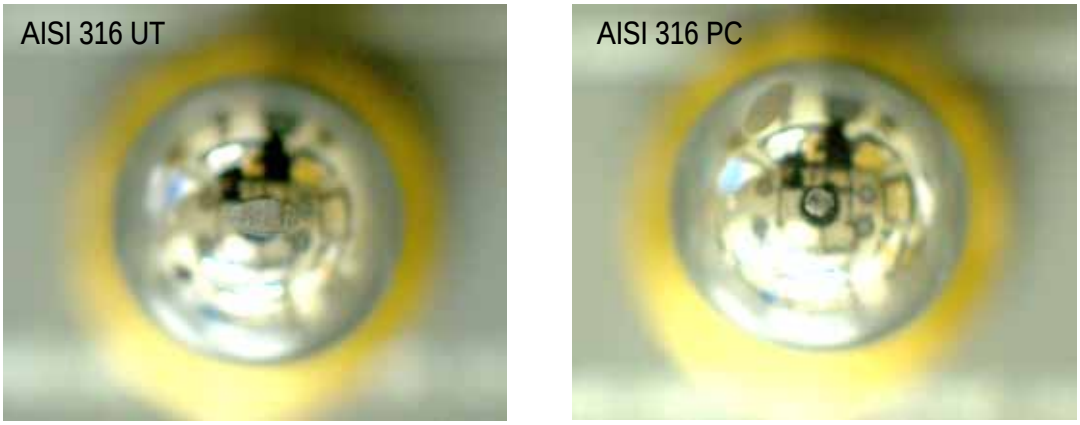

Figure 4.4-2: Appearance of the WC-Co ball worn against AISI 316 UT and AISI 316 PC

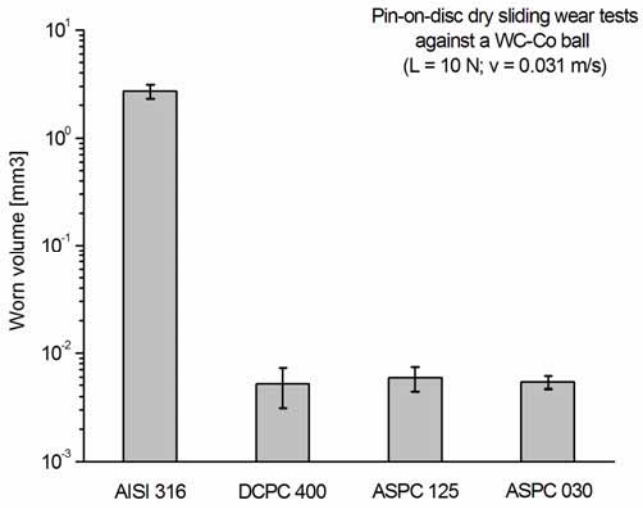

Figure 4.4-3: Measured worn volume after pin-on-disc test

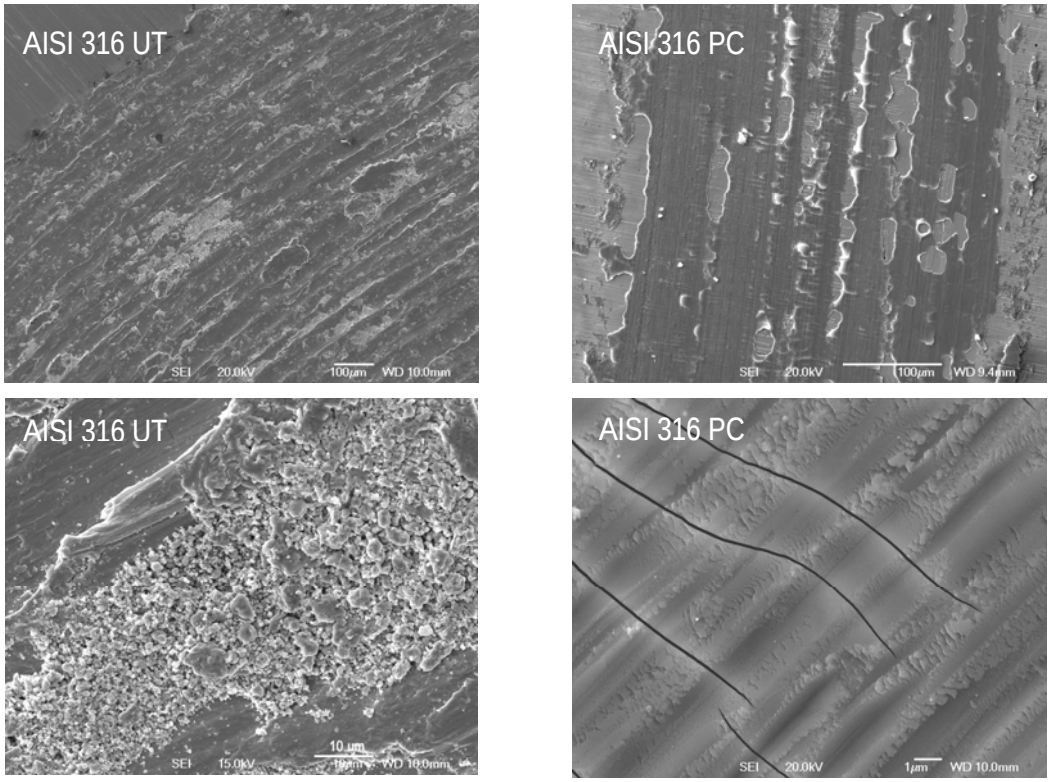

Figure 4.4-4: SEM images of the wear tracks on AISI 316 UT and AISI 316 PC

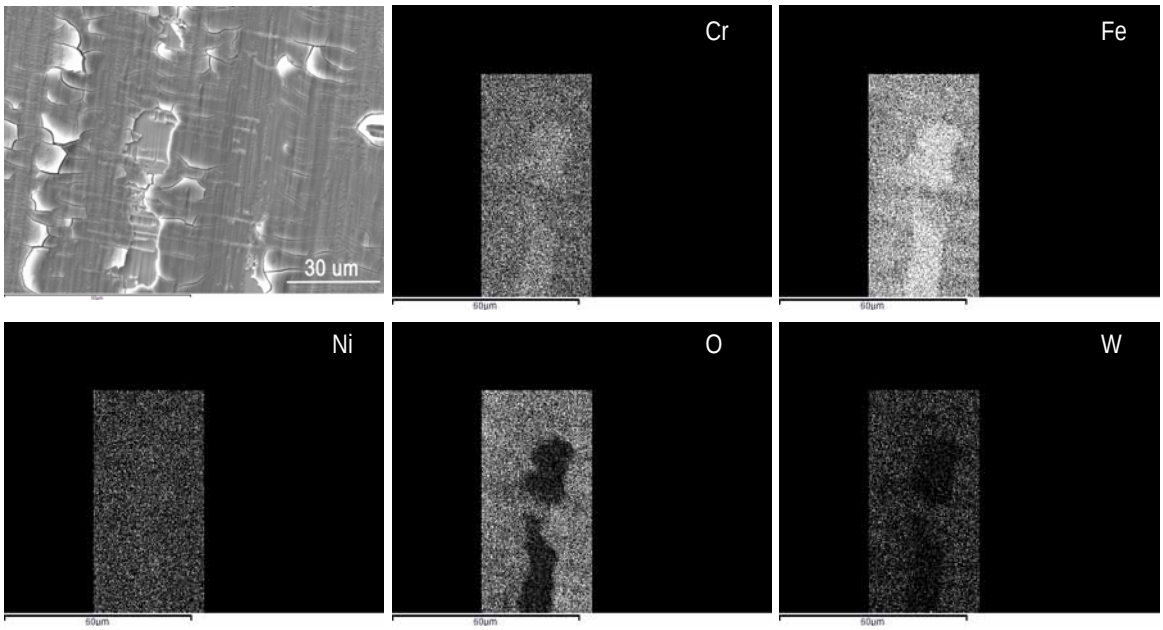

Figure 4.4-5: EDX maps on the wear track left on AISI 316 PC worn against WC-Co ball

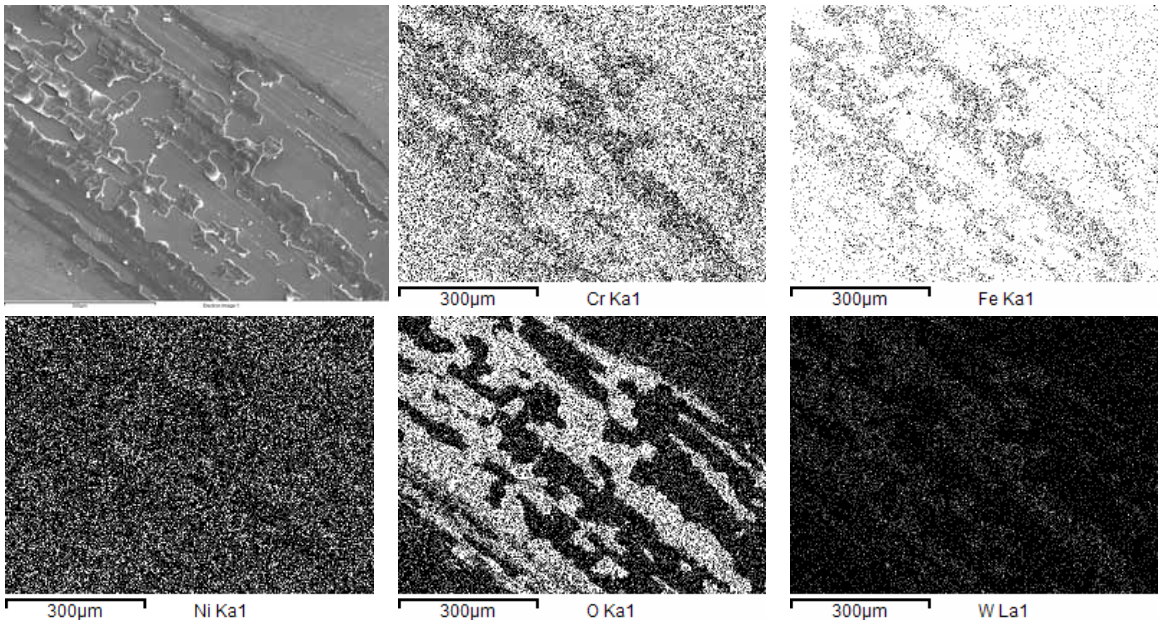

Figure 4.4-6: EDX maps on the wear track left on AISI 316 PC worn against WC-Co ball

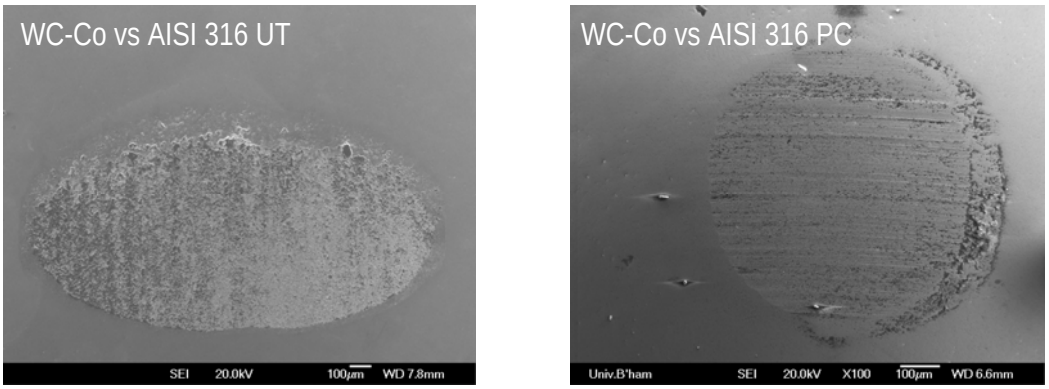

Figure 4.4-7: SEM images of the wear scars of WC-Co balls worn against AISI 316 UT and AISI 316 PC

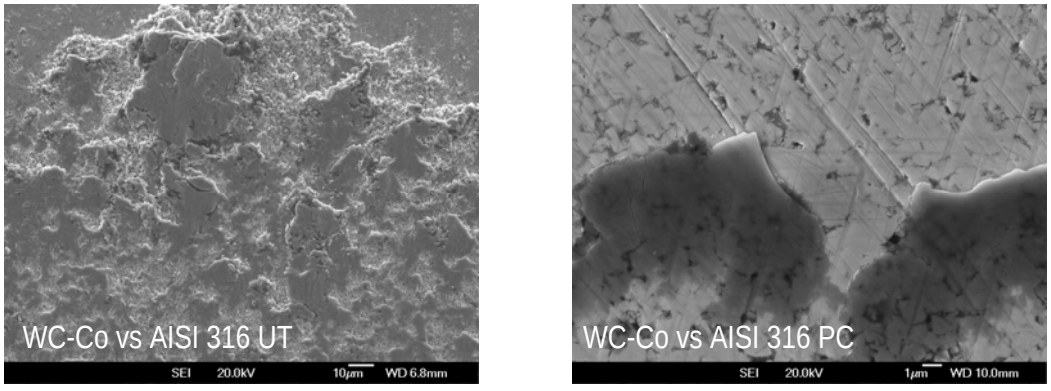

Figure 4.4-8: SEM images of the material accumulated at the trailing edge of the wear scar of WC-Co balls worn against AISI 316 UT and AISI 316 PC

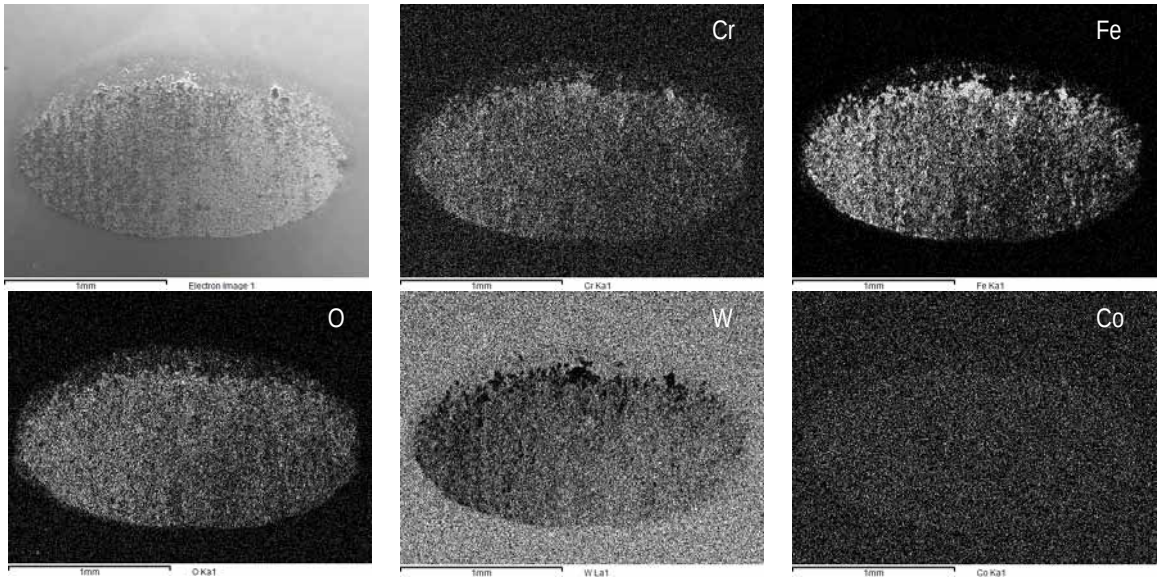

Figure 4.4-9: EDX mapping of the wear scar left on the WC-Co ball worn AISI 316 UT

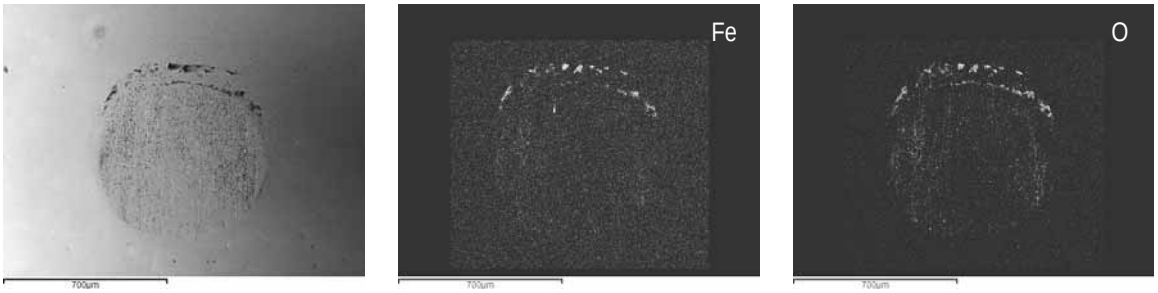

Figure 4.4-10: EDX map of the wear scar left on the WC-Co ball worn against AISI 316 PC

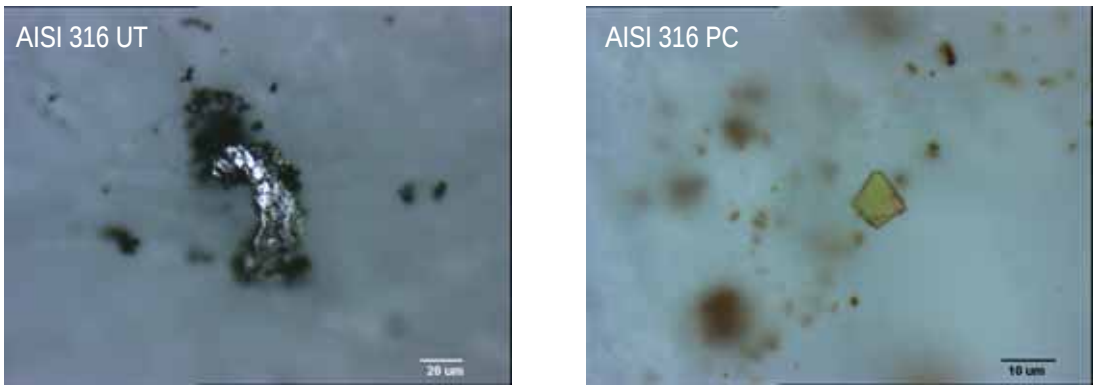

Figure 4.4-11: Wear debris from untreated and carburised AISI 316 respectively

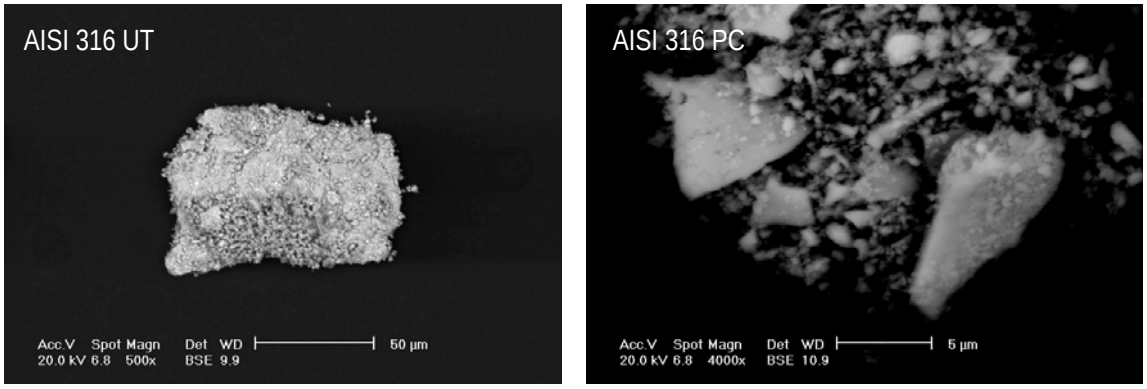

Figure 4.4-12: SEM BSE micrograph of wear debris from AISI 316 UT and AISI 316 PC

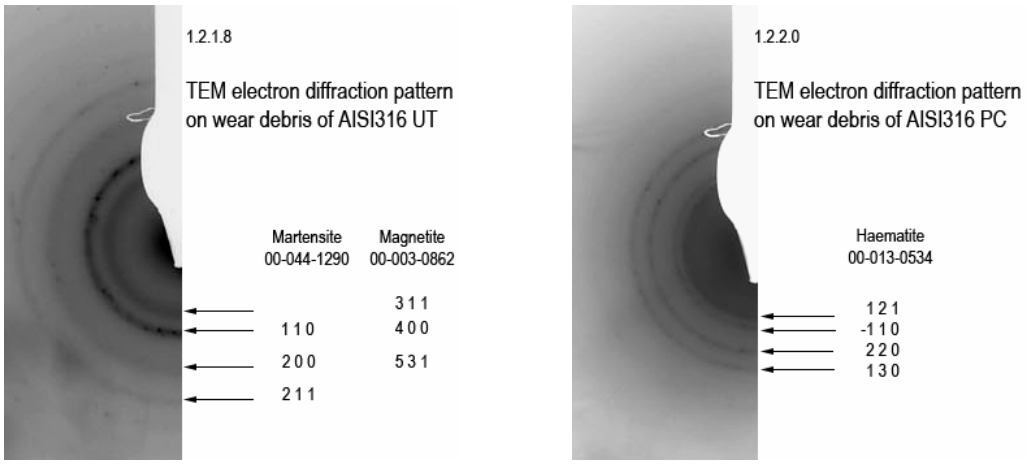

Figure 4.4-13: Electron diffraction patterns on wear debris from AISI 316 UT and AISI 316 PC

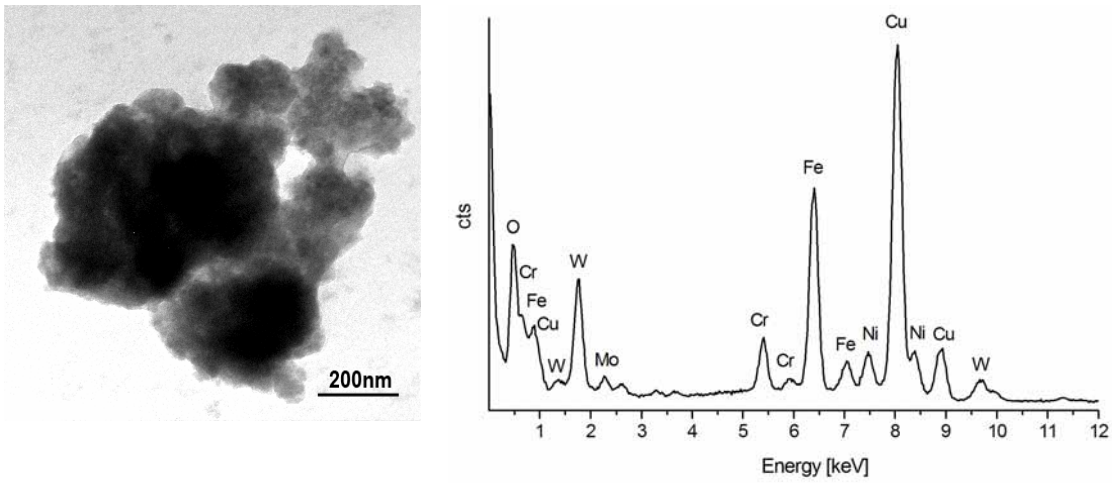

Figure 4.4-14: TEM micrograph of wear debris from AISI 316 PC and the EDX spectrum

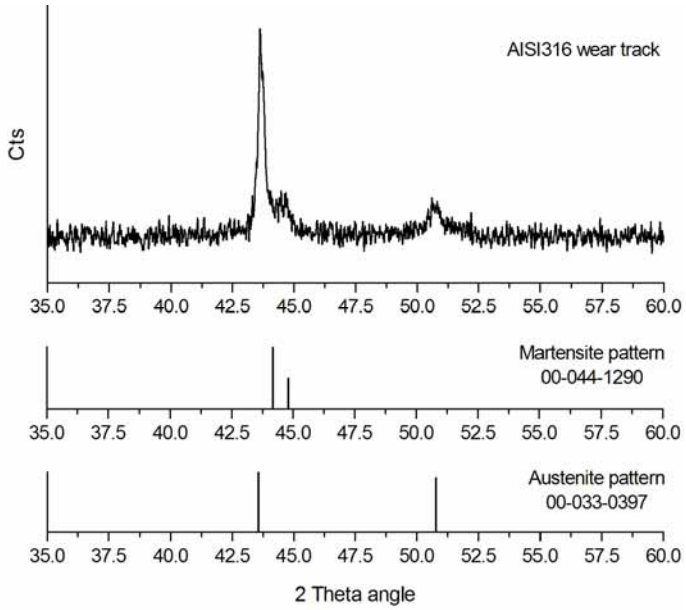

Figure 4.4-15: XRD pattern of the deformed material on the wear track of AISI 316 UT

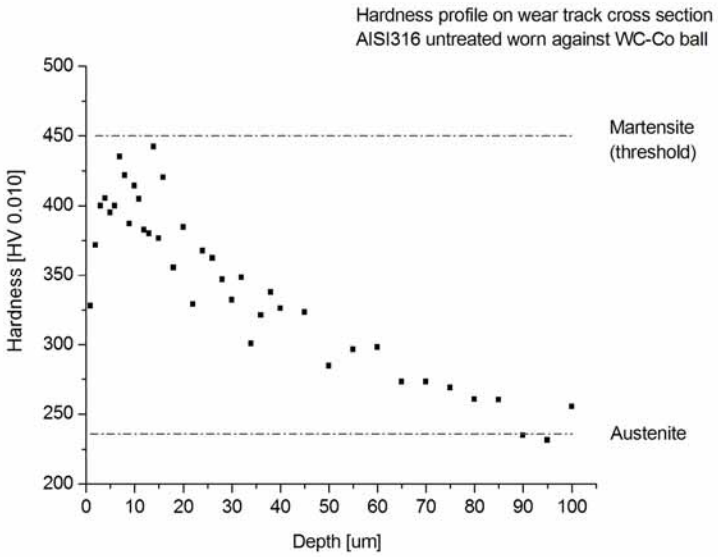

Figure 4.4-16: Hardness profile measured on the cross section of one AISI 316 UT sample worn against WC-Co

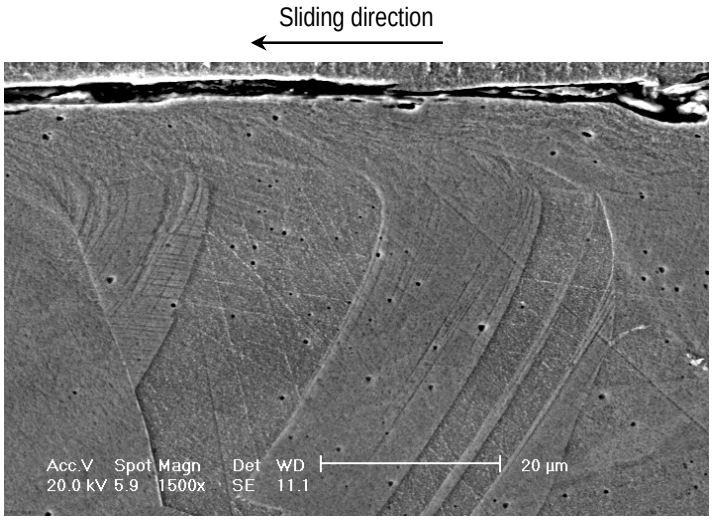

Figure 4.4-17: SEM cross section image of the wear track of AISI 316 UT worn against WC-Co

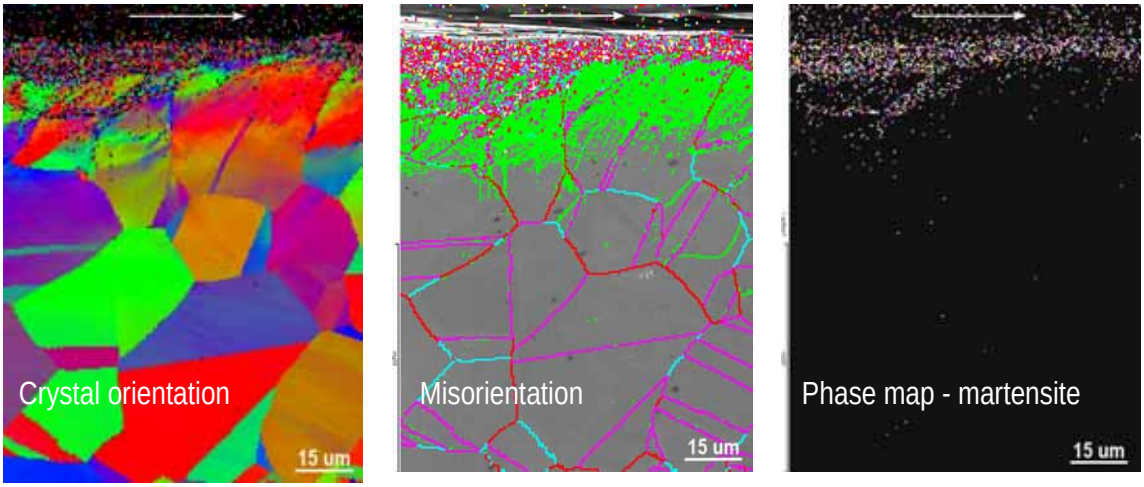

Figure 4.4-18: EBSD crystal orientation maps of the distorted layer, and martensite phase map on the cross section of the wear track of one AISI 316 UT specimen
The arrow indicates the sliding direction

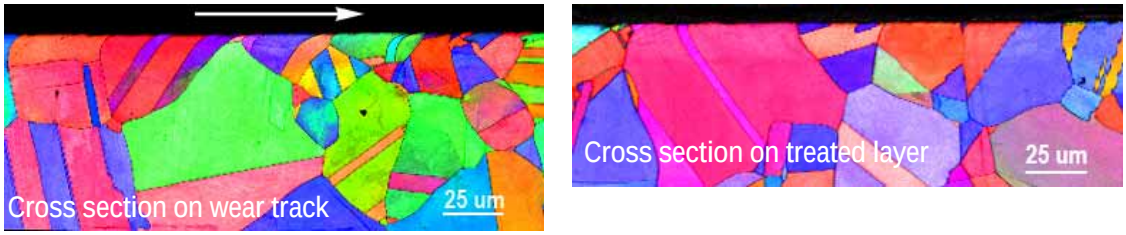

Figure 4.4-19: EBSD crystal orientation maps on cross sections of an AISI 316 PC specimen
The arrow indicates the sliding direction

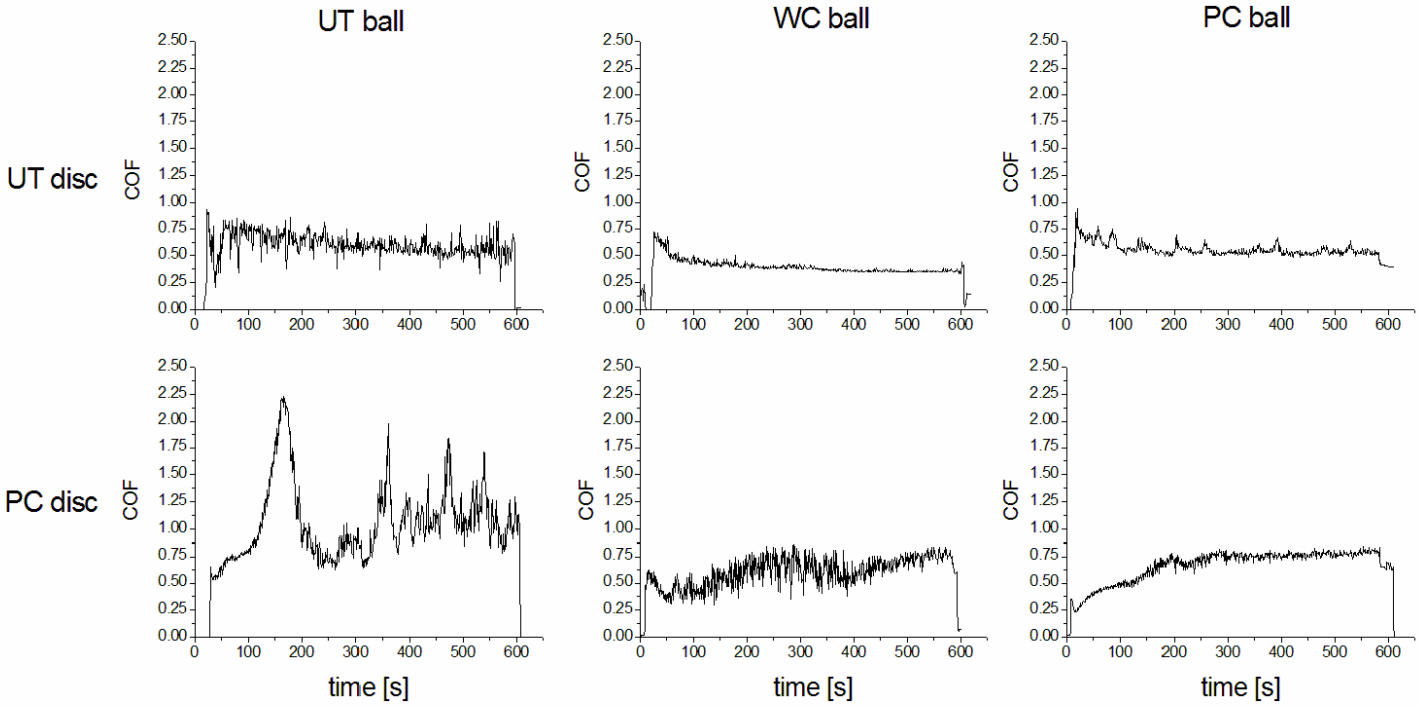

Figure 4.4-20: Coefficients of friction obtained from different material pairs

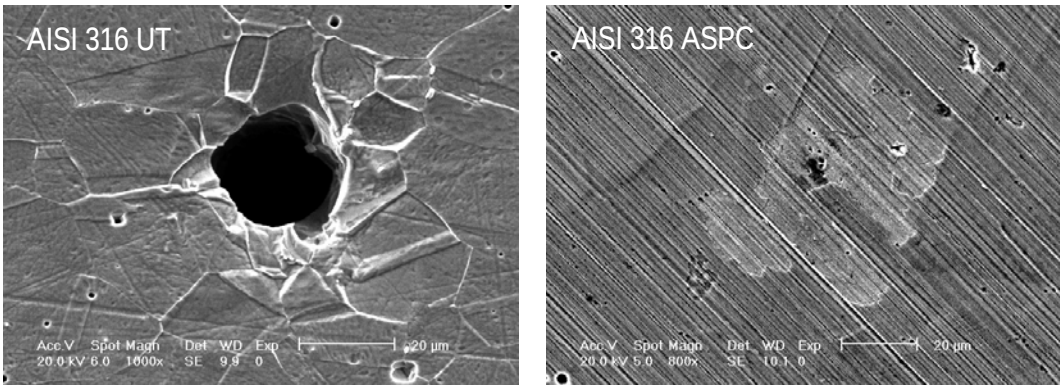

Figure 4.5-1: Immersion corrosion test in H_2SO_4 16% solution at room temperature for 120 h
AISI 316 – Attack on a MnS inclusion; ASPC – Deposition layer of carbides pealing off

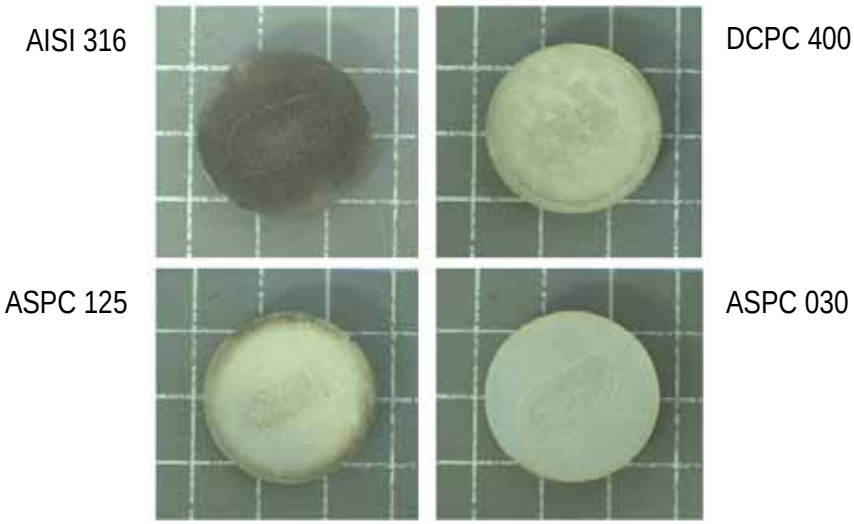

Figure 4.5-2: Surface appearance of AISI 316, DCPC 400 , ASPC 125 and ASPC 030 specimens corroded in boiling H_2SO_4 16% solution

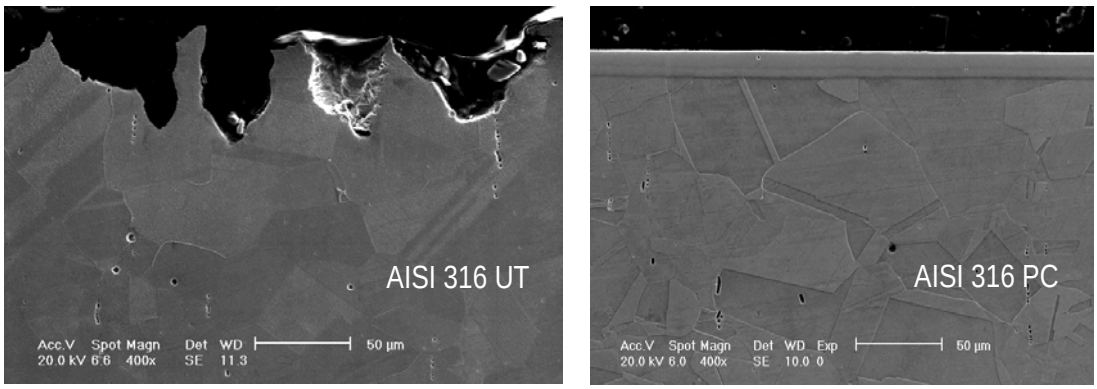

Figure 4.5-3: Cross section of AISI 316 UT and PC specimens exposed to boiling H_2SO_4 16% solution for 1 hour

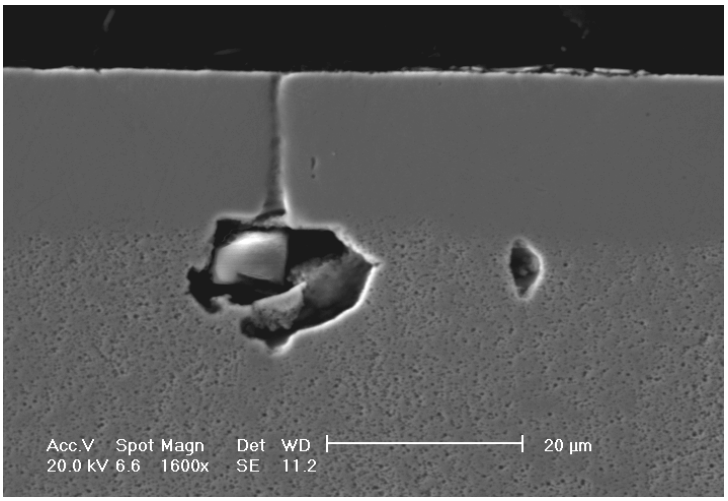

Figure 4.5-4: Cross section of a PC specimen exposed to boiling H_2SO_4 16% solution for 1 h
Localised attack on MnS inclusions

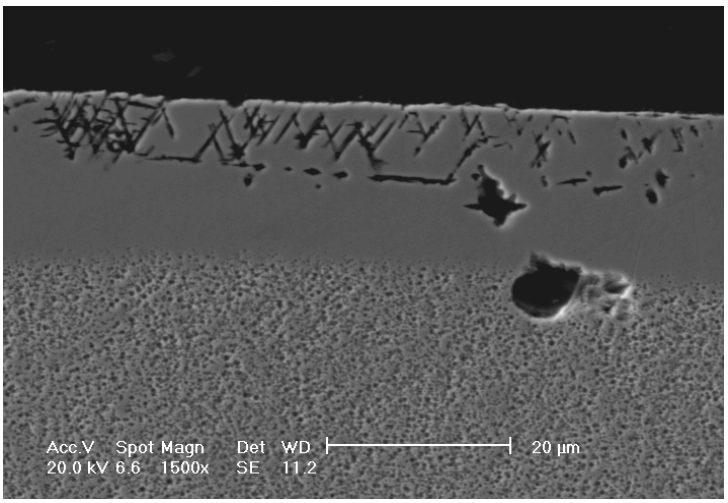

Figure 4.5-5: Cross section of a PC specimen corroded in boiling H_2SO_4 16% solution for 1 h
Localised attack on slip bands

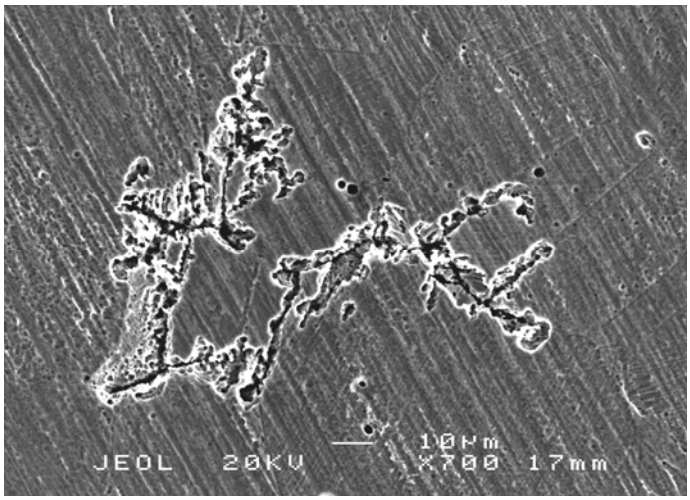

Figure 4.5-6: Plan view of a PC specimen immersed in boiling H_2SO_4 16% solution for 15 h
Localised attack on grain boundaries

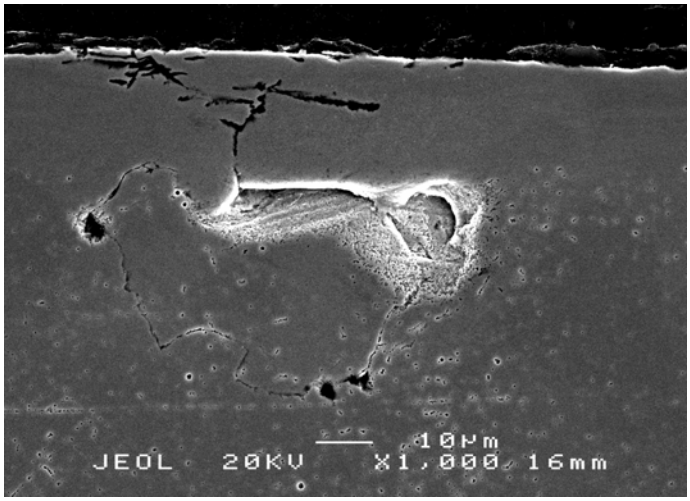

Figure 4.5-7: Cross section of a PC specimen corroded in boiling H_2SO_4 16% solution for 1 h
Corrosion progressing through grain boundaries of the AISI316 substrate once the EA layer had been penetrated

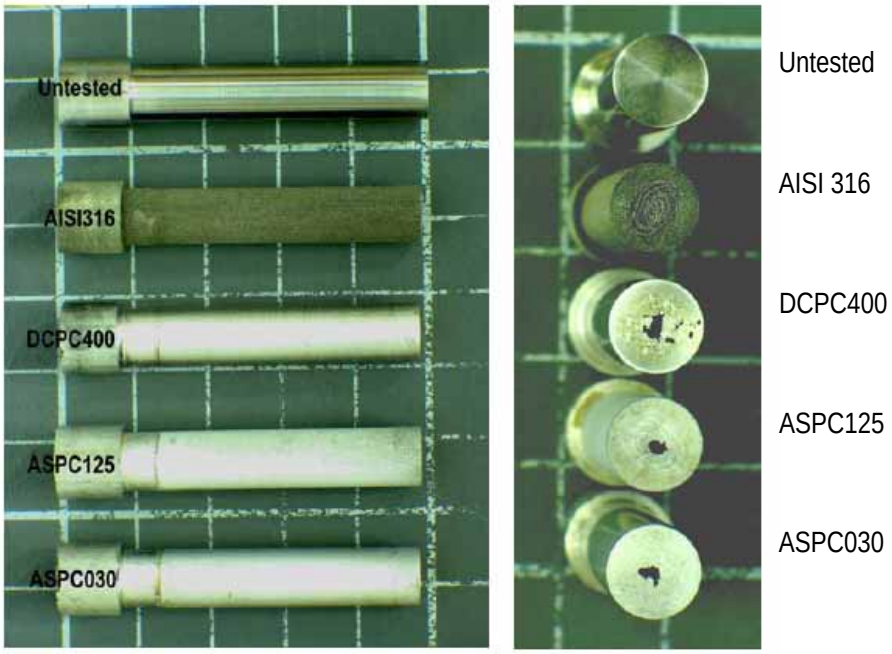

Figure 4.5-8: Rod samples used for corrosion tests in boiling H_2SO_4 16% solution

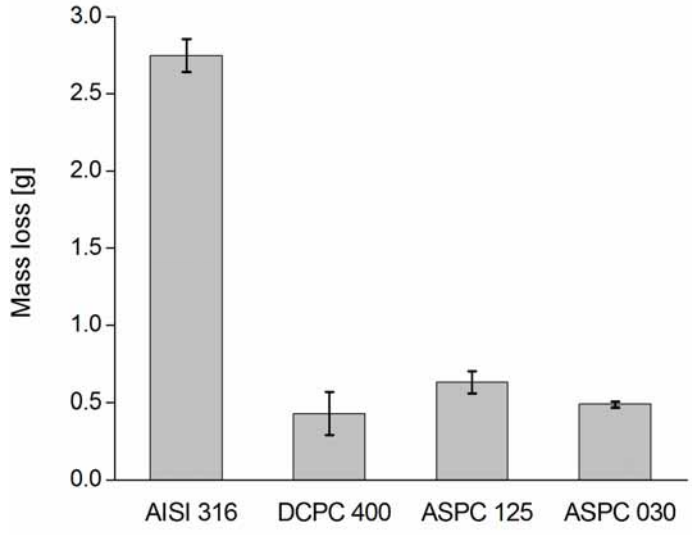

Figure 4.5-9: Mass loss specimens after immersion corrosion test in boiling H_2SO_4 16% solution for 20 hours

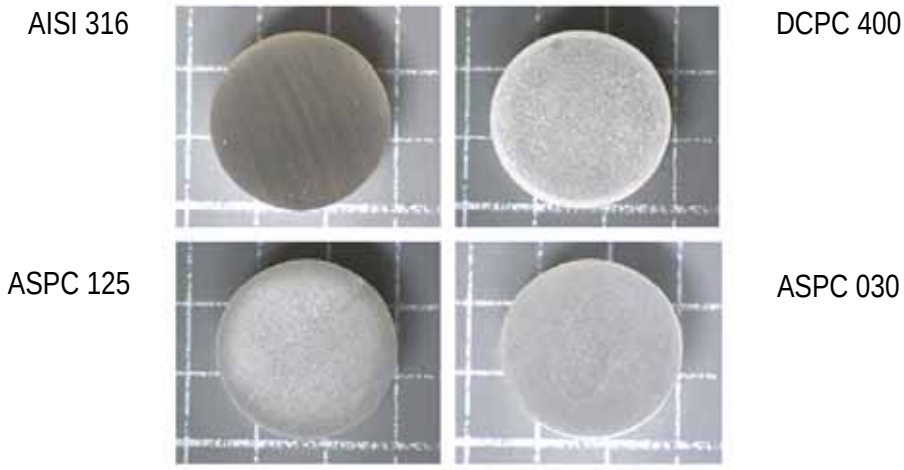

Figure 4.5-10: Coupon samples exposed to boiling H_2SO_4 16% solution with $CuSO_4$ for 20 h

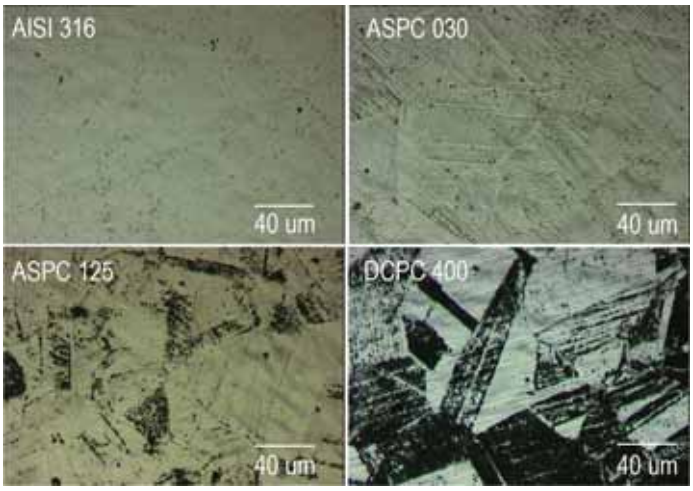

Figure 4.5-11: Optical micrographs of specimens corroded in boiling H_2SO_4 16% solution with $CuSO_4$ for 20 h

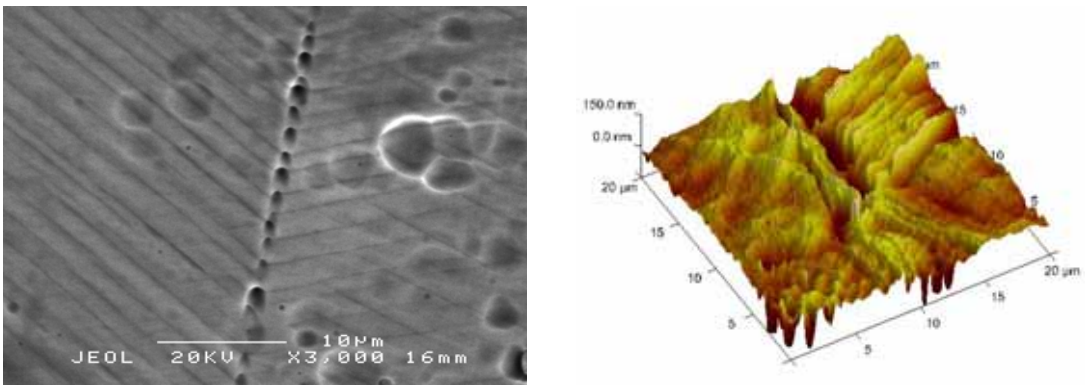

Figure 4.5-12: SEM micrograph of pits coalescing at the intersection of slip bands with a grain boundary, and AFM image of the attack on slip bands and formation of ditch grain boundary

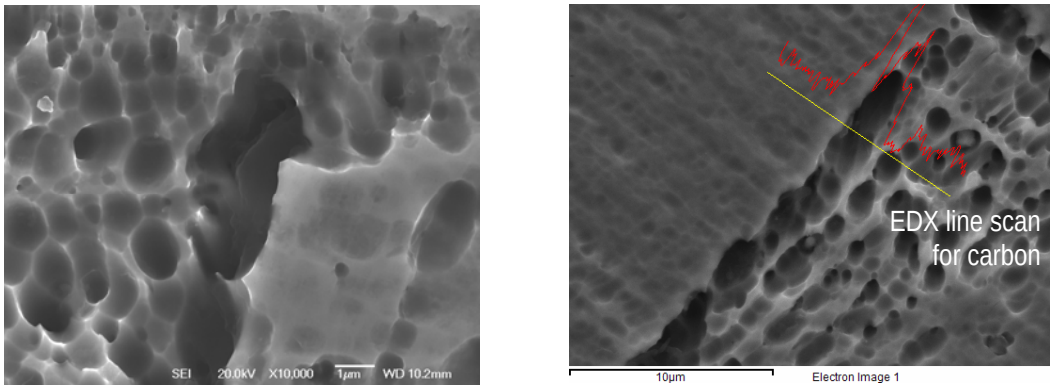

Figure 4.5-13: SEM micrograph of a ditch type grain boundary and EDX Carbon line scan on a similar boundary

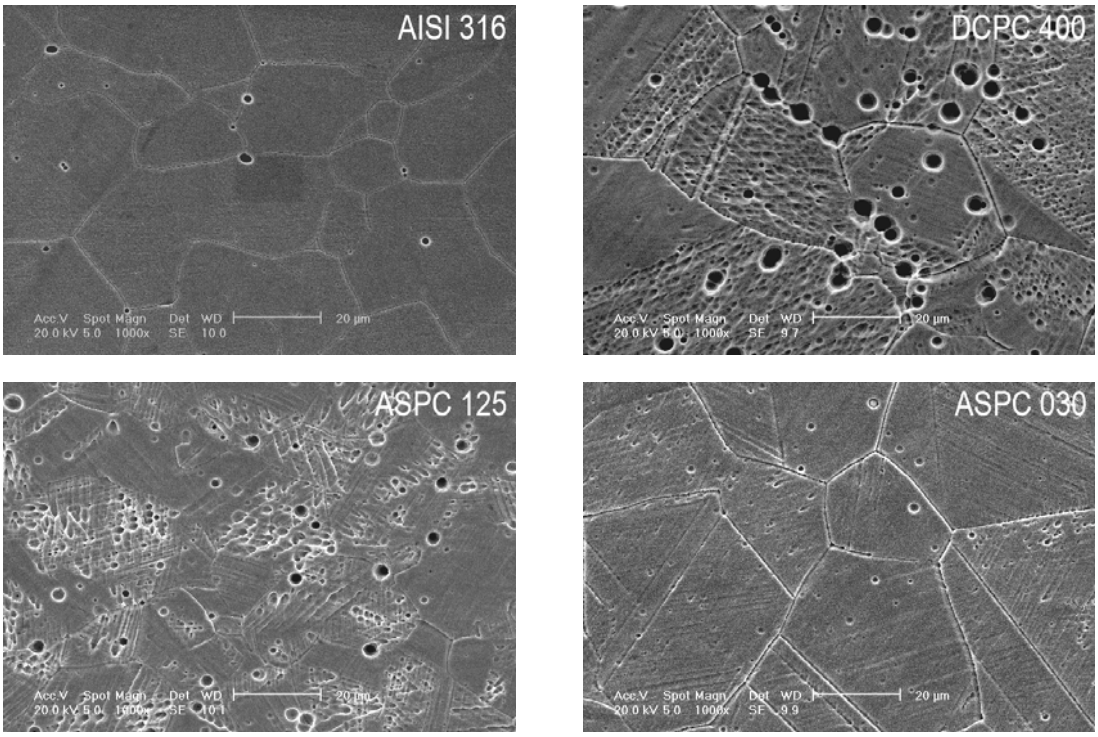

Figure 4.5-14: SEM micrographs of samples corroded in boiling HNO_3 20% solution for 240 hours

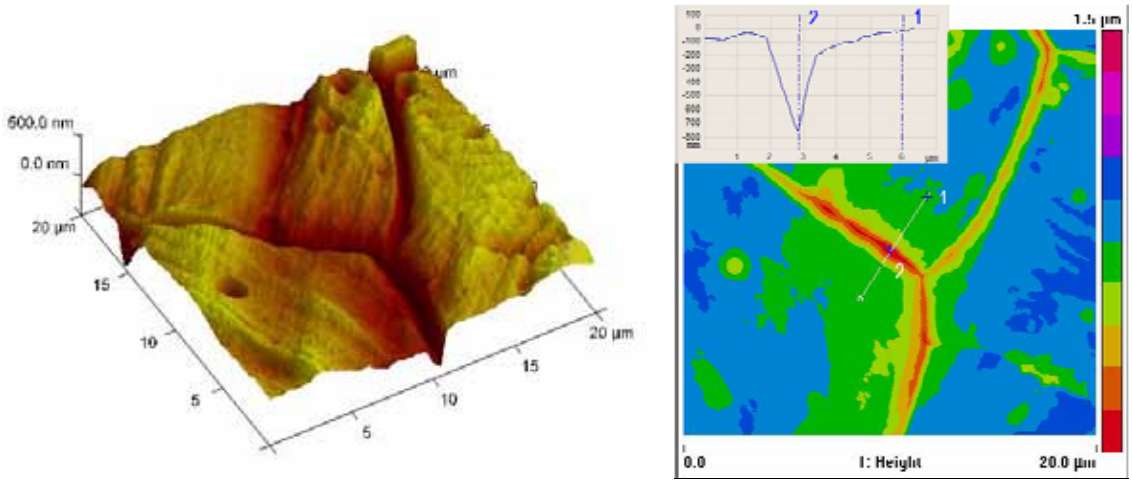

Figure 4.5-15: AFM image of localised corrosion at grain boundaries and cross section data. Sample DCPC 400 after immersion corrosion test in boiling HNO_3 20% solution for 240 hours

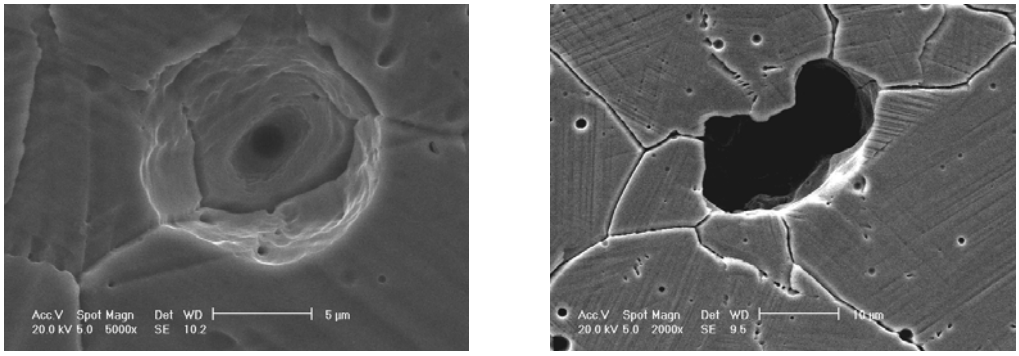

Figure 4.5-16: Localised attack on samples exposed to boiling HNO_3 20% solution for 240 h

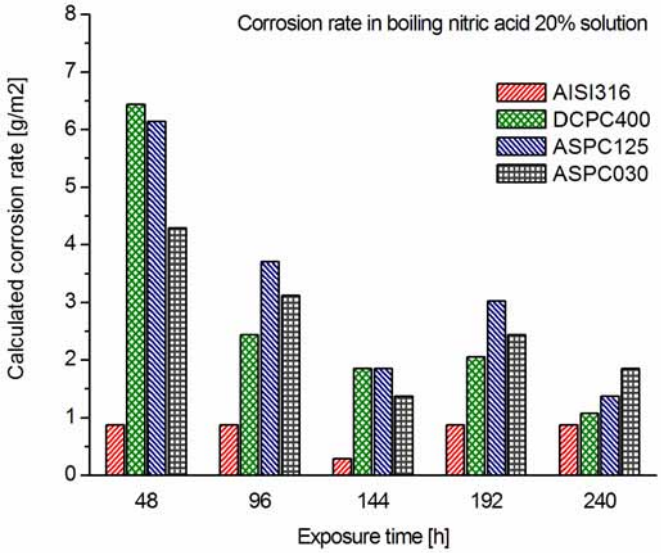

Figure 4.5-17: Corrosion rates in boiling HNO_3 20% solution for different periods of time

Carburising

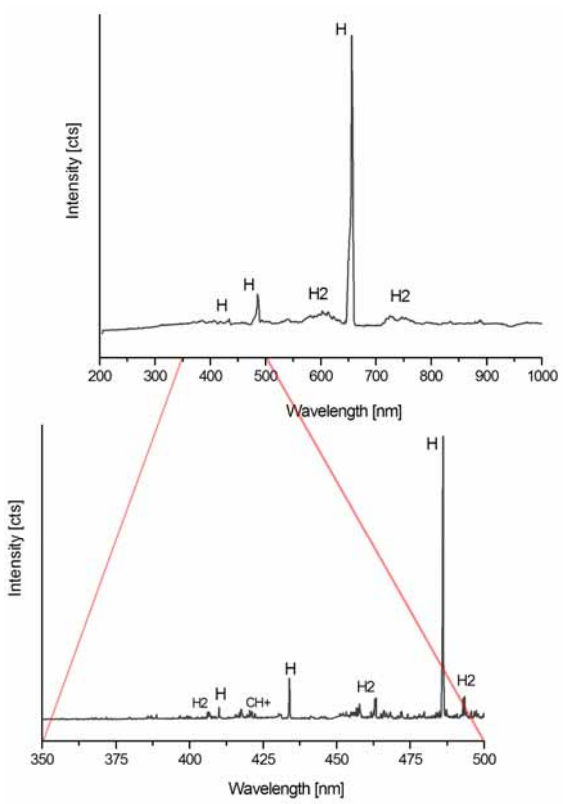

Figure 4.6-1: Low and high resolution spectra for plasma carburising

Nitrogen enhanced carburising

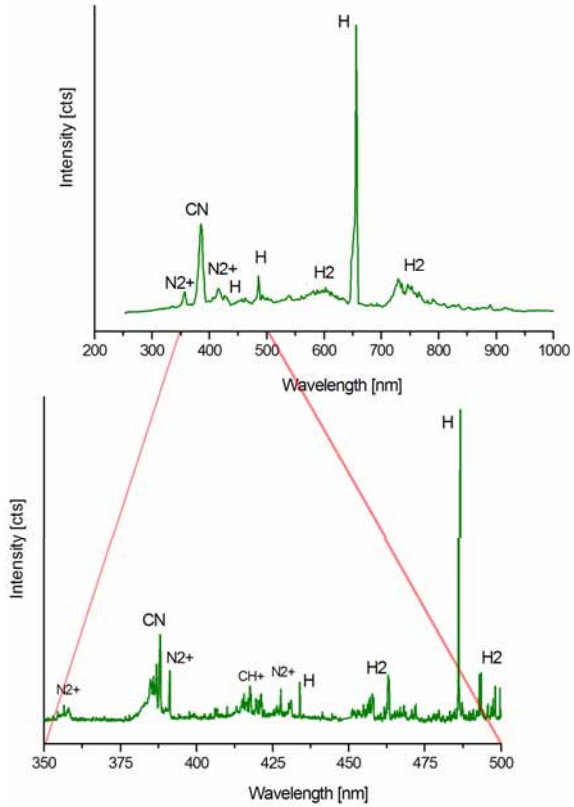

Figure 4.6-2: Low and high resolution spectra for nitrogen enhanced plasma carburising

Nitriding

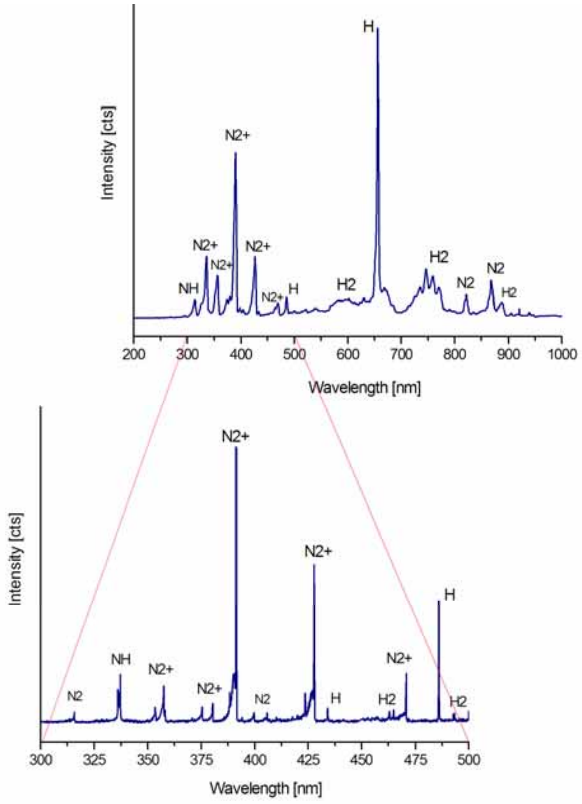

Figure 4.6-3: Low and high resolution spectra for plasma nitriding

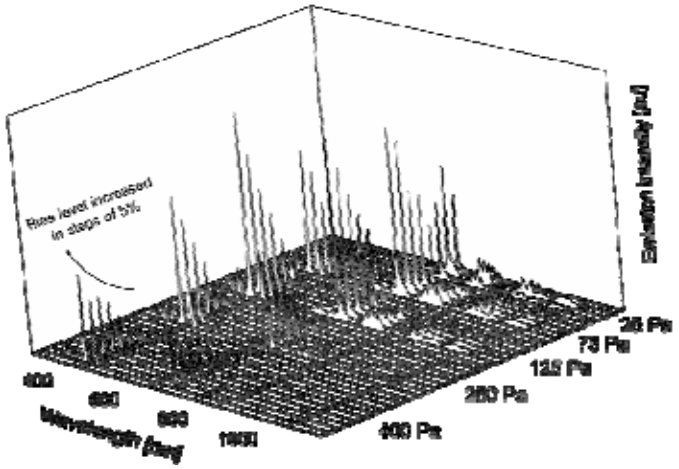

Figure 4.6-4: Simplified emission intensity map obtained for ASPN

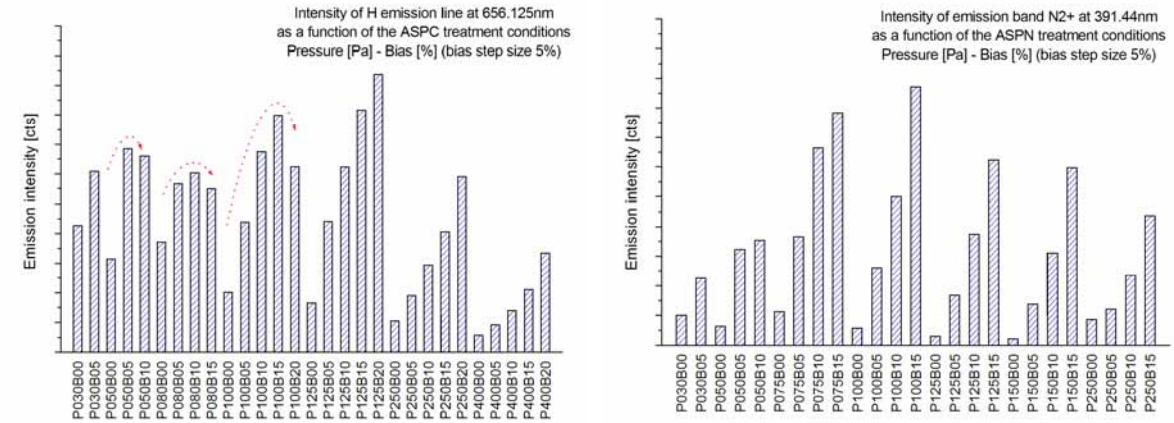

Figure 4.6-5: Summary of the OES intensity maps obtained under ASPC and ASPN treatment conditions

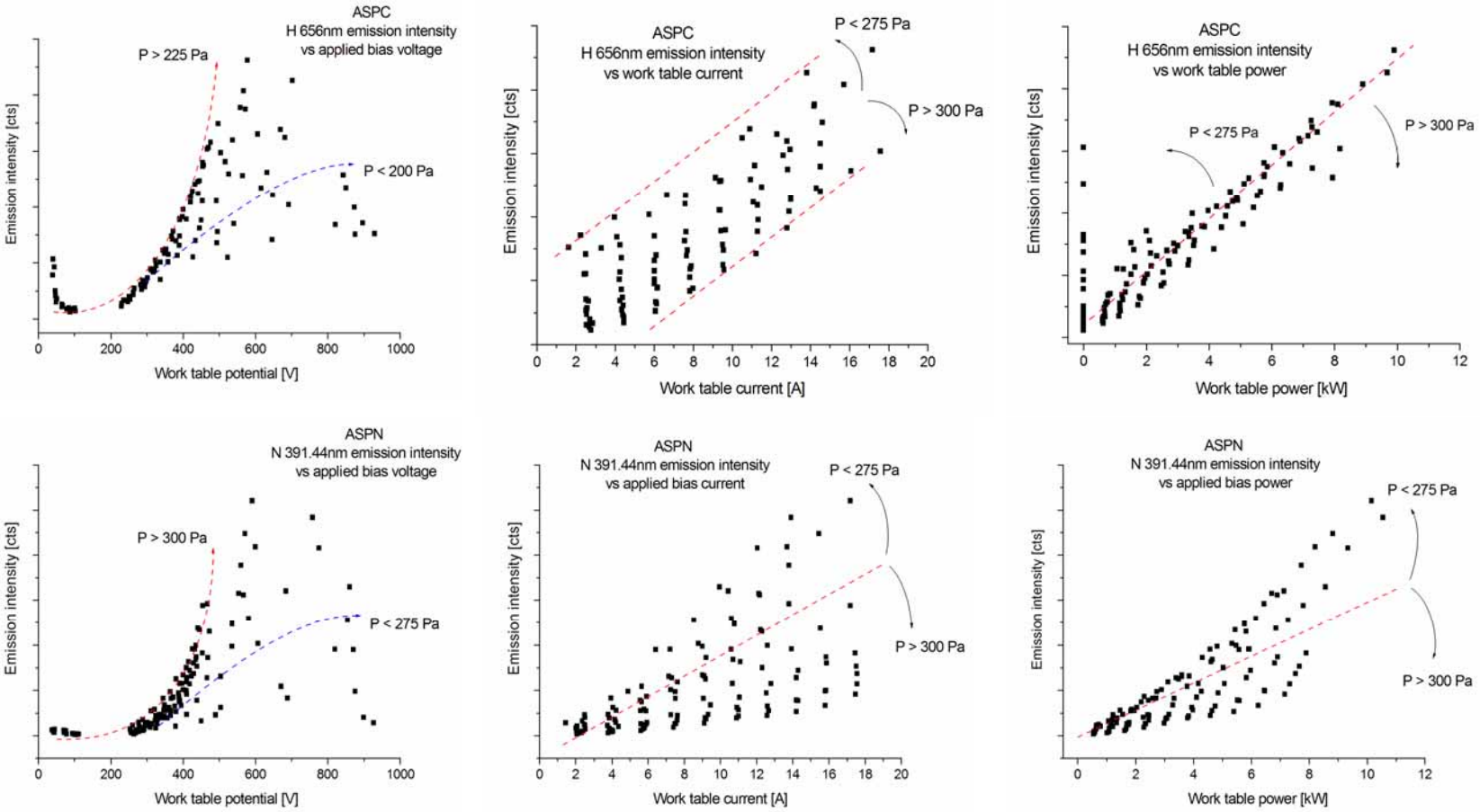

Figure 4.6-6: Correlation between OES emission intensity and the electric parameters of the furnace under ASPC and ASPN treatment conditions

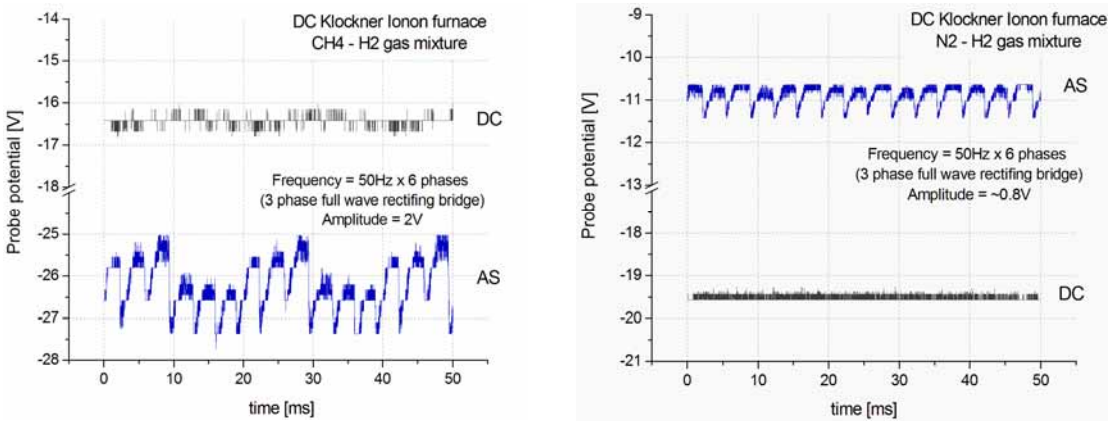

Figure 4.7-1: Oscillations in the floating potential measured with the IFP under DC and AS arrangements inside a DC furnace.

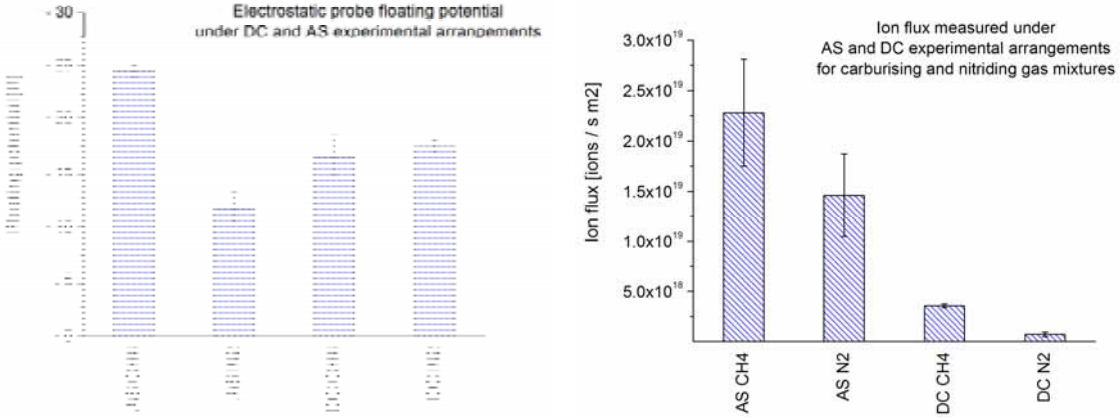

Figure 4.7-2: Floating potential and ion flux measured under DC and AS experimental arrangements inside a DC furnace, in carburising and nitriding gas mixtures

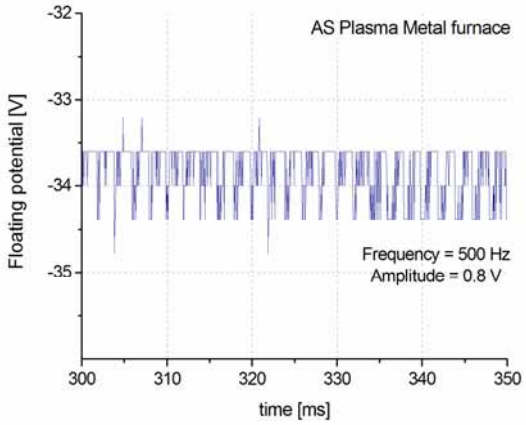

Figure 4.7.3: Oscillations observed in the FP of the IFP inside the AS industrial unit

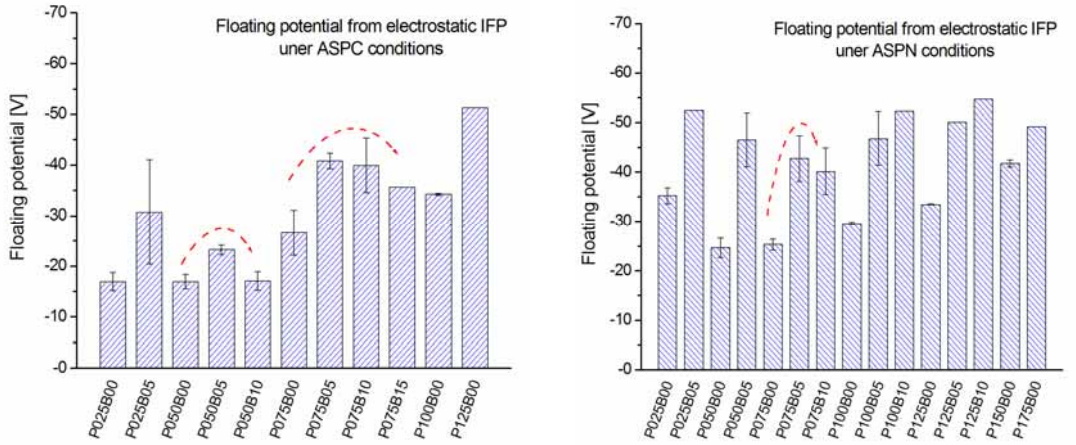

Figure 4.7-4: Average FP measured with the IFP under different ASPC and ASPN conditions

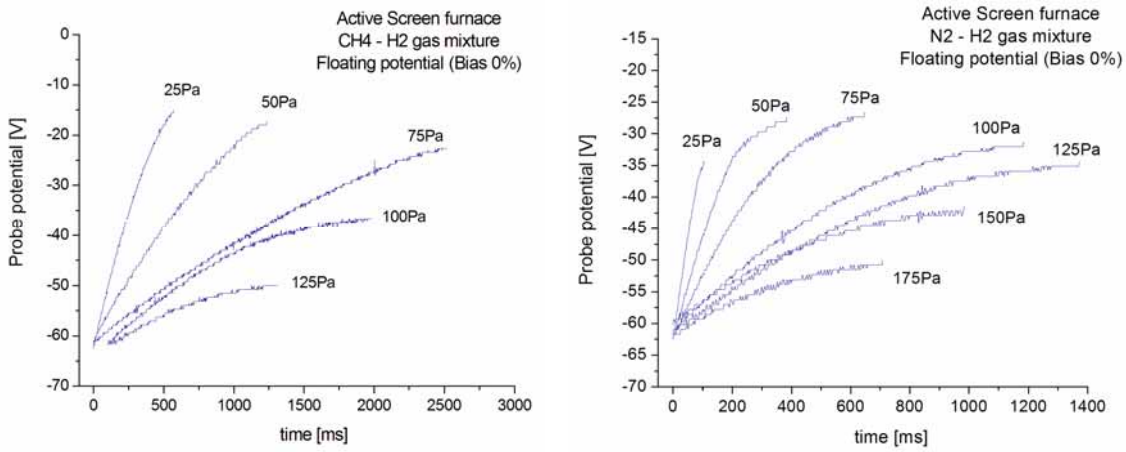

Figure 4.7-5: IFP drain curves obtained at floating potential in ASPC and ASPN conditions

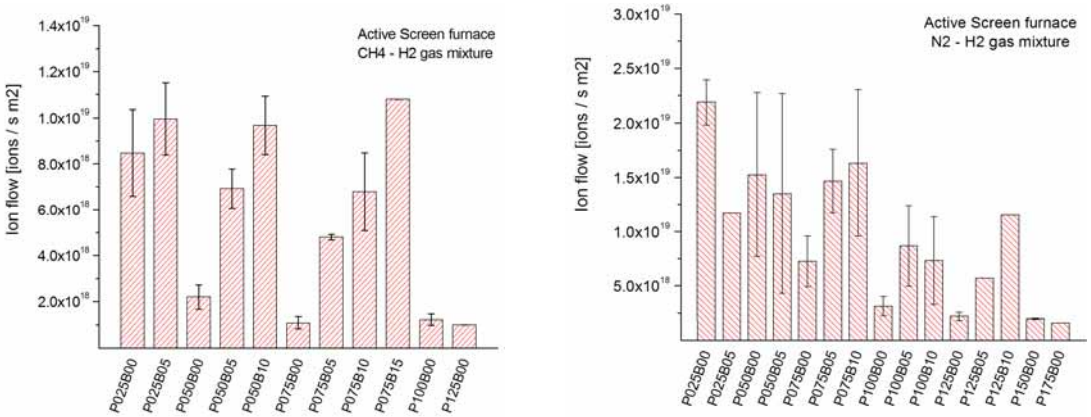

Figure 4.7-6: Ion flux calculated from the drain curves of the IFP in ASPC and ASPN conditions

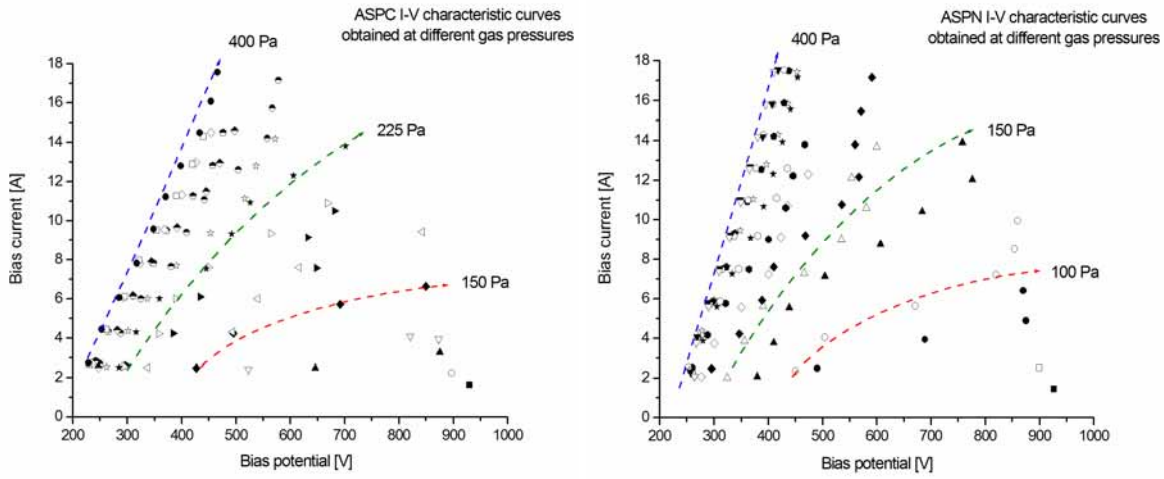

Figure 5.1-1: I-V electric curves obtained for ASPC and ASPN at different gas pressures

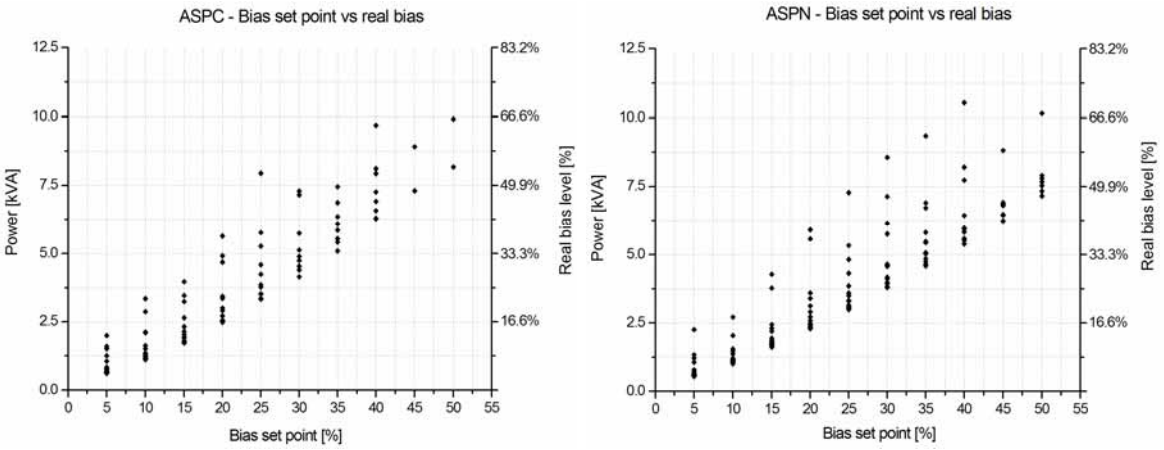

Figure 5.1-2: Bias set point and real bias power applied for ASPC and ASPN conditions

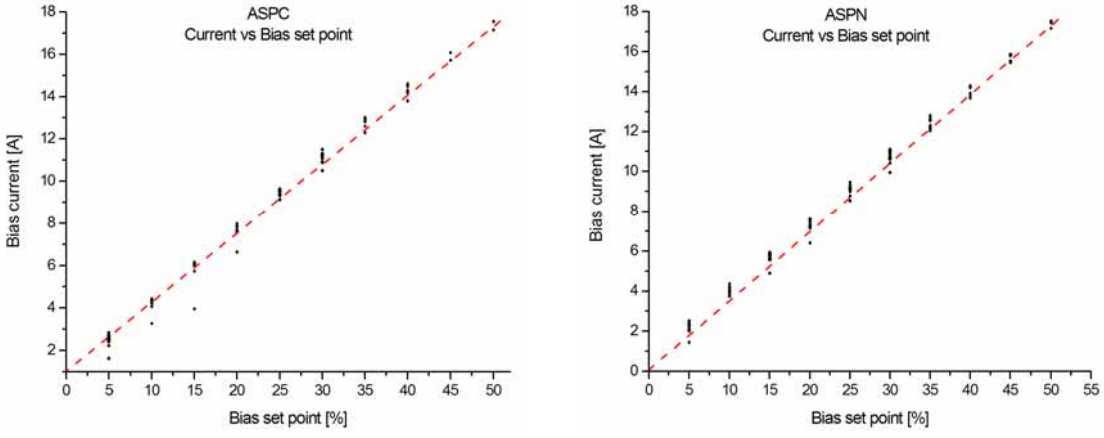

Figure 5.1-3: Bias current vs bias set point for ASPC and ASPN

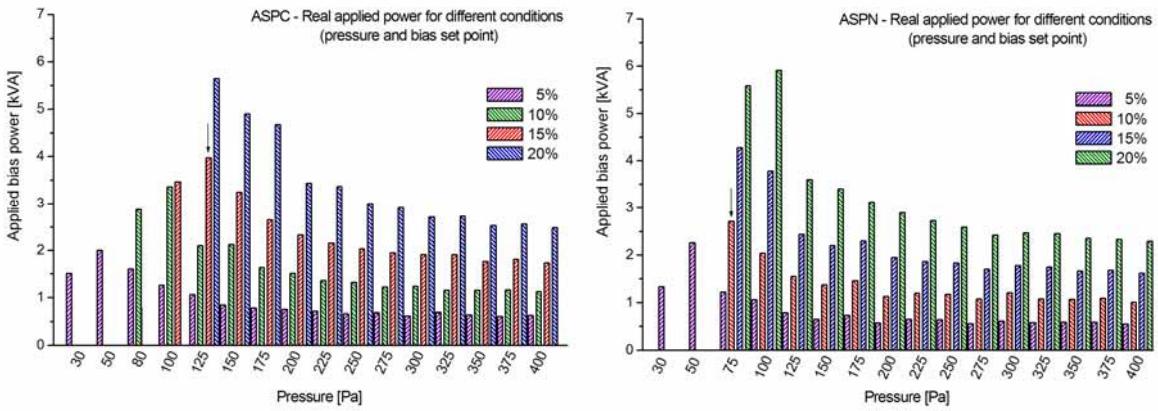

Figure 5.1-4: Worktable power for different ASPC and ASPN treatment conditions (bias levels and pressures)

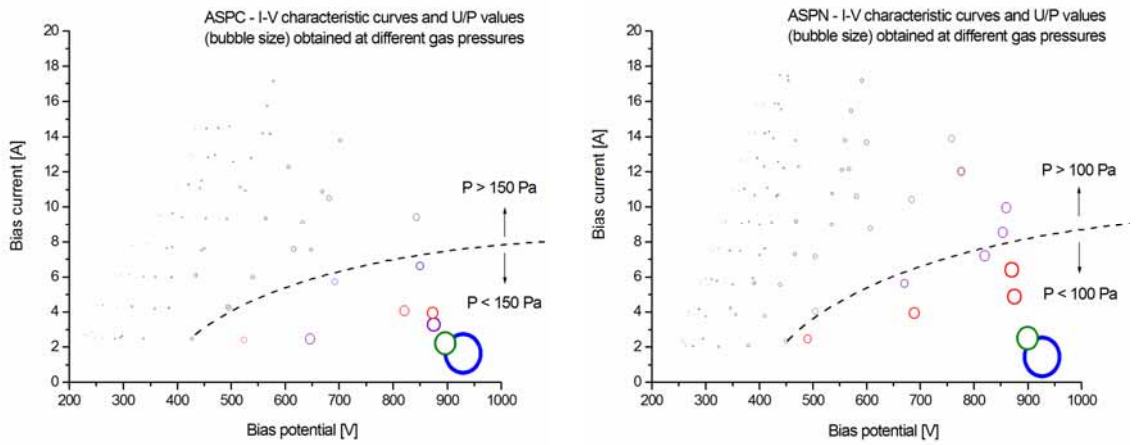

Figure 5.1-5: Characteristic I-V curves for ASPC and ASPN with E/p as bubble size

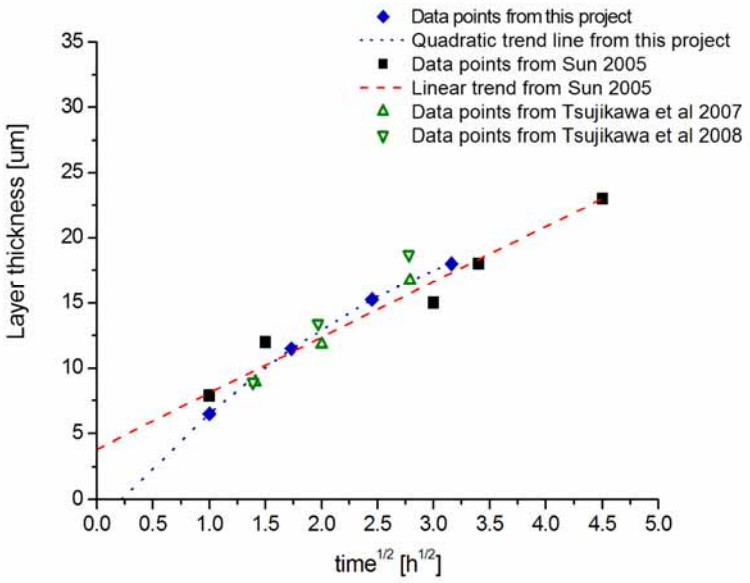

Figure 5.2.1: Layer thickness vs treatment time

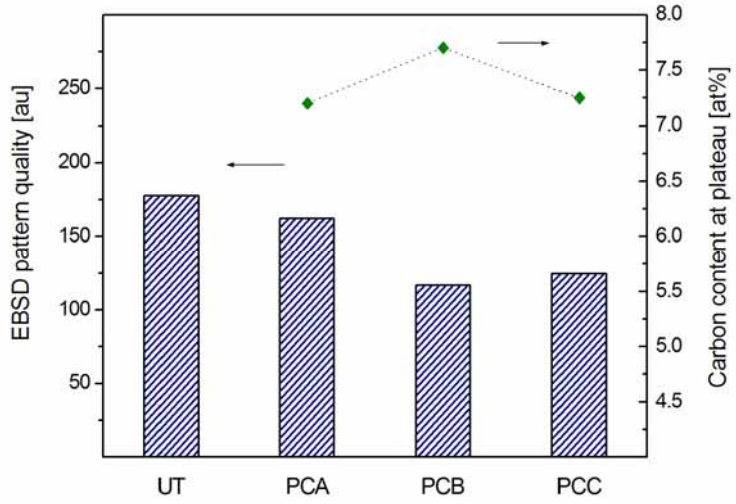

Figure 5.2-2: EBSD pattern quality vs carbon concentration at plateau (GDOES carbon profile)

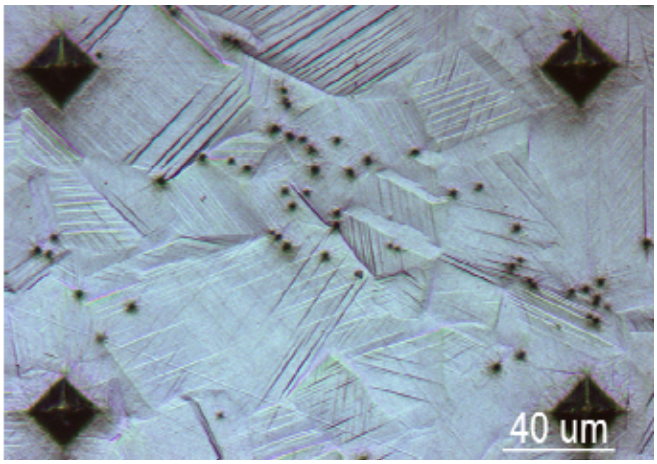

Figure 5.2-3: Optical micrograph on a plasma carburised specimen

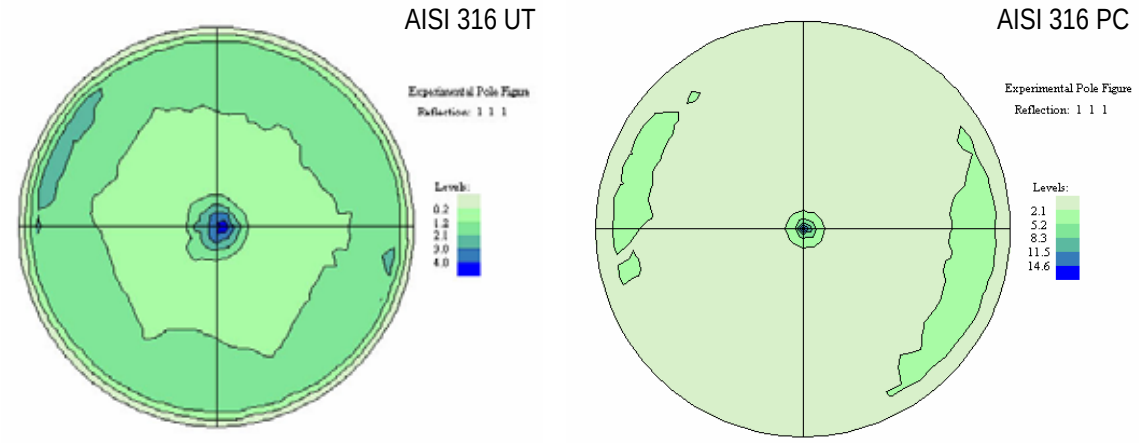

Figure 5.2-4: XRD pole figures obtained on AISI 316 UT and AISI 316 PC

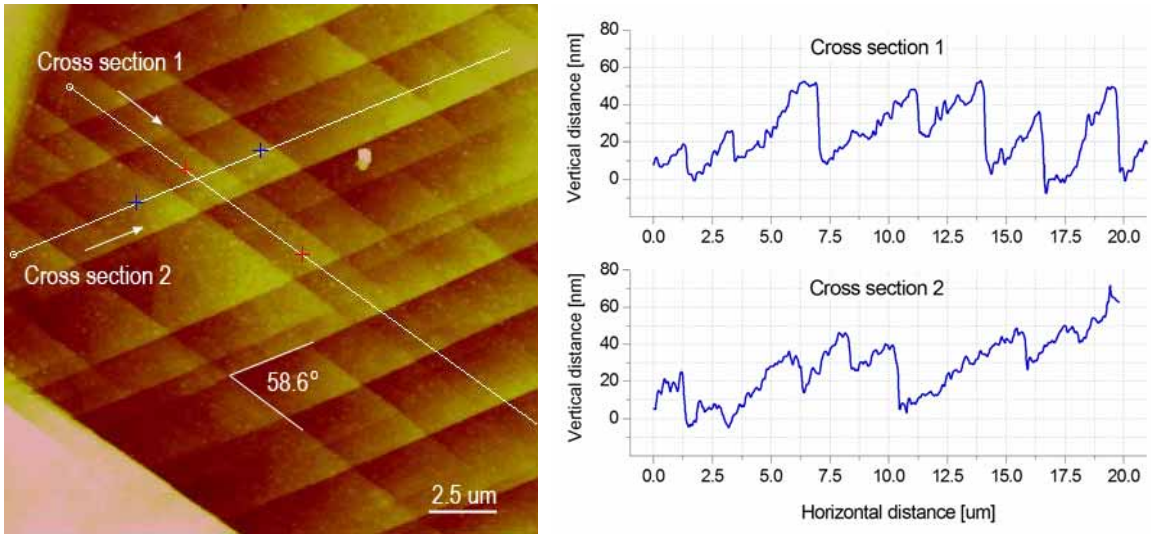

Figure 5.2-5: AFM image of a grain with activated crossed slip systems and cross section profiles

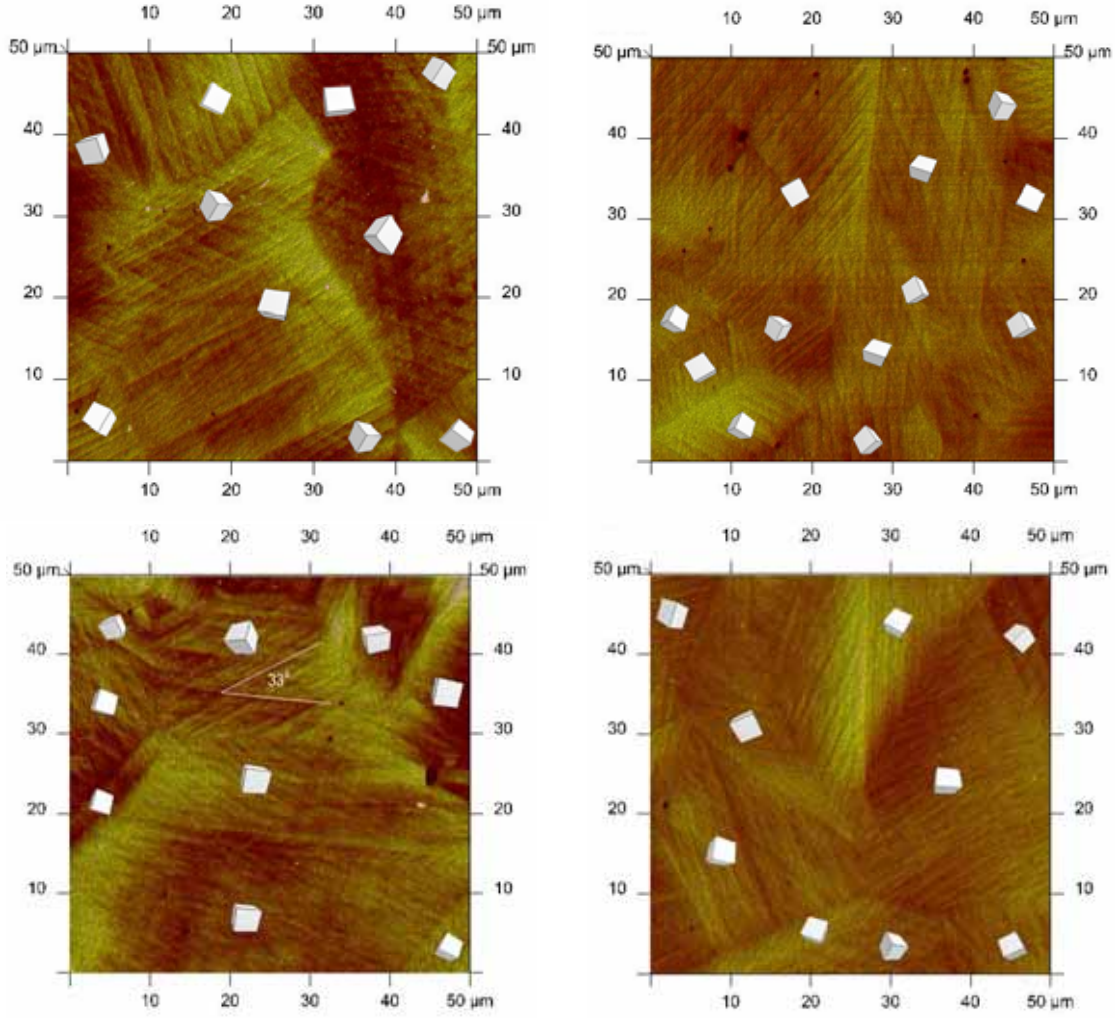

Figure 5.2-6: AFM plane view of PC samples and crystal mimic obtained from EBSD COMs

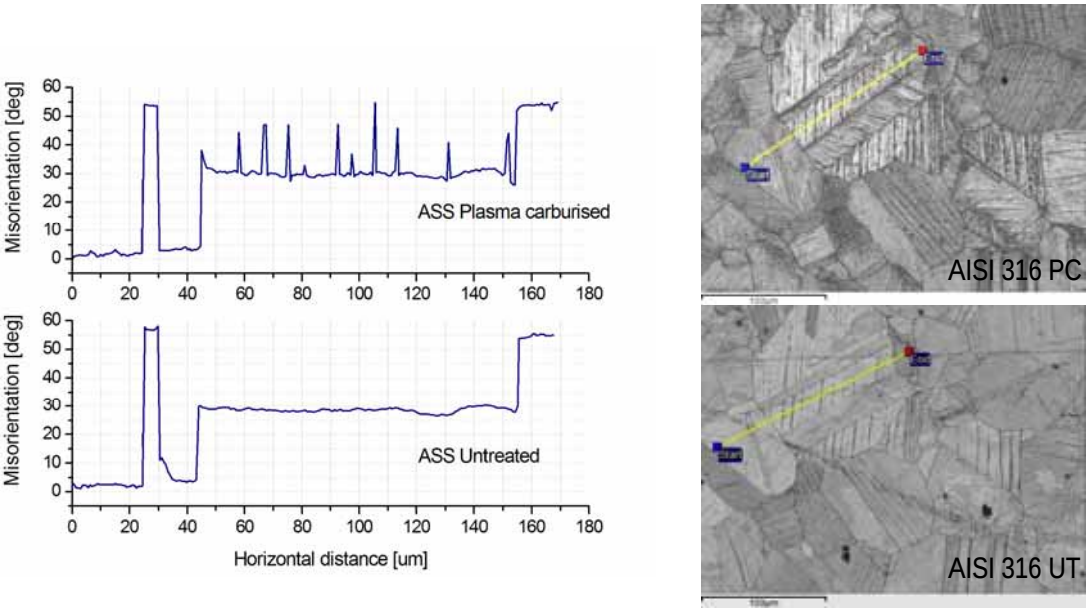

Figure 5.2-7: Misorientation measured by EBSD on the same area of the sample before and after plasma carburising

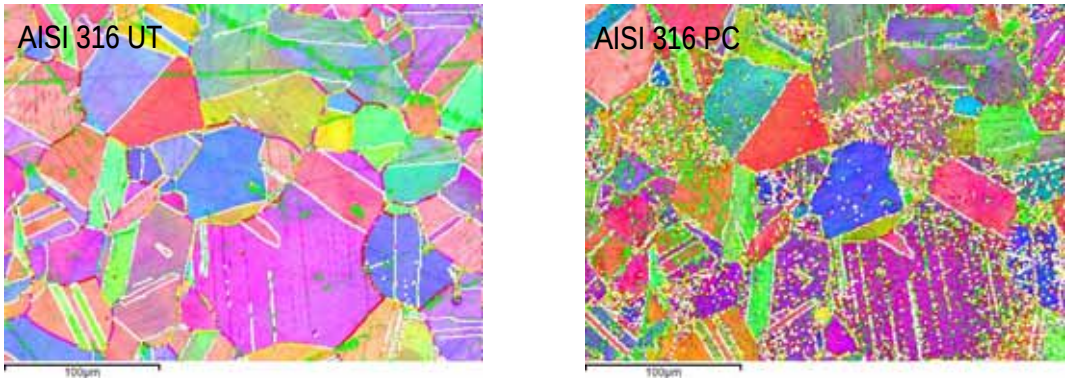

Figure 5.2-8: EBSD crystal orientation (normal direction) before and after PC respectively

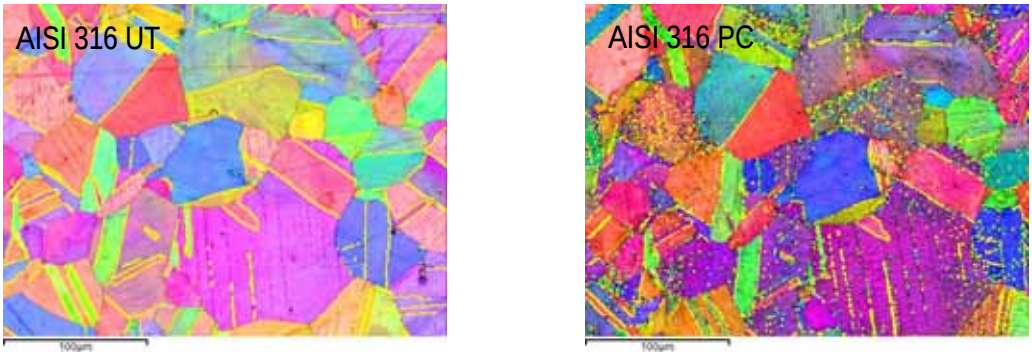

Figure 5.2-9: CSL Σ3 grain boundaries before and after PC respectively

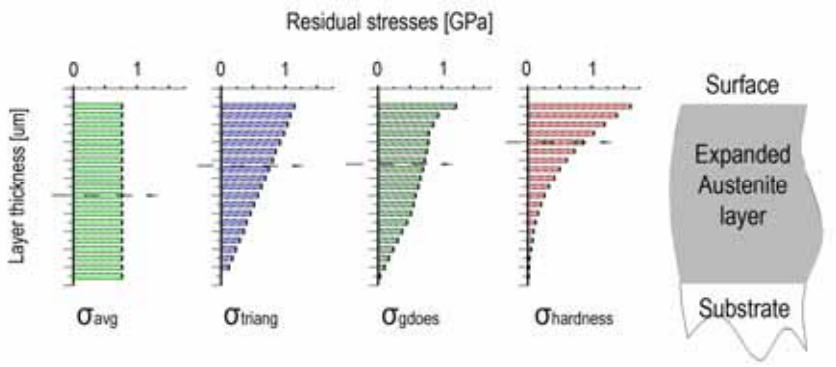

Figure 5.2-10: Distribution of residual stress: average, triangular, GDOES and strain hardened profiles

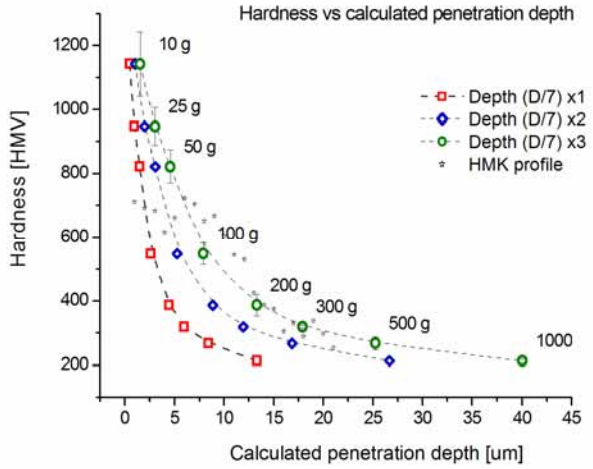

Figure 5.2-11: Hardness profiles calculated from LBC and Knoop hardness profile

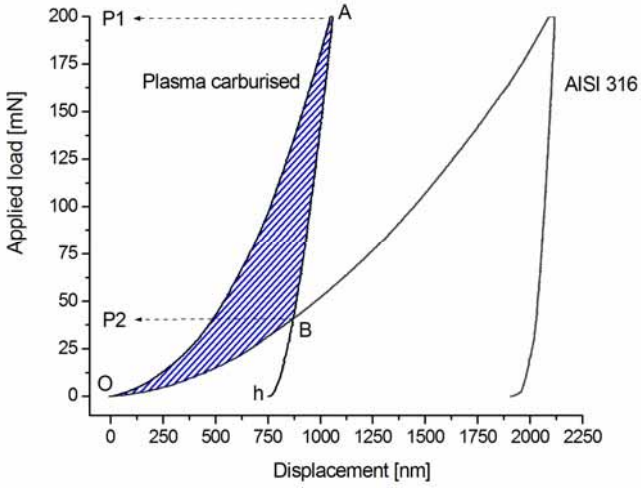

Figure 5.2-12: Estimation of residual stresses from instrumented indentation tests according to [238]

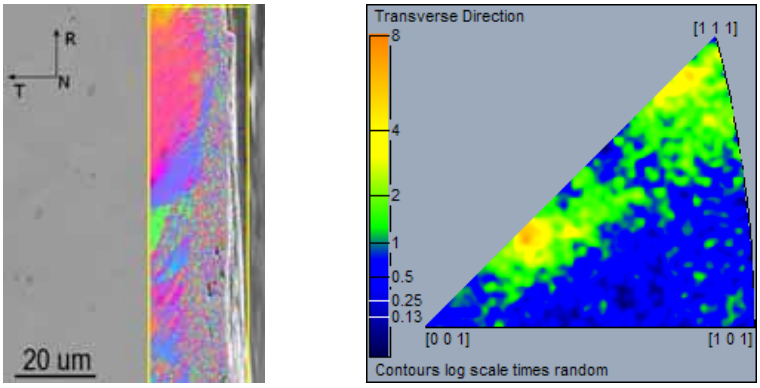

Figure 5.3.1-1: SE image of the cross section of a wear track on AISI 316 UT with EBSD COM superimposed and inverse pole figure obtained from that same area of the sample

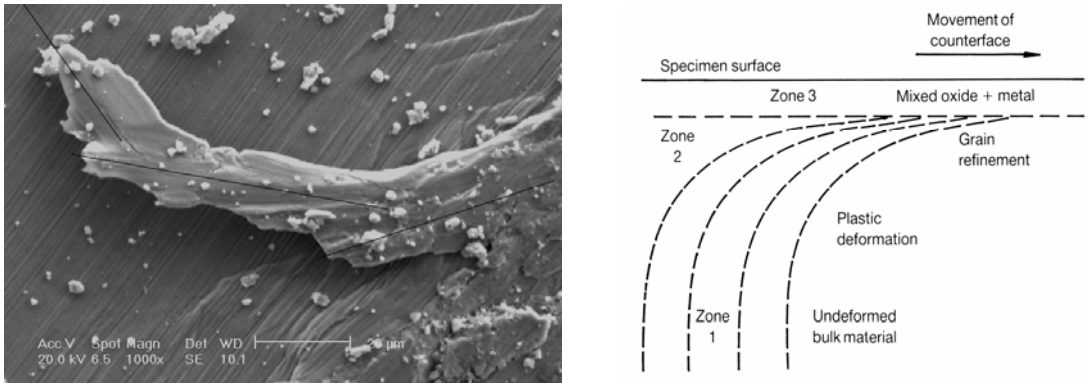

Figure 5.3.1-2: Signs of accumulated plastic strain (3 steps of deformation) at the edge of the wear track of AISI 316 UT, and schematics of the deformation in the subsurface region.

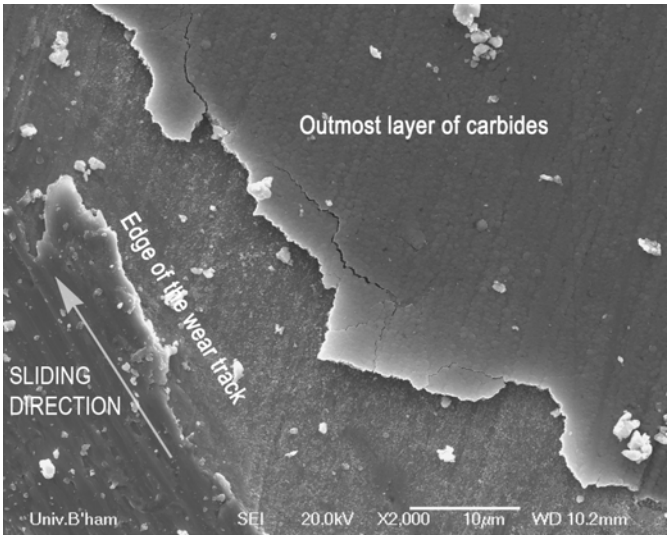

Figure 5.3.2-1: Failure of the layer of carbides at the edge of a wear track on AISI 316 PC

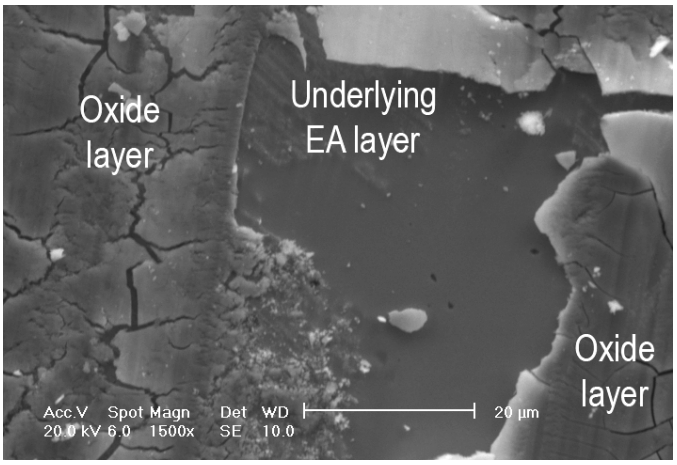

Figure 5.3.2-2: Smooth surface of the underlying EA layer, and protective oxide layer formed during sliding wear

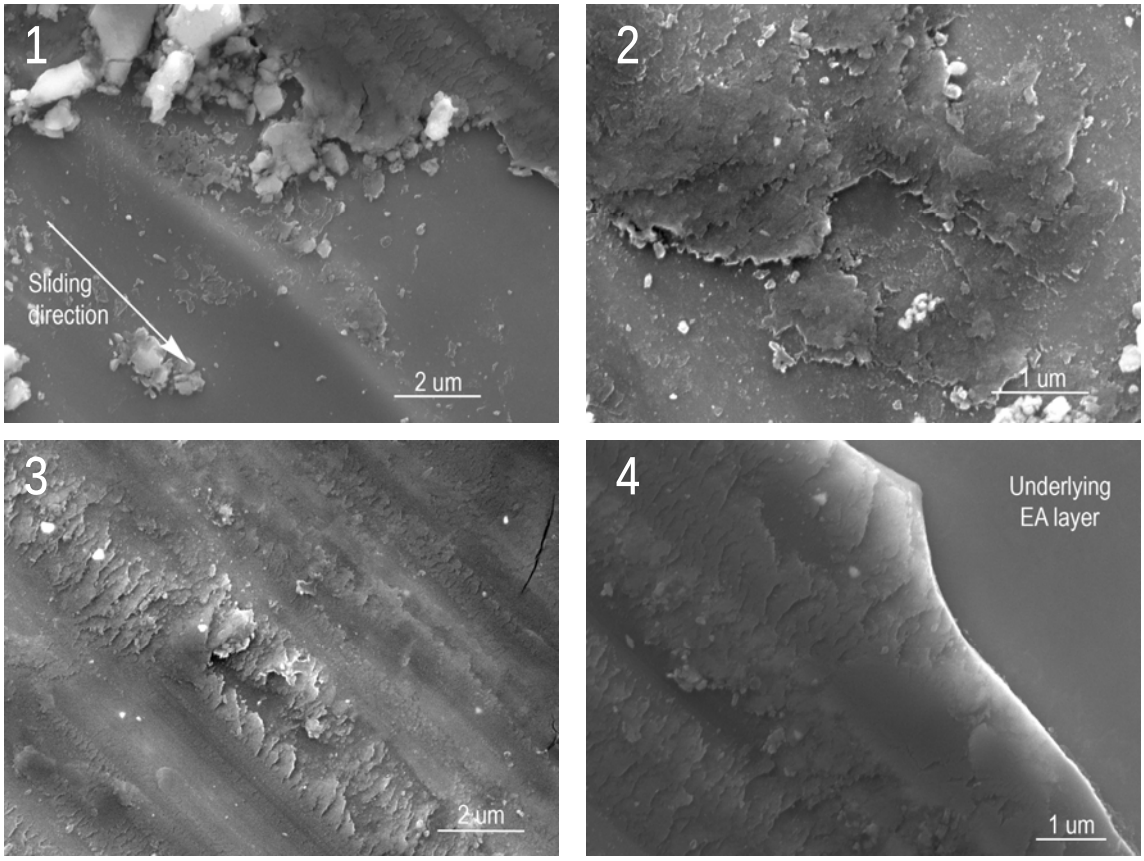

Figure 5.3.2-3: Genesis of the protective oxide layer on a PC specimen

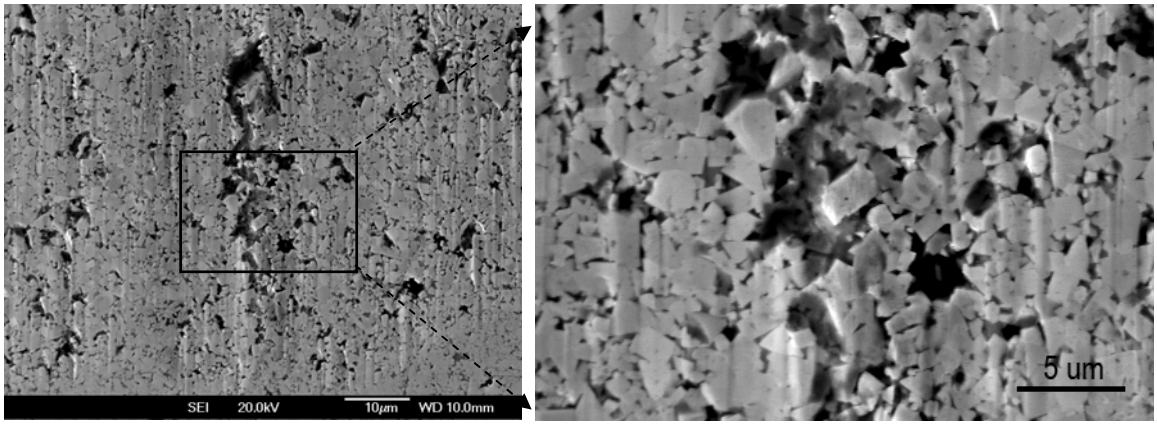

Figure 5.3.2-4: Detachment of WC particles from the counterpart ball

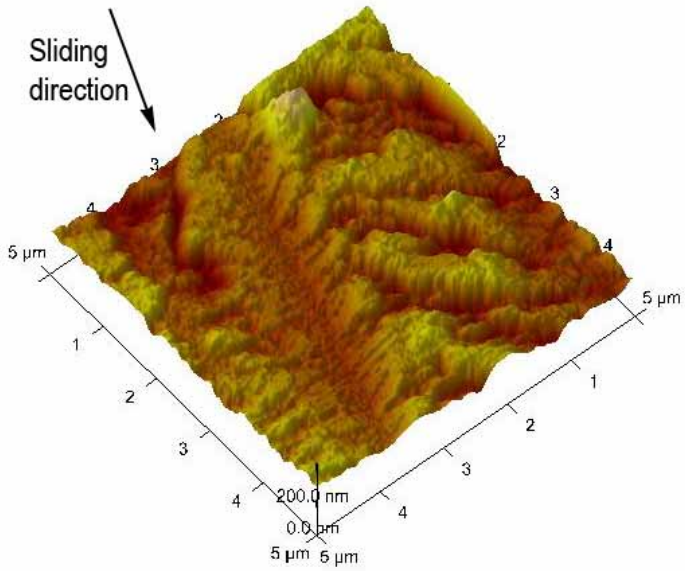

Figure 5.3.2-5: Morphology of the protective oxide layer on a PC specimen under AFM

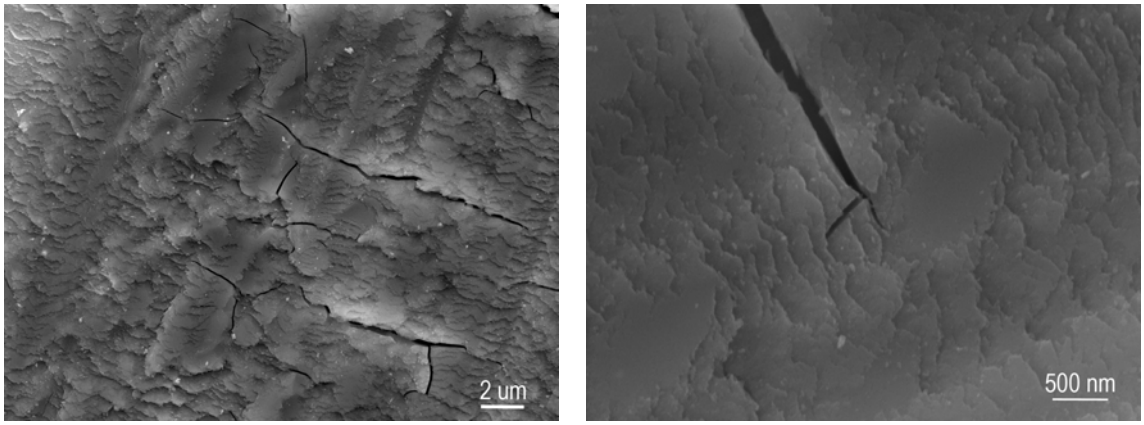

Figure 5.3.2-6: Crack propagation along the original deformation morphology in the protective oxide layer

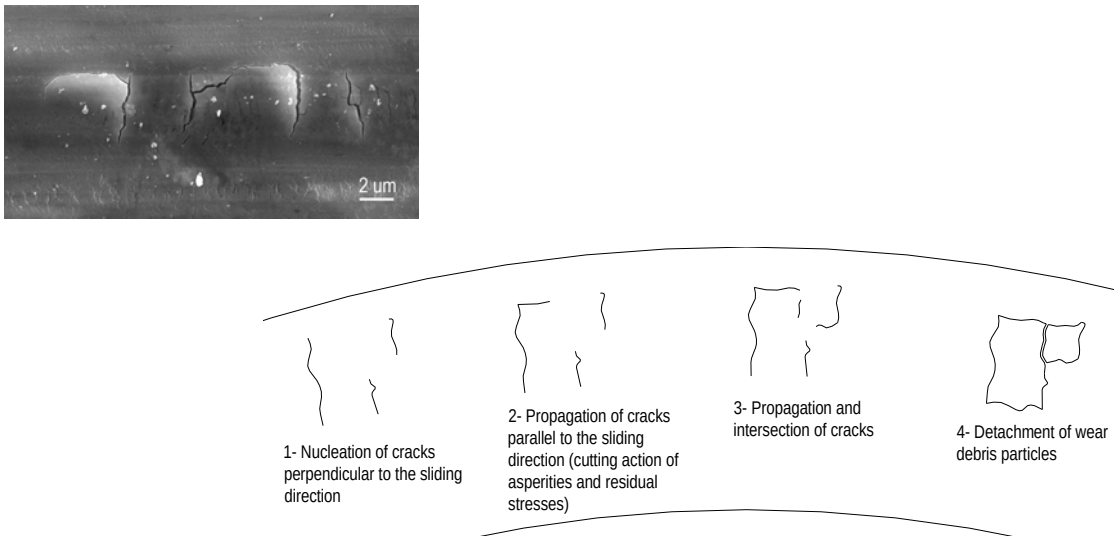

Figure 5.3.2-7: Process of detachment of wear debris from the protective oxide layer. SEM image and schematics

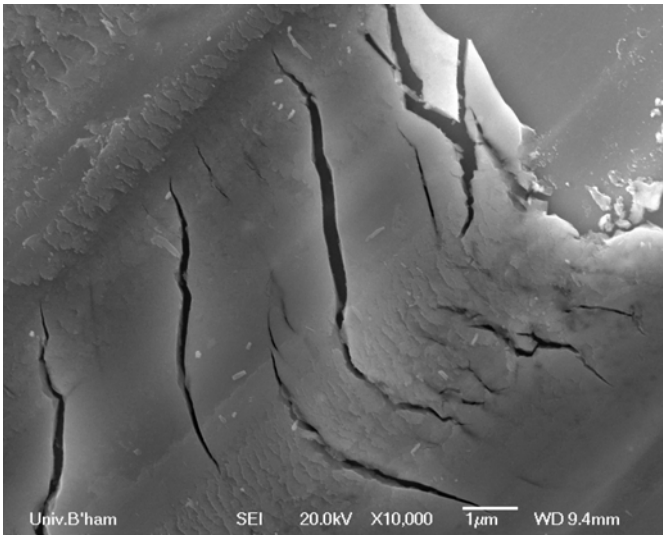

Figure 5.3.2-8: Cracks on a thick portion of the protective oxide layer

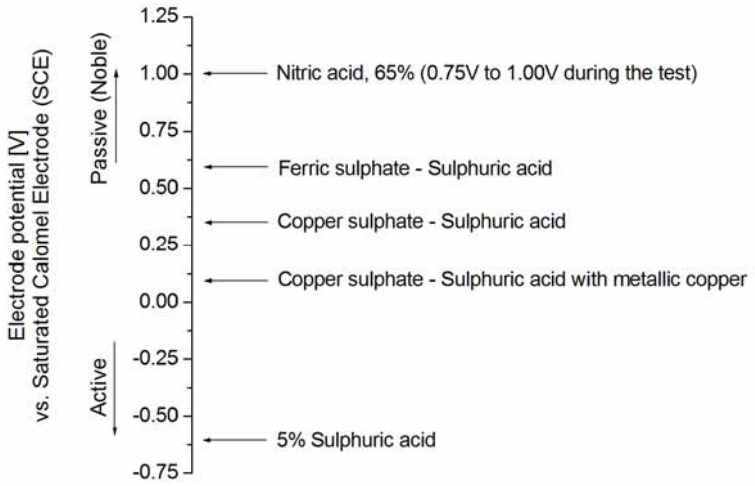

Figure 5.4.1-1: Corrosion potential of ASS in different acid solutions vs saturated calomel electrode [2]

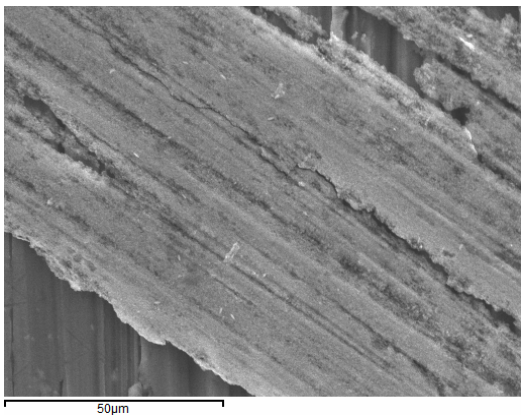

Element	Weight %
C	19.1
O	7.7
S	0.3
Cr	17.0
Mn	1.2
Fe	48.0
Ni	1.4
Cu	3.1
Mo	2.2

Figure 5.4.2-1: SEM micrograph and chemical composition according to EDX of material pealed off from a PC sample at early stages of a corrosion test in boiling sulphuric acid

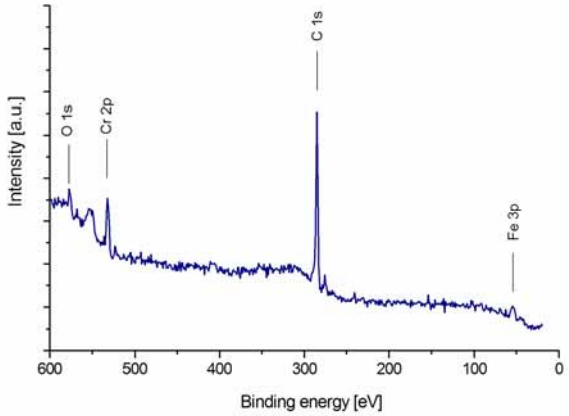

Figure 5.4.2-2: XPS spectrum obtained from the surface of an ASPC sample

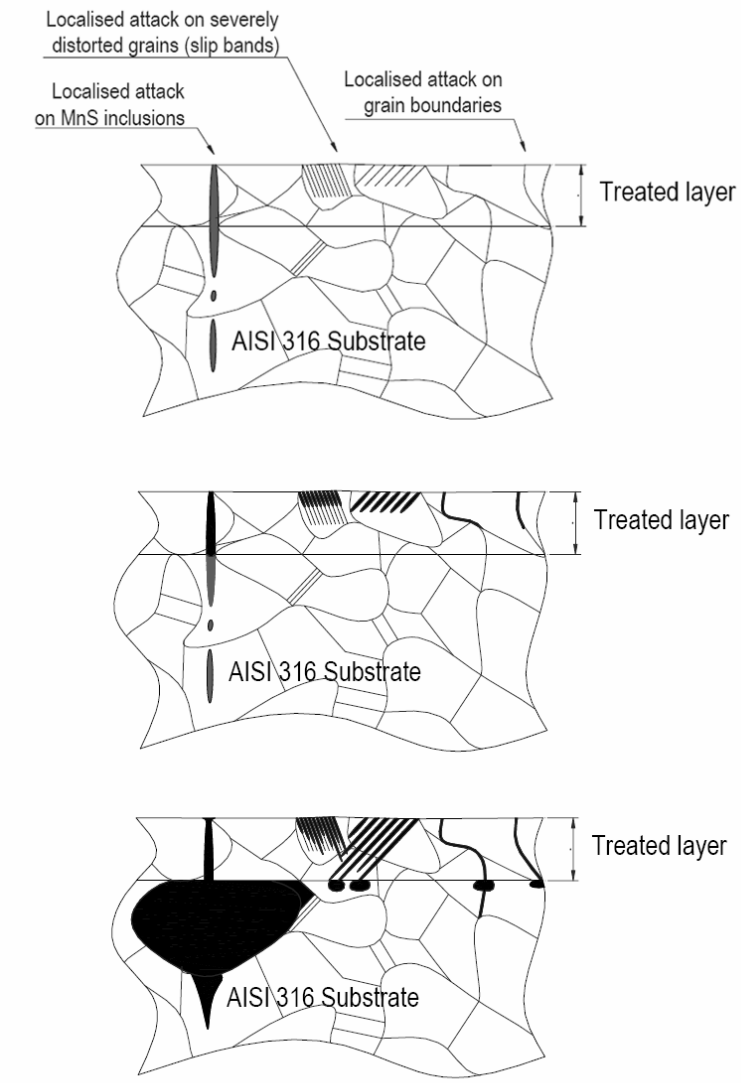

Figure 5.4.3-1: Schematics of the corrosion mechanisms observed on carbon expanded austenite

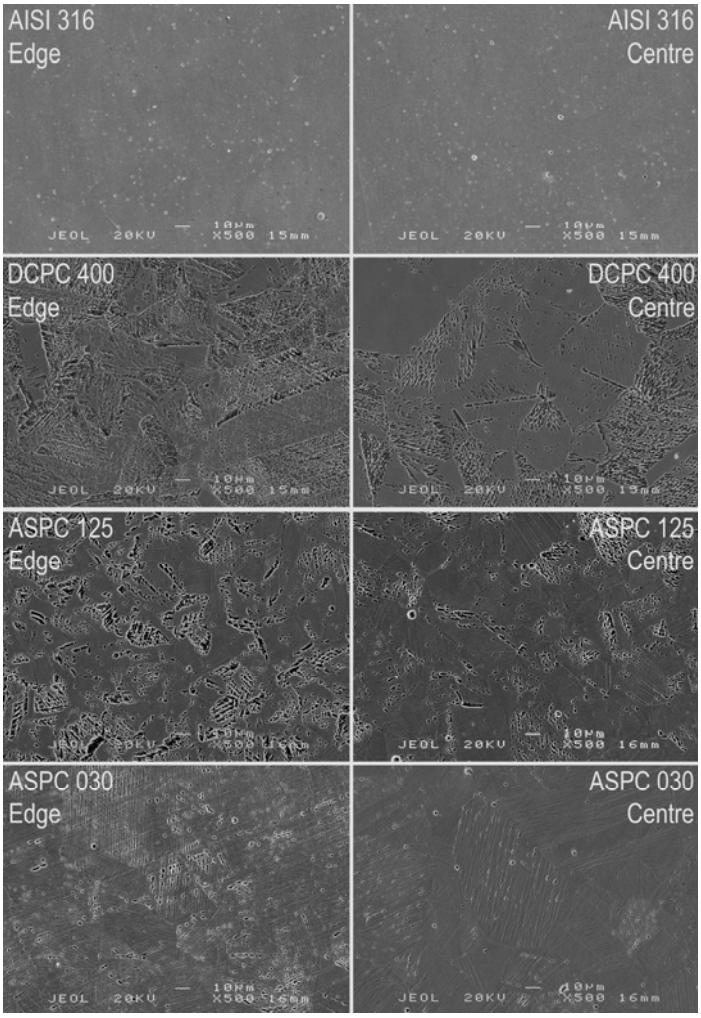

Figure 5.4.3-2: Morphology of specimens corroded in boiling H_2SO_4 16% solution with $CuSO_4$

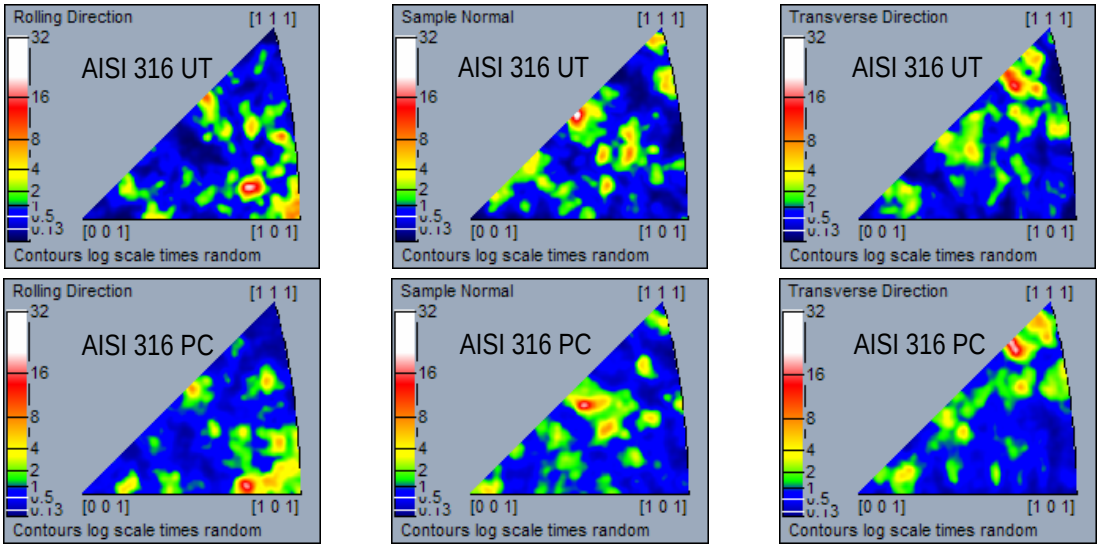

Figure 5.4.4-1: Inverse pole figures obtained by EBSD on the same area of the sample before and after PC

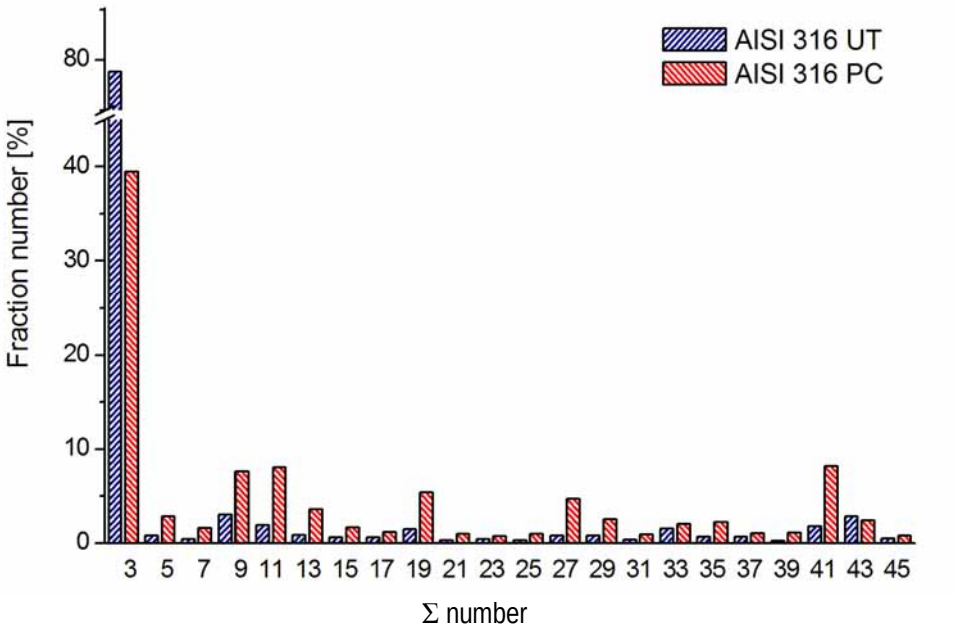

Figure 5.4.4-2: Fraction number of special grain boundaries before and after PC

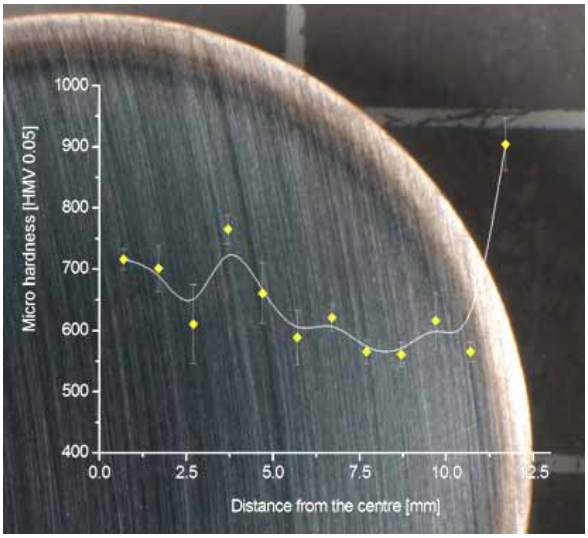

Figure 5.4.4-3: Edge effect revealed by microhardness measurements across the surface of a DCPC sample

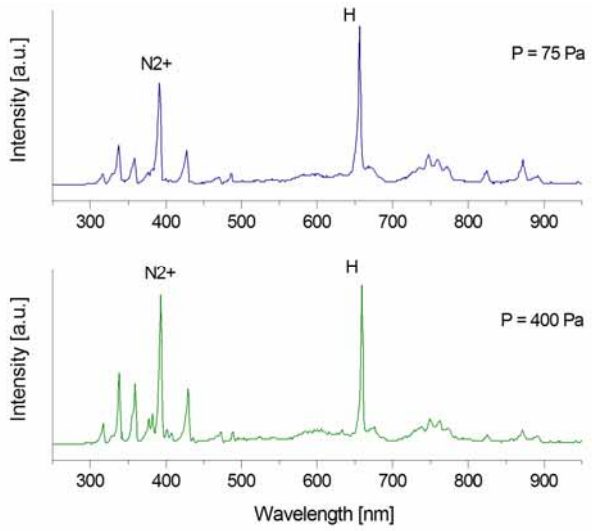

Figure 5.5.2-1: Optical emission spectra collected at different gas pressures in a 75% N_2 - 25% H_2 gas mixture

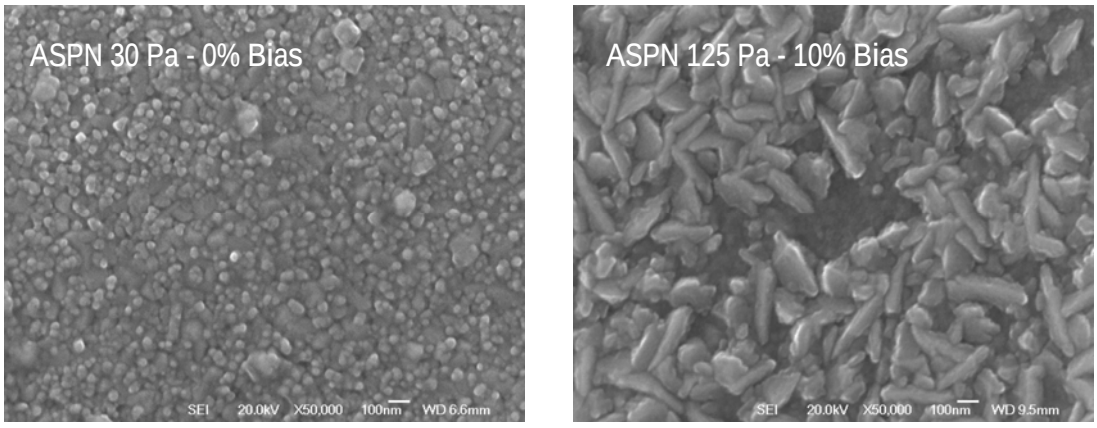

Figure 5.7.1-1: Morphology of the deposition layer under different ASPN treatment conditions

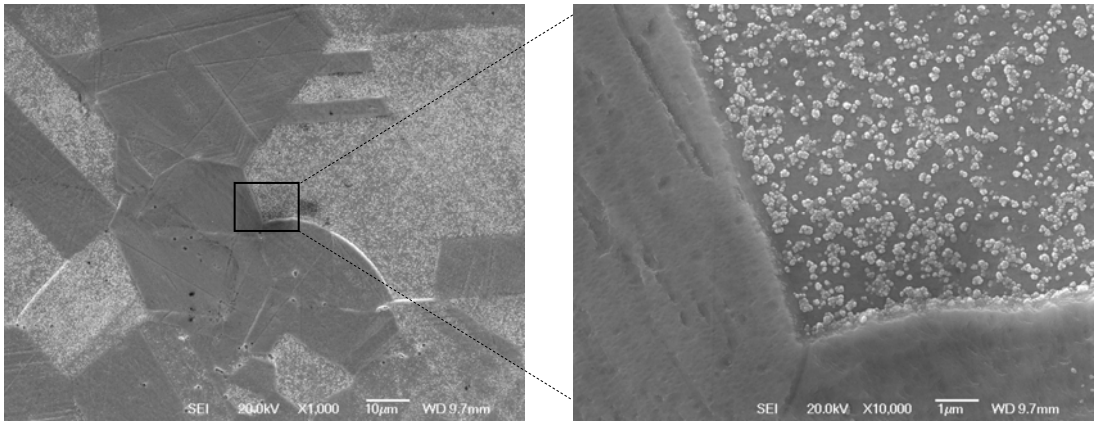

Figure 5.7.1-2: Deposition layer on grains with different crystallographic orientations

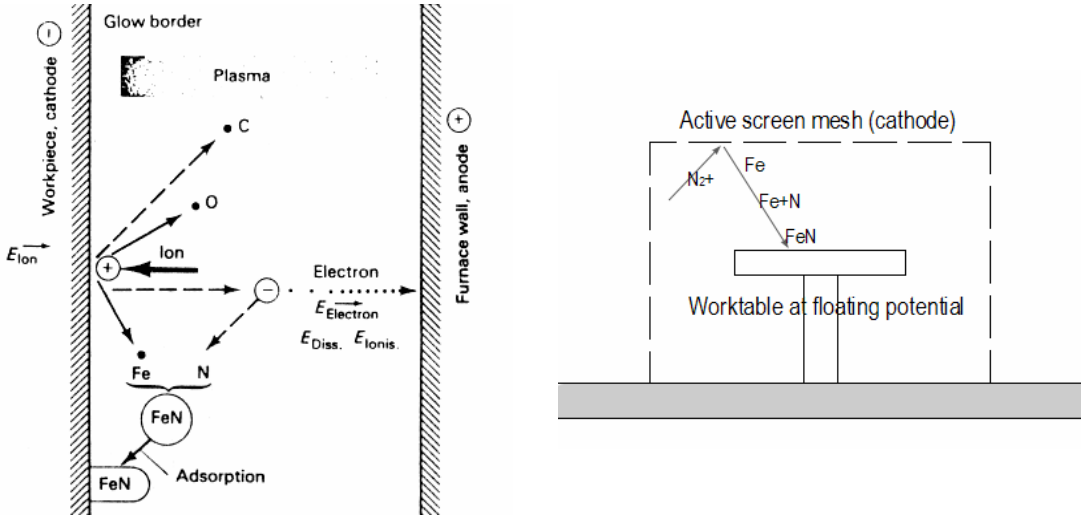

Figure 5.7.1-3: Sputtering and redeposition model for DC [154] and AS plasma nitriding

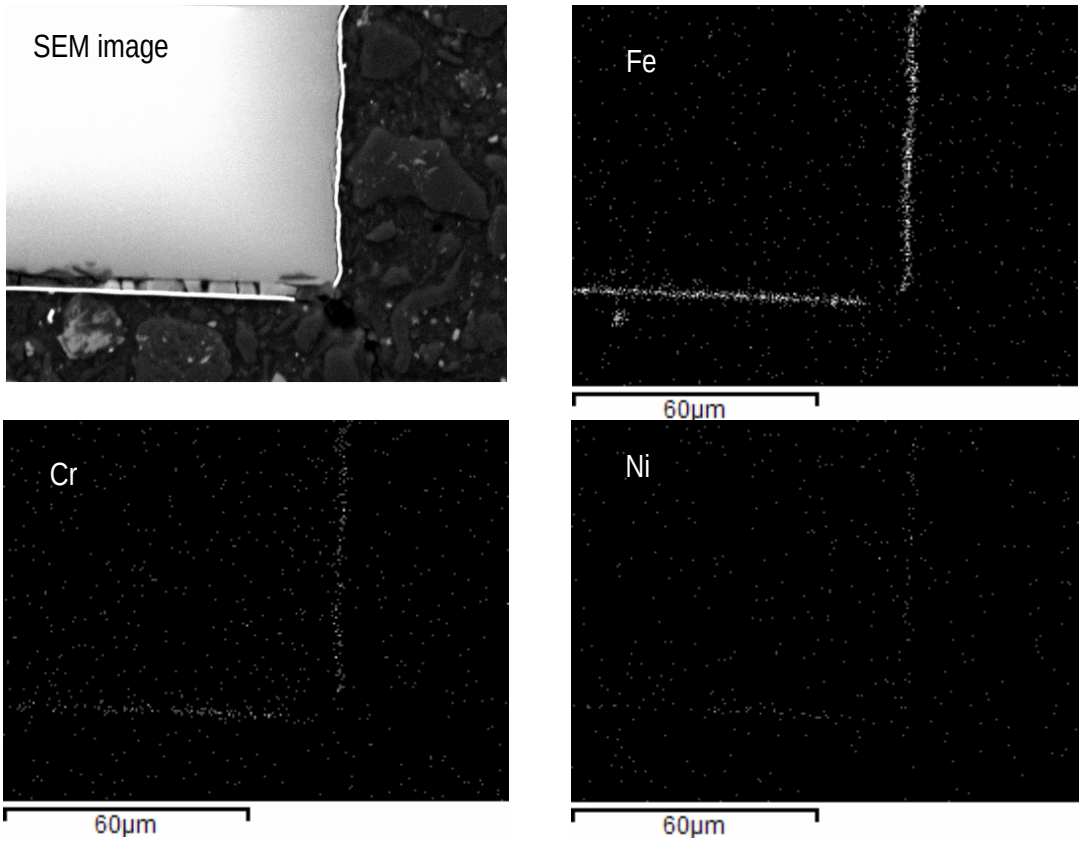

Figure 5.7.1-4: Deposition layer on a glass slide treated in an AS arrangement with an AISI 304 mesh

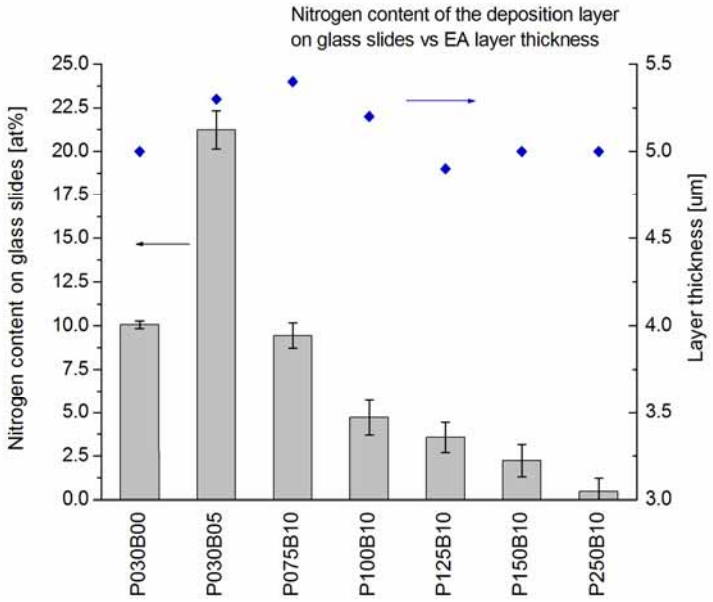

Figure 5.7.1-5: Deposition layer (EDX) vs expanded austenite layer thickness (GDOES)

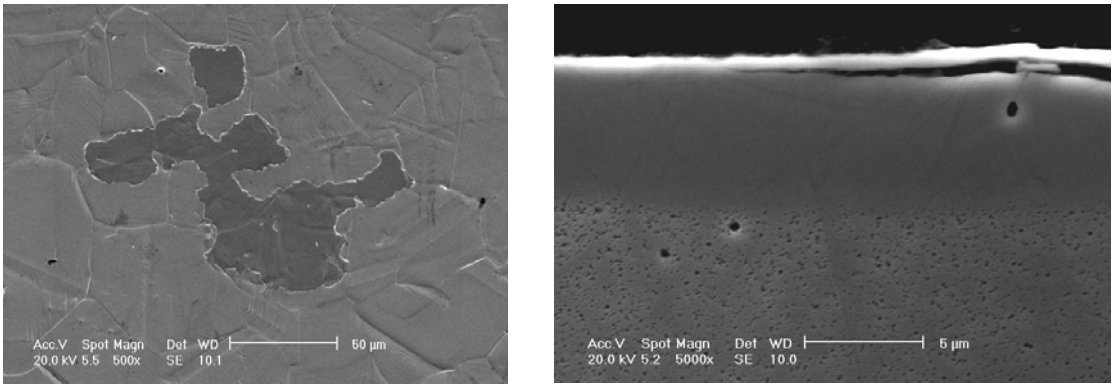

Figure 5.7.1-6: Detachment of the deposition layer of iron nitrides AS plasma nitrided at floating potential

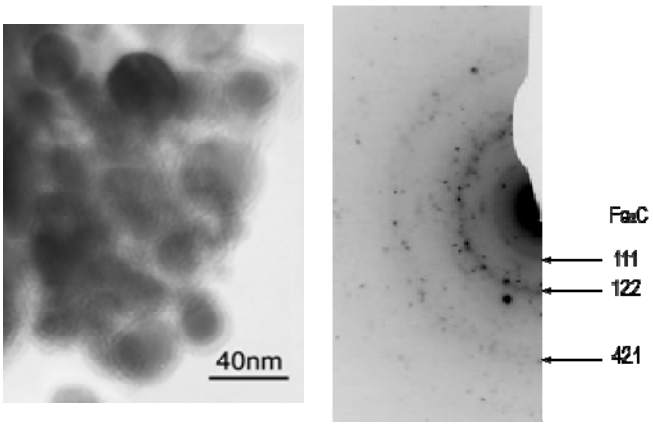

Figure 5.7.2-1: TEM micrograph of the deposited particles and EDP

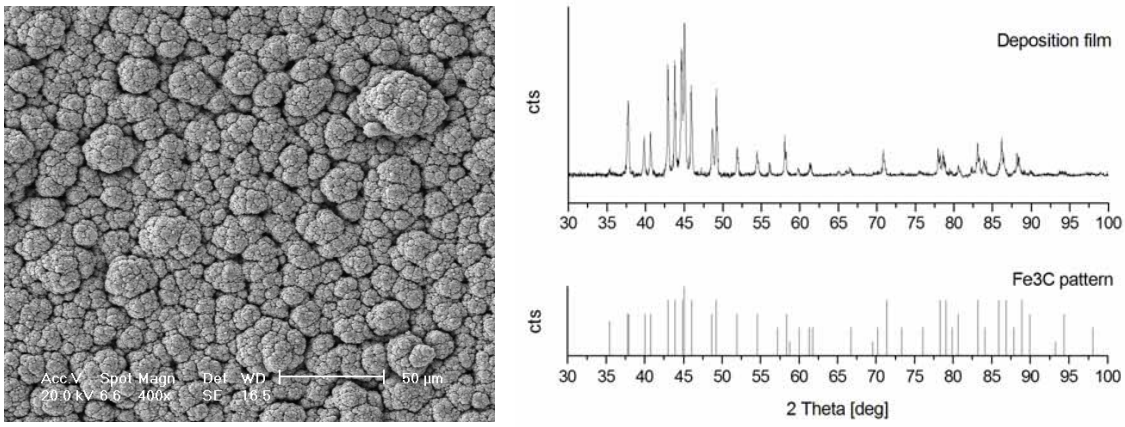

Figure 5.7.2-2: SEM micrograph and XRD pattern from carbide film deposited on the walls of the AS furnace

Appendix A: OES optical fibre probe construction details

The spectra collected with the telescope were useful to identify the active species present in the plasma, although no clear trend could be found when comparing the emission intensities at different treatment conditions. This can be explained considering that the mesh of the active screen furnace is designed to form hollow cathodes in different ways, depending on the treatment conditions. The existence of hollow cathodes in the field of view could not be avoided nor kept constant, and the emission intensity was significantly affected by them. Furthermore, it did not represent the conditions on the work table. Therefore, collection of light from the worktable, in the proximity of the samples or components was considered of interest.

Aomolin Ltd UV-Vis silica optical fibre of core diameter 100/110 μm (NA 0.22) was selected for the construction of the probe. The fibre was cut into 5 m long strings, and four strings were threaded together through the stainless steel shell. A bundle of four optical fibres was necessary in order to increase the intensity of the signal, which was otherwise too weak, especially when the high resolution grating was used, i.e. with larger spectral dispersion. This method was good enough for the purpose of the current work, although alignment was problematic, and probes made with single fibres of larger core diameter could be useful for future applications.

The shell of the feedthrough was made of a stainless steel tube, with a quick fit type flange on one end, which allowed an easy attachment to any of the standard instrumentation ports of the furnace (figure A.1). An insulating and temperature resistant ceramic adhesive, Aremco Ceramcast 586 ($ZrSiO_4$), was used to fill the gap between the optical fibres and the stainless steel tube, and the feedthrough was cured in an oven following the thermal cycle suggested by the supplier (table A-1). Finally, the outer side of the feed through was sealed with an epoxy resin to reduce the leaks and not to affect the quality of the vacuum in the furnace.

The optical fibre feedthrough was then installed in the active screen furnace and the fibres were placed on top of ceramic insulators. It is worth noting that if the optical fibres are subjected to the cathodic potential of the work table during the treatment, severe arcing takes place, with the associated instability of the process and risk of permanent damage or destruction of the optical fibres.

The polymeric buffer coating of the fibres did not resist the operating conditions, but a layer of metallic material was deposited on the fibres after only a few hours of exposure to the plasma. This metallic

coating was found to protect the fibres, making them tougher, and also contributed to block stray light from other parts of the plasma volume inside the furnace. Therefore, light was only collected from a small area in front of the open end of the fibres, achieving a spatial resolution much higher than with the telescope.

An insulating ceramic tube was used to aim the bundle of fibres in the direction of interest and to reduce deposition of sputtered material on their open ends. Nonetheless, deposition still blocked the fibres after several hours of exposure to the plasma and, as a result, it was necessary to cleave the fibres before each experiment, and to shorten the data collection time as much as possible in order to get intense and comparable signals.

The other ends of the optical fibres were stripped from the buffer polymer coating, cleaved and fitted with an SMA connector, to feed the signal into the Triax 180 spectrometer.

For the assessment of the transmission efficiency before and after exposure to the plasma environment, their respective transmission efficiencies, in the range 200 nm to 1100 nm, were recorded and compared. The exposed and unexposed optical fibres were fitted with Bullet bare fibre connectors and plugged into an Ocean Optics HL-2000-FHSA halogen light source (table A-2) and an Ocean Optics HR2000 high resolution miniature fibre optics spectrometer (table A-3).

Analysis of potential sources of error [1]

In order to confirm the validity of the collected signal, some of the probable sources of error were assessed. In first place, the effect of the plasma on the transmission efficiency of the optical fibres was considered. A deposition layer of, mainly, iron nitride covered a large proportion of the surface of the optical fibres exposed to the plasma (figure A-2), and the effect of this layer of material on the transmission efficiency was uncertain. Therefore, the transmission spectra of optical fibres exposed and unexposed to the plasma were compared. No significant difference was observed between the two transmission spectra (figure A-3), which indicated that the fibres were in good condition even after several tens of hours exposed to the N_2 - H_2 and CH_4 - H_2 plasma atmospheres.

In addition, the deposition layer was found to coat the open end of the optical fibres after only a few hours of exposure to the plasma, and this coating hindered light from being collected. For this reason,

the fibres had to be cleaved before each set of measurements. However, the cleavage mode of the fibres was of importance: whilst a clean cut perpendicular to the longitudinal axis produced the highest collection efficiency, a rough end significantly reduced the collected signal. Consequently, the cleavage mode was studied, and it was found that the optical fibres exposed to plasma were most frequently cleaved at 90º from their longitudinal axis (figure A-4). Furthermore, a poor condition of the open ends of the fibres could be identified and avoided before the experiment.

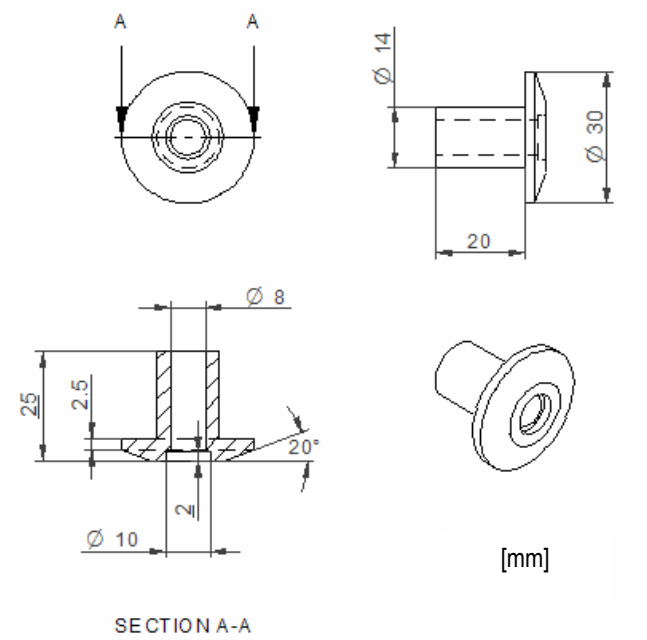

Figure A-1: Dimensions of the stainless steel shell for optical fibre feedthroughs

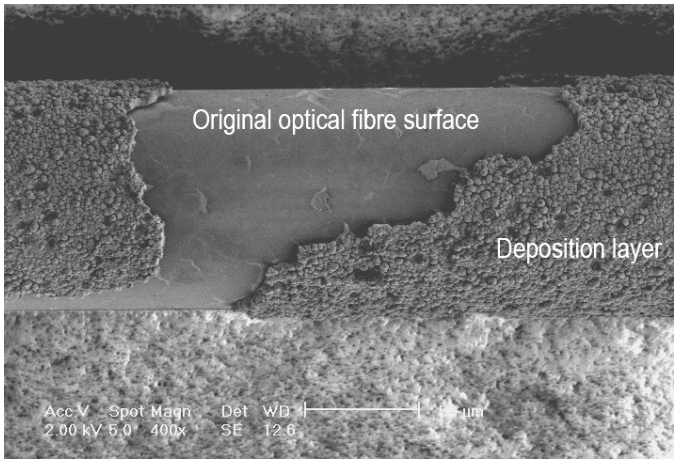

Figure A-2: Deposition layer observed on an optical fibre exposed to the plasma in an AS furnace

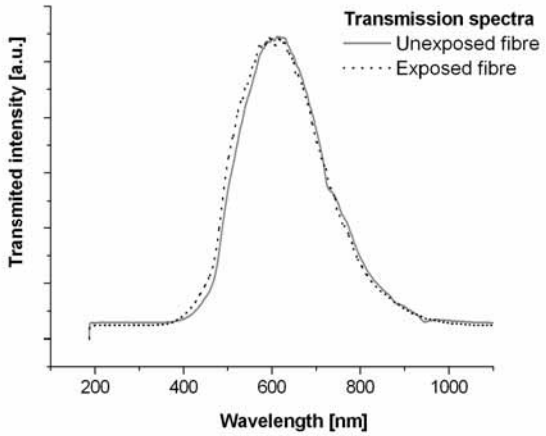

Figure A-3: Transmission spectra of optical fibres exposed and unexposed to the plasma

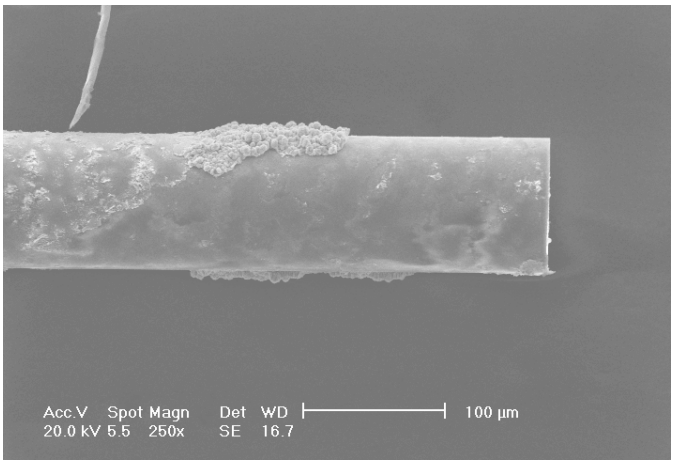

Figure A-4: Cleavage mode of optical fibres exposed to the plasma

Table A-1: Aremco Ceramcast 586 curing cycle

Type	Temperature	Time
Air	Room	8 hours (minimum)
Oven	200ºF (90ºC)	2 to 4 hours
Oven	250ºF (120ºC)	3 hours

Table A-2: Ocean Optics Halogen light source HL-2000-FHSA – Technical specifications

Variable	Value
HL-2000-FHSA	Includes filter holder, attenuator and shutter
Output	7 watts
Output to bulb	1.4 A @ 5 VDC
Wavelength range	360 nm-2 µm
Stability	0.5%
Drift	<0.3% per hour
Time to stabilise	~5 minutes
Bulb colour temperature	2,960 K

Table A-3: Ocean Optics HR2000 high resolution fibre optic spectrometer - Technical specifications

Variable	Value
Detector	Sony ILX511 linear CCD array
Detector Range	200 nm -1100 nm
Pixel size	14 µm x 200 µm
Optical bench	f/4, 101 mm focal length
Gratings	Choose from 13 different gratings
Pixel elements	2048
Entrance Aperture	5, 10, 25, 50, 100 or 200 µm wide slits or fibre (no slit)
Order-sorting filters	Installed longpass and bandpass filters
Stray Light	<0.05% at 600 nm; <0.10% at 435 nm
Dynamic Range	2×10^8 (system); 2000:1 for a single scan
Fibre Optic Connector	SMA 905 to single-strand optical fibre 0.22 NA)
Data Transfer Rate	Full scans into memory every 13 ms
Integration Time	3 ms to 65 s

Appendix B: Ion Flux Probe (IFP) construction details

OES is a very useful technique to provide information on the active species involved in the plasma. However, the information it yields is incomplete as it comes only from excited species, while no direct evidence is obtained from the electrons, which are the primary agents in the plasma. This kind of information can be obtained from electric probes, and it was thus the intention in this project to develop and use an electric probe as a complementary method for the OES plasma diagnostic technique.

A planar electric probe was made of copper, with a central disc as the actual probe and two guarding rings surrounding it (figure B-1). The guarding rings were meant to avoid edging effects on the central disc, making the sheath in front of it flat and even. The surface area of the central disc and the inner guarding ring are the same, while the exposed area of the outer guarding ring is twice as large (figure B-2). They were finely turned and the active surfaces were wet ground with silicon carbide grinding paper, and polished with activated colloidal silica.

The isolation between the central disc and the guarding rings was achieved using DuPont Nomex Aramid paper type 410 (table B-1). This type of temperature resistant insulating paper was found convenient in view of its thermal resistance, dielectric and mechanical properties and low cost. From two to four layers of 0.25 mm thick insulating paper were used in all cases and new insulating sheets and washers were used for each experiment. The paper was found to resist the treatment conditions here studied, but its use is not recommended for longer periods of time or higher temperatures.

The central disc was silver soldered to a copper wire and connected with the measuring circuit, through a standard electric feedthrough, by means of gold coated pin connectors (figure B-3). The guarding rings were not connected to the measuring circuit due to a technical inconvenient, and remained at floating potential during the experiments.

The probe was mounted on ceramic insulating tubes, to support it and insulate it from the high cathodic potential of the work table (up to 900 V DC). Two ceramic tubes were attached together by means of steel bolts, which also played the role of spacers for copper wires to be connected to the probe (figure B-1). To avoid deposition of conductive material on the live parts of the measuring circuit, the copper wire was insulated with ceramic beads throughout its length, and it was also guided inside an insulating

ceramic tube until the proximity of the probe. All the ceramic insulating tubes had to be wet ground and washed before each experiment to eliminate the layer of conductive material deposited on them.

Regarding the measuring circuit, tantalum capacitors were selected in view of their low electric charge leak rate in air, allowing retention of charge for longer times. The 63 V and 4.7 μF tantalum capacitors were connected to a 60 V DC power supply with a 10 Ω resistor in series. Heavy duty toggle switches were used for the connection and disconnection of the probe and the power supply. Finally, high speed 0.8 A fuses were used to protect the measuring circuit in case of electric fault, and the operating panel was conveniently earthed.

A low noise Instek GPS-6010 DC power supply with variable output voltage (0 V to 60 V) was connected to charge the capacitors and, subsequently, to bias the probe (table B-2). A Pico 2202 digital oscilloscope and 250 MHz oscilloscope probe, with an impedance of 50 MΩ and an attenuation power of 10, were used to acquire the drain curve of the tantalum capacitors (table B-3). The oscilloscope was connected to the USB port of a PC and the signal was monitored and stored in the hard drive of a PC using PicoScope 5.15.6 (32 bit) data collection software.

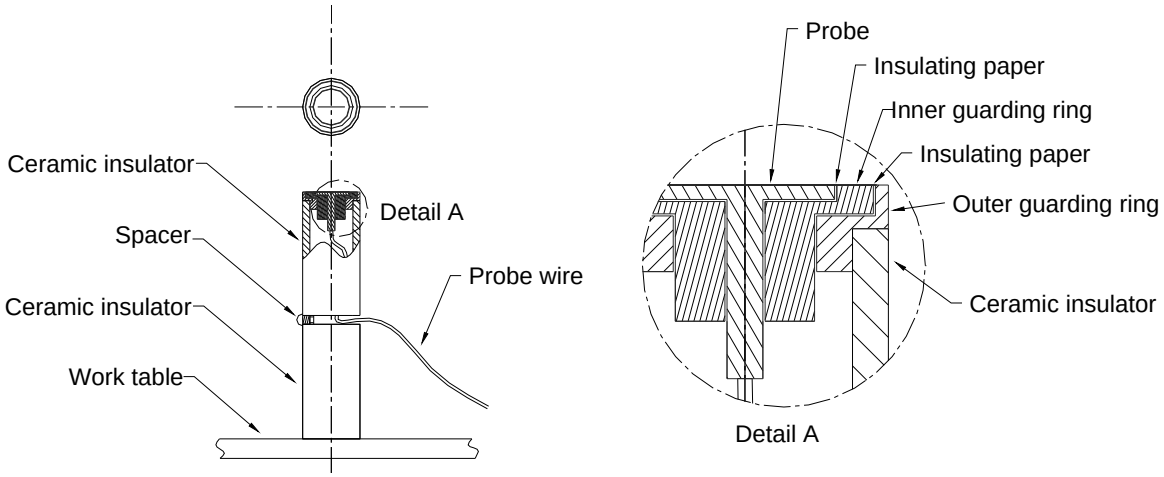

Figure B-1: Schematics and constructive details of the IFP

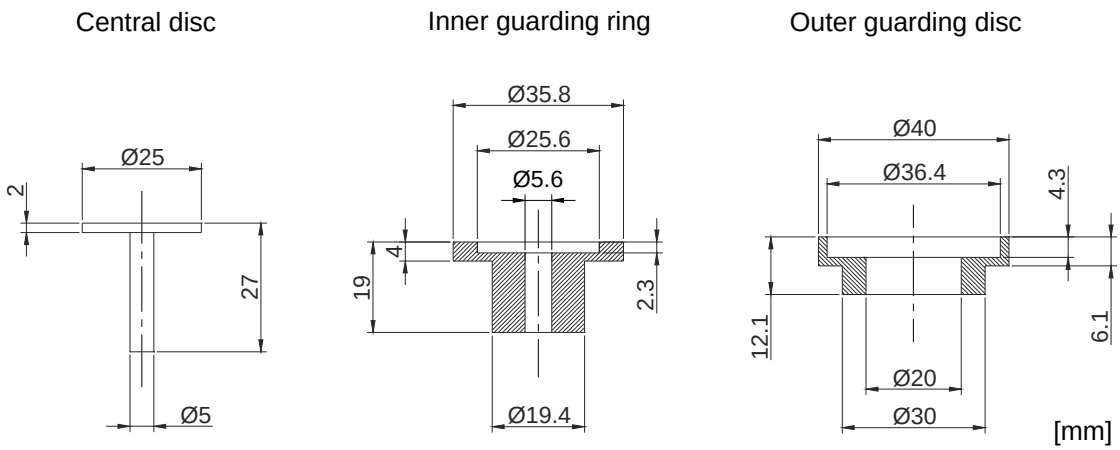

Figure B-2: IFP - Dimensions of the central disc, inner and outer guarding rings

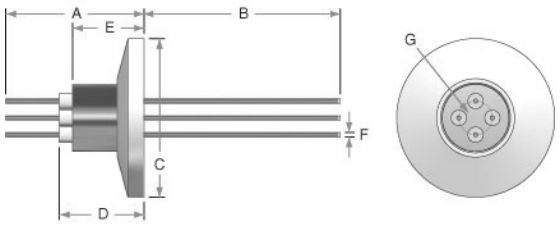

A	B	C	D	E	F	G	
0.93	1.57	1.57	0.53	0.43	0.032	0.25	[in]
23.6	39.9	39.9	13.5	11.0	0.81	6.3	[mm]

Figure B-3: Lesker EFT0043038A feedthrough – Stainless steel KF25 flange, 4 copper pins

Table B-1: DuPont Nomex Aramid Insulation paper type 410 – Technical specifications

Variable	Value
Nominal thickness	0.25 mm
Dielectric strength (AC rapid raise)	32 kV/mm
Dielectric Strength (full wave impulse)	63 kV/mm
Dielectric constant at 60 Hz	2.7
Dissipation factor at 60 Hz	6

Table B-2: Instek GPS-6010 DC power supply – Technical specifications

Constant Voltage Operation	
Line Regulation	0.01% +3 mV
Load Regulation	0.01% +3 mV (rating current 3 A) 0.01% +5 mV (rating current >3 A)
Ripple and Noise	0.5 mV_{rms} 5 Hz ~ 1 MHz (rating current 3 A) 1 mV_{rms} 5 Hz ~ 1 MHz (rating current >3 A)
Recovery Time	100 µs (50% load change, minimum load 0.5 A)
Output Range	GPS-6010: 0 V to 60 V, continuously adjustable
Constant Current Operation	
Line Regulation	0.2% +3 mA
Load Regulation	0.2% +3 mA
Ripple Current	3 mA_{rms}
Output Range	GPS-6010: 0 A to 1 A, continuously adjustable (HI/LO range switchable)
Meter	
Meter Type	Analogue voltmeter and analogue ammeter 2.5 class
Insulation	
Chassis and Terminal	20 MW or above (500 V DC)

Table B-3: Pico 2202 digital oscilloscope – Technical specifications

Vertical selection (signal axis)	
Bandwidth	5 MHz
Channels	2
Resolution	8 bits
Enhanced resolution	12 bits
Dynamic range	48 dB
Accuracy	3%
Input ranges	±50 mV, ±100 mV, ±200 mV, ±500 mV, ±1 V, ±2 V, ±5 V, ±10 V, ±20 V
Input characteristics	1 MΩ 20 pF
Overload protection	±100 V on single output
Input type	Single ended BNC connector
Input coupling	AC or DC (software controlled)
Horizontal selection (time axis)	
Sampling rate	40 MS/s (1 GS/s ETS)
Record length	8,000 samples
Time ranges	500 ns, 1 µs, 2 µs, 5 µs… up to 50 s, 100 s, 200 s per division
Time base accuracy	0.0001 with 3 ps jitter

Appendix C: Residual stresses formulas

Stoney's formula according to British Standard DD 1071-11:2005 [2]:

$$\sigma_0 = -\frac{1}{6}\frac{E_S}{1-\nu_S}\frac{d_S^2}{\delta_{EA}}\frac{1}{R} \qquad \text{(C.1)}$$

where σ_0 is the mean value of residual stress through the thickness of the layer, E_S is the elastic modulus of the substrate, ν_S is Poisson's ratio of the substrate, d_S and δ_{EA} are the thickness of the substrate and the layer of expanded austenite respectively, and R is the radius of curvature of the disc measured after the treatment (figure C-1).

Modified Stoney's formula proposed by A. Mézin [3]:

$$\sigma_0 = -\frac{1}{6}\frac{E_S}{(1-\nu_S)}\frac{d_S^2}{\delta_{EA}}\frac{1}{R}\left[1+\left(4\frac{E_{EA}(1-\nu_S)}{E_S(1-\nu_{EA})}-1\right)\frac{\delta_{EA}}{d_S}\right] \qquad \text{(C.2)}$$

where the first part of this formula is equivalent to the Stoney's formula described above, and the term between brackets is the proposed correction. Subscripts S and EA account for substrate (AISI 316) and expanded austenite respectively. The elastic modulus of EA was obtained from the instrumented hardness tests and the Poisson's ratio was considered equal to the untreated substrate.

Modified Stoney's formula proposed by Q. Wang et al. [4]:

$$\sigma_0 = -\frac{1}{6}\frac{E_S}{R}\frac{d_S^2}{\delta_{EA}}\left(1-\frac{\delta_{EA}}{d_S}\right) \qquad \text{(C.3)}$$

where the symbols have the same physical meaning as explained for the previous formulas.

XRD method proposed by Wagner et al. [5]:

The following expression was proposed to relate the stacking fault probability and the residual stress to the results obtained in a Bragg-Bentano geometry:

$$a_{hkl} = a_0 + a_0 G_{hkl} \cdot \alpha + a_0 (S_1)_{hkl} \sigma + m \cdot \cos\theta \cot\theta \qquad \text{(C.4)}$$

where a_{hkl} is the lattice parameter measured from the XRD data, a_0 is the lattice parameter of the annealed specimen, G_{hkl} is the fault parameter (table C-1), α is the stacking fault probability, S_1 is the elastic constant (table C-1), σ is the residual stress, m is the slope of the line in figure 4.2-11 and the value of cosθ·cotθ corresponding to a_{hkl}, which is the extrapolation function used in the same graph.

The second order reflections allow distinguishing both effects, namely the stacking fault and the residual stress, by making use of the following equation:

$$\Delta a_{hkl} = a_{hkl} - a_{hkl}^{app} = a_0 G_{hkl} \cdot \alpha + a_0 (S_1)_{hkl} \sigma - (a^{app} - a_0) \qquad \text{(C.5)}$$

where the superscript *app* refers to the apparent lattice parameter from the extrapolation of the trend line in figure 4.2-11 to cosθ·cotθ value of zero. For reflections (111) and (222), the second and third terms on the right side of the equation are equal so that this relation can be derived:

$$\frac{\Delta a_{111} - \Delta a_{222}}{a_0} = -0.0518 \cdot \alpha \qquad \text{(C.6)}$$

The value of α can be obtained from equation C.6 and inserted in equation C.4, which allows calculating the residual stress (table C-2)

Theory of thin plates and shells [6]:

Considering a thin plate as the one shown in figure C-1, and under the hypothesis of plane stress, i.e. biaxial isotropic residual stresses:

$$\sigma_z = 0 \qquad \text{(C.7)}$$

$$\sigma_x = \sigma_y = \sigma(z) \qquad \text{(C.8)}$$

The forces in the discs are balanced, but a bending moment is associated with the compressive residual stresses present in the EA layer. Consequently, the forces and moments per unit width can be obtained as:

$$f_x = f_y = \int_0^d \sigma(z) \cdot dz = 0 \qquad \text{(C.9)}$$

$$m_x, m_y = \int_0^d \sigma(z) \cdot \left(z - \frac{d}{2} \right) dz \neq 0 \qquad \text{(C.10)}$$

where f_x, f_y and m_x, m_y are the forces and moments per unit width respectively and d is the thickness of the disc.

On condition that the displacements associated with the bending of the discs are small compared to their thickness, and that the cross sections of the discs remain plane and rotate only with respect to the neutral axes, the theory of pure bending of plates applies, and the strains ε can be defined as:

$$\varepsilon_x = \frac{\sigma_x}{E} - \nu \frac{\sigma_y}{E} \qquad \text{(C.11)}$$

$$\varepsilon_y = \frac{\sigma_y}{E} - \nu \frac{\sigma_x}{E} \qquad \text{(C.12)}$$

where E is the Young's modulus and ν is Poisson's ratio. The bending moments per unit width can thus be defined as:

$$m_x = \frac{Ed^3}{12\left(1-\nu^2\right)} \cdot \left(\frac{1}{r_x} - \nu \frac{1}{r_y} \right) \qquad \text{(C.13)}$$

$$m_y = \frac{Ed^3}{12\left(1-\nu^2\right)} \cdot \left(\frac{1}{r_y} - \nu \frac{1}{r_x} \right) \qquad \text{(C.14)}$$

And in this particular case, the disc is bent into a sphere sector, so that both radii of curvature are equal:

$$\frac{1}{r_x} = \frac{1}{r_y} = -\varphi \Rightarrow m_x = m_y \qquad \text{(C.15)}$$

If we now consider the mean compressive residual stresses as the external load responsible for the bending of the disc:

$$\sigma_{avg}\delta\cdot\left(\frac{\delta+d}{2}\right)=\frac{Ed^3}{12\cdot(1-\nu)}\cdot\frac{1}{r} \quad \text{(C.16)}$$

where σ_{avg} is the average residual stress, δ is the EA layer thickness, and replacing the values listed in table C-3, σ_{avg} is found to be -0.770 GPa (sample ASPC P125B15).

If the stress distribution is approximated by a triangular distribution, and reducing the moments to the layer core interface it is obtained:

$$\left(\sigma_{surf}\frac{\delta}{2}\right)\cdot\left(\frac{2}{3}\delta\right)=\left(\sigma_{avg}\delta\right)\cdot\left(\frac{\delta}{2}\right) \quad \text{(C.17)}$$

$$\sigma_{surf}=\frac{3}{2}\sigma_{avg} \quad \text{(C.18)}$$

Using the previous calculated values, equation C.18 yields σ_{surf} = -1.155 GPa. A similar procedure is followed to calculate the residual stress profiles from GDOES carbon distribution and LBC strain hardening, yielding maximum residual stresses of -1.22 GPa and -1.61 GPa respectively.

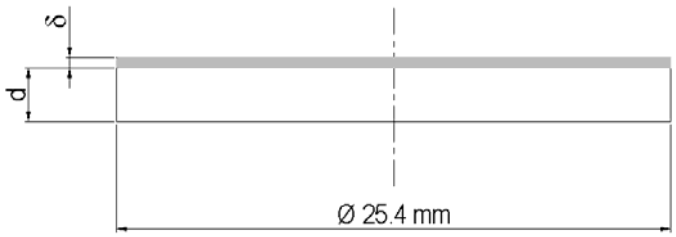

Figure C-1: Schematics of the thin discs used for the assessment of residual stresses (cross section): δ - expanded austenite layer thickness; d - disc thickness

Table C-1: Fault parameters and elastic constants for different reflections [7]

hkl	G_{hlk} x 10^2	$(S_1)_{hlk}$ x 10^5
111	-3.45	-0.97 kg/mm^2
200	+6.89	-2.97 kg/mm^2
220	-3.45	-1.47 kg/mm^2
311	+1.25	-2.03 kg/mm^2
222	+1.73	-0.97 kg/mm^2

Table C-2: Data used for the calculation of the residual stress on sample ASPC P125B15

hkl	a_{hkl}	a^{app}	a_0	α	m	cosθ·cotθ	σ
111	3.678 Å	3.6929 Å	3.68679 Å	0.0602	0.00255 Å	2.39	1.98 GPa
222	3.685 Å	3.6884 Å				0.65	

Table C-3: Parameters used for the calculation of residual stresses from the bending of thin discs

Parameter	Symbol	Value
Young's modulus	E	205 GPa
Poisson's ratio	v	0.305
Disc thickness	d	530 µm
Layer thickness	δ	20 µm
Radius of curvature	r	0.8962 m

List of references for appendices A, B and C

1. Corujeira Gallo, S., Machavaram, V. R., Fernando, G. F. and Dong, H.: *Probing active screen plasma using high-temperature optical fibre assisted OES method*, PSE 2008 (2008) Garmisch-Partenkirchen, Germany,

2. British Standard DD CEN/TS 1071-11:2005, 2005, "Advanced technical ceramics - Methods of test for ceramic coatings", BSI, London, www.bsi-global.com

3. Mezin, A.: *Coating internal stress measurement through the curvature method: A geometry-based criterion delimiting the relevance of Stoney's formula*, Surface and Coatings Technology (2006) 200, *18-19,* 5259-5267

4. Wang, Q., Ishikawa, H., Nakano, S., Ogiso, H. and Akedo, J.: *Curvature-based residual stress measurement for ion-implanted stainless-steel sheet*, Vacuum (2004) 75, *3,* 225-229

5. Wagner, C. N. J., Baisseau, J. P. and Aqua, E. N.: *X-Ray diffraction study of plastically deformed copper*, Transactions of the Metallurgical Society of AIME (1965) 233, *7,* 1280-1286

6. Timoshenko and Woinowsky-Krieger: *Theory of plates and shells*, 2nd Ed. (1959) London, McGraw Hill

7. Sun, Y., Li, X. Y. and Bell, T.: *X-ray diffraction characterisation of low temperature plasma nitrided austenitic stainless steels*, Journal of Materials Science (1999) 34, *19,* 4793-4802